

# **Response of noise-amplifier flows: From linear control to nonlinear jet breakup**

**Thèse N° 7227**

Présentée le 30 août 2019

à la Faculté des sciences et techniques de l'ingénieur  
Laboratoire de mécanique des fluides et instabilités  
Programme doctoral en mécanique

pour l'obtention du grade de Docteur ès Sciences

par

**Isha SHUKLA**

Acceptée sur proposition du jury

Prof. W. Curtin, président du jury  
Prof. F. Gallaire, directeur de thèse  
Prof. E. Lorenceau, rapporteuse  
Prof. A. Sevilla, rapporteur  
Dr M. Farhat, rapporteur

2019



To my family & Himank





# Acknowledgements

I view the four years of my PhD life as a test of my perseverance. But this thesis could not have been completed without the honest support of several people. The long list of people commences with François who supervised my work. I am extremely grateful to him for giving me the opportunity to work under him. His advice and enthusiasm guided me through the thesis and boosted my motivation in difficult times. I was, and will always be impressed by your broad and deep knowledge in the field, your passion for your work and your accurate intuition for solving problems. Thank you for being so patient, and helping me to improve!

I would like to sincerely thank Prof. Alejandro Sevilla, Prof. Elise Lorenceau and Prof. Mohamed Farhat, for having accepted to evaluate this work and for dedicating their time in reading this thesis in great details. I deeply appreciate the constructive discussion during and after the thesis defense. Your words have motivated me to continue my research further with more dedication. My gratitude also goes to Prof. William Curtin for kindly accepting to preside over the jury.

I am extremely indebted to the warm LFMI family who have been a constant source of support and happiness in these four years. Thank you Petra, not only for all the administrative help but also for making me feel so comfortable in my initial days of arrival in the lab. Thank you for being my friend/advisor and providing me the motivation at times when I felt a bit low. I will miss the endless hugs you gave me to make me happy. My pillar of support, Eunok, I thank you with all my heart for all your help and support with my thesis. The long and interesting discussions I had with you have improved the quality of my project. Thank you for always standing beside me as a sister. Thank you for your contagious craziness which I will miss wherever I go. Your passion and dedication towards your work is truly outstanding and I hope to become like you. Thank you Francesco for your precious theoretical help and for being extremely patient with me. Thank you Gioele for guiding me with your strong theoretical background and for your best chocolate cakes. Thank you Giacomo for sharing the office space with me for more than three years. I will always appreciate your positive attitude. Thank you Saviz, Lailai, Nicolas, Simon, Lorenzo, Gaétan, Mathias, Ludovic, Hervé, Giuseppe and Edouard for your help and guidance in the different phases of my PhD life. I am extremely grateful to the useful advice you guys gave me. Thank you to all the young PhDs in the lab, Shahab, PG, Alessandro and Yves-Marie. I wish you all the best for the coming years. Help each other to improve and remember to enjoy this time. Thank you Adrien Bressy for your efficiency and honest work. I was privileged to supervise you.

Thanks to Tobias and his whole group of ECPS, especially Florian and Sajjad. Thank you EMSI

## Acknowledgements

---

group, especially Martin and Ramin. You all made the lab life so much easier and we had so much fun together! I'm glad that I could find so many good friends among you.

A big thanks to all the precious friends that I made in and around Lausanne. Special thanks to John-Réné Uncle and Armida Aunty for being our guardians, for loving me and treating me as your family. Thank you Erica, Marta, Vlado, Laura, Christian, Mara, Dahye, Samuel, Marta, Matteo, Mengdi, Joyeeta, Jeremy and Zhouji for the happy moments we have spent together. Thank you Diana for being the best flatmate and one of my best friends. Thank you Aditya, Pallavi, Arjun, Florence, Kuldeep & family for all the good food and discussions we had on several occasions. Thank you Petra, François, Emma and Luca for making me feel as a part of your family, for taking special care of me and for your unconditional love.

The acknowledgement would not be complete without mentioning my parents who supported me throughout the countless years of school and university. I will always be very grateful for their encouragement, for their deep love and for their blessings for me on every single day. Thank you for believing in me. I would also like to thank my brother/soulmate and my sister-in-law with whom I am able to share all my experiences. A sweet thank you to my beautiful niece, my eternal source of bliss.

Last but not the least, Himank I would like to thank you from the bottom of my heart, for always being there for me in the most difficult times, for advising me, inspiring me and standing behind me as rock in all the ups and downs of life. Thank you for your selfless love and care. I would not have managed this journey especially without you.

*Lausanne, 31 July 2019*

Isha Shukla

# Abstract

Among hydrodynamically unstable flows, the *amplifier*-flows are characterized by their large amplification potential in presence of external noise. Since *amplifiers* do not have an intrinsic dynamics, a chosen forcing can be applied to eventually control the downstream evolution of such flows. With this aim, we intend to analyse the flow control in *amplifier*-flows, common examples being the flow in a backward facing step and the free surface capillary jet. We begin by analysing the flow control applied over a three-dimensional spanwise-modulating backward facing step. With the objective of reducing the lower recirculation length, we look for small amplitude optimal controls either by blowing/suction or by applying a wall deformation.

A similar approach is then applied for the free surface axisymmetric capillary jet. The analysis is simplified by using the one-dimensional equations of Eggers & Dupont (J. Fluid Mech., vol. 262, 1994, 205-221) which describe the flow using only the radius of the jet and its velocity as functions of the jet axial coordinate and time. We concentrate on two jet variations, one has a parallel base flow and the other has a spatially varying base flow due to the stretching effect of gravity. A local stability analysis is sufficient for analysing parallel base flows, whereas the spatially varying jets are analysed in the global framework. Further, we perform numerical simulations with the target of finding the optimal forcing which minimizes the intact jet length, also referred to as the breakup length. Unlike the parallel jets, the optimal forcing frequency for the spatially varying jet is dependent on the forcing amplitude. Similar results are then captured through the global resolvent analysis by introducing the forcing amplitude in the linear resolvent framework. Using a similar linear stability approach we then analyse the special case of silicone-in-silica jets inspired by the experimental results of Gumennik *et al.* (Nat. Commun., vol. 4, 2013, 2216). Based on the reformulated one-dimensional equations, we predict numerically the drop size as a function of given fibre feed speed, which is found to be in close accordance with the experimental results.

Finally, we explore experimentally the physical dynamics of drops rising in an external medium in a Hele-Shaw cell due to buoyancy. We specifically analyse the relation between the drop velocity and the mean film thickness magnitude around the drop. We present complete film thickness maps for these drops which highlight the ‘catamaran’ like shape often observed for similar drops in pressure driven flows inside the Hele-Shaw cell.

**Key words:** amplifier flows, backward facing step, hydrodynamic instability, Rayleigh-Plateau instability, Eggers & Dupont equation, jet breakup, optimal forcing, resolvent analysis, droplet dynamics in Hele-Shaw.



# Résumé

Au sein de la classe des écoulements instables, les écoulements amplificateurs de bruits sont caractérisés par leur fort potentiel d'amplification en réponse à un bruit extérieur. Dans la mesure où ces amplificateurs n'ont pas de dynamique propre, un forçage choisi est susceptible de contrôler l'évolution spatiale et temporelle de l'écoulement. Deux exemples nous permettent dans cette thèse d'appliquer cette stratégie de contrôle d'écoulements amplificateurs : l'écoulement au dessus une marche descendante et le jet capillaire. Dans un premier temps, nous analysons l'écoulement de marche descendante tridimensionnelle modulée transversalement. Dans la perspective de diminuer l'étendue de la zone de recirculation, nous recherchons un contrôle optimal de faible amplitude par injection/aspiration de fluide ou bien en appliquant une déformation à la paroi.

Une approche similaire est ensuite appliquée au cas d'un jet capillaire axisymétrique. L'analyse est ici simplifiée grâce à l'utilisation des équations unidimensionnelles d'Eggers & Dupont (J. Fluid Mech., vol. 262, 1994, 205-221) qui décrivent l'écoulement en utilisant le rayon local du jet et la vitesse comme des fonctions de l'espace et du temps. Deux variations sont analysées en détail : une première consiste en un jet doté d'un écoulement de base parallèle, et la deuxième d'un jet dont l'écoulement de base varie dans l'espace du fait de l'étirement induit par la pesanteur. Une analyse de stabilité locale est suffisante pour analyser l'écoulement de base parallèle. Pour l'écoulement de base dépendant de l'espace, en revanche, une analyse de stabilité globale est requise. Par la réalisation de simulations numériques, nous avons déterminé le forçage optimal permettant de minimiser la longueur du jet avant pincement. Au contraire des jets parallèles, les jets étirés par la pesanteur ont une fréquence de forçage optimale qui dépend de l'amplitude de ce forçage. Ces résultats de simulation sont retrouvés par analyse globale par fonction de transfert, en introduisant l'amplitude de forçage dans la résolvente linéaire. En utilisant une analyse de stabilité linéaire analogue, nous analysons finalement le cas particulier des jets "silicone-in-silica" inspirés par les résultats expérimentaux de Gumennik *et al.* (Nat. Commun., vol. 4, 2013, 2216). En adaptant les équations unidimensionnelles utilisées précédemment, nous parvenons à prédire numériquement la taille des gouttes en fonction du débit d'injection de la fibre et obtenons un très bon accord avec les résultats expérimentaux.

Enfin, nous étudions expérimentalement la dynamique de gouttes confinées dans une cellule de Hele-Shaw remplie d'un fluide moins dense. Ces gouttes, en mouillage nul, remontent la cellule sous l'effet de la pesanteur. Nous analysons en particulier la relation entre la topologie

## Résumé

---

du film de lubrification et la vitesse de la goutte. Le film de lubrification adopte une structure de type 'catamaran', en accord avec des précédentes observations pour des gouttes soumises à un gradient de pression.

**Mots clés : écoulements amplificateurs de bruit, marche descendante, instabilité hydro-dynamique, instabilité de Rayleigh-Plateau, équation d'Eggers & Dupont, éclatement de jet capillaire, forçage optimal, analyse par fonction de transfert, dynamique de gouttes en cellule de Hele-Shaw**

# Zusammenfassung

Unter allen hydrodynamisch instabilen Strömungen zeichnet sich die Verstärker-Strömung durch ihr großes Potential zu verstärken aus. Da Verstärker keine intrinsische Dynamik haben, wird die Wahl einer Kraft möglich, um die Strömungsentwicklung stromabwärts zu steuern. Zu dem Zweck die Strömungssteuerung zu analysieren, nehmen wir Bezug auf geläufige Beispiele wie die Strömung über eine rückwärtsgerichteten Stufe und eines Kapillarstrahls mit freier Oberfläche. Wir beginnen mit der Analyse der Steuerung einer Strömung über eine dreidimensionale rückwärtsgerichtete Stufe, die in Spannweitenrichtung moduliert ist. Mit dem Ziel die Länge der unteren Rezirkulationszone zu reduzieren, untersuchen wir die optimale Steuerung mit kleinen Amplituden, entweder durch Schub/Sog oder durch Deformation der Wand.

Einähnlicher Ansatz wird auch für die Untersuchung des achsensymmetrischen Kapillarstrahls mit freier Oberfläche gewählt. Die Analyse wird vereinfacht durch die eindimensionalen Gleichungen von Eggers & Dupont (J. Fluid Mech., vol. 262, 1994, 205-221), deren Beschreibung der Strömung lediglich auf dem Strahlradius sowie seiner Geschwindigkeit als Funktion von Axialkoordinate und Zeit basiert. Wir beschränken uns auf zwei Strahlvarianten, eine mit paralleler Basisströmung und eine andere mit räumlich variierender Basisströmung, die eine Abnahme des Strahlradius durch Schwerkraft beschreibt. Eine lokale Stabilitätsanalyse ist eine hinreichende Untersuchung für parallele Basisströmungen, während ein räumlich variierender Strahl eine globale Analyse verlangt. Des Weiteren machen wir numerische Simulationen mit dem Ziel eine optimale Steuerungskraft zu finden, welche die intakte Strahllänge minimiert, bzw. Die benötigte Länge für die Zerteilung des Strahls. Im Gegensatz zum parallelen Strahl ist die Frequenz der optimalen Steuerungskraft von der Steuerungsamplitude abhängig. ähnliche Ergebnisse bekommt man durch globale Analysen mittels Resolventen, wenn man die Steuerungsamplitude in der Resolventen berücksichtigt. Mit Hilfe eines ähnlichen linearen Stabilitätsansatzes untersuchen wir dann den Spezialfall eines Silikonstrahls in Silikagel, motiviert durch die Experimente von Gumennik *et al.* (Nat. Commun., vol. 4, 2013, 2216). Basierend auf den umformulierten eindimensionalen Gleichungen machen wir numerische Vorhersagen zu der Tropfengröße als Funktion von gegebener Einführgeschwindigkeit der Faser, welche mit den experimentellen Ergebnissen übereinstimmen.

Letztendlich untersuchen wir experimentell die Aufstiegsdynamik eines Tropfens durch den Auftrieb in einem externen Medium innerhalb einer Hele-Shaw-Zelle. Wir untersuchen spezifisch die Beziehung zwischen der Tropfengeschwindigkeit und der Magnitude der mittleren Filmdicke um den Tropfen. Für diese Tropfen erstellen wir vollständige Karten von Filmdicken,

## Zusammenfassung

---

welche insbesondere jene 'Katamaran'-artige Tropfenform zeigen, die häufig bei ähnlichen Tropfen in druckgetriebenen Strömungen einer Hele-Shaw-Zelle zu beobachten sind.

**Stichwörter:** Verstärker-Strömung, rückwärtsgerichtete Stufe, hydrodynamische Instabilität, Rayleigh-Plateau Instabilität, Eggers & Dupont Gleichung, Strahlzerteilung, optimale Steuerungskraft, Analyse mittels Resolventen, Tropfendynamik in Hele-Shaw



# Contents

<b>Acknowledgements</b>	<b>v</b>
<b>Abstract (English/Français/Deutsch)</b>	<b>vii</b>
<b>1 Introduction</b>	<b>1</b>
1.1 Jets: In nature and everyday life . . . . .	1
1.2 Linear stability theory . . . . .	3
1.2.1 Local stability analysis . . . . .	3
1.2.2 Global stability analysis . . . . .	8
1.2.3 Link between local and global stability analysis . . . . .	9
1.3 Amplifier flows studied in this thesis . . . . .	11
1.3.1 Backward facing step . . . . .	12
1.3.2 Capillary jets . . . . .	14
1.4 Droplet motion in confined microfluidic channels . . . . .	18
1.5 Thesis outline . . . . .	20
<b>2 Linear and nonlinear optimal control for flows in backward facing step</b>	<b>23</b>
2.1 Introduction . . . . .	23
2.2 Problem formulation . . . . .	26
2.2.1 Governing equations . . . . .	26
2.2.2 Sensitivity of the reattachment length: general expression . . . . .	28
2.2.3 Simplification: spanwise-harmonic control . . . . .	30
2.2.4 Optimal spanwise-periodic control . . . . .	31
2.3 Numerical method . . . . .	33
2.3.1 Linear analysis . . . . .	33
2.3.2 Three-dimensional DNS . . . . .	33
2.4 Stability properties of the zeroth-order base flow . . . . .	34
2.4.1 Global stability . . . . .	34
2.4.2 Optimal 3D steady forcing . . . . .	34
2.5 Results: optimal control for lower reattachment location . . . . .	37
2.5.1 Optimal wall actuation . . . . .	37
2.5.2 Optimal wall deformation . . . . .	39
2.6 Discussion . . . . .	40
2.7 Conclusion . . . . .	41

## Contents

---

2.8	Appendix . . . . .	44
2.8.1	Appendix: Second-order reattachment location modification . . . . .	44
2.8.2	Appendix: Simplification of the sensitivity operators . . . . .	46
2.9	Part II : Vaccination as a control strategy . . . . .	49
2.9.1	Numerical method . . . . .	50
2.9.2	Results and discussion . . . . .	51
<b>3</b>	<b>Capillary jet stability analysis using the one-dimensional Eggers &amp; Dupont equations</b>	<b>55</b>
3.1	Introduction . . . . .	55
3.2	The Eggers & Dupont equations . . . . .	56
3.3	Linear stability analysis of viscous jets . . . . .	59
3.3.1	Temporal stability analysis . . . . .	60
3.3.2	Absolute-convective stability analysis . . . . .	61
3.3.3	Spatial stability analysis . . . . .	62
3.4	Nonlinear simulations . . . . .	66
3.4.1	Governing equations . . . . .	66
3.4.2	Numerical scheme . . . . .	66
3.4.3	Numerical scheme validation . . . . .	68
3.4.4	Simulation results . . . . .	69
3.5	Conclusion . . . . .	72
<b>4</b>	<b>Amplitude dependent preferred mode of an axisymmetric single phase gravity-driven falling viscous jet</b>	<b>73</b>
4.1	Introduction . . . . .	74
4.2	Mathematical formulation . . . . .	76
4.3	Nonlinear simulations . . . . .	77
4.3.1	Governing equations . . . . .	78
4.3.2	Nonlinear simulations results . . . . .	78
4.4	Local stability analysis . . . . .	82
4.4.1	Local stability analysis for spatially varying jets . . . . .	82
4.4.2	Spatial stability analysis . . . . .	85
4.4.3	Weakly nonparallel stability analysis (WKBJ) . . . . .	87
4.5	Global stability analysis . . . . .	89
4.5.1	Global stability . . . . .	89
4.5.2	Global resolvent . . . . .	91
4.6	Response to white noise . . . . .	96
4.7	Conclusion and perspectives . . . . .	98
4.8	Appendix . . . . .	101
4.8.1	Numerical base state solution validation . . . . .	101
4.8.2	Effect of initial condition on breakup characteristics . . . . .	101
4.8.3	Effect of jet tip on breakup mechanism . . . . .	102
4.8.4	Comparison between resolvent and spatial analyses . . . . .	103

4.8.5	Linear operator for eigenvalue problem . . . . .	105
4.8.6	Global stability validation . . . . .	105
4.8.7	WKBJ formulation for axisymmetric 1D Eggers & Dupont equations . . .	107
<b>5</b>	<b>Particle size selection in capillary instability of locally heated co-axial fiber</b>	<b>113</b>
5.1	Introduction . . . . .	114
5.2	Problem formulation . . . . .	116
5.2.1	Equations of motion and boundary conditions . . . . .	117
5.2.2	Inner silicon core . . . . .	119
5.2.3	Outer silica cladding . . . . .	119
5.2.4	Reduced nonlinear governing equations . . . . .	120
5.3	Linear stability analysis . . . . .	121
5.3.1	Dispersion relation . . . . .	121
5.3.2	Temporal stability . . . . .	122
5.3.3	Spatio-temporal stability . . . . .	123
5.4	Nonlinear stability analysis . . . . .	126
5.4.1	Dimensionless governing equations . . . . .	126
5.4.2	Numerical scheme . . . . .	126
5.4.3	Numerical domain and parameter values . . . . .	128
5.4.4	Numerical results . . . . .	129
5.5	Conclusions and perspectives . . . . .	132
5.6	Appendix . . . . .	133
5.6.1	Validity of constant outer pressure assumption . . . . .	133
5.6.2	Numerical code validation for a jet in an inert medium . . . . .	135
5.6.3	Silicon-in-silica fiber with constant capillary number . . . . .	136
5.6.4	Selection of a truncated numerical domain . . . . .	138
5.6.5	Effect of surface tension on sphere size . . . . .	139
5.6.6	Comparison of nonlinear behaviors of silicon-in-silica fiber at constant capillary number and viscous jet . . . . .	139
<b>6</b>	<b>Film thickness distribution in gravity-driven pancake-shaped droplets rising in a Hele-Shaw cell</b>	<b>141</b>
6.1	Introduction . . . . .	142
6.2	Experimental setup . . . . .	144
6.3	Experimental acquisition of the drop characteristics and their comparison with 3D BIM simulations . . . . .	146
6.3.1	Experimental results for drop velocity . . . . .	146
6.3.2	Experimental results for film thickness . . . . .	147
6.3.3	Comparison with 3D simulations . . . . .	150
6.4	Analysis of the film thickness pattern . . . . .	151
6.4.1	Formulating the nonlinear 2D lubrication equation . . . . .	152
6.4.2	Qualitative analysis of thickness pattern using the linearized 2D lubrication equation . . . . .	155

## Contents

---

6.5	Conclusions and perspectives . . . . .	158
6.6	Appendix . . . . .	160
6.6.1	CCI working principle . . . . .	160
6.6.2	Derivation of two-dimensional nonlinear lubrication equation for pan- cake droplets . . . . .	160
<b>7</b>	<b>Conclusions and perspectives</b>	<b>163</b>
7.1	Summary . . . . .	163
7.2	Perspectives . . . . .	165
7.2.1	Sensitivity analysis of spatially varying jet . . . . .	165
7.2.2	Improvements for numerical scheme for capturing drop dynamics . . .	166
7.2.3	Obtaining the limit condition for static drops in Hele-Shaw cell . . . . .	169
	<b>Bibliography</b>	<b>184</b>
	<b>Curriculum Vitae</b>	<b>185</b>

# 1 Introduction

## 1.1 Jets: In nature and everyday life

Jets, defined as streams of fluid having almost a columnar shape, have captivated our interest both for their practical use and for their intricate breakup mechanism. They exist in varying length scales, from nature to everyday life. In nature, the formation of Pele's hair is a stunning example of highly viscous jets created during a volcanic eruption (see figure 3.1(a)). Named after the Hawaiian goddess of volcanoes, Pele's hair are thin strands of volcanic glass formed in the air during the fountaining of the molten lava. A single viscous strand with a diameter of less than 0.5 mm, can extend up to a length of 2 m (Shimozuru 1994; Eggers & Villermaux 2008). Such viscous filaments are also seen to elongate and stabilize in presence of gravity, as in the case of honey dripping from a spoon under its own weight (see figure 3.1(b)), where the highly thin jet can exceed lengths of 10 m (Javadi, Eggers, Bonn, Habibi & Ribe, 2013).

In contrast, if the gravitational force is opposite to the flow direction, it tends to amplify the preexisting destabilising effect in a jet, eventually accelerating its breakup into drops. This behaviour is evident in the case of an Archerfish, which hunts by spitting a water jet (sometimes as long as 3 m) at their prey (figure 3.1(c)). Surprisingly while doing so, they have a good estimate of the refractive index of air-water, the degree of bending of the jet due to gravity, and particularly the presence of the Rayleigh-Plateau instability, which breaks the water jet into several small drops as a consequence of the surface tension forces (Vailati, Zinnato & Cerbino, 2012).

At the microscale level, an everyday yet elegant application of the jets is in the use of ink-jet printer where highly thin jets are ejected to eventually breakup into drops of fixed size (figure 3.1(e)). Recently, the ink-jet technology has moved far beyond its original purpose in printing, for example to print integrated circuits, microarrays in biotechnology and to make optical elements (Basaran, 2002; Williams, 2006; Eggers & Villermaux, 2008) (see figure 3.1(f)-(i)).

In most of these processes which require a specific drop size, the breakup process is so sophisticated to tune, especially due to first, the presence of satellite drops which leads to a

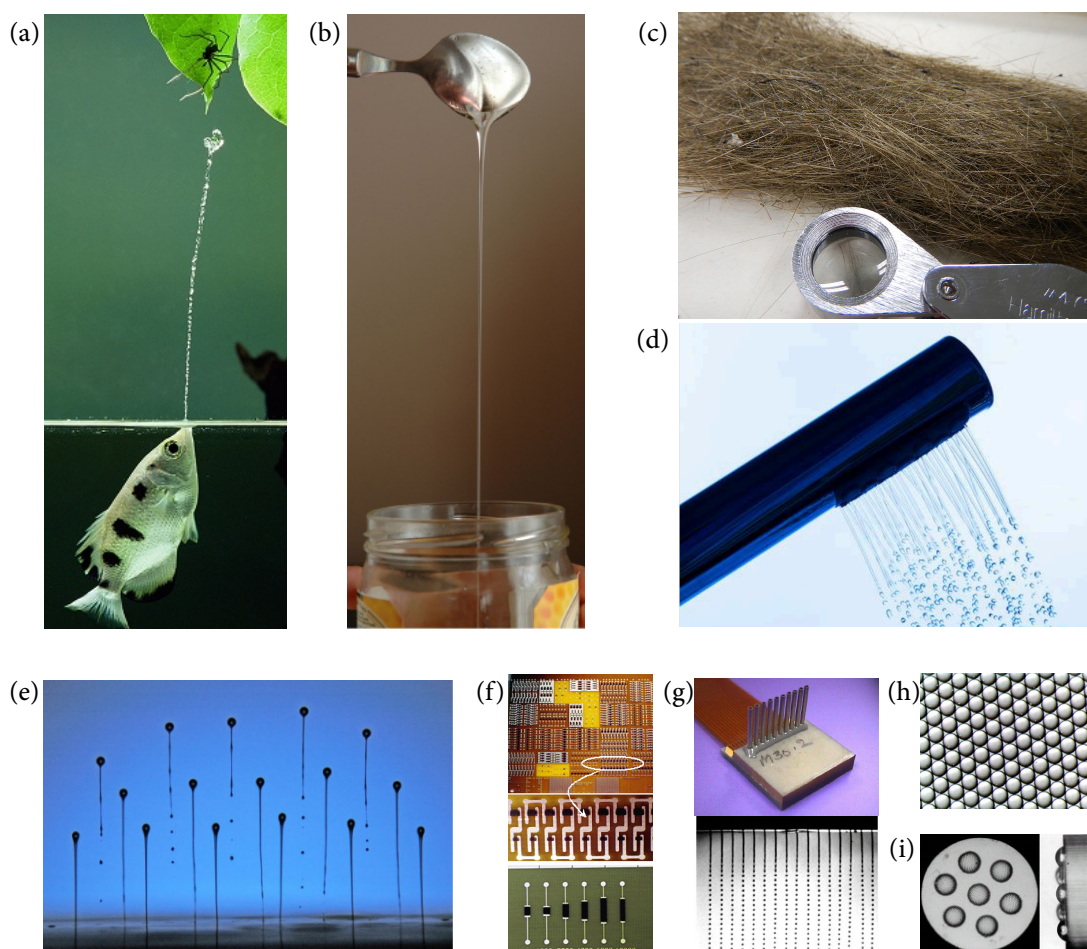


Figure 1.1 – (a) A spotted archerfish (*Toxotes chatareus*) spitting at a spider (taken from <https://www.warrenphotographic.co.uk>). (b) Viscous honey falling from a spoon. (Eggers & Villermaux, 2008) (c) Pele’s hair, with the hand lens as a scale (taken from <https://en.wikipedia.org>). (d) Several jets of water falling from a shower head. (e) Drops emerging from a bank of ink-jet nozzles. The drop heads are  $50\mu\text{m}$  and the tails width is less than  $10\mu\text{m}$  (10 times thinner than a human hair) (Eggers & Villermaux, 2008) Credit: Steve Hoath, Cambridge Engineering Department, Ink-jet Research Centre investigating the performance of ink-jet printers. (f) Integrated circuits printed using ink jets. (g) Piezoelectric drop-on-demand array printhead prototype. (h) Drug laden microspheres,  $50\mu\text{m}$  in diameter, produced using ink-jet technology. (i) Tip of a  $500\mu\text{m}$  optical fibre bundle with active elements printed at its tip ((f)-(i) taken from [www.microfab.com](http://www.microfab.com)).

bimodal size distribution and second, the fabrication limit of the nozzle geometry which restricts the minimum drop size (Eggers & Villermaux, 2008). To overcome this limitation, the nature of external forcing plays a vital role as has been seen in the presence of an electric field (Basaran 2002; Wijshoff 2010; Basaran, Gao & Bhat 2013), thermal field or presence of outer flow (Williams, 2006; Gumennik, Wei, Lestoquoy, Stolyarov, Jia, Rekemeyer, Smith, Liang, Grena, Johnson *et al.*, 2013), amplitude of initial perturbation (Pimbley & Lee 1977; Hilbing

& Heister 1996), as well as the presence of higher harmonics (Eggers, 1997; Chaudhary & Maxworthy, 1980; Xing, Boguslawski, Soucemarianadin, Atten & Attané, 1996; Barbet, Atten & Soucemarianadin, 1997; Driessen, Sleutel, Dijkman, Jeurissen & Lohse, 2014). A small modulation can thus, greatly impact the drop size distribution.

The subtle behaviour of these jets in presence of an external forcing motivates the clear comprehension of the underlying flow dynamics. In particular, how the time independent base flow looks like, the nature of forcing introduced, the response of the base flow in presence of the applied forcing and most crucially the optimal control that can be imparted on these flows using a selective forcing.

## 1.2 Linear stability theory

The classical linear stability analysis has proven to be a suitable tool to assess the stability of the steady base flow in presence of small perturbations. Depending on the degree of non parallelism of the base flow, the evolution of these infinitesimal perturbations is studied using either a *local* or a *global* approach. In either case, based on the stability analysis, base flows can be characterised as *amplifiers* (which are extremely sensitive to external noise) or *oscillators* (which have a dominant intrinsic dynamics resulting in self-sustained oscillations). A brief discussion of the local/global stability analysis methods and their respective domain of applicability is discussed in the following sections.

### 1.2.1 Local stability analysis

In view of the subsequent discussions, we describe a flow  $\mathbf{q}(y, z, t)$ , the time independent base state of which is given by  $\mathbf{q}_b(y, z)$ . Here  $z$  and  $y$  are the streamwise and cross-stream directions, respectively, and  $t$  denotes the time (note that for axisymmetric flows,  $y$  is replaced by  $r$ -the radial co-ordinate). A parallel or a weakly nonparallel base flow is defined as one in which the length scale over which the base flow varies in  $z$  is much larger than the length scale of the local perturbation (Schmid & Henningson, 2001; Chomaz, 2005; Charru, 2011). For parallel flows,  $\mathbf{q}_b$  is a function of  $y$  only. The local stability framework is suitable for such base flows, wherein the space and time evolution of small perturbations can be analysed. Applying an infinitesimal perturbation of magnitude  $\epsilon \ll 1$ , the system of governing equations are decomposed around the base flow as follows:

$$\mathbf{q}(y, z, t) = \mathbf{q}_b(y) + \epsilon \mathbf{q}'(y, z, t), \quad (1.1)$$

where the perturbations are explored using the normal mode expansion of the form,

$$\mathbf{q}'(y, z, t) = \tilde{\mathbf{q}}(y) e^{i(kz - \omega t)}, \quad (1.2)$$

## Chapter 1. Introduction

---

consisting of a complex wavenumber  $k$ , frequency  $\omega$  and eigenmode  $\tilde{\mathbf{q}}$ . If the applied infinitesimal perturbation decays to zero at infinite times, the flow returns to its base flow configuration and is deemed as locally stable. For the unstable case, where the disturbances do not die, the flow can be further characterised as absolutely unstable or convectively unstable depending upon the competition between the local dynamics and the flow advection (Bers, 1975; Huerre & Monkewitz, 1985).

Analytically, expanding the flow around the base flow, imposing the fluctuations in the form (1.2) and extracting terms of the order of  $\epsilon$  results in the formulation of the linearized equations expressed as,

$$\mathcal{M}[C, k, \omega]\tilde{\mathbf{q}}(y) = 0, \quad (1.3)$$

where  $\mathcal{M}$  denotes the linear operator and  $C$  is any dimensionless control parameter defining the flow (such as Reynolds, Ohnesorge, to name a few). The existence of a non trivial solution to (1.3) requires the non-invertibility of  $\mathcal{M}$  which constrains  $k$  and  $\omega$  to satisfy the dispersion relation

$$\Delta(\omega, k, C) = 0. \quad (1.4)$$

The solution of the dispersion relation is solved by considering either  $k \in \mathbb{R}$  or  $\omega \in \mathbb{R}$ , or considering both as complex  $(k, \omega) \in \mathbb{C}$ , which determines the stability of the base flow.

The selection of real  $k \in \mathbb{R}$  and complex  $\omega \in \mathbb{C}$ , defines the so-called *temporal* stability analysis which examines the temporal evolution of the perturbation in presence of a real spatial forcing. However, defining  $k \in \mathbb{C}$  and  $\omega \in \mathbb{R}$  refers to the *spatial* stability analysis where we look for the spatial evolution of the perturbation in response to the real forcing frequency.

Contrary to the *temporal* stability analysis, the *spatial* analysis can be ill posed if we operate in a regime where the flow is naturally unstable. In such cases, the domain of applicability for the spatial stability analysis can be conveniently determined through the absolute/convective stability analysis which considers both  $(k, \omega) \in \mathbb{C}$ , a study referred to as the *spatio-temporal* stability analysis.

### **Temporal stability analysis**

In the temporal stability analysis the growth of fluctuations in time is analysed. In this framework, the dispersion relation (1.4) is solved for complex  $\omega \in \mathbb{C}$  and real  $k \in \mathbb{R}$ . For the modal decomposition of the form  $e^{i(kz - \omega t)}$ , the growth rate of the perturbation is solely decided by the (positive) imaginary part of  $\omega$ . The flow is deemed as linearly unstable if the temporal growth rate  $\omega_i > 0$ .

### **Absolute/convective stability analysis**

In addition to  $\omega \in \mathbb{C}$ , if we now generalise  $k \in \mathbb{C}$  the stability for parallel base flows can be



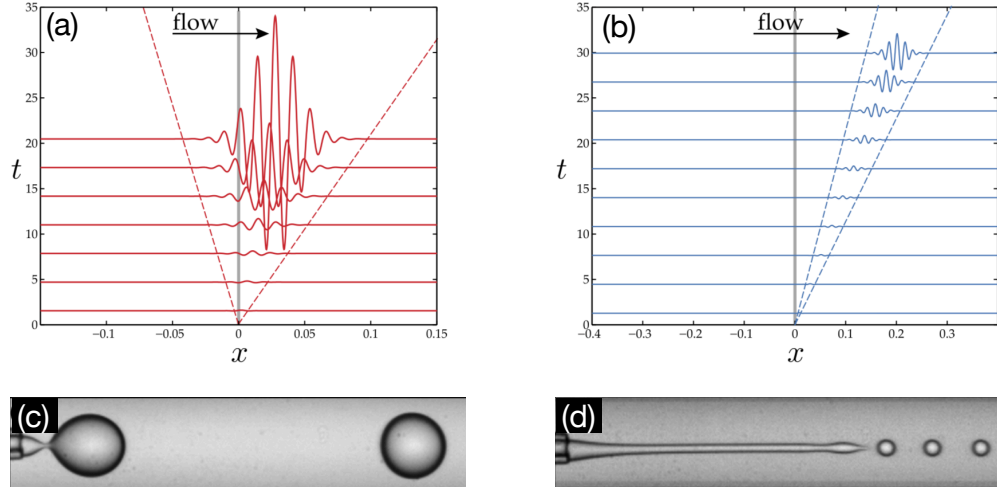


Figure 1.2 – (a)-(b) Impulse response of two wavepackets. Both cases are unstable, but (a) is absolutely unstable as the perturbation grows exponentially in the laboratory frame and (b) is convectively unstable as the perturbation decreases with time while moving away from the disturbance source (taken from Brun *et al.* (2015)). (c) Dripping-related to the absolutely unstable regime and (d) jetting-related to the convectively unstable regime, seen in co-flowing jets (original figure modified from Utada *et al.* (2007)).

analysed in the spatio-temporal framework which includes the effect of advection speed of the jet on its stability properties. In this framework, we define the impulse response of a system to a localised perturbation which generates a wave packet growing in space and time. In the laboratory framework, the spatio-temporal behaviour of the wave packet can be described in terms of the complex absolute wave number  $k_0$  and the corresponding complex absolute frequency  $\omega_0 = \omega(k_0)$ . The complex pair  $(k_0, \omega_0)$  is defined using the saddle point condition also called the Briggs-Bers zero-group velocity criterion, together with the dispersion relation

$$\frac{d\omega}{dk}(\omega_0, k_0) = 0, \quad \Delta(\omega_0, k_0, C) = 0. \quad (1.5)$$

The temporal evolution of the wave packet is then conveniently determined through the imaginary part  $\omega_{0,i}$ . For  $\omega_{0,i} > 0$  the system is absolutely unstable since the disturbance grows fast enough to invade entire domain in the laboratory frame without having sufficient time to travel downstream, as shown in figure 1.2(a). The coflowing jet (figure 1.2(c)) in the dripping regime is an example of an absolutely unstable system, where the imposed perturbations magnify instantaneously initiating a breakup close to the nozzle.

However, for  $\omega_{0,i} < 0$  the system is convectively unstable as the localised perturbations are allowed to convect downstream before they grow in the laboratory framework as shown in figure 1.2(b). The presence of high flow advection forces the applied disturbance to travel downstream as it continuously grows in space. The advantage of the convectively unstable flows is that the base flow, close to the localised impulse, returns to its innate features once the perturbation has travelled downstream. Examples can be seen in coflow jets (figure 1.2(d))

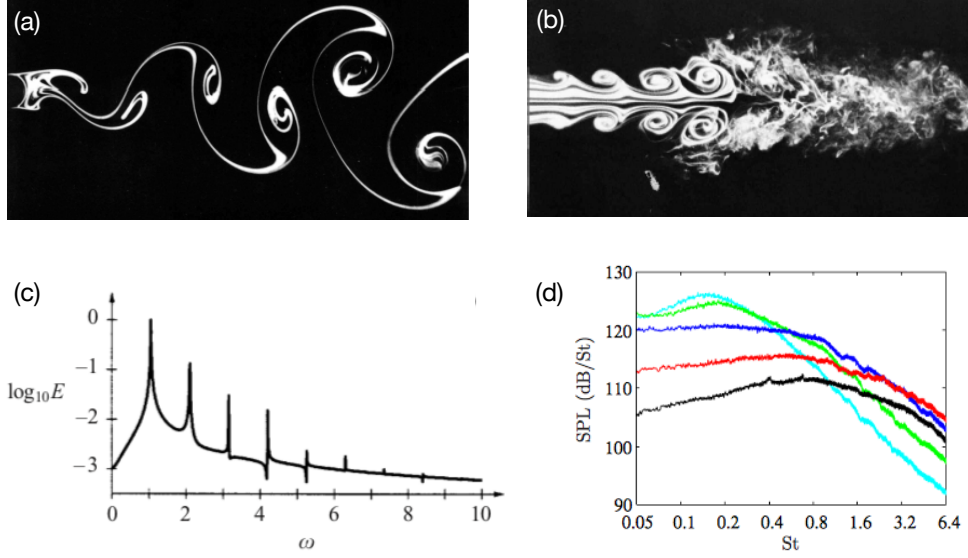


Figure 1.3 – (a) The flow around a cylinder at  $Re = 140$  (figure modified from Van Dyke 1982) representing an oscillator flow. (b) An example of amplifier flow-the turbulent jet (figure modified from Van Dyke 1982). (c) Power spectral density function extracted from a signal in the cylinder wake, which shows a clear peak in the frequency selection (obtained from Pier 2002). (d) Power spectral density function extracted from a signal in a turbulent jet in presence of external noise, which shows a larger response for a preferred region of noise (obtained from Barré *et al.* 2006).

in the jetting regime, where the initial perturbation travels downstream while amplifying and finally breaking up into drops.

The local convectively unstable flows, for example a turbulent jet (figure 1.3(b)), display inherently extrinsic dynamics and are considered as noise *amplifiers*, naturally amplifying any enforced perturbation (Chomaz, 2005; Schmid, 2007). They are seen to have a preferred selection for frequency in presence of an external forcing (figure 1.3(d)). Hence the spatial evolution of such flows is greatly influenced by the nature of the forcing (frequency, amplitude to name a few), which can be tailored to meet specific downstream flow characteristics.

In comparison, the local absolutely unstable flows, referred as *oscillators*, display intrinsic dynamics and develop self-sustained oscillations (figure 1.3(a)) with a clear peak in the frequency spectrum (figure 1.3(c)). This behaviour is in contrast to the *amplifiers* which in absence of an external forcing, present a broadband frequency spectrum without any specific frequency selection (Nichols & Lele, 2010). However, in presence of the external noise, the flow is seen to amplify strongly in a specific frequency band (Huerre & Monkewitz, 1985; Chomaz, Huerre & Redekopp, 1988; Chomaz, 2005). The choice of a self-excited frequency in the absolute regime, and its absence in the convective regime was also clearly demonstrated by Sevilla & Martinez-Bazan (2004), in which the authors analysed the vortex shedding in high Reynolds number bluff-body wakes.

### Spatial stability analysis

In the spatial stability analysis, the perturbations are expanded for  $k \in \mathbb{C}$  and  $\omega \in \mathbb{R}$ . Thus the spatial problem is equivalent to the signalling problem, in which the growth in space of the response to a sustained harmonically pulsating source at frequency  $\omega$  is considered. Indeed performing the spatial stability analysis in such a framework is ill posed for absolutely unstable base flows which have their own intrinsic dynamics. Thus the spatio-temporal analysis serves as a foundation, segregating flows which are convectively unstable, and hence suitable for the spatial analysis.

Following the modal expansion (1.2), the response at a real frequency  $\omega$ , is expressed as

$$\mathbf{q}'(y, z, t) = \hat{\mathbf{q}}(y) \exp \left[ i \left( k(\omega) z - \omega t \right) \right], \quad (1.6)$$

where  $k \in \mathbb{C}, \omega \in \mathbb{R}$ . Hence the growth rate of the perturbations propagating downstream (in the positive  $z$  direction) is solely determined by  $-k_i$ . The base flow is deemed unstable to external perturbations for  $k_i < 0$ .

However, if the base flow becomes weakly nonparallel, the exact spatial response cannot be captured using (1.6), since the weak non parallelism of the base flow induces the wavenumber  $k$  to be a function of  $z$  as well. The spatial response to external forcing of such weakly non parallel base flows can then be determined in the weakly non parallel framework (WKBJ) as discussed in the next section.

### Spatial stability analysis for weakly non parallel flows

If the base flow is not parallel but rather varies spatially in the streamwise direction, its non parallelism can be quantified using the streamwise evolution of the local length scale  $\delta(z)$  of the spatially varying flow parameters, for example the velocity, vorticity or the interface for free surface flows. Then the degree of spatial variation can be expressed through  $\eta = d\delta/dz$ . For  $\eta \ll 1$ , the base flow changes slowly along a gradually varying scale  $Z = \eta z$ , and at each location in  $Z$ , the flow can be approximated as parallel. In this framework, the spatial stability (for convectively unstable flows) of the weakly nonparallel base flow can be studied using the WKBJ formalism introduced by Bender & Orszag (1978), Gaster, Kit & Wygnanski (1985) and Huerre & Rossi (1998).

In this formalism, the base state and the global response to an external perturbation is expressed as a function of the slowly varying variable  $Z$  as follows:

$$\mathbf{q}'(y, Z, t) = \bar{\mathbf{q}}(y, Z) \exp \left[ i \left( \frac{1}{\eta} \int_0^Z k(Z', \omega) dZ' - \omega t \right) \right], \quad (1.7)$$

where the local eigenfunction  $\bar{\mathbf{q}}$  is further decomposed using the amplitude function  $A(Z)$ ,

$$\bar{\mathbf{q}}(y, Z) \sim A(Z) \hat{\mathbf{q}}^{(1)}(y; Z) + \eta \hat{\mathbf{q}}^{(2)}(y; Z) + \dots. \quad (1.8)$$

Here  $k(Z, \omega)$  is the local complex wavenumber obtained as a solution of the dispersion relation for a given  $\omega$  and  $\hat{q}(y; Z)$  its associated eigenfunction. In addition,  $A(Z)$  designates the envelope function smoothly connecting the slices of parallel spatial analyses. A methodic asymptotic expansion followed by the implementation of a compatibility condition finally leads to the solution of the  $A(Z)$ , which results in,

$$\mathbf{q}'(y, z, t) \sim A(\eta z) \hat{\mathbf{q}}^{(1)}(y; z) \exp\left(\int_0^z -k_i(z') dz'\right) \exp\left[i\left(\int_0^z k_r(z') dz' - \omega t\right)\right]. \quad (1.9)$$

Thus the response at a location  $z$  can be captured accurately by (i) including the integral of the spatial growth rate up to  $z$  and (ii) bridging the response at every  $z$  using the amplitude solution.

However, if the degree of spatial variation  $\eta \geq 1$ , the base flow stability can only be investigated in the global framework, which is discussed in the following section.

### 1.2.2 Global stability analysis

If the degree of non parallelism  $\eta$  is not negligible, the stability of the base flow can be suitably analysed using a global framework. The global stability of the base flow depends on the global interactions of the local flows. For example, a local convectively unstable flow can be globally stable since the perturbations are convected far downstream. Unlike the local analysis, since the base flow at the boundaries have to meet certain boundary conditions, or simply since it varies in the streamwise direction, the perturbations are no longer expressed through a Fourier transform in the streamwise direction. The base flow is a function of the streamwise direction  $z$  and the perturbed solutions are expanded using the form  $\mathbf{q}'(y, z, t) = \bar{\mathbf{q}}(y, z) e^{-i\omega t}$ . Thus the variation in  $z$  completely enters through the eigenfunction  $\bar{\mathbf{q}}$ . Based on the temporal growth rate, the base flow is defined as stable for  $\omega_i < 0$  and unstable for  $\omega_i > 0$ .

The globally stable flows, such as a jet flow (Crow & Champagne, 1971) or the flow across a two-dimensional backward facing step (up to  $Re \sim 1500$ ), behave as amplifiers, posing a high sensitivity to external forcing (Chomaz, 2005; Schmid, 2007). In contrast, a globally unstable flow, like the flow behind a cylinder behaves as an oscillator, characterized by a large enough region of absolute instability and developing self-sustained oscillations. To express the stability of such flows analytically, the linearized governing equations are reformulated as an eigenvalue problem of the form:

$$\frac{\partial \mathbf{q}'}{\partial t} = \mathcal{L} \mathbf{q}' \quad \text{or} \quad -i\omega \bar{\mathbf{q}} = \mathcal{L} \bar{\mathbf{q}}, \quad (1.10)$$

whose eigenvalues and eigenfunction express the long term behaviour of the base flow. The linear operator  $\mathcal{L}$  contains the information of the linear dynamics. The eigenvalue analysis results in a dominant eigenvalue  $\omega$ , whose imaginary part  $\omega_i$  governs the growth rate of the perturbation, and the eigenfunction  $\bar{\mathbf{q}}(y, z)$  which describes the structure of the perturbation.

For the unstable flow, the self sustaining oscillating frequency can be expressed through  $\omega_r$ . However, the eigenvalue analysis fails to predict the nature of response for stable amplifier flows, which shows a stable spectrum with no unstable eigenvalue. The amplifying potential of such flows in presence of an external forcing can be adequately studied using a global resolvent analysis.

The resolvent analysis is applicable only for globally stable flows where the external disturbances are not dominated by the intrinsic instability of the base flow. For a stable  $\mathcal{L}$ , the method is implemented by introducing the forcing function  $\mathbf{f}(y, z)e^{-i\omega t}$  in the linearized governing equations as follows:

$$\frac{\partial \mathbf{q}'}{\partial t} = \mathcal{L} \mathbf{q}' + \mathbf{f}(y, z)e^{-i\omega t}. \quad (1.11)$$

Assuming that the forcing function of frequency  $\omega$  will yield a response characterized by the same frequency (which holds true for linear stable systems once the transient has faded out and the permanent regime has been reached) leads to further simplification of (1.11). Introducing the resolvent operator  $\mathcal{R} = (i\omega \mathbb{I} + \mathcal{L})^{-1}$ , where  $\mathbb{I}$  is the identity matrix, the response of the base flow in presence of the external forcing can be expressed as,

$$\bar{\mathbf{q}}(y, z, \omega) = \mathcal{R}(\omega) \mathbf{f}(y, z). \quad (1.12)$$

Thus for a given forcing function whose structure is defined by  $\mathbf{f}(y, z)$ , the resolvent operator is equivalent to a transfer function, formulating the final output of a flow based on this forcing function and a given input frequency. The resolvent analysis is especially applied with the aim of finding the optimal forcing structure which leads to the most amplified response. The optimal forcing and the related response structure are obtained through a singular value decomposition of the resolvent operator, as described in detail in Farrell & Ioannou (1996), Schmid (2007) and Garnaud, Lesshafft, Schmid & Huerre (2013) among others.

### 1.2.3 Link between local and global stability analysis

The degree of spatial variation of the base flow determines the framework for analysing the flow stability, wherein a local analysis is sufficient for parallel flows (Huerre & Monkewitz, 1990) and the global framework is convenient for the streamwise varying flow (Chomaz, 2005). However, understanding the link between the two approaches is thought-provoking.

The local stability analysis can be bridged with the global analysis through the outcome of the saddle point condition, which marks the local transition from an absolutely unstable flow to a convectively unstable flow. Usually a flow which is local convectively unstable can be considered globally stable as the local perturbations may travel downstream, returning the base flow to stable condition. However, a prerequisite for a globally unstable flow is the existence of local absolute instability in a sufficient large portion of the global domain.

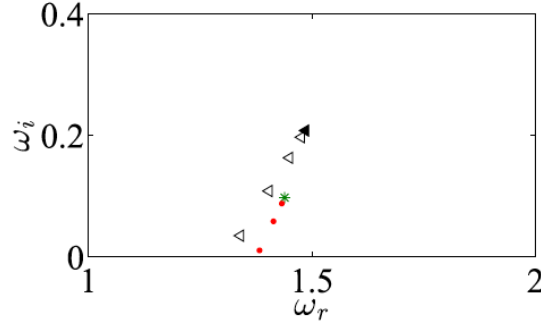


Figure 1.4 – Figure obtained from Augello *et al.* (2018) which shows the unstable global spectrum ( $\omega_i > 0$ ) for a coflowing jet in an injector device. The red dots (•) are the solution of the global stability analysis, while the green star (\*) the saddle point of the corrected dispersion relation which includes the flattening terms.

For the globally unstable flows, usually the dominant global frequency is coherent with the absolute local frequency  $\omega_{0,r}$  obtained by applying the Briggs-Bers zero-group velocity on the local dispersion relation at the most absolutely unstable streamwise station. More precisely the dispersion relation has to be plunged into the complex  $z$  domain where an additional saddle point condition has to be applied (Chomaz *et al.*, 1988; Huerre & Rossi, 1998). However, such complex  $z$  plane analyses can only be applied to quasi-parallel flows in the purely linear regime, and both base-flow non-parallelism and disturbance nonlinearity cannot be described within this framework (Chomaz, 2005).

In this direction, Hammond & Redekopp (1997) performed numerically the stability analysis for the flow across a bluff body for a given inflow condition. The resulting flow which was globally unstable developed a vortex shedding state at a global frequency of 0.1. They found that the structure of the global instability modes of a streamwise independent parallel base flow were equivalent to its local absolute instability modes. The global modes were obtained by introducing necessary boundary conditions whereas the absolute modes were attained through the dispersion relation. Moreover, the saddle point condition of the local theory predicted a frequency selection of 0.1006, quite comparable to the unstable global frequency. Similar conclusions were drawn by Heaton, Nichols & Schmid (2009), who applied the local-global theory for the wake across a blunt-edged plate.

Augello, Fani & Gallaire (2018) presented an identical analysis on a one-dimensional system of coflowing viscous jets in an injector device. They investigated the unstable global modes (obtained by imposing the Dirichlet boundary conditions both at inlet and outlet), for a  $z$  independent system (see figure 1.4). In the limit of an infinite streamwise extension of the domain, they found that the absolute mode (obtained from the local analysis and represented through green star (\*)) does indeed mark a point from which the sequence of global modes (represented through red dots (•)) emerges. In addition to the growth rate, the most amplified global mode frequency obtained for the infinite domain, was equivalent to the absolute frequency obtained from the saddle point condition.

Unlike the globally unstable flows, the stable flows require a different approach to relate it to the local analysis. The frequency selection seen for globally stable flows can be analysed through a resolvent analysis wherein the optimal frequency resulting in the most amplified response can be obtained. To consider a similar response to external forcing, the local spatial analysis (for parallel flows) or the WKBJ formalism (for the weakly non parallel flows) can be applied wherein the dispersion relation is solved for a given real  $\omega$  to obtain the complex  $k$ . The response due to a given frequency can then be quantified through the spatial growth rate ( $-k_i$ ). In this direction, Viola, Arratia & Gallaire (2016) studied the response of model trailing vortices subjected to a harmonic forcing. The frequency-selection mechanism was shown to be directly connected to the local stability properties of the flow, and was simultaneously investigated by a WKBJ approximation in the framework of weakly non-parallel flows and by the global resolvent approach. As shown in figure 1.5 they found an excellent agreement between the two approaches in predicting the overall response amplitude as well as the optimal forcing producing the most amplified flow.

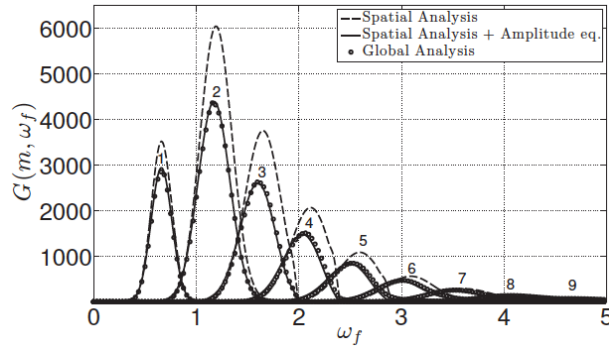


Figure 1.5 – Figure extracted from Viola *et al.* (2016). The plot shows the global gains of the responses excited by forcing at the inlet with the local direct mode. The solid black lines show the results of WKBJ analysis; the dashed lines correspond to the gains obtained by imposing unitary amplitude. The results obtained through a global resolvent are shown with circles.

### 1.3 Amplifier flows studied in this thesis

Globally stable or local convectively unstable base flows, commonly known as *amplifier* flows, have gathered a lot of interest owing to their unique flow features. Such flows do not have any intrinsic dynamics as the perturbations travel downstream without invading the entire domain, yet in the presence of an external forcing, they exhibit large amplification for a preferred frequency range; a feature often exploited for practical applications. Moving in this direction, in the following sections we will do a brief overview of the two canonical examples of *amplifier* flows studied in this thesis, (i) the flow inside a backward facing step and (ii) the capillary jet.

### 1.3.1 Backward facing step

The flow inside a backward facing step (BFS) (as shown in figure 1.6(a)) is a classical example of noise amplifiers that has been extensively studied theoretically, experimentally and numerically due to its simple geometry, and fundamentally owing to its representation of the flow seen in several industrial applications, such as airfoils at large attack angle, flows inside combustors, flows around buildings, industrial ducts and in the cooling of electronic devices, to name a few. The BFS is a prototype of such applications since it incorporates all the three major flow features seen in these devices- the flow separation, recirculation and reattachment - which can drastically alter the device performance.

Theoretically, the large amplification potential of the BFS can be captured by optimal transient growth analysis, optimal harmonic forcing or by evaluating the response to persisting noise on the globally stable base flow. The two dimensional (2D) BFS shows stable modes up to  $Re \sim 1500$  whereas for the 3D BFS (with an expansion ratio of 0.5), the first unstable modes start appearing at  $Re \approx 750$  (Barkley, Gomes & Henderson, 2002; Lanzerstorfer & Kuhlmann, 2012). For the stable flows within this threshold ( $Re = 500$ ), Blackburn, Barkley & Sherwin (2008) analysed the instabilities in the convective regime by computing the optimal transient growth and by performing direct numerical simulations for white-noise inlet velocity fluctuations. They concluded that the numerically obtained results showing the presence of 2D wave packets were related to the optimal disturbances found in the transient growth analysis. Extensive literature also exists about the calculation of gain due to harmonic forcing (Åkervik, Ehrenstein, Gallaire & Henningson, 2008 for a flat plate boundary layer, and Alizard, Cherubini & Robinet, 2009; Marquet & Sipp, 2010; Dergham, Sipp & Robinet, 2013; Garnaud *et al.*, 2013; Sipp & Marquet, 2013). Marquet & Sipp (2010) computed the optimal harmonic forcing for a

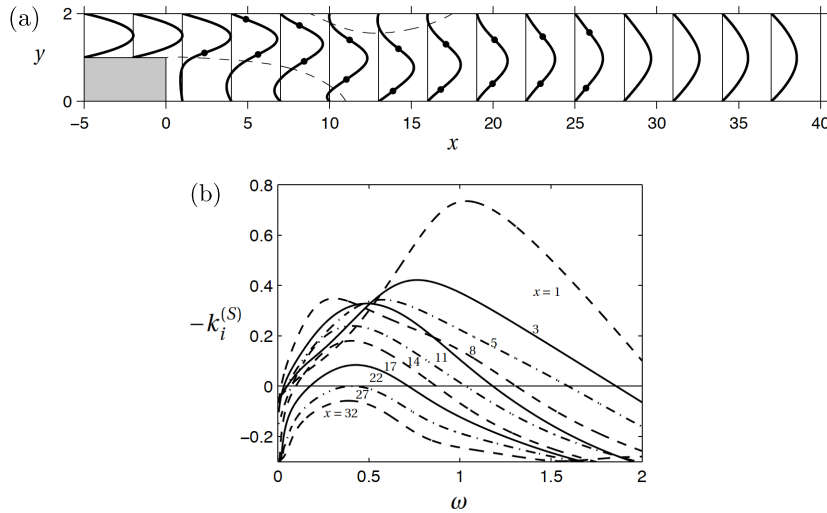


Figure 1.6 – (a) Profiles of streamwise velocity for  $Re = 500$  at different sections along  $x$  and (b) spatial growth rates from local stability analysis at the corresponding sections in  $x$ . The figure has been taken from Boujo & Gallaire (2015).



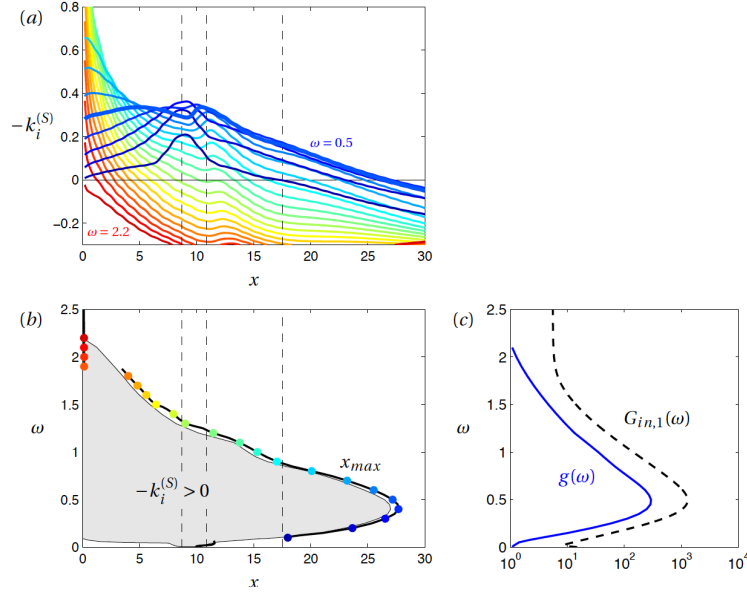


Figure 1.7 – Local stability analysis for  $Re = 500$  (a) Streamwise evolution of the spatial growth rate at different frequencies. (b) Region of instability (shaded area) with the maximum instability region at  $\omega = 0.5$ . (c) Integral amplification factor (solid line) from local analysis and optimal harmonic gain from global analysis. The figure has been extracted from Boujo & Gallaire (2015).

2D BFS at  $Re = 500$  and expansion ratio 0.5, and concluded that the most amplified frequency  $f_s = 0.075$  and the corresponding response structure was inline with the results of Blackburn *et al.* (2008).

Applying a similar framework, Boujo & Gallaire (2015) analysed the flow response globally/locally in a backward facing step at  $Re = 500$ , for both inlet/volume-small amplitude harmonic forcing. The optimal global forcing frequency was close to 0.5. Assuming the flow to be locally quasi-parallel, they then applied the local spatial theory, at each streamwise location in  $x$  as shown in figure 1.6(a). They found that the spatial growth rate  $-k_i$  had a decreasing trend moving downstream in  $x$  but had a non monotonic behaviour at certain frequencies (see figure 1.6(b)). Conversely plotting the growth rate as function of the streamwise direction for different frequencies (as shown in figure 1.7(a)), they found a local maximum between  $x = 9$  and 11. Since the perturbations grow spatially only as long as  $-k_i > 0$ , and then decay, the resulting amplification factor  $g(\omega)$  in the flow was obtained by integrating all the spatial growth rate  $-k_i$  in the entire domain for each  $\omega$  as:

$$g(\omega) = \exp \left( \int -k_i(x, \omega) dx \right). \quad (1.13)$$

Plotting the region of instability (figure 1.7(b)) or conversely the total gain  $G_{in,1} = \|\mathcal{R}\|$  with inlet forcing (figure 1.7(c)) as a function of the forcing frequency concluded that the optimal frequency from the local analysis was in good agreement to the global optimal harmonic gain.

For practical purposes it makes sense to design control strategies which can for example enhance mixing, or reduce the aerodynamic drag and vibration. This requires studying the sensitivity of the amplification mechanisms to small flow modifications. The sensitivity analysis, built on the framework of adjoint based methods, provides maps of sensitivity showing regions where a chosen quantity is the most affected by small-amplitude flow modifications. This analysis allows a systematic control design without employing time expensive parametric studies or without computing the actual flow.

In this context, as discussed in Boujo & Gallaire (2015), similar technique was applied to study the variation in eigenvalue with respect to flow modification and to steady control to obtain maps of sensitivity for the vortex shedding behind a cylinder (Hill, 1992). Later, similar methods were also applied by Bottaro, Corbett & Luchini (2003); Marquet, Sipp & Jacquin (2008); Meliga, Sipp & Chomaz (2010). An expression of sensitivity of the optimal harmonic gain due to a given flow modification and steady control was investigated by Brandt, Sipp, Pralits & Marquet (2011) for Tollmien-Schlichting and lift-up instability mechanisms. More recently, Boujo, Ehrenstein & Gallaire (2013), using similar methods, computed the sensitivity maps for a flow past a wall-mounted bump. Their analysis revealed that the sensitivity to volume control was dependent on the frequency. The sensitivity method was extended by the same authors for a 2D incompressible flow past a BFS (Boujo & Gallaire, 2015), by computing the sensitivity amplification for a flow subjected to stochastic forcing rather than harmonic forcing. Second, to represent more realistic situations, they derived the expression for sensitivity amplification when the flow is forced at the inlet rather than in the entire domain.

### 1.3.2 Capillary jets

Capillary jets, another typical example of amplifier flows, have been studied for almost two centuries owing to their easily observable behaviour. Unlike the BFS, where the downstream flow is allowed to evolve within the confined walls, the downstream amplification of perturbations along the free interface jets leads to their breakup into drops.

Commonly referred to as the Rayleigh-Plateau instability, the break up of liquid jets into drops was historically first analysed by Savart (1833), who concluded that the most unstable wavelength was almost 10 times the thread radius. For the qualitative observation, Savart developed a stroboscopic technique which led to the production of images as shown in figure 1.8. Later the experimental work of Plateau (1873) and the theoretical contribution of Rayleigh (1879), concluded that the physical mechanism leading to the jet breakup resulted from the dominance of surface tension forces over the viscous and inertial forces. Based on a static energy analysis of the liquid thread they found the criteria for the cut-off wavenumber. Additionally the most unstable wavelength, found by studying the jet dynamics, was impressively similar to Savart's observation.

However, it was noted that the existence of the jetting regime shown in figure 1.8, which is

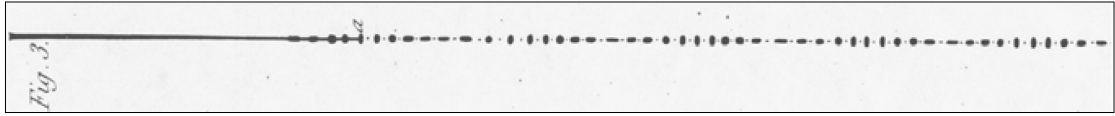


Figure 1.8 – A figure from Savart (1833) showing the breakup of a liquid jet 6 mm in diameter. One can clearly notice the successive oscillations of the drops as well as the presence of small satellite drops in between the main drops.

characterized by a considerably long liquid filament, was linked to the fluid properties and the imposed flow rate (Clanet & Lasheras, 1999; Ambravaneswaran, Subramani, Phillips & Basaran, 2004). Applying a very low flow rate resulted into a dripping regime (figure 1.9(a)), wherein the breakup would be initiated close to the nozzle. As the flow rate was progressively increased the jet would enter the dripping faucet regime (figure 1.9(b)) in which irregular sized drops at varying locations were formed. Increasing the flow rate further would finally result into the transition to the jetting regime (figure 1.9(c)).

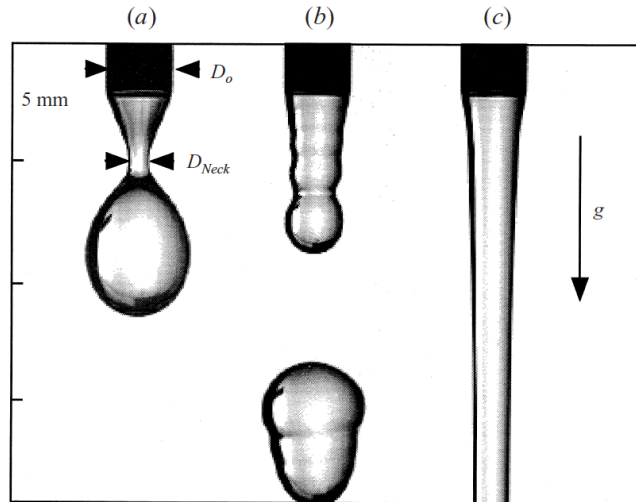


Figure 1.9 – The three regimes (a) dripping (b) dripping faucet (c) jetting observed as the inflow velocity is progressively increased. Figure obtained from Clanet & Lasheras (1999).

Theoretically, the evolution of the jet from the dripping to the jetting regimes marks the transition from an absolutely unstable to a convectively unstable flow. Leib & Goldstein (1986) found that there exists a critical flow rate below which the jet is absolutely unstable thus making it an ill posed problem for spatial analysis. In the convectively unstable regime, where the jet behaves as an amplifier flow, solving the dispersion relation in the framework of local stability analysis results in the most dominant wavenumber (Rayleigh mode) with the largest temporal growth rate. Successive experiments performed by Rutland & Jameson (1971) and more recently by González & García (2009) were consistent with the theory, where one could clearly see that the wavenumber imposing the quickest breakup of the jet was in close approximation of the Rayleigh mode (see figure 1.10).

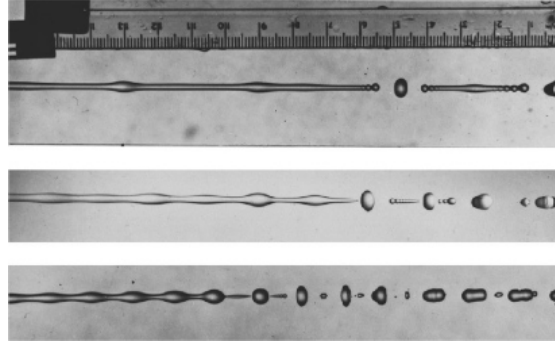


Figure 1.10 – Photographs of decaying jet for three different frequencies of excitation. From top to bottom the wavenumber of excitation is  $k = 0.075$ ,  $0.25$  and  $0.068$ . The bottom picture corresponds to a forcing which is close to the Rayleigh mode. Figure extracted from Rutland & Jameson (1971).

However, the local stability framework convenient for parallel jets cannot be directly applied for spatially varying jets. The jet flow depicted in figure 1.11 is an example of a gravitationally stretched viscous jet in the jetting regime. The stability of a spatially varying jet should ideally be examined using the global stability analysis and by including the non-parallel effects of the base flow. On this subject, Sauter & Buggisch (2005) approached the problem theoretically by defining a linear global mode that correlated with the self sustained oscillations of the falling jet, observed during the jetting (globally stable) to dripping (globally unstable) transition. The work of Sauter & Buggisch (2005) was extended by Rubio-Rubio, Sevilla & Gordillo (2013) experimentally and theoretically by increasing the range of liquid viscosities and nozzle diameters. They performed the global stability analysis of such spatially varying jets and confirmed through experiments that the globally observed unstable-stable transition was related to the changeover from the dripping to jetting regime. Moreover the experimentally observed dripping frequency was found to be in good agreement with the most unstable global frequency obtained from the linear analysis.



Figure 1.11 – Globally stable jet of silicone oil of viscosity 50 cSt, injected vertically downwards through a nozzle of radius 2.5 mm at a constant flow rate of  $7 \text{ ml min}^{-1}$ . Figure obtained from Rubio-Rubio *et al.* (2013).

In relation to the spatially varying stable base flow, more recently, Le Dizès & Villiermaux (2017) determined theoretically the jet response in presence of the most amplifying forcing frequency. Their analysis accounted for both the base state deformation and modification of local instability dispersion relation as the jet thins in the direction of gravity. Notably, extending the work of previous authors (Tomotika, 1936; Frankel & Weihs, 1985; Leib & Goldstein, 1986; Frankel &

Weihs, 1987; Senchenko & Bohr, 2005; Sauter & Buggisch, 2005; Javadi *et al.*, 2013) they used the local plane wave decomposition (WKB approximation) for their analysis. However, the gain resulting from a perturbation was computed by considering only the exponential (e) terms of the WKB approximation.

Because of their amplifying nature, the local convectively stable or the globally stable jets have varied practical applications. Since any applied forcing is intensified downstream resulting in the production of drops, the different controls for drop formation has drawn extensive interest. Hilbing & Heister (1996) had performed numerical simulations for very high speed jets to analyse the nonlinear evolution of the jet resulting into the formation of drops, for different forcing conditions. They found that increasing the magnitude of the forcing perturbation decreased the breakup length and changed the shape of the droplet. Notably, for very high amplitudes, the drops were seen to form a “squashed” shape due to the high velocity fluid encountering lower velocity fluid which has already exited the nozzle. Known as the “Klystron” effect, this phenomenon has been documented qualitatively by numerous researchers for very large forcing amplitudes (Dunne & Cassen, 1956; Harrie & Reardon, 1972; Meier, Klöpper & Grabitz, 1992).

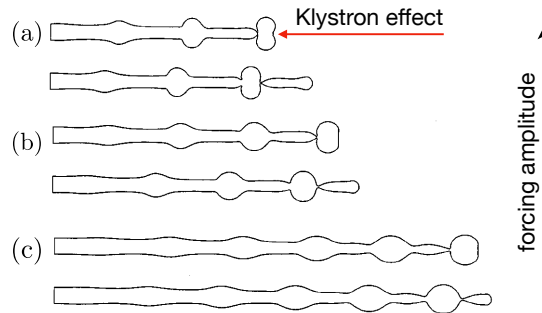


Figure 1.12 – Effect of inflow velocity disturbance magnitude at  $We = 100$  and  $k = 0.07$  for three different forcing amplitudes (a) 6%, (b) 4% and (c) 2% showing the jet profile before a main and a satellite drop are released. Figure has been obtained from Hilbing & Heister (1996).

Apart from the conventional methods for controlling the drops size; for example applying forcing characterized by a combination of frequencies, presence of an outer flow, electric and magnetic field as discussed in Section 1.1; the existence of a thermal field has also turned out to play a vital role on drop size control. In this regard, the Rayleigh plateau instability has been applied in the field of solid structures, where millimetre to nanometer-sized spherical particles are produced either by thermal drawing of a solid rod (Kaufman, Tao, Shabahang, Banaei, Deng, Liang, Johnson, Fink & Abouraddy, 2012) or by application of a localised flame. Gumennik *et al.* (2013) performed experiments in which a silicone-in-silica rod was fed at a constant feed speed  $V_f$  into a region of localized flame, thus melting the rod locally and allowing its breakup into drops which where later cooled down to obtain solid spheres (see figure 1.13(a)). They found a clear relationship between the sphere size and the feed velocity where the size of the sphere was seen to increase with increasing feed speed (see figure 1.13(b))-

(c)). Thus it can serve as a very convenient process parameter for adjusting the desired particle size, as opposed to tuning the temperature and/or material properties.

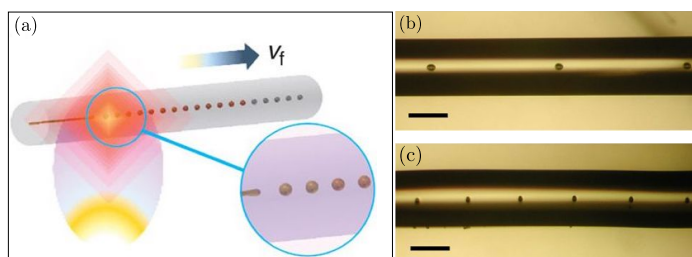


Figure 1.13 – (a) Schematics of the gradual liquefaction technique for producing silicone-in-silica jets. Drops formed in a  $4\mu\text{m}$  silicone core fibre (scale bar  $200\mu\text{m}$ ) at (b) high feed speed ( $90\mu\text{m/s}$ ) and (c) low feed speed ( $2\mu\text{m/s}$ ). Images have been taken from Gumennik *et al.* (2013).

### 1.4 Droplet motion in confined microfluidic channels

Several microfluidic techniques serve as qualified tools for research in pharmaceuticals, biotechnology, material engineering, food science and cosmetic industry, to name a few (Stone, Stroock & Ajdari, 2004; Weibel, DiLuzio & Whitesides, 2007; Seemann, Brinkmann, Pfohl & Herminghaus, 2011).

The microfluidic methods involve the controlled production of droplets and have become a reliable alternative to other classical bulk emulsification methods for generation of monodisperse droplets. Owing to the existing control techniques, liquid jets have emerged as a vital mode for the production of such monodisperse and uniform drops. Thus one of the primary aspects of this field is to understand the formation of droplets and liquid threads, which exceptionally depend on the jet flow rate, fluid properties (see figure 1.14) and the device geometry (Baroud, Gallaire & Danga, 2010; Christopher & Anna, 2007). For the co-axial injectors (figure 1.2(c-d)), a firm link could be established between the absolute/convective properties of the flow and the dripping or jetting nature of the jet (Utada, Lorenceau, Link, Kaplan, Stone & Weitz, 2005; Utada *et al.*, 2007; Guillot, Colin, Utada & Ajdari, 2007).

In most of the cases, after formation, the droplets flow inside microchannels with round or square cross-sections where the motion of the drop is predominantly one-dimensional. However, the presence of rectangular microchannels, with a large width-to-height aspect ratio, allows for 2D manipulations of the drops, thus reducing by far the structural complexity of such devices. When the drops are confined only by the upper and lower plates, as in the case of a Hele-Shaw cell, they acquire a ‘pancake’-like shape and are surrounded by a thin film of outer liquid (see figure 1.15(a)). Their motion can be controlled through varying fluid properties or the confinement between the plates. However, one of most fundamental factors needed for the efficient design of such devices is the accurate prediction of the drop velocity

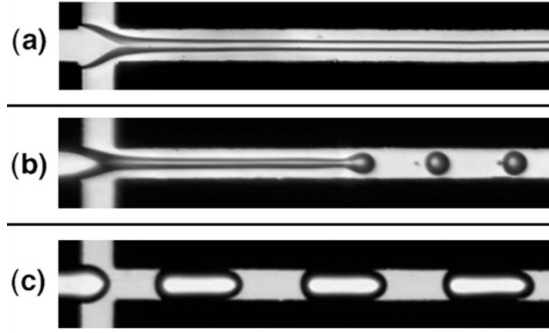


Figure 1.14 – (a) Threading (b) jetting and (c) dripping regime formed in a microfluidic device due to variation in coflow velocity ratio and the viscosity ratio. Modified image obtained from Cubaud & Mason (2008).

which is coupled to the magnitude of the lubricating film thickness around the drop.

The pioneering work, initiated for a long bubble translating inside a straight cylindrical tube (Taylor, 1961; Bretherton, 1961) showed the dependence of the bubble velocity on the film thickness at very low Capillary numbers ( $Ca < 10^{-3}$ ). Contrary to this, a flattened bubble/drop moving in the Hele-Shaw cell requires further exploration. In this direction, several works have been recently conducted to investigate the dynamics of a pressure-driven Hele-Shaw droplet (Huerre, Theodoly, Leshansky, Valignat, Cantat & Jullien, 2015; Reichert, Huerre, Theodoly, Valignat, Cantat & Jullien, 2018) who studied the shape and velocity of such drops and observed the so-called “catamaran” droplet shape as shown in figure 1.15(b-c). Such peculiar interfacial profile was also confirmed through numerical simulations performed by Ling, Fullana, Popinet & Josserand, 2016; Zhu & Gallaire, 2016. Recently, Keiser, Jaafar, Bico & Reyssat (2018) conducted experiments to study a sedimenting Hele-Shaw droplet, focusing on its velocity as a function of confinement, viscosity contrast and the lubrication capacity of the carrier phase.

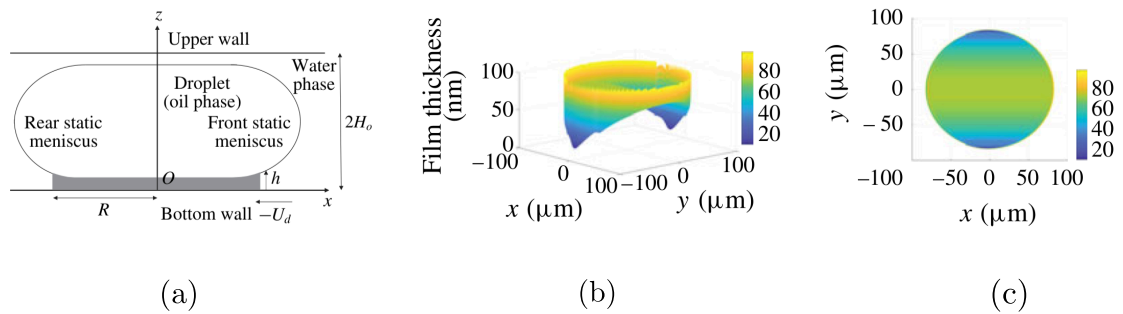


Figure 1.15 – Modified image obtained from Reichert *et al.* (2018). (a) Side view of the droplet in its frame of reference moving in a Hele-Shaw cell. The grey region marks the domain where the film thickness is obtained. (b) Numerical topography of the film thickness obtained for  $Ca = 7.2 \times 10^{-4}$  highlighting the catamaran-like shape. (c) Colormap of the film thickness in  $x$ - $y$  plane for the same Capillary number.

### 1.5 Thesis outline

This thesis (funded by FNS project number 200021-159957) mainly involves the study of the free surface jets characterized as amplifiers. On account of being a canonical example of amplifier flow, the BFS is considered as a stepping tool to explore the amplification potential of such systems. Next in the framework of linear stability analysis, the viscous jet and gravitationally stretched jet are discussed using one-dimensional (1D) lubrication equation. Further, we present the numerical results performed on the modified 1D equations especially formulated for the specific case of silicone-in-silica jets (Gumennik *et al.*, 2013). Finally, the experimental results of the film thickness distribution around a drop, moving due to bouyancy in a Hele-Shaw cell are presented.

**Chapter 2** discusses the flow over a 3D BFS, especially with the aim of exploiting its amplification potential to design control strategies, such that the smallest required control amplitude is capable of influencing the flow features. The optimal control is designed first using steady spanwise-periodic perturbations. In the second part, we show how the presence of the most amplified forcing can result in ‘vaccination’ of the stochastic disturbances present in such flows. This work was done jointly with E. Boujo and E. Yim, who developed the theory. I. Shukla ran and interpreted the 3D simulations.

**Chapter 3** introduces the 1D Eggers & Dupont equations (Eggers & Dupont, 1994). The simplified lubrication equation is then used in the local stability framework to perform the stability analysis of parallel viscous jets. Further, the linear results are compared to nonlinear simulations based on the same 1D equations.

**Chapter 4** investigates the stability in the framework of spatially varying jets under the influence of gravity which behave as amplifiers in the globally stable regime. Precisely, we explore the receptivity of the jet to external perturbations in this regime, through nonlinear simulations and resolvent analysis with the aim of finding the optimal forcing which results in the most amplified disturbance. This chapter also analyses the jet response using the WKB approximation. Finally the response of the jet in presence of stochastic disturbances is discussed.

**Chapter 5** tries to rationalize the particle size observed in the experiments of Gumennik *et al.* (2013) as well as its dependency on the feed speed. A simple 1D nonlinear governing equation for the motion of the silicon-silica interface, using long-wavelength approximations that have proven very accurate in the study of liquid jets (Eggers & Villermaux, 2008), is used for the analysis. Due to the failure of the linear stability analysis in such a system, we resort to a nonlinear stability analysis through numerical simulations of the reduced nonlinear governing equations, which recover, without any adjustable parameters, the relationship between sphere size and feed speed. This work was performed in collaboration with P.T. Brun at the very origin of the study and S. Mowlavi who has established the theoretical foundations of the equations and performed the stability analysis, together with I. Shukla, who has developed the numerical model and performed the nonlinear numerical simulations.



**Chapter 6** presents the experimental results of the shape, velocity and lubrication film thickness distribution of a droplet rising in a vertical Hele-Shaw cell. The droplet is surrounded by a stationary immiscible fluid and moves purely due to buoyancy. A low density difference between the two mediums helps to operate in a relatively low capillary number regime. The droplet is shown to exhibit the “catamaran” shape. This study was performed in collaboration with two former post-docs at LFMI, N. Kofman who helped setting up the experiments and L. Zhu who ran the 3D simulation. G. Balestra also helped for the theory. I. Shukla has led the entire study, done all measurements and worked on the interpretations.

Finally in **Chapter 7** we present a short conclusion and some future perspectives.



## 2 Linear and nonlinear optimal control for flows in backward facing step

**Remark** This chapter is largely inspired by the publication: *Optimal spanwise-periodic control for recirculation length in a backward-facing step flow*.

Eunok Yim<sup>1</sup>, Edouard Boujo<sup>2</sup>, Lorenzo Siconolfi<sup>1</sup>, Isha Shukla<sup>1</sup> and François Gallaire<sup>1</sup>

<sup>1</sup>Laboratory of Fluid Mechanics and Instabilities, Ecole Polytechnique Fédérale de Lausanne,  
1015 Lausanne, Switzerland

<sup>2</sup>LadHyX, UMR CNRS 7646, École Polytechnique, 91128 Palaiseau, France

**Author contributions** E.B. and F.G. conceived the project. E.B, F.G. and E.Y developed theoretical model. E.Y. performed the project. L.S. and I.S. performed the simulations and analyzed data. E.Y. and E.B wrote the manuscript for Part I and I.S. wrote the manuscript for Part II, both with inputs from F.G. F.G. supervised the research.

Submitted in *Physical Review Fluids*

### 2.1 Introduction

The flow over a backward facing step (BFS) is a quintessential example of a noise amplifier flow. Any small perturbation initially applied either decays in time or is progressively convected downstream of the perturbation source, letting the flow eventually return to its base flow configuration. In terms of global linear stability properties, the BFS flow for an expansion ratio of 2 was found globally stable to two-dimensional (2D) perturbations regardless of the Reynolds number. In contrast, three-dimensional (3D) perturbations periodic in the spanwise direction first become statically unstable, for  $Re \geq 748$  (Barkley *et al.*, 2002), where

the Reynolds number is defined with the maximum incoming velocity  $U_{in}$ , the kinematic viscosity  $\nu$  and the step height  $h$ . Despite their asymptotic decay, 2D perturbations can undergo large amplification in space and time due to non-normal effects (Marquet & Sipp, 2010), in accordance with the locally convectively unstable nature of the flow Boujo, Fani & Gallaire (2015).

From a practical point of view, the flow over a BFS is of importance since it serves as a prototype of several non-parallel flows in complex geometries as in airfoils, cavities and diffusers, to name a few. The BFS geometry facilitates the study of both the flow separation and the flow reattachment, thus incorporating the two most dominant features of separated flows. While several techniques based on a practical approach exist for flow control in such geometries, the application of the theory of optimal flow control to separated flows has only started quite recently.

Among the empirical flow control approaches, the use of spanwise-periodic structures is particularly promising. In the context of flow separation, Pujals, Depardon & Cossu (2011) have demonstrated that using arrays of suitably shaped cylindrical roughness elements, streaks can be artificially forced on the roof of a generic car model, the so-called Ahmed body, which suppress the separation around the rear-end. More generally, spanwise wavy modulations have been recognized, mainly through an iterative trial and error method, as an efficient method of control in several flow configurations: for flows past bluff bodies to regulate vortex shedding (Tanner, 1972; Zdravkovich, 1981; Tombazis & Bearman, 1997; Bearman & Owen, 1998; Choi, Jeon & Kim, 2008), for circular cylinders (Ahmed & Bays-Muchmore, 1992; Ahmed, Khan & Bays-Muchmore, 1993; Lee & Nguyen, 2007; Lam & Lin, 2008; Zhang, Katsuchi, Zhou, Yamada & Han, 2016), for rectangular cylinders (Lam, Lin, Zou & Liu, 2012) and in airfoils (Lin, Lam, Zou & Liu, 2013; Serson, Meneghini & Sherwin, 2017), to name a few.

The effectiveness of steady spanwise waviness to control nominally two-dimensional flows has been rationalized through the generalization of sensitivity analysis (Hill, 1992; Marquet *et al.*, 2008) to second order. In the case of spanwise-periodic control of 2D flows, the linear sensitivity indeed vanishes at first order and the leading-order variation eventually depends quadratically on the 3D control amplitude (Hinch, 1991; Cossu, 2014; Boujo *et al.*, 2015). This dependence has been already established through the works of Hwang, Kim & Choi (2013); Del Guercio, Cossu & Pujals (2014*a,b,c*) and Tammisola, Giannetti, Citro & Juniper (2014). The control effectiveness relies on two main features: the linear amplification potential of spanwise-periodic disturbances through amplification mechanisms like the lift-up mechanism, and the quadratic sensitivity of the flow on the resulting flow modifications.

In this study, we use the reattachment length as proxy for the noise amplifying potential of the separated flow in conjunction with a quadratic sensitivity analysis. The significance of the reattachment location as an indicator of the flow stability has already been substantiated through the works of Sinha, Gupta & Oberai (1981) and Armaly, Durst, Pereira & Schönung (1983). More recently, Boujo & Gallaire (2014*b*) investigated the link between reattachment

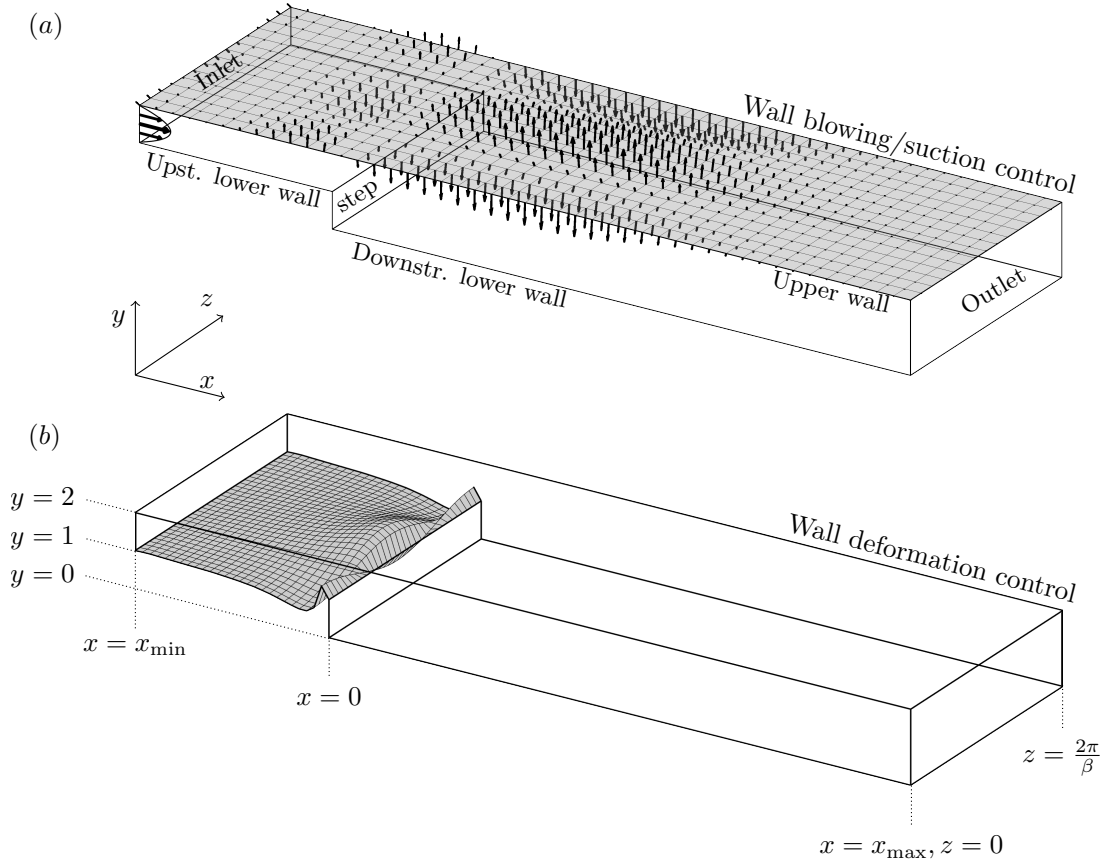


Figure 2.1 – Sketches of steady spanwise-periodic control (wavenumber  $\beta$ ) in a backward facing step: (a) wall blowing/suction applied on the upper wall and (b) wall deformation applied on the upstream lower wall.

point and stability properties in separated flows. They found that the reattachment point was highly sensitive to the control, with its sensitivity map deeply resembling that of the backflow area and recirculation area. Further, these three sensitivity maps resembled closely that of the optimal harmonic gain, implying that the flow becomes a weaker amplifier as the recirculation length decreases, i.e. as the reattachment point moves upstream.

In this direction, we aim to exploit the amplification potential of the stable flow in a 3D BFS to design optimal control strategies, such that the smallest required control amplitude is capable of influencing the recirculation strength, here quantified by the recirculation length. We thereby generalize the framework of Boujo, Fani & Gallaire (2019) designed to optimally control the nominally 2D growth rate using steady spanwise-periodic perturbations to the optimal quadratic control of the recirculation length. We derive a second-order sensitivity tensor, the scalar product of which with any arbitrary control yields the modification in reattachment location.

The optimization in spanwise-periodic control is applied for a BFS as shown in figure 2.1, with

an expansion ratio 2. The geometry is bounded by  $x = [-5 \ 50]$  and  $y = [0 \ 2]$ . The spanwise width is fixed at  $z = [0 \ 2\pi/\beta]$  where  $\beta$  is the periodicity of the wall modulation. We aim at optimizing the reattachment location (see figure 2.3) using optimal wall actuation (figure 2.1a) and optimal wall deformation (figure 2.1b). The Reynolds number is fixed at 500 throughout the analysis. This ensures that the flow is stable to the steady 3D instability that occurs at  $Re = 748$  with spanwise wavenumber  $\beta = 0.9$  (Barkley *et al.*, 2002).

The paper is organized as follows. Section 2.2 describes the problem formulation, general expression of the second-order sensitivity tensor with the mean flow correction and the optimization procedure used to compute the optimal control. The numerical method applied for the sensitivity analysis and validation of the results are presented in Section 2.3. A brief discussion on the global stability of the non-modified zeroth-order base flow is shown in Section 2.4. Finally, the optimal wall actuation and wall deformation for minimizing the lower reattachment location are discussed in Section 2.5. We summarize and discuss the limitations of this theory in Section 2.7.

## 2.2 Problem formulation

### 2.2.1 Governing equations

We consider a steady 2D base flow  $\mathbf{Q}(x, y) = (\mathbf{U}, P)^T(x, y) = (U, V, P)^T(x, y)$  in a domain  $\Omega$  with the boundary  $\Gamma$  which satisfies the incompressible steady Navier-Stokes equation as

$$\nabla \cdot \mathbf{U} = 0, \quad \mathcal{N}(\mathbf{Q}) = 0, \quad \text{in } \Omega, \quad (2.1)$$

$$\mathbf{U} = 0, \quad \text{on } \Gamma, \quad (2.2)$$

where  $\mathcal{N}(\mathbf{Q}) \equiv \mathbf{U} \cdot \nabla \mathbf{U} + \nabla P - Re^{-1} \nabla^2 \mathbf{U}$  with the Reynolds number  $Re$  defined with the maximum inlet velocity (plane Poiseuille) and the step height.

If there is a separated region, and a wall defined by  $y = y_w(x)$  where reattachment occurs, then the reattachment location  $x_r$  is characterized by vanishing wall shear stress:

$$\left. \frac{\partial U_t}{\partial n} \right|_{x=x_r, y=y_w(x_r)} = 0. \quad (2.3)$$

For the sake of simplicity, we now focus on the BFS flow: the reattachment location reduces to  $\partial_y U(x_r, 0) = 0$  for a horizontal wall  $y = 0$ ; in addition, the flow separates at  $x_s = 0$ , so the recirculation length  $l_c = x_r - x_s$  is simply  $l_c = x_r$ . We assume that a 3D steady control of small amplitude  $\epsilon$  is applied on an arbitrary boundary  $\Gamma_c$  with the actuation velocity  $\mathbf{U}_c(x, y, z)$

(and/or a volume control  $\mathbf{C}(x, y, z)$ ) such that

$$\nabla \cdot \mathbf{U} = 0, \quad \mathcal{N}(\mathbf{Q}) = \epsilon \mathbf{C} \quad \text{in } \Omega, \quad (2.4)$$

$$\mathbf{U} = \epsilon \mathbf{U}_c \quad \text{on } \Gamma_c, \quad (2.5)$$

$$\mathbf{U} = \mathbf{0} \quad \text{on } \Gamma \setminus \Gamma_c. \quad (2.6)$$

This 3D control modifies the 2D base flow as:

$$\mathbf{Q}(x, y, z) = \mathbf{Q}_0(x, y) + \epsilon \mathbf{Q}_1(x, y, z) + \epsilon^2 \mathbf{Q}_2(x, y, z) + \dots, \quad (2.7)$$

where the  $\mathbf{Q}_i$  are solutions of the modified base flow equations at orders  $\epsilon^0$ ,  $\epsilon^1$  and  $\epsilon^2$ :

$$\mathcal{N}(\mathbf{Q}_0) = \mathbf{0} \quad \text{in } \Omega, \quad \mathbf{U}_0 = \mathbf{0} \quad \text{on } \Gamma, \quad (2.8)$$

$$\mathbf{A}_0 \mathbf{Q}_1 = (\mathbf{C}, 0)^T \quad \text{in } \Omega, \quad \mathbf{U}_1 = \mathbf{U}_c \quad \text{on } \Gamma_c, \quad \mathbf{U}_1 = \mathbf{0} \quad \text{on } \Gamma \setminus \Gamma_c, \quad (2.9)$$

$$\mathbf{A}_0 \mathbf{Q}_2 = (-\mathbf{U}_1 \cdot \nabla \mathbf{U}_1, 0)^T \quad \text{in } \Omega, \quad \mathbf{U}_2 = \mathbf{0} \quad \text{on } \Gamma, \quad (2.10)$$

and where  $\mathbf{A}_0$  is the Navier-Stokes operator linearized about the zeroth-order base flow  $\mathbf{Q}_0$ ,

$$\mathbf{A}_0 = \begin{bmatrix} \mathbf{U}_0 \cdot \nabla () + () \cdot \nabla \mathbf{U}_0 - Re^{-1} \nabla^2 () & \nabla () \\ \nabla \cdot () & 0 \end{bmatrix}. \quad (2.11)$$

The control and the resulting flow modification alter the reattachment location as

$$x_r(z) = x_{r0} + \epsilon x_{r1}(z) + \epsilon^2 x_{r2}(z) + \dots. \quad (2.12)$$

In this expression,  $x_{r0}$  is the reattachment location of the uncontrolled flow  $\mathbf{Q}_0$ ,

$$\left. \frac{\partial U_0}{\partial y} \right|_{x=x_{r0}, y=0} = 0. \quad (2.13)$$

Similarly, the first-order variation  $x_{r1}(z)$  is the reattachment location of the first-order flow modification  $\mathbf{Q}_1$ , characterized implicitly by a vanishing wall shear stress condition,

$$\left. \frac{\partial U_1}{\partial y} \right|_{x=x_{r1}, y=0, z} = 0, \quad (2.14)$$

and expressed explicitly as (Boujo & Gallaire, 2014a,b, 2015):

$$x_{r1}(z) = - \left. \frac{\partial_y U_1}{\partial_{xy} U_0} \right|_{x=x_{r0}, y=0}. \quad (2.15)$$

The notation  $x_{r1}(z)$  in (2.14)-(2.15) is meant to emphasize that the reattachment line is modulated in the spanwise direction. When the control is harmonic in  $z$ , as considered in this study, it can actually be shown that  $\mathbf{Q}_1$  and  $x_{r1}$  are purely harmonic too. As a result, the first-order variation  $x_{r1}(z)$  has a zero mean. In contrast, the second-order variation  $x_{r2}(z)$  has a non-zero

mean in general: as detailed in Appendix 2.8.1, it reads

$$x_{r2}(z) = \left[ -\frac{\partial_y U_2}{\partial_{xy} U_0} + \frac{(\partial_y U_1)(\partial_{xy} U_1)}{(\partial_{xy} U_0)^2} - \frac{(\partial_{xxy} U_0)(\partial_y U_1)^2}{2(\partial_{xy} U_0)^3} \right]_{x=x_{r0}, y=0} \quad (2.16)$$

$$= x_{r2,I} + x_{r2,II} + x_{r2,III}. \quad (2.17)$$

This expression shows that the reattachment location is modified at second order via two effects:  $x_{r2,I}$  depends linearly on the second-order flow modification  $\mathbf{Q}_2$ , and  $x_{r2,II}$  and  $x_{r2,III}$  depend quadratically on the first-order flow modification  $\mathbf{Q}_1$ .

### 2.2.2 Sensitivity of the reattachment length: general expression

We introduce the field  $\mathbf{S}_I$  and the operators  $\mathbf{S}_{II}$  and  $\mathbf{S}_{III}$  such that the second-order variation  $x_{r2}$  can be expressed with scalar products,

$$x_{r2}(z) = (\mathbf{S}_I | \mathbf{U}_2) + (\mathbf{U}_1 | \mathbf{S}_{II} \mathbf{U}_1) + (\mathbf{U}_1 | \mathbf{S}_{III} \mathbf{U}_1), \quad (2.18)$$

where the three terms of the right-hand side correspond to the three terms of (2.16)-(2.17), respectively,

and  $(\cdot | \cdot)$  is the Hermitian scalar product in the domain  $\Omega$  defined as  $(\mathbf{a} | \mathbf{b}) \equiv \int_{\Omega} \mathbf{a}^* \mathbf{b} d\Omega$  with the superscript  $*$  indicating complex conjugate. For integration along a boundary  $\Gamma$ , an angled bracket is used:  $\langle \mathbf{a} | \mathbf{b} \rangle \equiv \int_{\Gamma} \mathbf{a}^* \mathbf{b} d\Gamma$ . Omitting the notation  $y = 0$ , one identifies from (2.16)-(2.17):

$$\mathbf{S}_I = \frac{-1}{\partial_{xy} U_0(x_{r0})} \delta(x_{r0}) \mathbf{e}_x \partial_y, \quad (2.19)$$

$$\mathbf{S}_{II} = \frac{1}{(\partial_{xy} U_0(x_{r0}))^2} \delta(x_{r0}) (\mathbf{e}_x \partial_y)^\dagger \otimes (\mathbf{e}_x \partial_y), \quad (2.20)$$

$$\mathbf{S}_{III} = \frac{-\partial_{xxy} U_0(x_{r0})}{2(\partial_{xy} U_0(x_{r0}))^3} \delta(x_{r0}) (\mathbf{e}_x \partial_y)^\dagger \otimes (\mathbf{e}_x \partial_y), \quad (2.21)$$

where  $\delta(x, y)$  is the 2D Dirac delta function, and the superscript  $^\dagger$  denotes the adjoint of an operator defined as  $(\mathbf{a} | \mathbf{S} \mathbf{b}) = (\mathbf{S}^\dagger \mathbf{a} | \mathbf{b})$ . Note that the operators  $\mathbf{S}_I$ ,  $\mathbf{S}_{II}$  and  $\mathbf{S}_{III}$  depend only on  $\mathbf{U}_0$ . From (2.10),  $\mathbf{Q}_2$  is uniquely determined by  $\mathbf{Q}_1$ , such that the first term of the right-hand side of (2.18) can be expressed as

$$x_{r2,I} = (\mathbf{S}_I | -\mathbf{A}_0^{-1}(\mathbf{U}_1 \cdot \nabla \mathbf{U}_1)) = (\mathbf{A}_0^{\dagger -1} \mathbf{S}_I | -\mathbf{U}_1 \cdot \nabla \mathbf{U}_1) = (\mathbf{U}^\dagger | -\mathbf{U}_1 \cdot \nabla \mathbf{U}_1) = (\mathbf{U}_1 | \mathbf{S}_I' \mathbf{U}_1), \quad (2.22)$$

where we have introduced the 2D adjoint base flow  $\mathbf{U}^\dagger(x, y)$ , defined by

$$\mathbf{A}_0^\dagger \mathbf{U}^\dagger = \mathbf{S}_I, \quad (2.23)$$



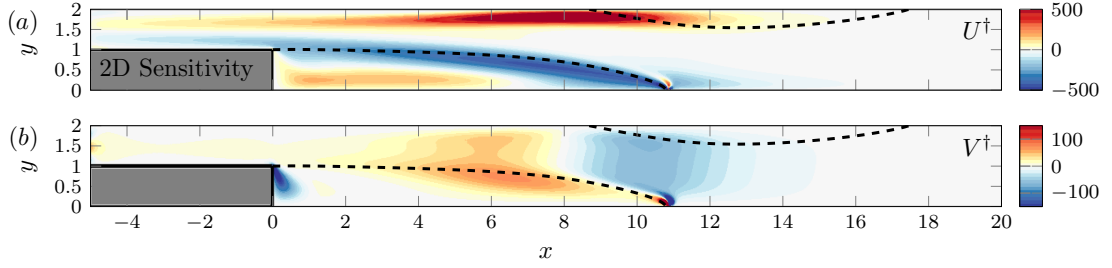


Figure 2.2 – 2D adjoint base flow (a)  $U^\dagger$  and (b)  $V^\dagger$ . The dashed lines indicate lower and upper walls recirculation regions which is delimited by the wall and the separating streamline (separatrix).

with  $\mathbf{A}_0^\dagger$  the adjoint Navier-Stokes operator. The adjoint base flow, depicted in figure 2.2, depends only on  $\mathbf{U}_0$ , and is the same adjoint base flow  $\mathbf{U}^\dagger$  as in Boujo & Gallaire (2014a, 2015) where it represents the first-order sensitivity of the reattachment location  $x_r$  to a steady 2D volume forcing. In the last equality of (2.22), we could introduce the operator  $\mathbf{S}_{I'}$  (dependent on  $\mathbf{U}^\dagger$ ) because the expression is quadratic in  $\mathbf{U}_1$ . The second-order variation can therefore be expressed quadratically in any flow modification  $\mathbf{U}_1$  via a single operator for second-order sensitivity to flow modification:

$$x_{r2}(z) = (\mathbf{U}_1 | \mathbf{S}_{2,\mathbf{U}_1} \mathbf{U}_1) \quad \text{where} \quad \mathbf{S}_{2,\mathbf{U}_1} = \mathbf{S}_{I'} + \mathbf{S}_{II} + \mathbf{S}_{III}. \quad (2.24)$$

Finally, using (2.9), one can introduce operators for the second-order sensitivity to control, dependent only on the uncontrolled flow  $\mathbf{U}_0$ , and such that for any control:

$$x_{r2}(z) = (\mathbf{C} | \mathbf{S}_{2,\mathbf{C}} \mathbf{C}) + \langle \mathbf{U}_c | \mathbf{S}_{2,\mathbf{U}_c} \mathbf{U}_c \rangle, \quad (2.25)$$

where

$$\mathbf{S}_{2,\mathbf{C}} = \mathbf{P}^T \mathbf{A}_{0,\mathbf{C}}^{\dagger -1} \mathbf{S}_{2,\mathbf{U}_1} \mathbf{A}_{0,\mathbf{C}}^{-1} \mathbf{P}, \quad (2.26)$$

$$\text{and} \quad \mathbf{S}_{2,\mathbf{U}_c} = \mathbf{P}^T \mathbf{A}_{0,\mathbf{U}_c}^{\dagger -1} \mathbf{S}_{2,\mathbf{U}_1} \mathbf{A}_{0,\mathbf{U}_c}^{-1} \mathbf{P}. \quad (2.27)$$

Here  $\mathbf{P}$  is the prolongation matrix that converts the velocity-only space to velocity-pressure space such that  $\mathbf{P}\mathbf{U} = (\mathbf{U}, 0)^T$  and  $\mathbf{P}^T \mathbf{Q} = \mathbf{U}$ , and  $\mathbf{A}_{0,\mathbf{C}}$  and  $\mathbf{A}_{0,\mathbf{U}_c}$  are defined by the volume-control-only and wall-control-only versions of (2.9), respectively:

$$\mathbf{A}_{0,\mathbf{C}} \mathbf{Q}_1 = (\mathbf{C}, 0)^T \quad \text{in } \Omega, \quad \mathbf{U}_1 = \mathbf{0} \quad \text{on } \Gamma, \quad (2.28)$$

$$\mathbf{A}_{0,\mathbf{U}_c} \mathbf{Q}_1 = \mathbf{0} \quad \text{in } \Omega, \quad \mathbf{U}_1 = \mathbf{U}_c \quad \text{on } \Gamma_c, \quad \mathbf{U}_1 = \mathbf{0} \quad \text{on } \Gamma \setminus \Gamma_c. \quad (2.29)$$

### 2.2.3 Simplification: spanwise-harmonic control

Let us now assume a spanwise-harmonic control of the form

$$\mathbf{U}_c(x, y, z) = \begin{pmatrix} \tilde{U}_c(x, y) \cos(\beta z) \\ \tilde{V}_c(x, y) \cos(\beta z) \\ \tilde{W}_c(x, y) \sin(\beta z) \end{pmatrix}, \quad \mathbf{C}(x, y, z) = \begin{pmatrix} \tilde{C}_x(x, y) \cos(\beta z) \\ \tilde{C}_y(x, y) \cos(\beta z) \\ \tilde{C}_z(x, y) \sin(\beta z) \end{pmatrix}. \quad (2.30)$$

The first-order flow modification is also spanwise-harmonic, of same wavenumber  $\beta$ :

$$\mathbf{Q}_1(x, y, z) = \begin{pmatrix} \tilde{U}_1(x, y) \cos(\beta z) \\ \tilde{V}_1(x, y) \cos(\beta z) \\ \tilde{W}_1(x, y) \sin(\beta z) \\ \tilde{P}_1(x, y) \cos(\beta z) \end{pmatrix}. \quad (2.31)$$

The quadratic term  $-\mathbf{U}_1 \cdot \nabla \mathbf{U}_1$  in (2.10) is then the sum of 2D terms (spanwise invariant terms, i.e. of wavenumber 0) and 3D terms (of wavenumber  $2\beta$ ), which we denote  $\mathbf{f}^{2D}(x, y) + \mathbf{f}^{3D}(x, y, z)$ . As a result, the second-order flow modification has the same form:  $\mathbf{Q}_2^{2D}(x, y) + \mathbf{Q}_2^{3D}(x, y, z)$ . Similarly, the second and third terms in (2.16)-(2.17) and (2.18) have the same form too, and finally the second-order reattachment location modification reads

$$x_{r2}(z) = x_{r2}^{2D} + x_{r2}^{3D}(z) \quad (2.32)$$

where

$$x_{r2}^{2D} = \left[ -\frac{\partial_y U_2^{2D}}{\partial_{xy} U_0} + \frac{(\partial_y \tilde{U}_1)(\partial_{xy} \tilde{U}_1)}{2(\partial_{xy} U_0)^2} - \frac{(\partial_{xxy} U_0)(\partial_y \tilde{U}_1)^2}{4(\partial_{xy} U_0)^3} \right]_{x=x_{r0}, y=0} \quad (2.33)$$

$$= x_{r2,I}^{2D} + x_{r2,II}^{2D} + x_{r2,III}^{2D}. \quad (2.34)$$

Because  $x_{r2}^{3D}(z)$  is harmonic of zero mean, we now focus on the spanwise-invariant component  $x_{r2}^{2D}$ . Its expression can be simplified, taking advantage of the specific form (2.30) of the control:

$$x_{r2}^{2D} = \left( \tilde{\mathbf{C}} \mid \tilde{\mathbf{S}}_{2,\tilde{\mathbf{C}}} \tilde{\mathbf{C}} \right) + \left\langle \tilde{\mathbf{U}}_c \mid \tilde{\mathbf{S}}_{2,\tilde{\mathbf{U}}_c} \tilde{\mathbf{U}}_c \right\rangle, \quad (2.35)$$

where  $\tilde{\mathbf{S}}_{2,\tilde{\mathbf{C}}}$  and  $\tilde{\mathbf{S}}_{2,\tilde{\mathbf{U}}_c}$  are spanwise-invariant versions of the second-order sensitivity operators (2.26)-(2.27) (see detailed expressions in Appendix 2.8.2).

Figure 2.3(a) visualizes the 3D flow modification with spanwise-periodic control. Here the control is applied only on the upstream part ( $x < 0$ ) of the lower wall, with amplitude  $\epsilon = 0.003$  (see figure 2.8 for the actuation vector). As shown in the sketch of Fig. 2.3(b), the reattachment location  $x_r(z)$  is decomposed into zeroth-order  $x_{r0}$  (uncontrolled), first-order  $x_{r1}(z)$  (of zero mean), and second-order  $x_{r2}$ . As mentioned earlier, the second-order component is further divided into a zero-mean 3D part  $x_{r2}^{3D}(z)$  and a mean 2D part  $x_{r2}^{2D}$ . Therefore, the spanwise-

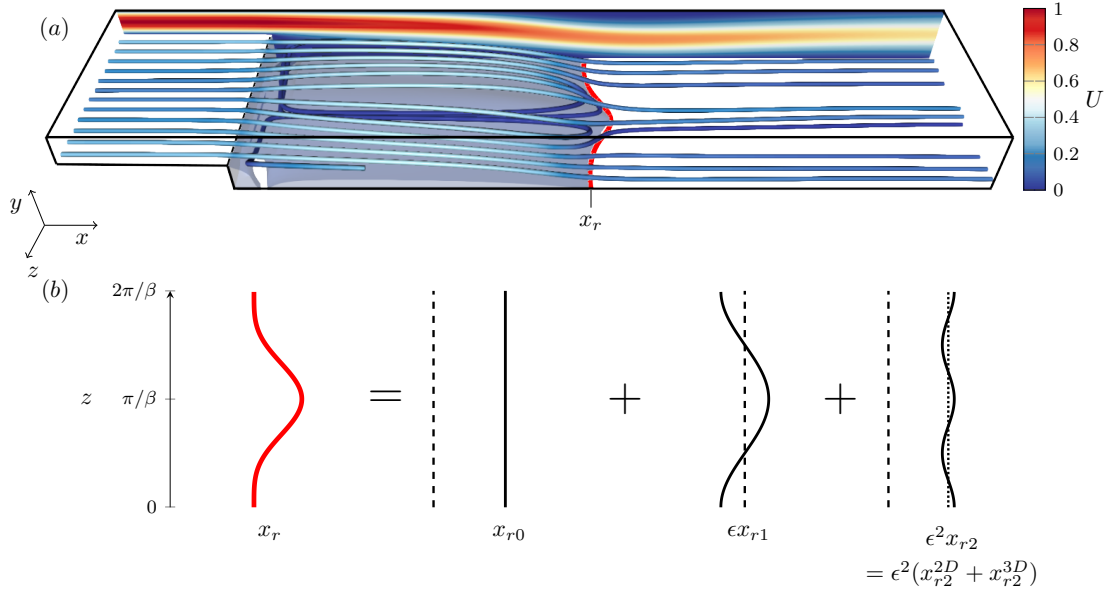


Figure 2.3 – (a) An example of 3D DNS base flow modified by a wall blowing/suction control (using the same control as in figure 2.8 with  $\epsilon = 0.003$ ). The streamlines starts at  $(x, y) = (-5, 1.05)$  at different spanwise positions in  $z$ . The shaded contour indicates the zero  $x$ -velocity  $U = 0$  iso-surface at lower wall (another recirculation bubble on the upper wall exists but is not shown here). The thick red line indicates the lower reattachment location ( $\partial_y U = 0$ ). (b) Decomposition of the reattachment location  $x_r$  into zero  $x_{r0}$ , first  $x_{r1}$  and second  $x_{r2}$  order components. The spanwise averaged reattachment location is  $\bar{x}_r = x_{r0} + \epsilon^2 x_{r2}^{2D}$ .

averaged reattachment location is

$$\bar{x}_r = x_{r0} + \epsilon^2 x_{r2}^{2D}, \quad (2.36)$$

which is our control interest. The second-order variation  $x_{r2}^{2D}$  is now referred to as mean correction.

#### 2.2.4 Optimal spanwise-periodic control

In this section, we show the optimal control for the reattachment location. The formulation is similar to Boujo *et al.* (2019) except that the matrices are all real in this case while in the study of Boujo *et al.* (2019) it was complex since they were dealing with the unstable flow with complex eigenvalues. Hence, we only introduce the procedure briefly on the optimization of the mean correction by the boundary control  $\tilde{\mathbf{U}}_c$  only since the derivation for a volume control  $\tilde{\mathbf{C}}$  is similar.

### Optimal spanwise-periodic wall actuation

The optimal control is now defined to find the maximum/minimum singular value of the sensitivity operator  $\tilde{\mathbf{S}}_{2,\tilde{\mathbf{U}}_c}$ . For minimizing the reattachment location (mean correction) by actuating the wall boundaries, the optimization is

$$\min_{\|\tilde{\mathbf{U}}_c\|=1} (x_{r2}^{2D}) = \min \frac{\langle \tilde{\mathbf{U}}_c | \frac{1}{2} (\tilde{\mathbf{S}}_{2,\tilde{\mathbf{U}}_c} + \tilde{\mathbf{S}}_{2,\tilde{\mathbf{U}}_c}^T) \tilde{\mathbf{U}}_c \rangle}{\langle \tilde{\mathbf{U}}_c | \tilde{\mathbf{U}}_c \rangle} = \frac{1}{2} \lambda_{\min} (\tilde{\mathbf{S}}_{2,\tilde{\mathbf{U}}_c} + \tilde{\mathbf{S}}_{2,\tilde{\mathbf{U}}_c}^T), \quad (2.37)$$

which indicates that the smallest eigenvalue in equation (2.37) is the mean correction and the actuation vector is the corresponding singular vector.

### Optimal spanwise-periodic wall deformation

For the sake of open loop control, deforming the geometry can be more interesting than a steady wall velocity actuation. Hence, one can deduce the wall deformation using the wall velocity actuation (Boujo *et al.*, 2019). At all rigid wall boundaries, the velocity should vanish and it is the same for when the wall is deformed with a small deformation  $\epsilon y_1$  and with the Taylor expansion,

$$\begin{aligned} \mathbf{U}(y_0 + \epsilon y_1) &= \mathbf{U}_0(y_0 + \epsilon y_1) + \epsilon \mathbf{U}_1(y_0 + \epsilon y_1) + \dots \\ &= \mathbf{U}_0(y_0) + \epsilon [y_1 \partial_y \mathbf{U}_0(y_0) + \mathbf{U}_1(y_0)] + \dots = \mathbf{0}. \end{aligned} \quad (2.38)$$

This reads the relation between streamwise velocity component  $\tilde{U}_c$  and the wall deformation  $y_1$  as

$$\tilde{U}_1(y_0) = -y_1 \frac{\partial U_0(y_0)}{\partial y} = \tilde{U}_c. \quad (2.39)$$

Then, the mean correction  $x_{r2}^{2D}$  can now be expressed with the small wall deformation  $y_1$  as

$$\begin{aligned} x_{r2} &= \langle \tilde{U}_c | \tilde{\mathbf{S}}_{2,\tilde{U}_c} \tilde{U}_c \rangle = \langle -\partial_y U_0(y_0) \tilde{y}_1 | -\tilde{\mathbf{S}}_{2,\tilde{\mathbf{U}}_c} \partial_y U_0(y_0) \tilde{y}_1 \rangle \\ &= \langle \tilde{y}_1 | \mathbf{M}^\dagger \tilde{\mathbf{S}}_{2,\tilde{\mathbf{U}}_c} \mathbf{M} \tilde{y}_1 \rangle = \langle \tilde{y}_1 | \tilde{\mathbf{S}}_{2,\tilde{y}_1} \tilde{y}_1 \rangle, \end{aligned} \quad (2.40)$$

where  $\mathbf{M}$  is the weighting matrix with the wall shear  $-\partial_y U_0(y_0)$ . Finally, the optimization with the unit-norm wall deformation  $y_1$  reads

$$\min_{\|\tilde{y}_1\|=1} (x_{r2}^{2D}) = \min \frac{\langle \tilde{y}_1 | \frac{1}{2} (\tilde{\mathbf{S}}_{2,\tilde{y}_1} + \tilde{\mathbf{S}}_{2,\tilde{y}_1}^T) \tilde{y}_1 \rangle}{\langle \tilde{y}_1 | \tilde{y}_1 \rangle} = \frac{1}{2} \lambda_{\min} (\tilde{\mathbf{S}}_{2,\tilde{y}_1} + \tilde{\mathbf{S}}_{2,\tilde{y}_1}^T). \quad (2.41)$$

## 2.3 Numerical method

### 2.3.1 Linear analysis

The sensitivity analysis and the optimization have been conducted using the method described by (Boujo & Gallaire, 2014a, 2015; Boujo *et al.*, 2019). The problem is discretized with a finite element method using FreeFem++ (Hecht, 2012) with P2 and P1 Taylor-Hood elements for velocity and pressure, respectively. The typical number of elements is  $1.57 \times 10^5$  with clustered mesh near the reattachment point yielding  $10^6$  degrees of freedom. The uncontrolled base flow (2.8) is obtained by the Newton method. Eigenvalues are solved with a restarted Arnoldi method.

At the inlet ( $x = -5$ ), a Poiseuille flow condition is given with the scaled maximum velocity 1 and the pressure free outlet condition is applied at the outlet ( $x = 50$ ). For  $Re = 500$ , the reattachment location for lower wall is 10.87. With mesh density, the reattachment point varies little from 10.88 (crude mesh,  $4.5 \times 10^4$  no. elements) to 10.87 (finest mesh,  $1.65 \times 10^5$  no. elements).

### 2.3.2 Three-dimensional DNS

Direct numerical simulations (DNS) are also carried out for validation of the theory and using the open-source code NEK5000 (Fischer, Lottes & Kerkemeier, 2008). This massively parallel code is based on the spectral element method where spatial domain is discretized using hexahedral elements. The unknown parameters are obtained using  $N$ th-order Lagrange polynomial interpolants, based on the Gauss-Lobatto-Legendre quadrature points in each spectral element with  $N \geq 6$ . A third order backward differentiation formula (BDF3) is employed for time discretization. For the spatial discretization, the diffusive terms are treated implicitly whereas the convective terms are estimated using a third order explicit extrapolation formula (EXT3). Since the explicit extrapolations of the convective terms in the BDF3-EXT3 scheme enforce a restriction on the time step for iterative stability (Karniadakis, Israeli & Orszag, 1991), we chose the time step such as to have a Courant number  $CFL \approx 0.5$ .

The computational domain and the boundary conditions are in accordance with the specifications of the backward facing step used in the sensitivity analysis. Additionally, we impose periodic boundary conditions in the spanwise direction where the spanwise width captures only one period  $z = [0, 2\pi/\beta]$  for the purpose of validation. Certain cases employing optimal spanwise modulation required the analysis of a double period domain with  $z = [0, 4\pi/\beta]$ . The domain is discretized using a structured multiblock grid consisting of 36200 and 72400 spectral elements for maximum spanwise width of  $2\pi/\beta$  and  $4\pi/\beta$ , respectively.

## 2.4 Stability properties of the zeroth-order base flow

In this section, we shall investigate the characteristics of the non-modified zeroth-order base flow. For a backward facing step, the flow separates and reattaches and a recirculation bubble exists between these two points. The backward facing step with an expansion ratio 2 (total height/step height) at  $Re = 500$ , there exist two recirculation bubbles: one on the lower wall developing rear of the step  $x = [0 \ 10.87]_{y=0}$  and the other one on upper wall between  $x = [8.7 \ 17.5]_{y=2}$ . In this section, we show some linear characteristics of the zeroth-order base flow.

### 2.4.1 Global stability

First, we investigate the eigenvalues of the system as well as the optimal response to the 3D perturbation of the 2D base flow. We assume a normal mode perturbation with the complex eigenvalue  $\lambda$  and spanwise periodicity  $\beta_0$  as  $\mathbf{q}' = \hat{\mathbf{q}}(x, y) \exp(\lambda t + i\beta_0 z)$ . Note that we use a subscript  $_0$  to indicate the eigenmode wavenumber which should be distinguished from the control wavenumber  $\beta$ . Then, we solve a generalized eigenvalue problem of linear equation around the uncontrolled 2D base flow,

$$\lambda \hat{\mathbf{q}} = \tilde{\mathbf{A}}_0 \hat{\mathbf{q}}, \quad (2.42)$$

with vanishing boundary conditions at the walls. The leading eigenvalues for  $Re = 500$  are shown in figure 2.4 as a function of the spanwise wavenumber  $\beta_0$ . For the purpose of comparison later with the gain, the leading growth rate is plotted as an inverse of the absolute value of  $\lambda$ . All the leading eigenvalues have negative growth rate, i.e. decaying perturbation, and zero frequency except for  $\beta_0 = 0.4$  and  $\beta_0 = 0.5$ . There exists two local maximums ( $\beta_0 = 0.1$  and  $\beta_0 = 1$ ) and one local minimum ( $\beta_0 = 0.5$ ), it decreases monotonically for  $\beta_0 > 1$ . This result is very much in line with the study of Barkley *et al.* (2002) for  $Re = 450$ . They showed that 3D global instability emerges when Reynolds number is higher than  $Re = 748$ . Some selected global modes of streamwise velocity  $\hat{U}_1$  are shown in figures 2.5 for  $\beta_0 = 0.1, 0.5$  and  $1$ . For  $\beta_0 = 0.1$ , the mode is localized  $x = 10$  which is near the lower reattachment and upper separation points. For  $\beta_0 = 0.5$ , the mode is focused on  $x > 10$  while it is localized  $x < 10$  for  $\beta_0 = 1$ .

### 2.4.2 Optimal 3D steady forcing

For such a stable flow, it is interesting to investigate what kind of external disturbance amplifies the system most. Here we consider in particular a steady spanwise-harmonic steady forcing  $\mathbf{f} = \hat{\mathbf{f}}(x, y) \exp(i\beta z)$  acting on the wall boundaries  $\Gamma$ , and resulting linearly in a steady spanwise-periodic response  $\mathbf{q} = \hat{\mathbf{q}}(x, y) \exp(i\beta z)$  via

$$\tilde{\mathbf{A}}_0 \hat{\mathbf{q}} = \mathbf{B}_f \hat{\mathbf{f}}, \quad (2.43)$$

where  $\mathbf{B}_f$  limits active forcing regions to the walls. The linear amplification efficiency can be measured with a linear gain, for instance as the ratio of the norms of the forcing velocity and response velocity:

$$G = \frac{\|\hat{\mathbf{q}}\|}{\|\hat{\mathbf{f}}\|}. \quad (2.44)$$

This ratio can be maximized: the linear optimal gain is given by the largest singular value of the resolvent operator and the optimal forcing vector is the associated singular vector (see details in Garnaud *et al.*, 2013; Boujo & Gallaire, 2015). The optimal gain with the steady wall actuation is shown in figure 2.4. The optimal gain takes the similar qualitative behavior to the inverse of the absolute eigenvalue of the global mode. The maximum gain is  $G = 326$  with  $\beta = 0.1$  which corresponds to the least stable global mode with the same value of  $\beta_0$ . Similarly,  $\beta = 0.5$  is the local minimum and the second local maximum is located at  $\beta = 0.8$  slightly lower than the global eigenvalue. The response behaves as the shortest distance of the forcing frequency to the eigenvalue of the system. This result demonstrates the  $\varepsilon$ -pseudospectral property (Trefethen, Trefethen, Reddy & Driscoll, 1993; Schmid, 2007). Some selected responses  $\hat{\mathbf{U}}_1$  are depicted in figure 2.6. Indeed, for  $\beta = 0.1$  and 1, the responses are similar to the corresponding eigenvectors. For  $\beta = 0.5$ , however, the response is slightly different from the global mode since the least stable global mode has a non-zero frequency while the considered response is steady.

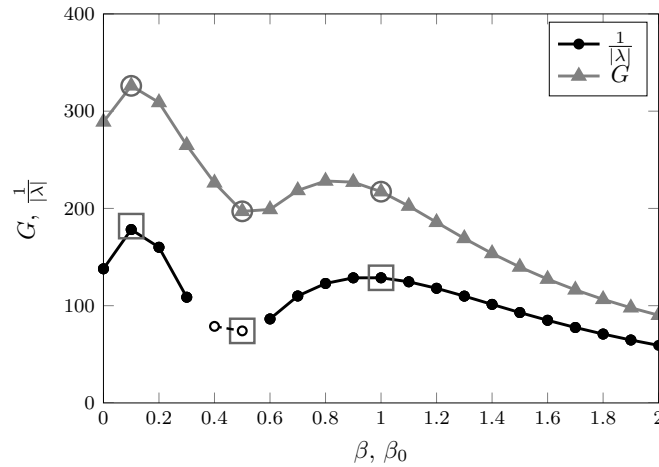


Figure 2.4 – Leading eigenvalues represented as inverse of distance from the origin  $1/|\lambda|$  and optimal gain  $G$  as a function of spanwise wavenumber  $\beta$  ( $\beta_0$ ) for  $Re = 500$ . The filled circles indicate zero frequency ( $\lambda_i = 0$ ) and empty circles are for non-zero frequency.

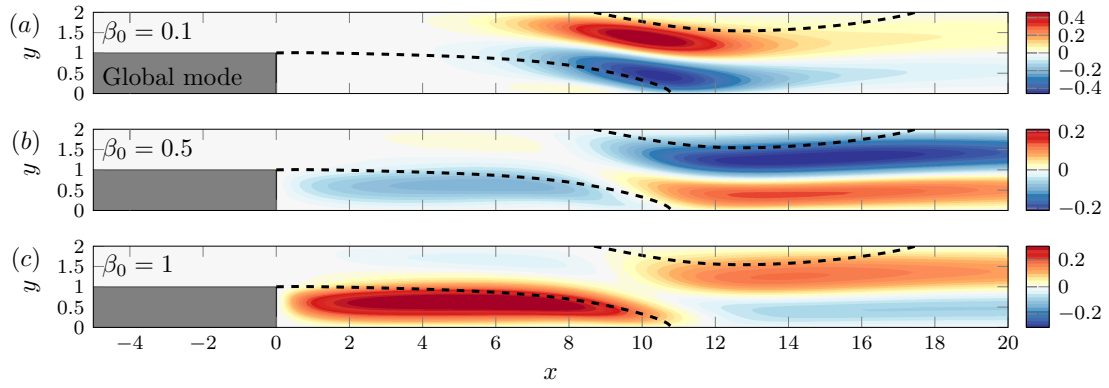


Figure 2.5 – Streamwise velocity of the least stable global modes for (a)  $\beta_0 = 0.1$ , (b)  $\beta_0 = 0.5$  and (c)  $\beta_0 = 1$ . In (a) and (c)  $\tilde{U}_1$  is represented (steady eigenmode) while in (b) its real part  $\text{Re}(\tilde{U}_1)$  is shown (unsteady eigenmode).

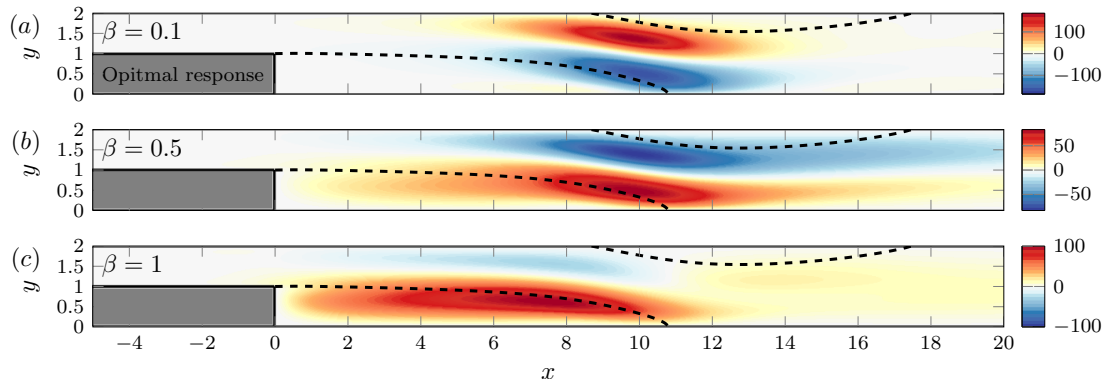


Figure 2.6 – Streamwise velocity (real part  $\text{Re}(\hat{U}_1)$ ) of the optimal response to steady forcing for (a)  $\beta = 0.1$ , (b)  $\beta = 0.5$  and (c)  $\beta = 1$ .



## 2.5 Results: optimal control for lower reattachment location

### 2.5.1 Optimal wall actuation

Figure 2.7a shows the optimal mean correction  $x_{r2}^{2D}$  as a function of  $\beta$  for different wall actuation scenarios: actuation on upper wall with only wall normal velocity  $\tilde{V}_c$  and on the upstream lower wall with  $\tilde{V}_c$  or with the wall tangential velocity  $\tilde{U}_c$ . Note that the 3D velocity controls can be retrieved as  $(U_c, V_c, W_c)(x, y, z) = (\tilde{U}_c(x, y) \cos(\beta z), \tilde{V}_c(x, y) \cos(\beta z), \tilde{W}_c(x, y) \sin(\beta z))$ . The wall restriction has been implemented by modifying the prolongation matrix  $\mathbf{P}$ .

The wall normal control  $(0, V_c, 0)$  on upper wall has the minimum at  $\beta = 0.6$  while actuating the upstream lower wall is most efficient at  $\beta = 1$ . However, wall tangential actuation  $U_c$  on upstream lower wall has a negligible impact on the reattachment length with the minimum  $x_{r2}^{2D} = -10^3$  at  $\beta = 1.1$  which is 60 times smaller than the wall normal control. This holds for other types of wall controls (not shown) that actuating on the wall normal velocity  $\tilde{V}_c$  is generally more efficient than actuating wall tangential parts both  $\tilde{U}_c$  and  $\tilde{W}_c$ . The detailed individual contributions of the terms I, II and III in (2.34) for the mean correction are shown in figure 2.7b,c. for upper wall,  $\tilde{V}_c$  and upstream lower wall,  $\tilde{V}_c$ , respectively. In both cases, the term I, which is a linear function of the second-order flow modification, contributes the most on the mean correction while the terms II and III, who depend quadratically to the first-order flow modification, have negligible or counteracting influences on the mean correction. The control vectors for the upper wall for  $\beta = 0.6$  and upstream lower wall for  $\beta = 1$  are shown in figure 2.8. The control has the maximum actuation velocity at  $x \simeq 6$  for upper wall control and for upstream lower wall, it is located at  $x = 0$  where the flow separates due to the step corner. The linear gain due to the control is shown in figure 2.9a for the two types of wall controls. The gain is estimated as the ratio between the response  $\|\tilde{\mathbf{U}}_1\|$  and the control  $\|\tilde{\mathbf{U}}_c\|$ . Since  $\|\tilde{\mathbf{U}}_c\| = 1$ , the gain is simply the amplitude of the response  $G^2 = (\tilde{\mathbf{U}}_1 | \tilde{\mathbf{U}}_1)$ . The linear gains for maximizing  $G$  from (2.44) for the corresponding restricted walls are also shown in the same figure. The control induced gain is close to the optimal gain and their response vectors  $\tilde{\mathbf{U}}_1$  (not shown) are also very similar to each other. This indicates that the recirculation length  $x_r$  has close relation to the amplification potential of the system as reported by Boujo & Gallaire (2014b).

Figure 2.9b now shows the spanwise averaged reattachment length  $\bar{x}_r$  computed from 3D DNS along with the sensitivity prediction for the reattachment location  $x_r^{2D} = x_0 + \epsilon^2 x_{r2}^{2D}$  as a function of actuation amplitude  $\epsilon$  for the upstream lower wall control case. The agreement is very good until the actuation amplitude  $\epsilon \simeq 0.001$  after which it starts to differ due to the strong nonlinear effect. For  $\epsilon = 0.001$ , one can conclude that 0.1% actuation reduces the reattachment location by 0.55% (upstream lower wall control) which is about 5.5 times of the control amplitudes.

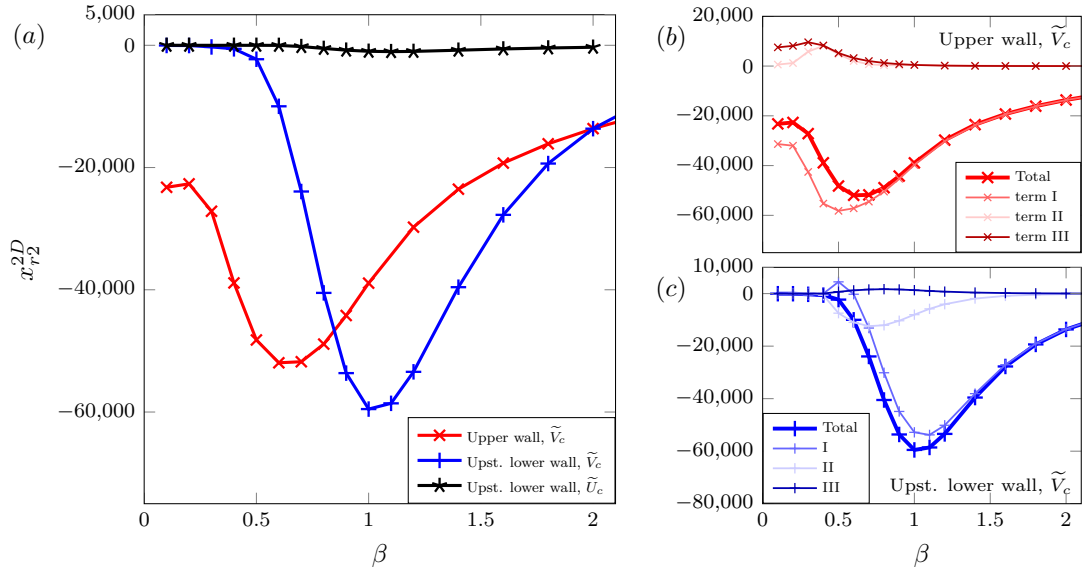


Figure 2.7 – (a) Optimal mean correction  $x_{r2}^{2D}$  control by wall blowing/suction to minimize the mean reattachment length  $\bar{x}_r$  as a function of spanwise wavenumber  $\beta$  for actuation on different walls. The individual contributions of the terms I, II and III in (2.34) (their 2D components) on the total mean correction are detailed in (b) for upper wall,  $\tilde{V}_c$  and (c) for upstream lower wall,  $\tilde{V}_c$  controls.

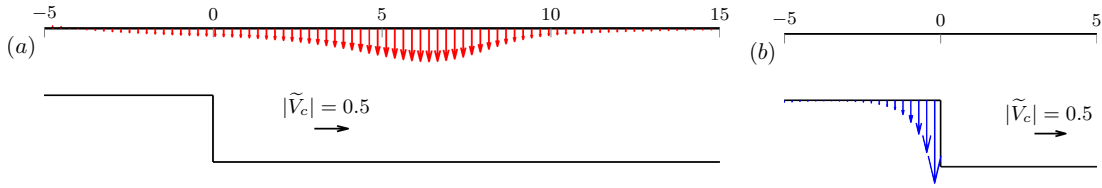


Figure 2.8 – Optimal control  $(0, \tilde{V}_c, 0)$  (a) on the upper wall for  $\beta = 0.6$  and (b) on the upstream lower wall for  $\beta = 1$ .

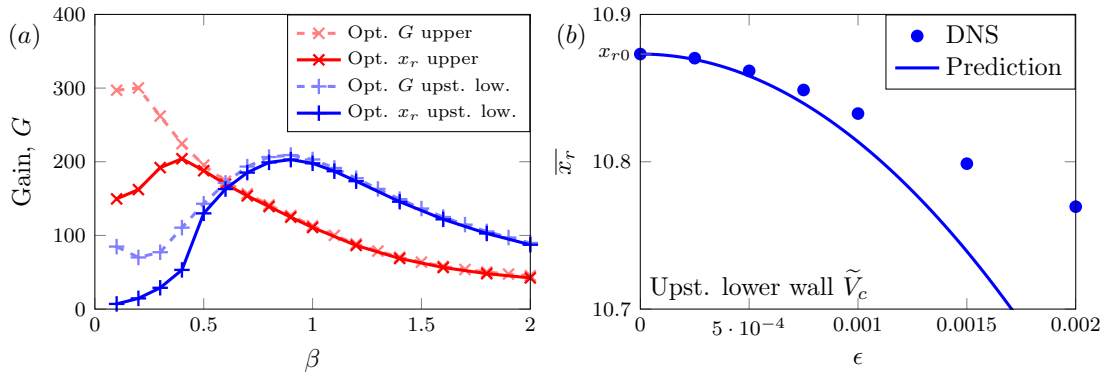


Figure 2.9 – (a) Linear gain  $G$  for steady spanwise-periodic wall blowing/suction: control  $\tilde{V}_c$  minimizing  $x_r$  (solid lines) and control  $\hat{\mathbf{f}}$  maximizing  $G$  (dashed lines). (b) The mean reattachment length  $\bar{x}_r$  as a function of the control amplitude for upstream lower wall actuation for  $\beta = 1$  and  $Re = 500$ . Line: sensitivity prediction, symbols: 3D DNS simulation.

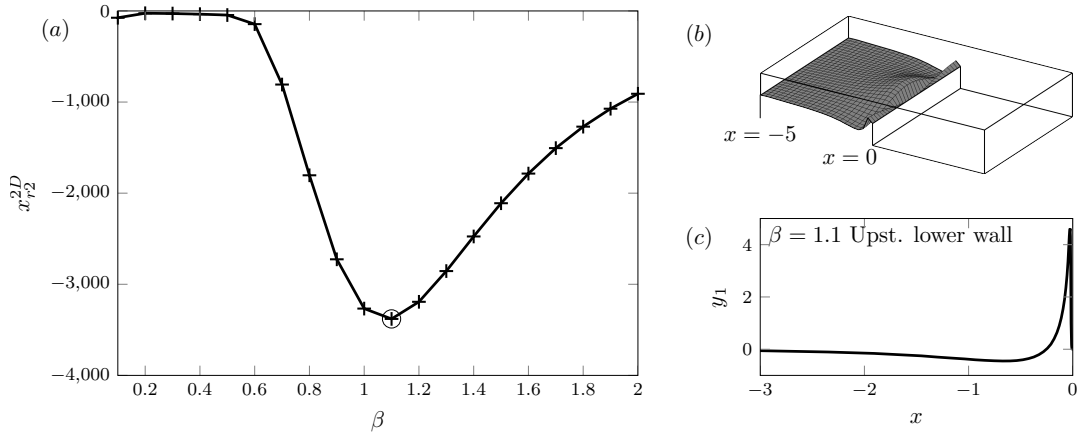


Figure 2.10 – (a) Effect of the optimal upstream lower wall deformation as a function of spanwise wavenumber  $\beta$ . (b) 3D visualization of upstream lower wall deformation  $y_1$  and (c) 2D view  $\tilde{y}_1$  where  $y_1 = \tilde{y}_1 \cos(\beta z)$ .

### 2.5.2 Optimal wall deformation

Here, we investigate the optimal wall deformation for minimizing the lower reattachment point. For simplicity, we focus only on the upstream lower wall deformation. The wall deformation is computed using (2.39). We also applied a smoothing filter on  $y_1$  near the step corner since  $\partial_y U_0$  goes to infinity at the step corner which is defined as  $F_w = 1/(\exp(2C_k(x + x_s)) + 1)$  where  $C_k = 250$  and  $x_s = 0.02$ . Figure 2.10 shows the optimal control  $x_{r2}^{2D}$  as a function of  $\beta$ . The most effective spanwise wavenumber is  $\beta = 1.1$ , similar to the wall actuation case. However, the efficiency is much lower than the velocity control. The minimum  $x_{r2}^{2D}$  is about 15 times less efficient than using the wall blowing/suction on the upstream lower wall. This is due to the fact that the wall deformation is a function of wall tangential velocity  $\tilde{U}_c$  (weighted with  $\partial_y U_0$ ) which has only a small contribution to  $x_{r2}^{2D}$  compared to the wall normal control  $\tilde{V}_c$  as shown in figure 2.7. Although less effective, the wall deformation on the upstream lower wall still results the mean correction about  $x_{r2}^{2D} = -3.7 \times 10^3$  for  $\beta = 1.1$ .

Figure 2.10b,c show the example of wall deformation  $y_1$  and 2D component  $\tilde{y}_1$  which relates  $y_1 = \tilde{y}_1 \cos(\beta z)$ . As shown, the wall deformation is the maximum just before the step where the flow separates. The 3D DNS result of the mean reattachment location as a function of deformation amplitude is shown in figure 2.11a. A good agreement has been found until  $\epsilon = 0.0075$ . At this point, the mean reattachment location is decreased to 10.7. It can be interpreted that 0.75% of wall deformation leads 1.5% mean correction. For higher amplitude of deformation ( $\epsilon > 0.01$ ), the mean reattachment location departs from the prediction curve. Figure 2.11b shows  $\bar{x}_r$  as a function of  $\beta$  for a fixed deformation amplitude  $\epsilon = 0.005$ . Generally, the prediction and 3D DNS show good agreement across different spanwise wavenumber  $\beta$  with the maximum error for  $\beta = 1.1$  as  $|\bar{x}_{r,DNS} - x_r^{2D}|/\bar{x}_{r,DNS} \approx 0.002$ .

For a larger deformation amplitude  $\epsilon = 0.015$ , the flow becomes unstable. Figure 2.12 shows

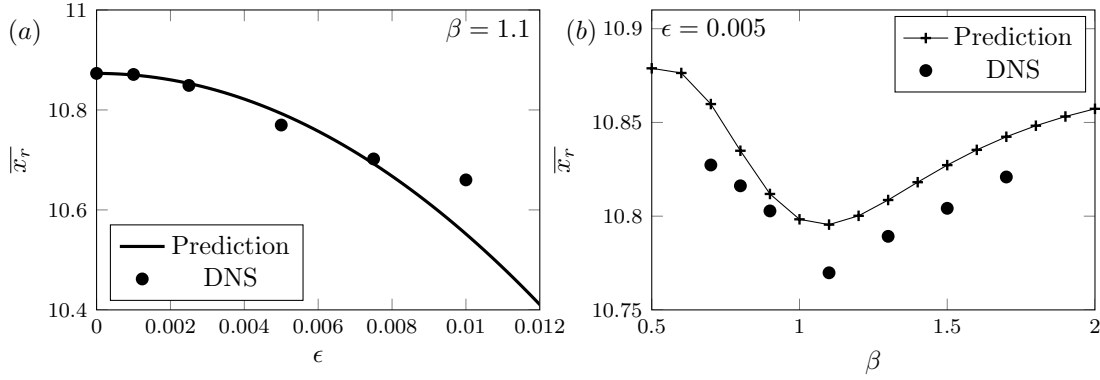


Figure 2.11 – Effect of the optimal wall deformation on the mean reattachment point (a) as a function of  $\epsilon$  for fixed  $\beta = 1.1$  and (b) as a function of  $\beta$  for fixed  $\epsilon = 0.005$ .

an instant flow field with iso-values of spanwise velocity  $W = \pm 0.03$ . Because the zero order base flow has no  $W$  component, the instant  $W$  velocity field can be approximated as velocity perturbation. The perturbation develops just after the step and contaminates the flow around  $x = [5 \ 40]$ . From top view (figure 2.12b), we see that clear mode separation in  $z$  at the nodal points of  $\sin(\beta z)$ . From the side view (figure 2.12c), the perturbation forms chevron patterns. The perturbation oscillates in time with a fundamental frequency  $\omega = 0.55$  ( $St = 0.088$ ). Boujo *et al.* (2015) had reported the destabilizing effect on spanwise periodic control on parallel shear flow. They showed that both the fundamental  $\beta$  and sub-harmonic  $\beta/2$  modes can be excited due to the sub-harmonic resonance mechanism (Herbert, 1988; Hwang *et al.*, 2013). However, in our DNS with the double spanwise domain size ( $z = [0 \ 4\pi/\beta]$ ) whose minimum spanwise-wavenumber is  $\beta/2$ , the perturbation does not show any  $\beta/2$  sub-harmonic mode. Instead, only harmonics of  $n\beta$  ( $n = 1, 2, 3, \dots$ ) exist and it can be seen from the top view (figure 2.12b).

## 2.6 Discussion

Although the optimization procedure finds the most efficient spanwise-periodic control, the effect on the mean recirculation length appears relatively small. In light of this observation, it is worth comparing the optimal 2D and 3D blowing/suction. One can show that the optimal 2D wall control is equal to the sensitivity to 2D wall control, given by the adjoint stress at the wall ( $P^\dagger \mathbf{I} + Re^{-1} \nabla \mathbf{U}^\dagger$ )  $\mathbf{n}$ , where  $(\mathbf{U}^\dagger, P^\dagger)$  is the adjoint base flow (see Sec. 2.2.2) and  $\mathbf{n}$  the outward unit normal vector (Boujo & Gallaire, 2014a,b, 2015). Since the tangential component is generally much smaller than the normal one, we simply consider the sensitivity to 2D normal actuation as the optimal control  $(0, V_c)$ . Figure 2.13 compares the 3D control optimized on the upstream lower wall ( $\beta = 1$ ) to its 2D counterpart, both normalized to norm 1. The linear response  $\delta \mathbf{U}$  to the 2D control is largest and positive near the lower reattachment point, resulting in a positive wall shear stress  $\partial_y \delta U$  at that location, as expected if  $x_r$  is to be minimized. Via the spanwise-periodic first-order flow modification  $\mathbf{U}_1$  (not shown), the

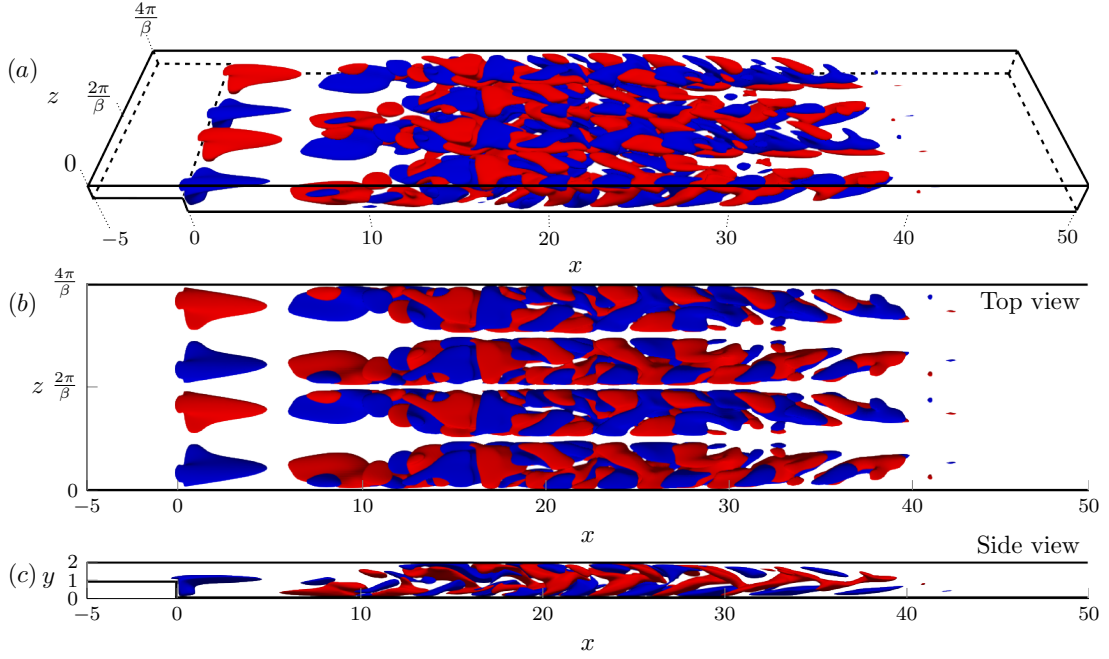


Figure 2.12 – Iso-contours for instantaneous spanwise velocity field  $W = \pm 0.03$  for upstream lower wall deformation with the amplitude  $\epsilon = 0.015$ : (a) oblique view, (b) top view and (c) side view.

optimal 3D control induces a mean second-order flow modification  $\mathbf{U}_2^{2D}$  that is qualitatively similar to  $\delta\mathbf{U}$ , resulting in a positive wall shear stress  $\partial_y U_2^{2D}$ , and therefore a negative  $x_{r2,I}$  (we do not investigate  $x_{r2,II}$  and  $x_{r2,III}$  since they are much smaller, as shown in Fig. 2.7). Fig. 2.14 shows the same quantities optimized on the upper wall ( $\beta = 0.6$  for the 3D control), and again a qualitatively similar wall shear stress. Although  $\mathbf{U}_2^{2D}$  is much larger than  $\delta\mathbf{U}$ , it must be kept in mind that 2D and 3D controls of the same amplitude  $\epsilon$  yield a 2D modification that scales linearly and a 3D modification that scales quadratically, respectively, i.e. like  $\epsilon\delta\mathbf{U}$  and  $\epsilon^2\mathbf{U}_2^{2D}$ . Spanwise-periodic controls should therefore become more efficient for large enough amplitudes, as previously observed for flow stabilization (Del Guercio *et al.*, 2014*a,b,c*; Boujo *et al.*, 2015), and as shown in Fig. 2.15. In practice it may happen that, as the control amplitude increases, the actual efficiency is limited by deviation from the sensitivity prediction (Sec. 2.5.1) or by the flow becoming unstable (Sec. 2.5.2). This can be tested on a case-by-case basis, once promising control candidates have been identified. In this respect, the concept of second-order sensitivity and the associated optimization method allow for a systematic exploration of the best candidates for spanwise-periodic control.

## 2.7 Conclusion

Initially motivated by the link between recirculation length and stability properties in separated amplifier flows, we have focused on the mean reattachment location as an indicator for

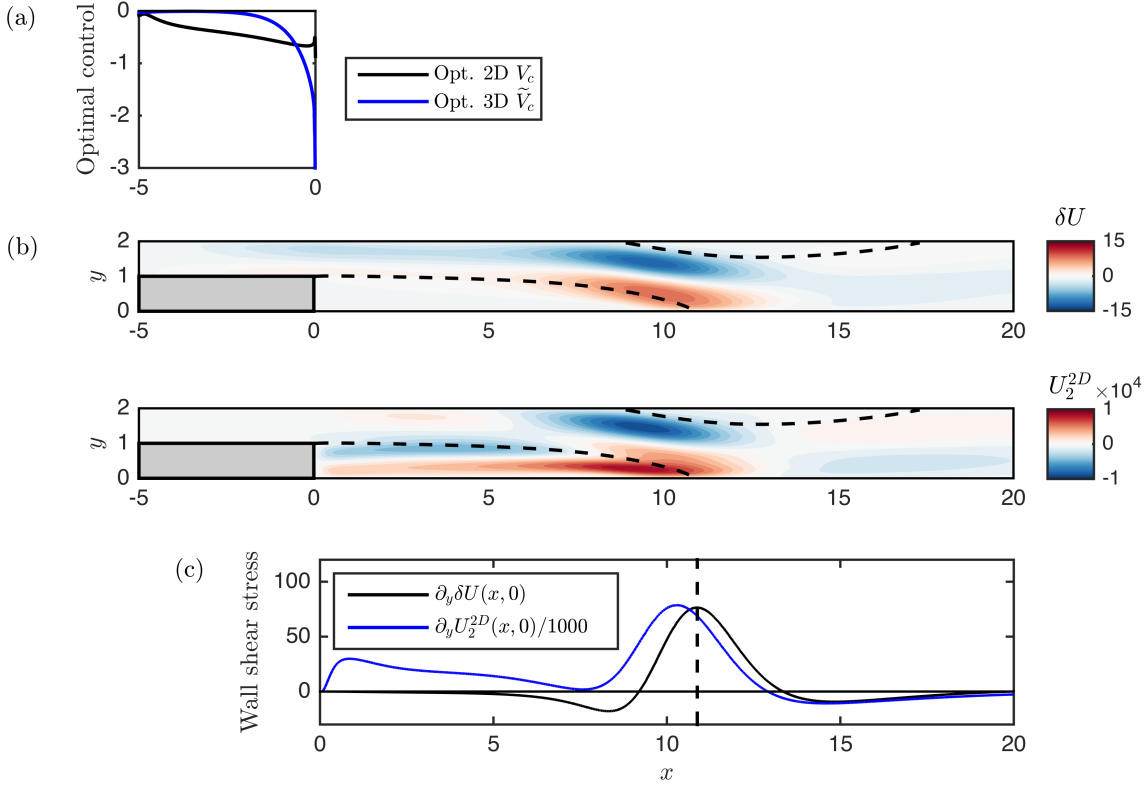


Figure 2.13 – (a) Optimal 2D and 3D ( $\beta = 1$ ) vertical controls on the upstream lower wall. (b) Leading-order mean flow modifications (streamwise component). (c) Corresponding wall shear stress on the lower wall.

the noise amplifying potential in a 3D backward facing step of expansion ratio 2 and fixed Reynolds number  $Re = 500$ . In this context, our goal was to control the reattachment location on the BFS lower wall with optimal spanwise-periodic control (steady wall blowing/suction or wall deformation) based on the second-order sensitivity analysis introduced by Boujo *et al.* (2019) for the linear stability properties of the circular cylinder flow.

A second-order sensitivity tensor for the reattachment location has been derived, such that modification of the reattachment location is obtained as a scalar product of this tensor and any arbitrary control. For the specific case of spanwise-harmonic control, the sensitivity tensor was then further simplified, i.e. made independent of  $z$ . When the control is spanwise harmonic, the first-order reattachment modification takes the same periodicity with zero mean value, while the second-order modification has a non-zero mean value. Thereby, we have looked for optimal controls that minimize the second-order mean correction.

For wall blowing/suction, we have shown that tangential control has a negligible influence while normal control is the most effective. The optimal wavenumber  $\beta$  depends on the control location:  $\beta = 0.6$  is optimal when controlling on the upper wall, and  $\beta = 1$  when

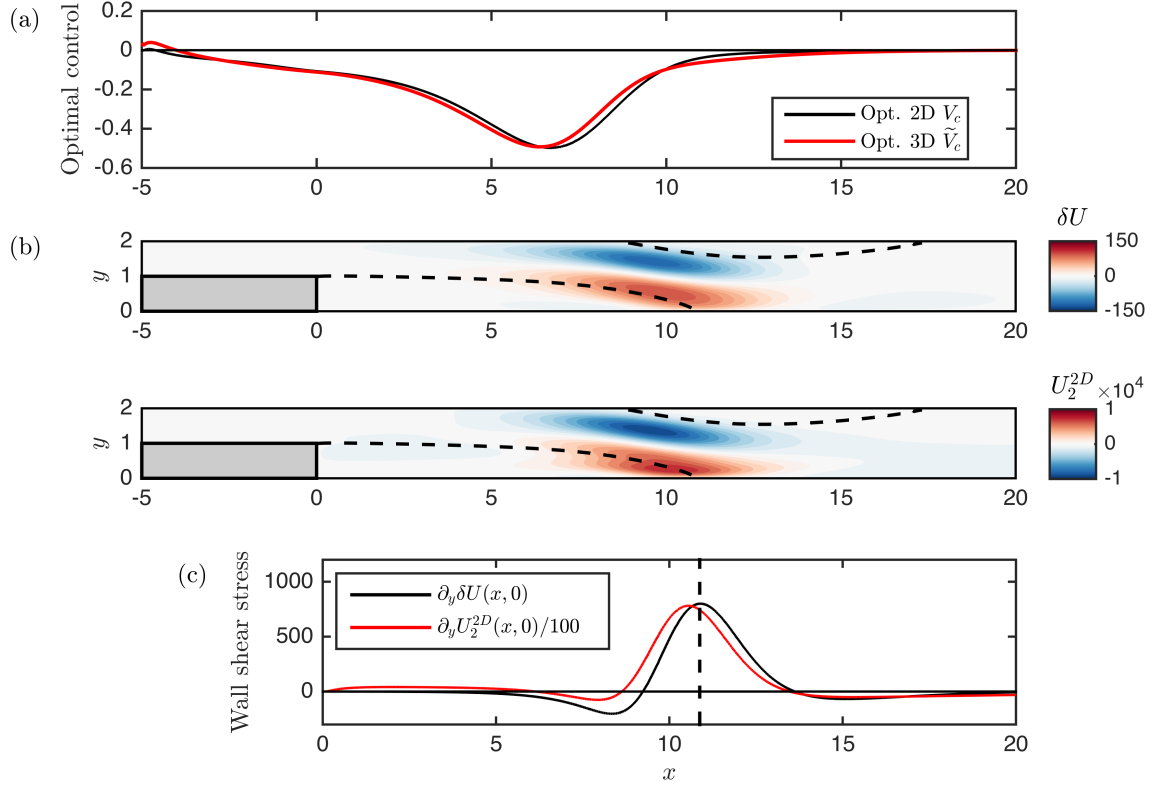


Figure 2.14 – (a) Optimal 2D and 3D ( $\beta = 0.6$ ) vertical controls on the upper wall. (b) Leading-order mean flow modifications (streamwise component). (c) Corresponding wall shear stress on the lower wall.

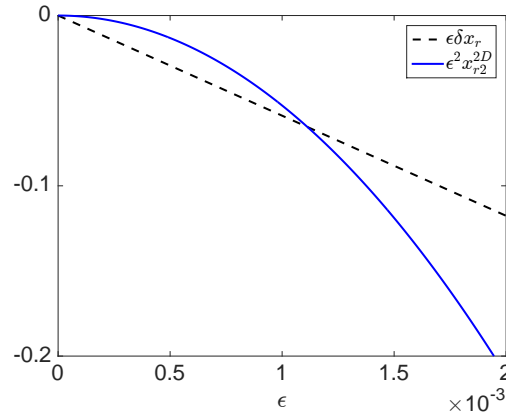


Figure 2.15 – Effect on the reattachment location  $x_r$  of the optimal vertical 2D control and optimal vertical 3D control ( $\beta = 1$ ) of amplitude  $\epsilon$ , on the upstream lower wall.

controlling on the upstream lower wall control. The linear gain for this actuation resembles the optimal gain for 3D steady forcing, indicating that the amplification potential of the BFS is

indeed linked to the recirculation length, as also observed by Boujo & Gallaire (2014*b*). Direct numerical simulations have validated the quadratic behaviour of the mean reattachment length modification. The sensitivity prediction is valid until a control amplitude  $\epsilon \simeq 0.001$ ; for larger amplitudes, 3D DNS results start to deviate from the quadratic prediction.

The optimal wall deformation has also been studied. We have focused on deformation of the upstream lower wall, with a constraint that restricts the wall deformation to be null at the step corner. This wall control is generally less effective than wall blowing/suction and its optimal wavenumber is slightly shifted to  $\beta = 1.1$ . DNS validation has shown that the sensitivity prediction is valid until a deformation amplitude  $\epsilon \simeq 0.008$ ; beyond this amplitude, strong non-linearity appeared and destabilized the flow.

Finally, the optimal 3D spanwise-periodic control was compared with the optimal 2D control. The resulting wall shear stress (which is directly linked to the modification of the reattachment location) is two or three orders of magnitude larger for 3D controls than for 2D ones. Since 2D and 3D controls depend linearly and quadratically on the control amplitude, respectively, the 3D control is more efficient for large enough control amplitude. In order to determine which of the two controls is best at which amplitude, additional studies are required once the optimal 3D control has been identified. This limitation can be tackled if the mean flow modification is taken into account in the optimization, for instance with a semi-linear approach (Mantič-Lugo, C., Arratia & Gallaire, 2014; Meliga, Boujo & Gallaire, 2016).

We have not investigated the stability of the controlled flow in a systematic way. It may well be that the first-order flow modification, although it induces no mean variation of  $x_r$ , alters the flow stability. Clarifying whether this is the case or not would be possible, for a given control, using linear stability analysis (Floquet or 3D global), or non-linear DNS.

## 2.8 Appendix

### 2.8.1 Appendix: Second-order reattachment location modification

Recall the definition of the reattachment location (Boujo & Gallaire, 2014*a,b*, 2015):

$$x_r = \int_0^\infty H(-\partial_y U(x, 0)) \, dx, \quad (2.45)$$

where  $H$  is the Heaviside function such that  $H(\theta < 0) = 0$  and  $H(\theta > 0) = 1$ . This expression yields indeed the reattachment location since the wall shear stress  $\partial_y U(x, 0)$  is negative in the recirculation region. Hereafter, we omit  $y = 0$  for brevity. Substituting

$$U = U_0 + \epsilon U_1 + \epsilon^2 U_2 + O(\epsilon^3) \quad (2.46)$$



into (2.45), one obtains:

$$\begin{aligned}
 x_r &= \int_0^\infty H[-\partial_y U_0 - \epsilon \partial_y U_1 - \epsilon^2 \partial_y U_2 + O(\epsilon^3)] dx \\
 &= \int_0^\infty \left\{ H(-\partial_y U_0) - [\epsilon \partial_y U_1 + \epsilon^2 \partial_y U_2 + O(\epsilon^3)] H'(-\partial_y U_0) + \frac{1}{2} [\epsilon \partial_y U_1 + O(\epsilon^2)]^2 H''(-\partial_y U_0) \right\} dx \\
 &= \int_0^\infty H(-\partial_y U_0) dx \\
 &\quad - \epsilon \int_0^\infty (\partial_y U_1) H'(-\partial_y U_0) dx \\
 &\quad + \epsilon^2 \int_0^\infty \left\{ (-\partial_y U_2) H'(-\partial_y U_0) + \frac{1}{2} (\partial_y U_1)^2 H''(-\partial_y U_0) \right\} dx + O(\epsilon^3). \tag{2.47}
 \end{aligned}$$

The zeroth-order term is the reattachment location  $x_{r0}$  of the uncontrolled flow. The first-order term  $x_{r1}$  is linear in  $U_1$  and is therefore zero when averaging over  $z$ . The second-order term contains derivatives of  $H$ , that can be obtained defining  $G(x) = H(-\partial_y U(x, 0)) = H(\theta)$  and using the relations

$$G'(x) = \frac{d(H(\theta))}{dx} = \frac{dH}{d\theta} \frac{d\theta}{dx} = -H'(\theta) \partial_{xy} U, \tag{2.48}$$

$$\begin{aligned}
 G''(x) &= \frac{d}{dx} (-H'(\theta) \partial_{xy} U) \\
 &= -H'(\theta) \frac{d}{dx} (\partial_{xy} U) - \frac{d(H'(\theta))}{dx} \partial_{xy} U \\
 &= -H'(\theta) \partial_{xxy} U - \frac{d^2 H}{d\theta^2} \frac{d\theta}{dx} \partial_{xy} U \\
 &= -H'(\theta) \partial_{xxy} U + H''(\theta) (\partial_{xy} U)^2, \tag{2.49}
 \end{aligned}$$

which yields

$$H'(\theta) = -\frac{G'(x)}{\partial_{xy} U} = \frac{\delta(x - x_r)}{\partial_{xy} U}, \tag{2.50}$$

$$H''(\theta) = \frac{1}{(\partial_{xy} U)^2} (H'(\theta) \partial_{xxy} U + G''(x)) = \frac{1}{(\partial_{xy} U)^2} \left( \frac{\delta(x - x_r)}{\partial_{xy} U} \partial_{xxy} U - \delta'(x - x_r) \right), \tag{2.51}$$

with  $\delta(x)$  the Dirac delta function. The second-order term thus becomes:

$$\begin{aligned}
 x_{r2} &= \int_0^\infty \left\{ (-\partial_y U_2) H'(\theta_0) + \frac{1}{2} (\partial_y U_1)^2 H''(\theta_0) \right\} dx \\
 &= \int_0^\infty \left\{ (-\partial_y U_2) \frac{\delta(x-x_r)}{\partial_{xy} U_0} + \frac{1}{2} \frac{(\partial_y U_1)^2}{(\partial_{xy} U_0)^2} \left( \frac{\delta(x-x_r)}{\partial_{xy} U_0} \partial_{xxy} U_0 - \delta'(x-x_r) \right) \right\} dx \\
 &= -\frac{\partial_y U_2(x_{r0})}{\partial_{xy} U_0(x_{r0})} + \frac{1}{2} \frac{(\partial_y U_1)^2}{(\partial_{xy} U_0)^2} \frac{\partial_{xxy} U_0}{\partial_{xy} U_0} \Big|_{x_{r0}} + \frac{1}{2} \frac{d}{dx} \left[ \frac{(\partial_y U_1)^2}{(\partial_{xy} U_0)^2} \right] \Big|_{x_{r0}} \\
 &= -\frac{\partial_y U_2}{\partial_{xy} U_0} \Big|_{x_{r0}} + \frac{(\partial_y U_1)(\partial_{xy} U_1)}{(\partial_{xy} U_0)^2} \Big|_{x_{r0}} - \frac{(\partial_{xxy} U_0)(\partial_y U_1)^2}{2(\partial_{xy} U_0)^3} \Big|_{x_{r0}}.
 \end{aligned} \tag{2.52}$$

### 2.8.2 Appendix: Simplification of the sensitivity operators

With a spanwise-periodic control of the form

$$\mathbf{U}_c(x, y, z) = \begin{pmatrix} \tilde{U}_c(x, y) \cos(\beta z) \\ \tilde{V}_c(x, y) \cos(\beta z) \\ \tilde{W}_c(x, y) \sin(\beta z) \end{pmatrix}, \quad \mathbf{C}(x, y, z) = \begin{pmatrix} \tilde{C}_x(x, y) \cos(\beta z) \\ \tilde{C}_y(x, y) \cos(\beta z) \\ \tilde{C}_z(x, y) \sin(\beta z) \end{pmatrix}, \tag{2.53}$$

the 1st-order flow modification is of the form

$$\mathbf{Q}_1(x, y, z) = \begin{pmatrix} \tilde{U}_1(x, y) \cos(\beta z) \\ \tilde{V}_1(x, y) \cos(\beta z) \\ \tilde{W}_1(x, y) \sin(\beta z) \\ \tilde{P}_1(x, y) \cos(\beta z) \end{pmatrix}. \tag{2.54}$$

Let us consider the first term  $x_{r2,1}$  in (2.16)-(2.18). Given the form of  $\mathbf{Q}_1$ , the right-hand side  $-\mathbf{U}_1 \cdot \nabla \mathbf{U}_1$  of (2.10) is the sum of 2D and 3D terms:

$$\mathbf{f}^{2D}(x, y) = -\frac{1}{2} \begin{pmatrix} (\tilde{U}_1 \partial_x + \tilde{V}_1 \partial_y - \beta \tilde{W}_1) \tilde{U}_1 \\ (\tilde{U}_1 \partial_x + \tilde{V}_1 \partial_y - \beta \tilde{W}_1) \tilde{V}_1 \\ 0 \end{pmatrix}, \tag{2.55}$$

$$\mathbf{f}^{3D}(x, y, z) = -\frac{1}{2} \begin{pmatrix} (\tilde{U}_1 \partial_x + \tilde{V}_1 \partial_y + \beta \tilde{W}_1) \tilde{U}_1 \cos(2\beta z) \\ (\tilde{U}_1 \partial_x + \tilde{V}_1 \partial_y + \beta \tilde{W}_1) \tilde{V}_1 \cos(2\beta z) \\ (\tilde{U}_1 \partial_x + \tilde{V}_1 \partial_y + \beta \tilde{W}_1) \tilde{W}_1 \sin(2\beta z) \end{pmatrix}. \tag{2.56}$$

The spanwise-harmonic forcing  $\mathbf{f}^{3D}(x, y, z)$  induces a 3D spanwise-harmonic response  $\mathbf{Q}_2^{3D}(x, y, z)$  that yields a zero-mean variation  $x_{r2,1}^{3D}(z)$ . By contrast, the 2D forcing term  $\mathbf{f}^{2D}(x, y)$  induces

the 2D response

$$\mathbf{Q}_2^{2D}(x, y) = \begin{pmatrix} U_2^{2D}(x, y) \\ V_2^{2D}(x, y) \\ 0 \\ P_2^{2D}(x, y) \end{pmatrix} \quad (2.57)$$

that yields a non-zero mean  $x_{r2,I}^{2D}$ . Recalling (2.22), one can therefore write

$$x_{r2,I}^{2D} = \left( \mathbf{U}^\dagger \mid \mathbf{f}^{2D} \right) \quad (2.58)$$

$$= -\frac{1}{2} \iint U^\dagger (\tilde{U}_1 \partial_x + \tilde{V}_1 \partial_y - \beta \tilde{W}_1) \tilde{U}_1 + V^\dagger (\tilde{U}_1 \partial_x + \tilde{V}_1 \partial_y - \beta \tilde{W}_1) \tilde{V}_1 \quad (2.59)$$

$$= -\frac{1}{2} \iint \tilde{U}_1 (U^\dagger \partial_x \tilde{U}_1 + V^\dagger \partial_x \tilde{V}_1 - \beta \tilde{W}_1 U^\dagger) + \tilde{V}_1 (U^\dagger \partial_y \tilde{U}_1 + V^\dagger \partial_y \tilde{V}_1 - \beta \tilde{W}_1 V^\dagger) \quad (2.60)$$

$$= (\tilde{\mathbf{U}}_1 \mid \tilde{\mathbf{S}}_I \tilde{\mathbf{U}}_1), \quad (2.61)$$

where the simplified second-order sensitivity operator

$$\tilde{\mathbf{S}}_I = -\frac{1}{2} \begin{bmatrix} U^\dagger \partial_x & V^\dagger \partial_x & 0 \\ U^\dagger \partial_y & V^\dagger \partial_y & 0 \\ -\beta U^\dagger & -\beta V^\dagger & 0 \end{bmatrix} \quad (2.62)$$

can be seen formally as a 2D restriction of the operator  $\mathbf{U}^\dagger \cdot \nabla ()^T$ .

Let us now consider the second and third terms  $x_{r2,II}$  and  $x_{r2,III}$  in (2.16)-(2.18). Given (2.54), it is straightforward to show that

$$x_{r2,II}^{2D} = (\tilde{\mathbf{U}}_1 \mid \tilde{\mathbf{S}}_{II} \tilde{\mathbf{U}}_1), \quad x_{r2,III}^{2D} = (\tilde{\mathbf{U}}_1 \mid \tilde{\mathbf{S}}_{III} \tilde{\mathbf{U}}_1), \quad (2.63)$$

where the simplified second-order sensitivity operators are

$$\tilde{\mathbf{S}}_{II} = \frac{1}{2(\partial_{xy} U_0(x_{r0}))^2} \delta(x_{r0}) (\mathbf{e}_x \partial_y)^\dagger \otimes (\mathbf{e}_x \partial_{xy}), \quad (2.64)$$

$$\tilde{\mathbf{S}}_{III} = \frac{-\partial_{xxy} U_0(x_{r0})}{4(\partial_{xy} U_0(x_{r0}))^3} \delta(x_{r0}) (\mathbf{e}_x \partial_y)^\dagger \otimes (\mathbf{e}_x \partial_y), \quad (2.65)$$

Finally, the mean second-order variation is

$$x_{r2}^{2D} = (\tilde{\mathbf{U}}_1 \mid \tilde{\mathbf{S}}_{2,\tilde{\mathbf{U}}_1} \tilde{\mathbf{U}}_1) \quad \text{where} \quad \tilde{\mathbf{S}}_{2,\tilde{\mathbf{U}}_1} = \tilde{\mathbf{S}}_I + \tilde{\mathbf{S}}_{II} + \tilde{\mathbf{S}}_{III}, \quad (2.66)$$

and the second-order sensitivities to control defined by (2.35) read

$$\tilde{\mathbf{S}}_{2,\tilde{\mathbf{C}}} = \mathbf{P}^T \tilde{\mathbf{A}}_{0,\tilde{\mathbf{C}}}^{\dagger}{}^{-1} \tilde{\mathbf{S}}_{2,\tilde{\mathbf{U}}_1} \tilde{\mathbf{A}}_{0,\tilde{\mathbf{C}}}^{-1} \mathbf{P} \quad (\text{volume-forcing-only } \tilde{\mathbf{A}}_{0,\tilde{\mathbf{C}}}), \quad (2.67)$$

$$\tilde{\mathbf{S}}_{2,\tilde{\mathbf{U}}_c} = \mathbf{P}^T \tilde{\mathbf{A}}_{0,\tilde{\mathbf{U}}_c}^{\dagger}{}^{-1} \tilde{\mathbf{S}}_{2,\tilde{\mathbf{U}}_1} \tilde{\mathbf{A}}_{0,\tilde{\mathbf{U}}_c}^{-1} \mathbf{P} \quad (\text{wall-forcing-only } \tilde{\mathbf{A}}_{0,\tilde{\mathbf{U}}_c}), \quad (2.68)$$

with

$$\tilde{\mathbf{A}}_0 = \begin{bmatrix} U_0 \partial_x + V_0 \partial_y + \partial_x U_0 - \tilde{D} & \partial_y U_0 & 0 & \partial_x \\ \partial_x V_0 & U_0 \partial_x + V_0 \partial_y + \partial_y V_0 - \tilde{D} & 0 & \partial_y \\ 0 & 0 & U_0 \partial_x + V_0 \partial_y - \tilde{D} & -\beta \\ \partial_x & \partial_y & \beta & 0 \end{bmatrix}, \quad (2.69)$$

$$\tilde{D} = Re^{-1}(\partial_{xx} + \partial_{yy} - \beta^2). \quad (2.70)$$

## 2.9 Part II : Vaccination as a control strategy

The work presented in the previous sections discussed the implementation method of small amplitude active-passive controls on a backward facing step (BFS) flow to regulate the downstream evolution of the perturbations. However, in realistic situations, the flow is influenced by the presence of naturally occurring external disturbances (white noise) present at the geometry inlet. For flows up to  $Re = 748$  in a BFS, the high amplification potential of the stable flow greatly magnifies the downstream evolution of these disturbances (Barkley *et al.*, 2002).

In this context, the response of such amplifier flows to ‘white noise’ has been analysed by Mantič-Lugo & Gallaire (2016) where the gain  $G(A_n)$ , expressed as the ratio of the amplitude of the response to white noise level  $A_n$ , was obtained, as shown in figure 2.16. From this figure, we observe that the gain decreases as  $A_n$  increases and eventually saturates to a small value for larger white noise levels. However, for the white noise level  $A_n < 0.005$  the gain is still sufficiently high. Hence, to control the response of the BFS flow in presence

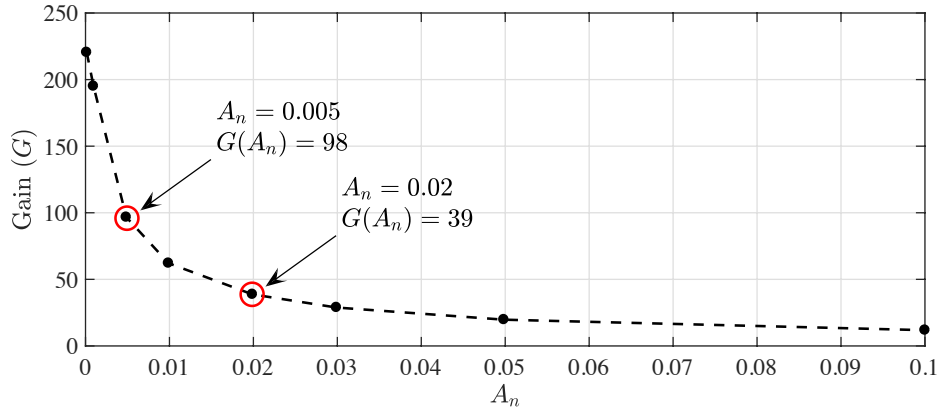


Figure 2.16 – Gain as a function of white noise level. The plot has been reproduced from Mantič-Lugo & Gallaire (2016).

of inlet white noise, we propose the method of *vaccination* (a term due to C. Cossu in a private communication) wherein we aim to vaccinate the flow against natural disturbances, by introducing a specific disturbance which decreases the overall stochastic response. Indeed the choice of the controlling disturbance and its amplitude are the crucial criteria that govern the overall flow stability.

Since the idea is to introduce a forcing which once naturally grown is capable of suppressing the further development of the more uncontrollable instabilities, we employ the optimal harmonic volume forcing obtained for a BFS at  $Re = 500$  and retrieved through the work of Marquet & Sipp (2010) and Mantič-Lugo & Gallaire (2016). As seen in figure 2.17, the optimal dimensionless forcing frequency is concentrated at  $St = 0.075$ , where  $St = f_{Hz} h / U_{in}$  denotes the Strouhal number resulting in the amplification of the flow to 7400. The optimal forcing  $\mathbf{F}$  and its response  $\mathbf{u}'$ , in the streamwise direction for the given configuration, are shown in figure 2.18 where we observe that the forcing is mainly concentrated in the upstream wall in

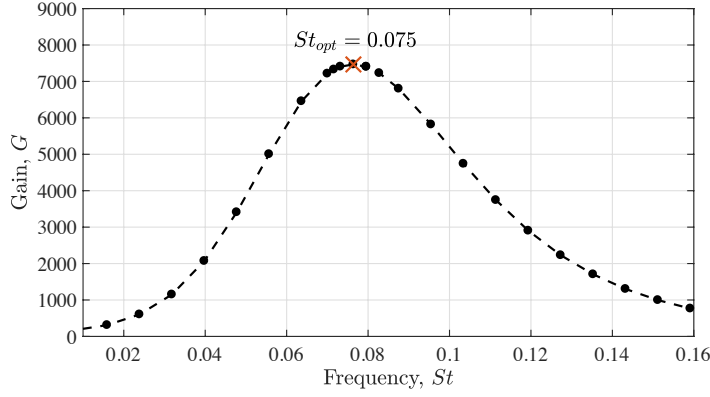


Figure 2.17 – Gain as a function of forcing frequency expressed in terms of the Strouhal number. The optimal frequency  $St_{opt} = 0.075$ , is represented by the red cross. The data has been reproduced based on the work of Mantič-Lugo & Gallaire (2016).

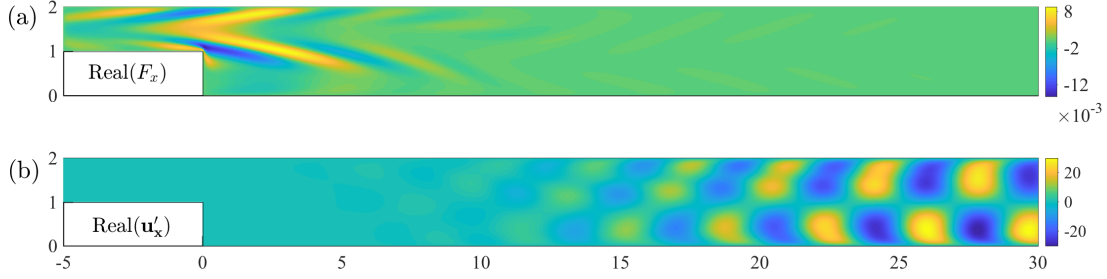


Figure 2.18 – (a) Optimal volume forcing at  $St = 0.075$  and (b) the resulting response, both represented for the streamwise direction. Results have been reproduced from Mantič-Lugo & Gallaire (2016)

the proximity of the step and the maximum response is obtained further downstream.

Thus, with the defined forcing structure, we are only left with optimizing the control amplitude which achieves the best overall *vaccination*.

### 2.9.1 Numerical method

We begin our analysis by considering a BFS of the same configuration as shown in figure 2.1 without any spanwise modulations and with  $Re = 500$ . To replicate physical systems, we introduce a band-limited white noise by filtering the digital random signal with a band limiting frequency  $f = 1$ . We formulate this physical perturbation in a similar way as in Mantič-Lugo & Gallaire (2016). The noise is normalised to have zero mean, unit variance and unit power, with a constant value for power spectral density (PSD). Finally we impose this filtered white noise as an inlet velocity condition (at  $x = -5$ ), and the pressure free outlet condition is applied at the outlet ( $x = 50$ ). The modelled white noise has a fixed level of  $A_n = 0.02$ .

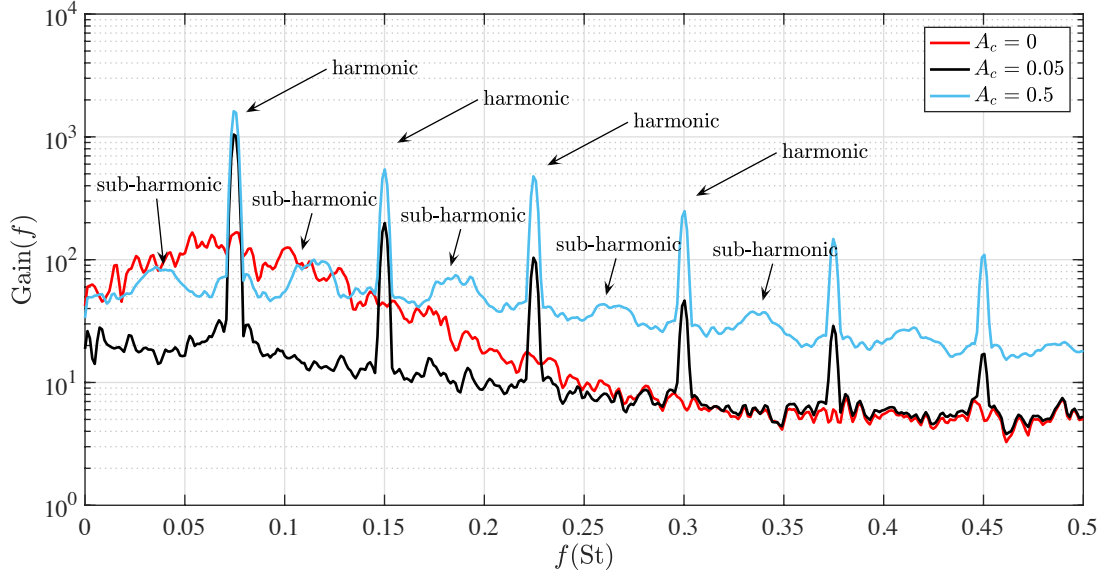


Figure 2.19 – Gain as a function of the frequency for three different control amplitudes  $A_c$ . The control amplitude  $A_c = 0$  refers to the flow in absence of any control.

The three dimensional problem is discretized with a finite element method using FreeFem++ (Hecht, 2012) using P2 and P1 Taylor-Hood elements such that  $[U, V, W, P] = [P2, P2, P2, P1]$ . The typical number of elements is  $3.78 \times 10^4$  with clustered mesh near the reattachment point yielding  $7.7 \times 10^4$  degrees of freedom. The base flow is obtained by the Newton method.

### 2.9.2 Results and discussion

To control the incoming disturbances, we exploit the existing amplification potential of the BFS in a vaccination strategy by exciting the flow periodically using the optimal harmonic volume forcing obtained from figure 2.17 and 2.18a. Hence, with the fixed noise level at  $A_n = 0.02$ , and the fixed control structure at  $St = 0.075$ , the control amplitude  $A_c$  is systematically increased from  $5 \times 10^{-5}$  to 0.5, to see its impact on the stochastic response. The overall energy response over the entire domain for fixed control amplitude  $A_c$  and as a function of frequency  $f$  is obtained as,

$$E_{res}(f) = \int_{\Omega} u'^2(f) + v'^2(f) d\Omega, \quad (2.71)$$

where  $u'(f)$  and  $v'(f)$  are the  $x$  and  $y$  velocity perturbation components obtained using the pwelch function in MATLAB. Using equation (2.71), the gain for  $A_c$  in terms of the frequency is expressed as,

$$G(A_c, f) = \frac{\sqrt{E_{res}(f)}}{A_n}, \quad (2.72)$$

where  $E_{res}$  varies as the control amplitude  $A_c$  is changed. In figure 2.19, we show the comparison of the gain spectrum for  $A_c = 0.05$  and  $0.5$  with the uncontrolled state  $A_c = 0$ . Compared to the uncontrolled state, in presence of the control  $A_c = 0.05$ , we observe that the gain spectrum decreases overall except at the control frequency and its harmonics. Thus the control vaccinates most of the natural disturbances at the expense of a higher response at the control frequency (and its harmonics). For a larger amplitude of  $0.5$ , the response is seen to be excited additionally at the sub-harmonics, which enhances the overall gain spectrum. Thus the gain envelope obtained for the two different control amplitudes drives one to evaluate the optimal control amplitude resulting in the most efficient *vaccination*. For this purpose we use the total gain defined within the band limiting signal and expressed as,

$$G_{tot}(A_c) = \int_0^1 \text{Gain}(A_c, f) df, \quad (2.73)$$

as a scale for comparison. Figure 2.21 shows the total gain  $G_{tot}$  obtained from equation (2.73) as a function of different control amplitudes, where we see that  $G_{tot}$  increases as  $A_c$  increases.

However, the gain expression (2.73) also includes the energy of the response at the particular control frequency  $St = 0.075$  and its harmonics, which are the major contributors of the gain as seen in figure 2.19. Thus, we reformulate the gain by assuming a small frequency gap  $\delta f = \pm 0.002$  around the control frequency  $0.075$  and its harmonics, from which we exclude the contribution of the response on  $G_{tot}$  (as illustrated in figure 2.20). In the first case we exclude the energy response  $E_{res}$  only around the particular control frequency  $0.075$  (shown in red in figure 2.20) and in the second case we remove  $E_{res}$  around all the harmonics of the control frequency including at  $f = 0.075$  (shown in black in figure 2.20).

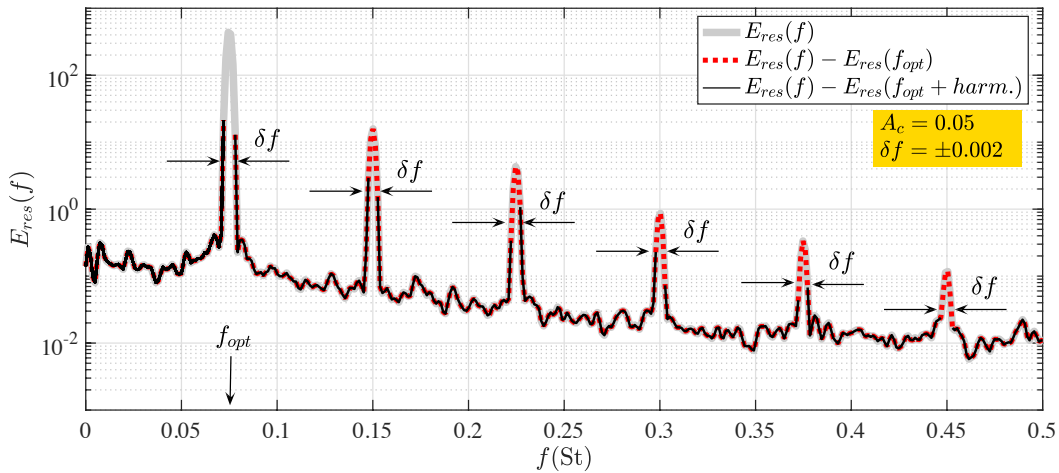


Figure 2.20 – Energy response as a function of frequency for a fixed noise level  $A_n = 0.02$  and control amplitude  $A_c = 0.05$ . The red dashed curves represents the response by excluding the one present at  $f_{opt}$  whereas excluding the response at all the harmonics results in obtaining the response shown in black.  $\delta f$  denotes the frequency gap centred around the harmonics within which the energy response is excluded in both the situations.



The resulting gain is presented through the red and blue curves respectively in figure 2.21, where we see that removing the response contribution at the control frequency reduces drastically  $G_{tot}$  for all control amplitudes. Compared to the gain in presence of an uncontrolled flow (as shown in figure 2.16), the presence of control results in a much lower amplification for most the naturally amplified frequencies. We further conclude that for the given flow conditions,  $A_c = 0.05$  is the most effective control amplitude, imposing the most efficient *vaccination* against the natural disturbances. Comparing the gain spectrum for the uncontrolled state at  $A_c = 0$  to the one in presence of the most effective amplitude  $A_c = 0.05$  (see figure 2.19), we also state that the *vaccination* strategy is especially suitable if the final aim is to reduce the stochastic gain over a low frequency band below the optimal control frequency, in other words for  $St < 0.075$ . Finally we confirm the robustness of the *vaccination* method by performing a similar analysis for a smaller white noise level  $A_n = 0.005$  which has a gain of  $\approx 100$  in absence of any control (see figure 2.16). However, applying a control with the optimal amplitude  $A_c = 0.05$ , lowers the gain by an order of 65% as shown with the blue curve in figure 2.22.

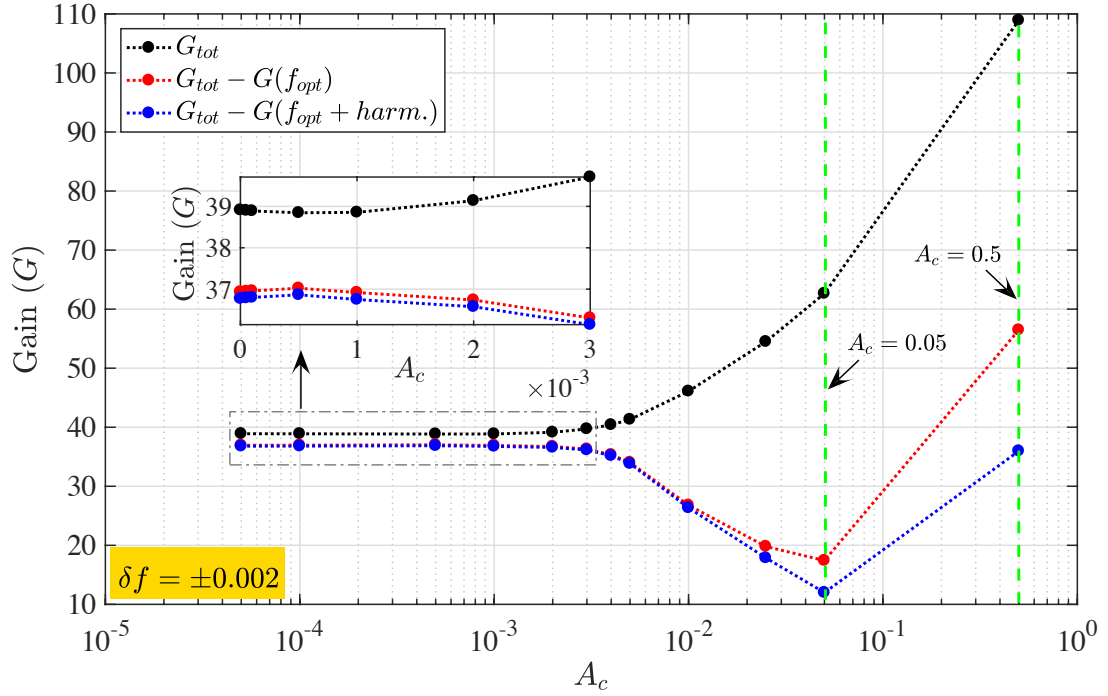


Figure 2.21 – Total gain  $G_{tot}$  (in black), expressed as a function of control amplitudes  $A_c$  for fixed noise level of  $A_n = 0.02$ . The curve in red represents the gain after removing the energy response at  $St = 0.075$ , and in blue after removing the response at all the harmonics of the control frequency along with the particular frequency itself.

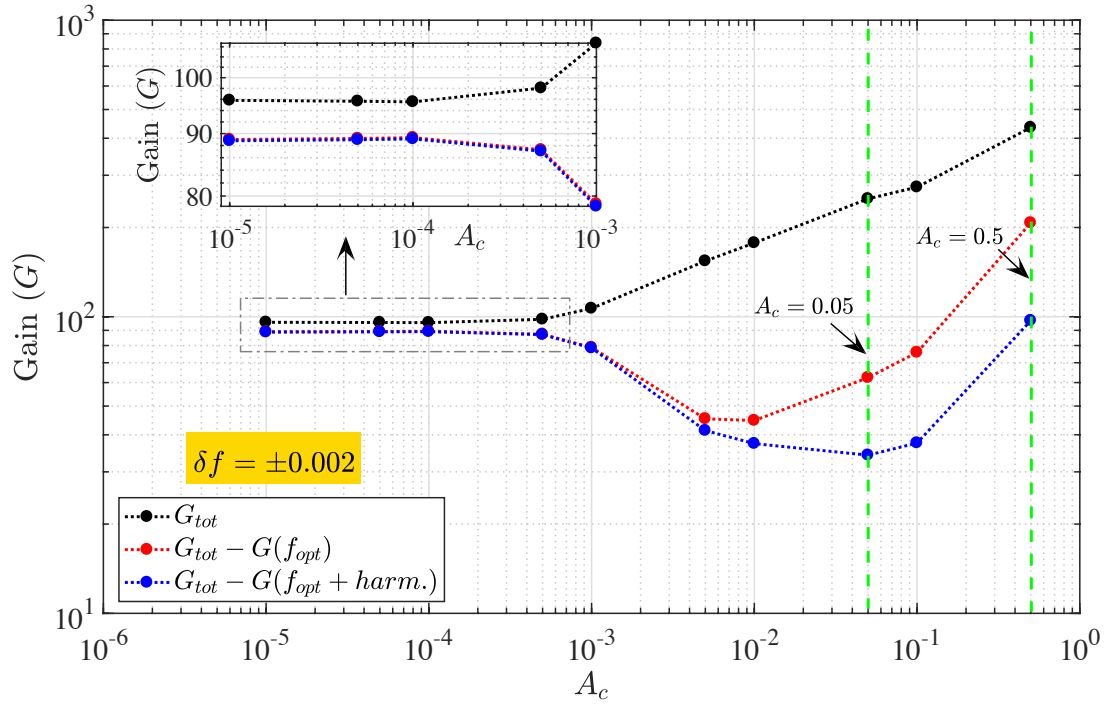


Figure 2.22 – Total gain  $G_{tot}$  (in black), expressed as a function of control amplitudes  $A_c$  for fixed noise level of  $A_n = 0.005$ . The curve in red represents the gain after removing the energy response at  $St = 0.075$ , and in blue after removing the response at all the harmonics of the control frequency along with the particular frequency itself.

# 3 Capillary jet stability analysis using the one-dimensional Eggers & Dupont equations

## 3.1 Introduction

Rooted on the study of numerous plasma instabilities (Briggs, 1964; Bers, 1983) and the pioneering work of Huerre & Monkewitz (1990), the classical linear stability theory has been proven to be a relevant tool to analyse fluid instabilities in presence of infinitesimal perturbations. Based on the space and time evolution of these perturbations, the flows can be categorised either as linearly stable or unstable. A stable base flow is defined as one in which the small perturbations either decay in space or time close to the source or are convected downstream away from the source of disturbance, letting the base flow return back to quietness.

Analytically, the stability of such base flows can be carried out in a local or a global framework, depending on the degree of streamwise variation of the base flow (Schmid & Henningson, 2001; Chomaz, 2005; Charu, 2011). A parallel or weakly nonparallel base flow can be studied using the local framework, wherein the Briggs-Bers zero-group criterion is applied to find the transition from absolutely to convectively unstable flows. The global analysis, however, simply defines the flow stability based on the temporal growth rate of the perturbation. A local convectively unstable base flow can be globally stable since the perturbations are advected away from their source. On the contrary, a flow which is locally absolutely unstable at all streamwise locations results into a globally unstable flow (Huerre & Monkewitz, 1990).

The globally stable or locally convectively unstable flow are often associated to an *amplifier* flow, for example the flow along a backward facing step for sufficiently low Reynolds numbers or a jet in the jetting regime. Such flows are extremely sensitive to external noise, naturally amplifying any applied perturbation (Chomaz, 2005; Schmid, 2007). However, for the liquid jet with a free interface, the incoming disturbance is convected downstream, culminating

### Chapter 3. Capillary jet stability analysis using the one-dimensional Eggers & Dupont equations

---

into its breakup into drops, a feature that cannot be captured in every aspect through the linear theory. Especially, the interface shape close to the breakup location and the presence of satellite drops can only be described through nonlinear simulations. However, close to the breakup, the interface of the jet becomes zero locally, thus making the nonlinear simulations extremely costly.

To avoid the use of such expensive three-dimensional simulations, Eggers & Dupont (1994), Brenner, Shi & Nagel (1994) and García & Castellanos (1994) were among the first (see Eggers & Villermaux (2008) for a historical perspective) to provide a reduced one-dimensional (1D) form of the Navier-Stokes equation for the axisymmetric jet with a free interface. García & Castellanos (1994) developed not only the leading order but also several higher-order 1D approximations of the Navier-Stokes equations. Eggers & Dupont (1994) especially considered a detailed comparison of the reduced one-dimensional equations and the experiments. Since then, the accuracy of the 1D Eggers & Dupont equations has since been established by several authors numerically and experimentally (Ambravaneswaran, Phillips & Basaran, 2000; Ambravaneswaran, Wilkes & Basaran, 2002; Yildirim, Xu & Basaran, 2005; Subramani, Yeoh, Suryo, Xu, Ambravaneswaran & Basaran, 2006; van Hoeve, Gekle, Snoeijer, Versluis, Brenner & Lohse, 2010). Eggers & Villermaux (2008) provide a meticulous overview of the 1D model comparing its results to the solution of the full Navier-Stokes equations.

Since the main aim of the thesis is to analyse the response of an axisymmetric jet to externally applied forcing, a reduced 1D set of equations served as a crucial base to the analysis, especially in the interest of capturing satellite drops, the interface shape and length before the jet breakup. Thus in this chapter, we give a brief overview of the 1D Eggers & Dupont equations in Section 3.2, which is largely inspired by the publication of the same authors. Further through the local stability analysis, we classify the criteria for transition from an absolutely unstable to a convectively unstable flow in Section 3.3.2. We then formulate a numerical scheme to carry out nonlinear simulations of the 1D Eggers & Dupont equations in Section 3.4.2. The validation of the numerical scheme is presented in Section 3.4.3 and some future perspectives to the use of these equations are discussed in Section 3.5.

## 3.2 The Eggers & Dupont equations

We consider an axisymmetric column of fluid with density  $\rho$ , dynamic viscosity  $\mu$  and surface tension  $\gamma$  as shown in figure 3.1. The surrounding medium is considered evanescent and is neglected. At the nozzle outlet, the jet has a radius of  $h_0$  and velocity of  $U$ . In the axisymmetric co-ordinates  $(r, z)$  the incompressible Navier-Stokes equation for the flow of the jet reads as,

$$\partial_t \mathbf{u} + (\mathbf{u} \cdot \nabla) \mathbf{u} = -\frac{1}{\rho} \nabla p + \frac{\mu}{\rho} \Delta \mathbf{u} + \mathbf{g}, \quad (3.1)$$

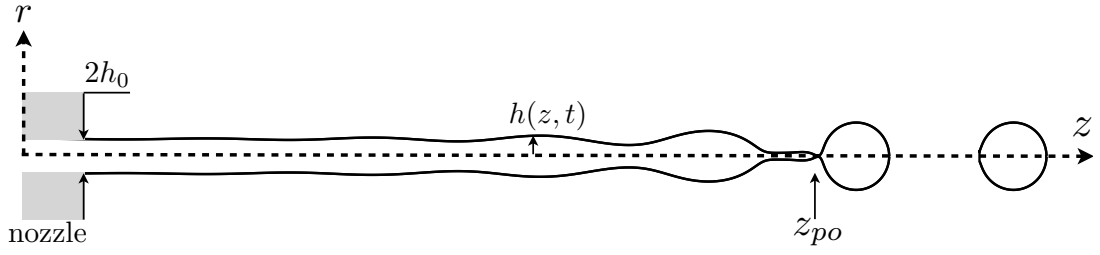


Figure 3.1 – Flow domain and notations used for the governing equations.

where the velocity  $\mathbf{u} = u\mathbf{e}_z + v\mathbf{e}_r$  and the pressure  $p$  are flow variables. The acceleration due to gravity  $g$  points in the positive  $z$  direction. The continuity equation for the flow reads,

$$\nabla \cdot \mathbf{u} = 0. \quad (3.2)$$

We now introduce the height function  $h(z, t)$  which describes the surface of the cylindrical jet. The free jet interface moves at the same velocity as the fluid and hence applying the kinematic boundary condition we obtain,

$$\partial_t h + u \partial_z h = v \Big|_{r=h}. \quad (3.3)$$

The dynamic boundary condition at the free interface gives,

$$\sigma \cdot \mathbf{n} \Big|_{r=h} = -\gamma C \mathbf{n}, \quad (3.4)$$

where the stress tensor  $\sigma$  is expressed as,

$$\sigma = -p\mathbb{I} + \mu(\nabla \mathbf{u} + \nabla \mathbf{u}^T), \quad (3.5)$$

and the unit normal vector  $\mathbf{n}$  to the interface, pointing towards the inert surrounding medium is defined as,

$$\mathbf{n} = \frac{(-\partial_z h, 1)}{\sqrt{1 + \partial_z h^2}}. \quad (3.6)$$

Finally the mean curvature  $C$ , defined as  $C = -\nabla \cdot \mathbf{n}$ , is expressed in cylindrical co-ordinates as

$$C = \frac{1}{h(1 + h'^2)^{1/2}} - \frac{h''}{(1 + h'^2)^{3/2}}, \quad (3.7)$$

where the prime denotes the derivation with respect to  $z$ . Thus, the interface  $h(z, t)$  is coupled to the governing equations (3.1-3.2) through the kinematic (3.3) and dynamic (3.4) boundary conditions applied at the free surface.

The assumption of the typical radial length scale of the liquid jet being much smaller compared to its longitudinal length scale, allowed Eggers & Dupont (1994) to use the long-wavelength

### Chapter 3. Capillary jet stability analysis using the one-dimensional Eggers & Dupont equations

approach for characterizing the jet flow. They expanded the velocity and pressure fields in Taylor series around the axis of the jet  $r = 0$ ,

$$u(r, z, t) = u_0(z, t) + u_2(z, t)r^2 + \dots, \quad (3.8a)$$

$$v(r, z, t) = -\frac{1}{2}u_0'(z, t) - \frac{1}{4}u_2'(z, t)r^3 - \dots, \quad (3.8b)$$

$$p(r, z, t) = p_0(z, t) + p_2(z, t)r^2 + \dots \quad (3.8c)$$

In equation (3.8a), the longitudinal velocity is described by the uniform flow velocity  $u_0$  in addition to some second order correction terms. The transversal velocity (3.8b), is conveniently formulated by inserting (3.8a) into the continuity equation (3.2). The above formulations are inserted in the momentum (3.1) and continuity (3.2) equations. Finally the normal and tangential forces at the interface  $r = h$  (defined explicitly in Eggers & Dupont, 1994) help in reducing the system of governing equations to a one-dimensional (1D) form, expressed as,

$$\frac{\partial u_0}{\partial t} = -u_0 \frac{\partial u_0}{\partial z} - \frac{\gamma}{\rho} \frac{\partial C}{\partial z} + \frac{3\mu}{\rho} \left[ \frac{2}{h} \frac{\partial h}{\partial z} \frac{\partial u_0}{\partial z} + \frac{\partial^2 u_0}{\partial z^2} \right] + g. \quad (3.9)$$

At the leading order the kinematic boundary condition (3.3) reduces to,

$$\frac{\partial h}{\partial t} = -u_0 \frac{\partial h}{\partial z} - \frac{1}{2} \frac{\partial u_0}{\partial z} h. \quad (3.10)$$

The leading-order one-dimensional mass (3.10) and momentum (3.9) equations are coupled together and are henceforth referred to as the 1D Eggers & Dupont equations. Note that at the leading order, the velocity at the jet interface is approximated by  $u_0$ , which is the uniform flow velocity at  $r = 0$ . Hereafter, in all the equations we replace  $u_0 \equiv u$ .

In absence of gravitational force, the dimensionless form of the equations, obtained by choosing  $h = \tilde{h}h_0$  and  $u = \tilde{u}h_0/\tau_i$ , where  $h_0$  is the nozzle radius,  $\tau_i = \sqrt{\rho h_0^3/\gamma}$  is the inertial time scale, ignoring the *tilde* are written as,

$$\frac{\partial h}{\partial t} = -\frac{1}{2h} \frac{\partial}{\partial z} (h^2 u), \quad (3.11a)$$

$$\frac{\partial u}{\partial t} = -u \frac{\partial u}{\partial z} - \frac{\partial p}{\partial z} + 3Oh \left( \frac{2}{h} \frac{\partial h}{\partial z} \frac{\partial u}{\partial z} + \frac{\partial^2 u}{\partial z^2} \right), \quad (3.11b)$$

where,  $p$  is the nondimensional pressure obtained by introducing the a pressure scale  $\gamma/h_0^2$ . The system of equations (3.11) are governed by the dimensionless number Ohnesorge  $Oh = \mu/\sqrt{\rho\gamma h_0}$  expressed as the ratio of the viscous forces to inertial and surface tension forces. A high  $Oh$  stabilises the jet by decreasing the instability growth rate.

Using the associated characteristic velocity ( $h_0/\tau_i$ ), the non-dimensional boundary conditions for the jet at nozzle inlet are reduced to  $h(0, t) = 1$  and  $u(0, t) = \sqrt{We}$ , where,  $We$  represents the Weber number  $We = \rho h_0 U^2/\gamma$ , and it measures the ratio between the kinetic energy and the surface energy.

The steady state form of the continuity equation (3.11a) gives the relation between the steady state shape  $h_b$  and velocity  $u_b$  as,

$$h_b^2 u_b = Q = \sqrt{We}, \quad (3.12)$$

where the expression on the right hand side is obtained from the flow condition at the nozzle exit. Hence the steady state velocity is simply expressed as  $\sqrt{We}/h_b^2$ . Since the base state of the 1D Eggers & Dupont equations for viscous jet is unaffected by any external body forces, we consider it to be a cylinder of constant radius  $h_b = 1$  with the corresponding velocity  $u_b = \sqrt{We}$ .

### 3.3 Linear stability analysis of viscous jets

The linear stability analysis of purely parallel jets, can be analysed in the local framework by estimating the growth of small perturbations about the base state. In the case of a homogeneous base flow, a Fourier transform is applied which naturally introduces perturbations of the form  $e^{i(kz-\omega t)}$ , where  $k$  denotes the spatial wavenumber and  $\omega$  the temporal frequency. Thus considering the normal mode perturbations, the flow variables  $h(z, t)$  and  $u(z, t)$  are decomposed as:

$$h(z, t) = h_b + \epsilon \hat{h} e^{i(kz-\omega t)}, \quad (3.13a)$$

$$u(z, t) = u_b + \epsilon \hat{u} e^{i(kz-\omega t)}, \quad (3.13b)$$

where the perturbation amplitude  $\epsilon \ll 1$ , and  $\hat{h}$ ,  $\hat{u}$  are the eigenmodes. Additionally, for the sake of streamlining the results of the linear analysis with that of the numerical analysis presented in section 3.4, we further replace  $h^2$  by  $a$ . Hence the perturbation  $\hat{h} = 2\hat{a}$ .

In general, the wavenumber and the frequency are both complex,  $(k, \omega) \in \mathbb{C}$ . The selection of real  $k \in \mathbb{R}$  and complex  $\omega \in \mathbb{C}$ , defines the so-called *temporal* stability analysis which examines the temporal evolution of the perturbation in presence of a real spatial forcing. However, defining  $k \in \mathbb{C}$  and  $\omega \in \mathbb{R}$  refers to the *spatial* stability analysis where we look for the spatial evolution of the perturbation in response to the real forcing frequency.

Contrary to the *temporal* stability analysis, the *spatial* analysis can be ill posed if we operate in a regime where the flow is naturally unstable. In such cases, the net response of the flow is usually influenced by the natural unforced growth, an aspect which can be captured by considering both  $(k, \omega) \in \mathbb{C}$ , a study referred to as the *spatio-temporal* stability analysis. This analysis defines the flow as convectively unstable or absolutely unstable, the latter being related to the ill disposed problem for analysing the *spatial* stability.

The stability analysis for each of the above mentioned three cases can be studied by formalizing the dispersion relation which couples  $\omega$  and  $k$ . Inserting the modal decomposition (3.13) into

### Chapter 3. Capillary jet stability analysis using the one-dimensional Eggers & Dupont equations

equation (3.11) and linearising about  $(a_b, u_b)$  leads to the dispersion relation,

$$\omega = \sqrt{We}k - \frac{3iOhk^2}{2} \pm i\sqrt{\frac{k^2 - k^4}{2} + \frac{9Oh^2k^4}{4}}. \quad (3.14)$$

The dispersion relation (3.14) can be solved for the relevant stability analyses by considering either  $k \in \mathbb{R}$  or  $\omega \in \mathbb{R}$ ; or considering both as complex  $(k, \omega) \in \mathbb{C}$ .

#### 3.3.1 Temporal stability analysis

If we are interested in the temporal response of small spatial perturbations imposed on the jet, we use the temporal stability approach wherein the dispersion relation (3.14) is solved for complex  $\omega \in \mathbb{C}$  for a given real  $k \in \mathbb{R}$ . For the flow to be linearly unstable, the imaginary  $\omega_i > 0$  for a given  $k$ . Imposing this condition in equation (3.14), we obtain analytically the cutoff wavenumber  $k_{cut} = 1$  beyond which the flow is always stable, for all values of  $Oh$  and  $We$ .

Within the cutoff regime, we then look for the maximum wavenumber  $k_{max}$  which leads to the most amplified temporal evolution  $\omega_{i,max}$  by plotting the temporal growth rate as a function of the wavenumber for different  $Oh$  and  $We$  as shown in figure 3.2. Figure 3.2(a) shows that

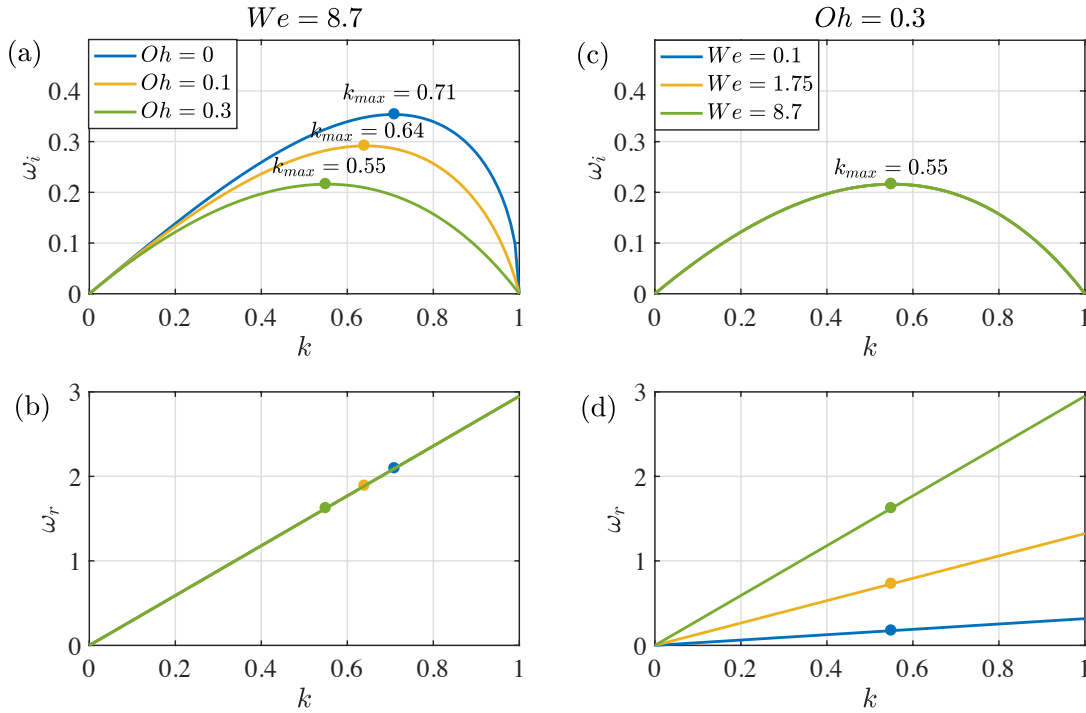


Figure 3.2 – (a) and (b) show  $\omega_i$  and  $\omega_r$  as a function of wavenumber for different  $Oh$  and at constant  $We$ . (c) and (d) show the same for different  $We$  and at constant  $Oh$ . In either case, • denotes the maximum  $\omega_i$  and the related  $\omega_r$ .



both the wavenumber  $k_{max}$  which produces the maximum temporal growth rate and the resulting  $\omega_{i,max}$ , decreases as  $Oh$  increases, thereby showing that the stability of the parallel jet intensifies due to the viscous effects. Contrary to this, the advection speed of the jet, denoted by  $We$  does not govern the temporal growth rate as shown in figure 3.2(c) and only modifies the respective  $\omega_r$ .

The simplistic dispersion relation for the parallel jet allows to derive an analytical expression for  $k_{max}$  as follows:

$$k_{max} = \sqrt{\frac{1}{2 + 3\sqrt{2}Oh}}. \quad (3.15)$$

For a purely inviscid jet, the above expression further simplifies to give  $k_{max} = 0.71$ .

#### 3.3.2 Absolute-convective stability analysis

In addition to  $\omega \in \mathbb{C}$  if we now generalise  $k \in \mathbb{C}$ , the stability for parallel base flows can be analysed in the spatio-temporal framework, which includes the effect of advection speed of the jet on its stability properties. In this framework, we define the impulse response of a system to a localised perturbation which generates a wave packet growing in space and time. The spatio-temporal behaviour of the wave packet can be described in terms of the complex absolute wave number  $k_0$  and the corresponding complex absolute frequency  $\omega_0 = \omega(k_0)$  whose imaginary part  $\omega_{0,i}$  will determine the temporal evolution of the wave packet. For  $\omega_{0,i} > 0$  the system is absolutely unstable since the disturbance grows fast enough to invade entire domain in the laboratory frame and for  $\omega_{0,i} < 0$  the system is convectively unstable as the localised perturbations are allowed to convect downstream before they grow in the laboratory framework. The complex pair  $(k_0, \omega_0)$  is defined using the saddle point condition or the Briggs-Bers zero-group velocity criterion, together with the dispersion relation

$$\frac{d\omega}{dk}(\omega_0, k_0) = 0, \quad D(\omega_0, k_0) = 0, \quad (3.16)$$

where  $D$  represents the dispersion relation, and,

$$\frac{\partial \omega}{\partial k} = \sqrt{We} - 3iOhk \pm i \frac{1 - 2k^2 + (3Ohk)^2}{\sqrt{2(1 - k^2) + (3Ohk)^2}}. \quad (3.17)$$

Equation (3.16) identifies the critical dimensionless speed  $We_{crit}$ , for a fixed  $Oh$ , which signifies the saddle points of the jet for an absolute to convective instability transition as shown in figure 3.3 with the full and dashed lines. The full and dashed curves are obtained numerically starting from either a low or a high  $Oh$  number, respectively, which physically correspond to a relatively inviscid or inertialess jet. For both a pure inviscid or in contrast an inertialess jet, the dispersion relation can be simplified further to obtain the absolute to convective transition criteria. In the limit  $Oh \rightarrow 0$ , this criteria is retrieved as  $We = 4$  and for  $Oh \rightarrow \infty$ , it is expressed

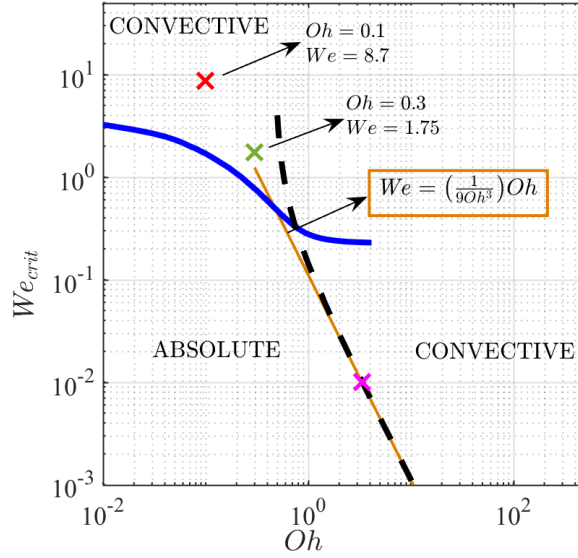


Figure 3.3 – The plot shows the absolute-convective transition (represented by full (in blue) and dashed (in black) lines) for viscous jets.

as  $\sqrt{We}Oh = 1/3$  (Augello, 2015). For simplicity, we express the latter criteria in the form of a straight line with a slope of  $(9Oh^3)^{-1}$  as shown in figure 3.3. We observe that the viscous jet saddle points are in accordance with these values at low and high  $Oh$  limits. Note here that the expression  $\sqrt{We}Oh$  can be simplified as the Capillary number,  $Ca = \mu U/\gamma$ , which compares the advection speed with the relevant capillary wave speed in the viscous-dominated regime.

For the intermediate values of  $Oh$  we obtain two saddle points, thus giving two distinct values of the absolute-convective transition criteria. Each saddle point corresponds to one of the inviscid or inertialess limits, but we could not clarify which was the relevant one in the intermediate  $Oh$  range.

### 3.3.3 Spatial stability analysis

Figure 3.3 identifies the absolutely unstable regime, where the spatial stability analysis due to external harmonic forcing is ill posed. Indeed the forced response at a given real frequency  $\omega$  will be mixed with the naturally growing wave packet which will invade the entire domain. In contrast, the spatial stability analysis is well posed in the convectively stable regime where the response is primarily dominated by the forced response.

However, the spatial stability problem is not as straightforward as the temporal stability problem owing to the existence of several spatial branches as presented in Guerrero, González & García (2016). As in the given case, the solution of the dispersion relation (3.14) for  $k \in \mathbb{C}$  and  $\omega \in \mathbb{R}$ , results in four roots of  $k$ . Moreover, the classification of the dominant  $k$  wave

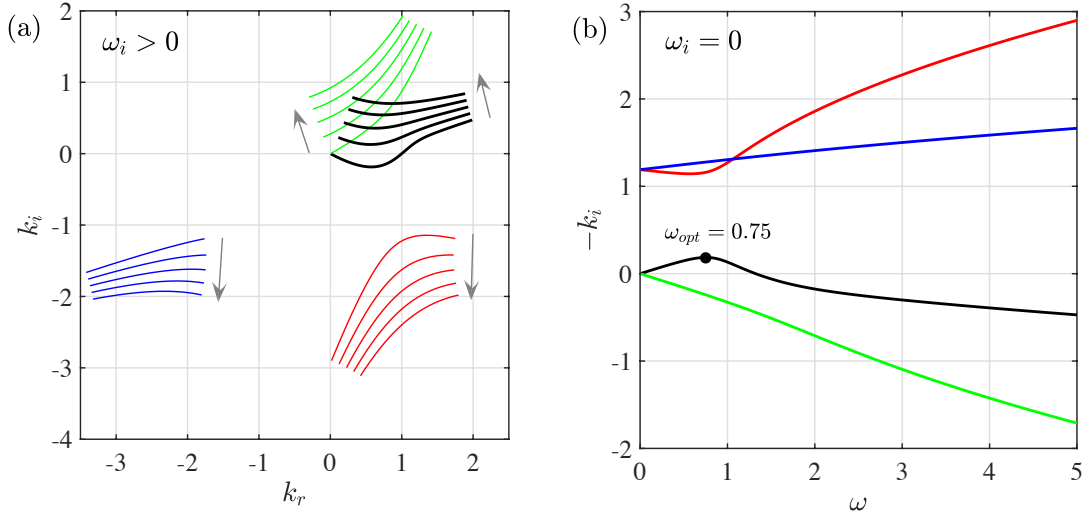


Figure 3.4 – (a) The four  $k$  branches shown in four different colours, obtained as a solution of the dispersion relation for complex  $\omega$  for a jet defined by  $Oh = 0.3$  and  $We = 1.75$ . The arrows represent the direction of movement of the waves for increasing values of  $\omega_i$ . (b) Growth rate ( $-k_i$ ) plotted as a function of the frequency for the four  $k$  branches for  $\omega_i = 0$  with the dominant  $k$  branch represented in black.

requires the identification of the propagation direction of these waves which can be precisely done as described below.

The dispersion relation (3.14) is first solved for a given range of complex  $\omega$  by adding an artificial imaginary part  $\gamma > \omega_{i,max}$  (Gallaire & Brun, 2017). The solution consists of upstream (referred as  $k^-$ ) and downstream (denoted by  $k^+$ ) propagating branches. To identify these branches, we successively lower the artificial  $\gamma$  to 0, unless a saddle point appears at  $\omega_{0,i} > 0$  if the flow is absolutely unstable. This helps to separate the branches into the upper  $k_i > 0$  and lower  $k_i < 0$  planes, as shown in figure 3.5(a) with the two  $k^+$  branches denoted by the black and green colour and the two  $k^-$  waves by the red and blue colour. For a downstream propagating  $k^+$  branch damped in space, the associated  $k_i > 0$ .

Next to identify the most amplified downstream propagating wavenumber, we plot the spatial growth rate  $-k_i$  as a function of the real forcing frequency  $\omega$  as shown in figure 3.5(b) from where we conclude that the branch in black has a growth rate which is positive and has a preferential maximum growth rate for a given frequency. Hence we chose the  $k$  wave corresponding to this  $-k_i$  branch as the relevant wavenumber for all frequencies whose growth rate  $-k_i$  determines the spatial stability. The base flow is considered linearly unstable if  $-k_i > 0$ .

Further to see the dependence of  $Oh$  and  $We$  number on  $-k_i$ , we plot the spatial growth rate as a function of forcing frequency as shown in figure 3.5(a) and 3.5(c). Higher the  $Oh$  and  $We$ , more stable is the base flow and lower is the spatial growth rate as seen from the plots. The

### Chapter 3. Capillary jet stability analysis using the one-dimensional Eggers & Dupont equations

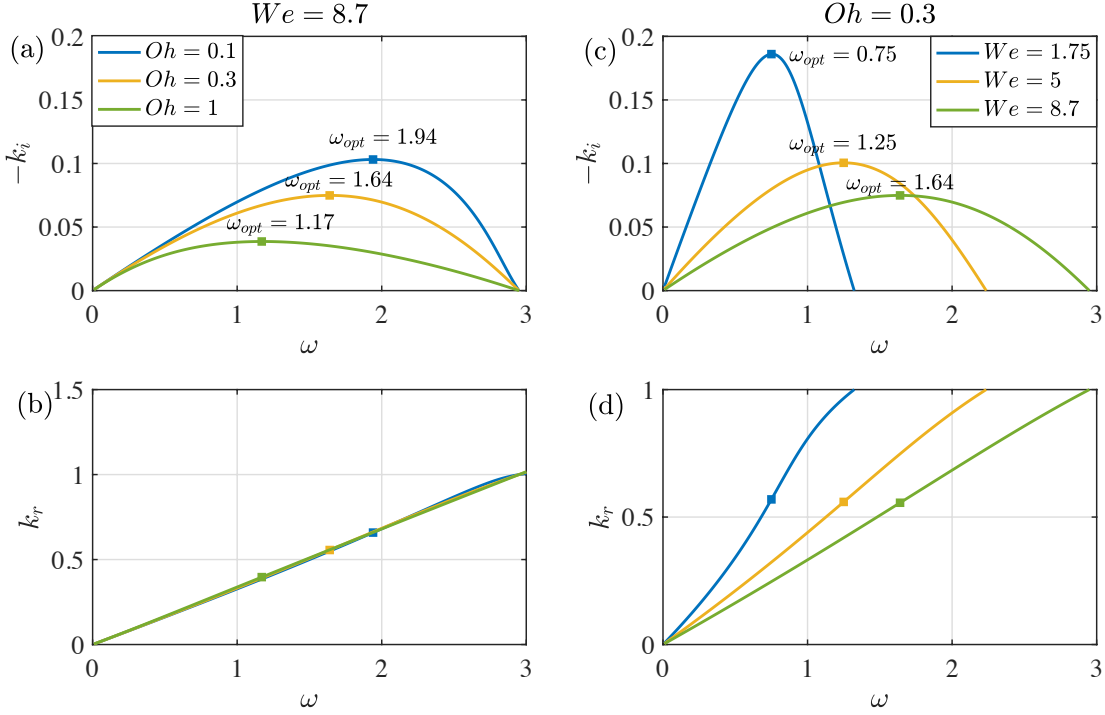


Figure 3.5 – (a) and (b) show  $-k_i$  and  $k_r$  as a function of real frequency for different  $Oh$  and at constant  $We$ . (c) and (d) show the same for different  $We$  and at constant  $Oh$ . In either case,  $\blacksquare$  denotes the maximum  $-k_i$  and the related  $k_r$ .

optimal forcing  $\omega_{opt}$  resulting in the maximal  $-k_i$  decreases as  $Oh$  increases (see figure 3.5(a)) however we see an opposite trend for the  $We$  in figure 3.5(c) where higher the advection, higher is the  $\omega_{opt}$ . Nevertheless, the resulting  $k_r$  obtained at  $\omega_{opt}$  are independent of the variation in  $We$  as seen in figure 3.5(d)).

#### Spatial gain

Representing the eigenmode  $[a, u]$  by  $\hat{\mathbf{q}}$ , for a known  $k$  branch the spatial response at a real  $\omega$  can be expressed as,

$$\mathbf{q}'(z, t) = \hat{\mathbf{q}}(z) \exp \left[ i \left( \int_0^z k(z') dz' - \omega t \right) \right]. \quad (3.18)$$

Thus the response  $\mathbf{q}'$  at a given  $z$  incorporates all the  $k$  waves up to  $z$ . For the parallel base flow the expression (3.18) further simplifies to

$$\mathbf{q}'(z, t) = \hat{\mathbf{q}}_{z=0} \exp \left[ i \left( kz - \omega t \right) \right]. \quad (3.19)$$

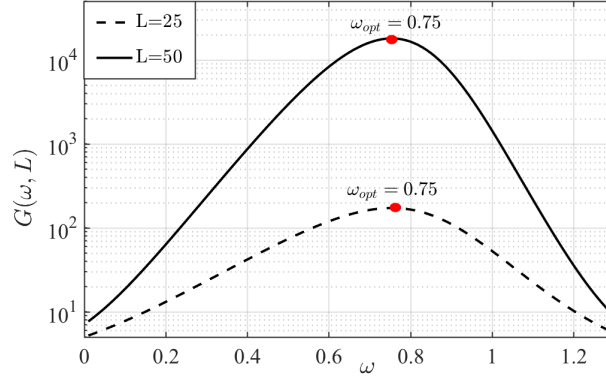


Figure 3.6 – Comparison of gain and  $\omega_{opt}$  obtained from the spatial analysis for two different domain sizes  $L = 25$  and  $L = 50$  for a jet characterized by  $Oh = 0.3$  and  $We = 1.75$ .

The amplitude of the overall response in a domain of size  $L$ , at  $\omega$  can be expressed using the L2 norm for complex variables, expressed as

$$\|\mathbf{q}'\| = \left\| \int_0^L \hat{\mathbf{q}}_{z=0} \exp(ikz) dz \right\|. \quad (3.20)$$

While doing the above, the eigenmode at every location in  $z$  including the nozzle exit is normalized to have an amplitude of 1. This implies that the amplitude of the forcing at the inlet is  $\|f\| = 1$ . Classically, the amplification due to a given forcing at frequency  $\omega$  can be expressed through the gain, which is defined as the ratio between the amplitude of the response and the amplitude of the input forcing:

$$G(\omega, L) = \frac{\|\mathbf{q}'\|}{\|f\|}. \quad (3.21)$$

In particular it is of interest to determine the largest amplification factor,

$$G_{max}(\omega_{opt}, L) = \max \left\| \int_0^L \hat{\mathbf{q}}_{z=0} \exp(ik(\omega)z) dz \right\|. \quad (3.22)$$

This allows us to determine the optimal forcing frequency  $\omega_{opt}$  producing the maximal gain. We apply the above formulation for a jet flow characterized by  $Oh = 0.3$  and  $We = 1.75$  which exists in the convectively unstable regime (as denoted by the green cross in figure 3.3). Figure 3.6 shows the spatial gain as a function of forcing frequency for two arbitrary domain sizes  $L = 25$  and  $50$ , where the gain is seen to increase with an increases in  $L$ . However, irrespective of the domain size, the optimal forcing frequency  $\omega_{opt} = 0.75$ , which is in accordance with the one obtained for the maximum spatial growth rate  $-k_i$  (refer figure 3.5(c)).

### 3.4 Nonlinear simulations

For the parallel jets, the local stability analysis is limited to the prediction of the most unstable forcing. Often, the external forcing does not result in the breakup of fixed sized drops, rather the regular sized drops are followed by much smaller ‘satellite drops’. Thus, to unravel the true interface evolution, including the shape close to the breakup point where the interface height  $h$  approaches to a zero value, we need a nonlinear analysis that captures the exact response of the jet.

We perform such nonlinear simulations by slightly modifying the nonlinear governing equations (3.11). The numerical scheme and its validation with the results of van Hoeve *et al.* (2010), are presented in the following sections. Finally the nonlinear model is used to evaluate the jet response to different external forcing and the optimal forcing hence obtained is compared to the prediction of the local analysis.

#### 3.4.1 Governing equations

In order to remove the singularity in expression (3.11b) for the pressure, when  $h(z, t) \rightarrow 0$ , we define the interface height  $h(z, t)$  in terms of function  $a(z, t)$  where  $a = h^2$ . The governing equations (3.11) thus transform into,

$$\frac{\partial a}{\partial t} = -\frac{\partial}{\partial z}(au), \quad (3.23a)$$

$$\frac{\partial u}{\partial t} = -u\frac{\partial u}{\partial z} - \frac{\partial p}{\partial z} + 3Oh\left(\frac{\partial}{\partial z}\left(a\frac{\partial u}{\partial z}\right)\frac{1}{a}\right), \quad (3.23b)$$

$$p = \frac{\left(2 - \frac{\partial^2 a}{\partial z^2}\right)a + \left(\frac{\partial a}{\partial z}\right)^2}{2\left(\frac{1}{4}\left(\frac{\partial a}{\partial z}\right)^2 + a\right)^{\frac{3}{2}}}. \quad (3.23c)$$

The base state solution for the jet interface  $a_b = h_b^2$ . In absence of external forcing, the jet inlet is defined by  $a_b(0, t) = 1$  and  $u_b(0, t) = \sqrt{We}$ . The nonlinear governing equations are closed with periodic boundary conditions.

#### 3.4.2 Numerical scheme

The governing equations (4.7) are first discretized in space, after which the resulting ordinary differential equations (ODE) are integrated in time. Diffusion terms are evaluated using second-order finite differences, with a central scheme for intermediate nodes and a forward or backward scheme for boundary nodes. Advection terms are obtained using a weighted upwind scheme inspired by Spalding (1972) hybrid difference scheme. Unlike the latter, which approximates the convective derivative using a combination of central and upwind schemes, we evaluate the derivative based on a combination of forward and backward finite differences.

An advection term  $dA/dz$  is evaluated at node  $i$  as

$$\left(\frac{dA}{dz}\right)_i = \beta \left(\frac{dA}{dz}\right)_{i,b} + (1 - \beta) \left(\frac{dA}{dz}\right)_{i,f}, \quad (3.24)$$

where indices  $b$  and  $f$  refer to the backward and forward finite difference schemes, and  $\beta$  is a weight coefficient that depends on the local value of velocity  $u$  at node  $i$  together with a parameter  $\alpha$ ,

$$\beta = \frac{\tanh(\alpha u_i) + 1}{2}. \quad (3.25)$$

For the entire work presented in this thesis, the numerical stability was always ensured by using a 10-point stencil. Thus, the backward difference term relies on a stencil that spans nodes  $i - 5$  to  $i + 4$ , and the forward difference term employs nodes  $i - 4$  to  $i + 5$ . For large enough downstream or upstream velocities,  $\beta$  will tend to 1 or 0 respectively; hence (5.29) reduces to a regular upwind difference scheme. For smaller velocity magnitudes in between, (5.29) produces a weighted combination of backward and forward differences. In our simulations, we choose  $\alpha = 50$  so that the transition between the backward and forward difference schemes mostly occurs when  $|u| < 0.05$ . Finally, advection terms at nodes close to the boundary are evaluated based on the values of the closest 9 adjoining nodes.

After obtaining all spatial derivatives, the resulting ODEs are integrated using the MATLAB solver `ode23tb`, which implements a trapezoidal rule and backward differentiation formula known as TR-BDF2 (Bank, Coughran, Fichtner, Grosse, Rose & Smith, 1985), and uses a variable time step to reduce the overall simulation time.

The numerical domain  $L$  is taken sufficiently large to capture the breakup of the jet. The jet interface is initialized by a semicircle of whose radius is of length one and the velocity is kept constant at  $\sqrt{We}$ . For the remaining part of the domain the interface and its velocity is initialized to zero.

At every time step, the solution is evaluated for three conditions: (i) *Pinch-off (breakup)*: It is defined as when the value of  $a$  passes below a threshold value of  $10^{-5}$ . The corresponding time  $t_{po}$  is saved and the position of the jet tip is updated as  $N_{tip} = N_{po}$ , where  $N_{po}$  is the pinch-off location. The solution for  $a$  and  $u$  beyond  $N_{tip}$  is set to zero. For subsequent time steps,  $N_{tip}$  has two possibilities – it can either advance or recede, which requires the following two conditions. (ii) *Advancing jet*: The values of  $a$  at nodes  $N_{tip} - 1$  and  $N_{tip}$  are extrapolated to find  $a$  at  $N_{tip} + 1$ . If the extrapolated value is larger than a predefined value of  $5 \cdot 10^{-3}$ , the parameter  $N_{tip}$  is incremented by 1, and  $a$  and  $u$  at the new  $N_{tip}$  are assigned values extrapolated from its previous two neighbours. (iii) *Receding jet*: If the value of  $a$  at  $N_{tip}$  falls below a predefined value of  $10^{-3}$ ,  $a$  and  $u$  at  $N_{tip}$  are set to zero and the parameter  $N_{tip}$  is reduced by 1. These three conditions enable the numerical integration of the governing equations in a way that captures accurately the breakup of the jet and the motion of the tip.

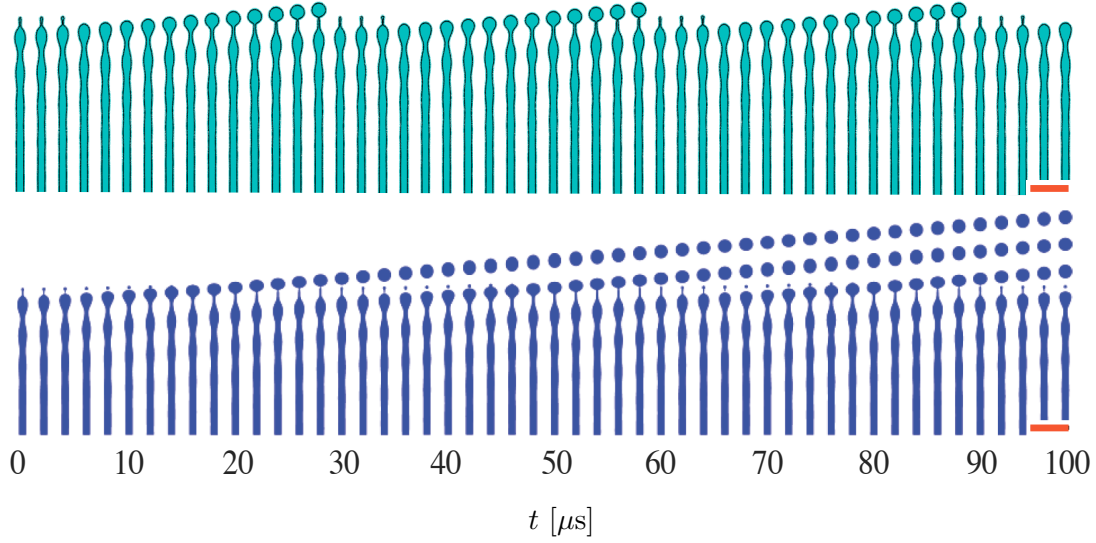


Figure 3.7 – Numerical solutions of the governing equations (4.7) for a jet in an inert medium with  $Oh = 0.1$  and  $We = 8.7$  (a) Results from our numerical scheme described in Section 3.4.2 and (b) experimentally-validated numerical results of van Hoeve *et al.* (2010). The red bar corresponds to a length scale of  $200 \mu\text{m}$ .

### 3.4.3 Numerical scheme validation

In this section, we show the validation of our numerical scheme described in the previous section for the simulations of reduced 1D Eggers & Dupont (1994) equations represented by the equation (4.7). For the purpose of validation, we use the numerical data of van Hoeve *et al.* (2010) which are described for micro-jets of initial radius  $h_0 = 18.5 \mu\text{m}$  with density  $\rho = 1098 \text{ kg/m}^3$ , viscosity  $\eta = 3.65 \text{ mPa.s}$ , and surface tension  $\gamma = 67.9 \text{ mN/m}$ . The jet is injected at a constant flow rate  $Q = 0.35 \text{ mL/min}$ , corresponding to an initial jet velocity  $U_0 = Q/(\pi h_0^2) = 5.4 \text{ m/s}$ . The flow can thus be described by the dimensionless numbers  $Oh = 0.1$  and  $We = 8.7$ .

To initiate jet breakup in their numerical simulations, a harmonic modulation of the dimensional nozzle radius is applied as follows:

$$h(z=0, t) = h_0 + \delta \sin 2\pi n t, \quad (3.26)$$

with  $\delta/h_0 \approx 0.005$  the forcing amplitude, and  $n$  the driving frequency. The latter is selected to match the optimum wavelength  $\lambda_{opt}$  for jet breakup, that is,  $n = U_0/\lambda_{opt}$ . To ensure a constant flow rate  $Q$  through the nozzle, the dimensional velocity is modulated correspondingly as

$$u_0(z=0, t) = \frac{h_0^2 U_0}{[h(z=0, t)]^2}. \quad (3.27)$$

The amplitude of the wave imparted by the forcing at the nozzle grows until it equals the



radius of the jet. Pinch-off or jet breakup is then defined as when the minimum width of the jet is below a predefined value set to  $10^{-3}h_0$ .

In our numerical simulations, we compute solutions to the governing equations (4.7) with the same harmonic forcing and flow parameters as in van Hoeve *et al.* (2010). A hemispherical droplet described by  $h = (h_0^2 - z^2)^{1/2}$  is used as initial condition for the shape of the jet, the tip of which is therefore initially at  $z = h_0$ . The velocity is initialized to  $u_0$  everywhere along the jet. A fixed number of grid points, corresponding to a discretization size  $dz = 0.05$ , is uniformly distributed throughout the entire domain. The final validation is presented in Figure 3.7, which shows comparison of the time series of the dynamics of jet breakup obtained from our numerical scheme and the numerical results from van Hoeve *et al.* (2010).

The jet breakup is characterized by the break up period  $\Delta T_{po}$  and the breakup length  $l_c$ . In the permanent regime, when the breakup of the jet occurs at the same location along the axial direction, we define  $l_c$  as the stable length of the jet between the nozzle exit and the breakup location. In this regime  $\Delta T_{po}$  is expressed as the time between two consecutive breakups at the breakup location.

For both figures, the evolution of the jet shape is shown at time intervals of  $2\mu\text{s}$ . Our numerical model predicts a  $\Delta T_{po} = 25\mu\text{s}$  and a  $l_c = 856\mu\text{m}$ . The results of van Hoeve *et al.* (2010), have a  $\Delta T_{po} \approx 26 - 30\mu\text{s}$  and a  $l_c \approx 800\mu\text{m}$ . The error in breakup length between the two codes can be explained by the difference in grid size. Overall, figure 3.7 shows a good agreement between both results and validates our numerical scheme.

#### 3.4.4 Simulation results

##### Forced simulations

For the validation of the numerical scheme at  $Oh = 0.1$  and  $We = 8.7$ , we imposed an inlet disturbance both in shape and velocity, at a frequency which was deduced from the wavenumber. To analyse if indeed this forcing frequency was the optimal one to produce maximum amplification, we carried out further nonlinear simulations close to the imposed forcing frequency. The strength of a given perturbation was determined on the basis of the stable jet intact length before the breakup  $l_c$ , obtained when the jet flow enters a permanent regime. Performing the simulations for two different forcing amplitudes  $\epsilon = 0.005$  and  $0.001$  as shown in figure 3.8(b), we observe that the optimal frequency  $\omega_{opt} = 2.06$ , producing the shortest  $l_c$ . The  $\omega_{opt}$  is independent of the forcing amplitude and is in close agreement with the results of spatial analysis shown in figure 3.5(a). However, smaller the forcing amplitude, larger the value of  $l_c$ , due to the decreasing amplifying potential of the flow.

Next, we carried out similar simulations for another convective case  $Oh = 0.3$  and  $We = 1.75$ , but with a slightly modified forcing. We modelled the external forcing on the jet by perturbing

### Chapter 3. Capillary jet stability analysis using the one-dimensional Eggers & Dupont equations

only the inlet velocity using a forcing of the form,

$$u_f(0, t) = \text{Re}(\epsilon e^{i\omega t}) = \epsilon \cos(\omega t). \quad (3.28)$$

Thus, in presence of the forcing, the boundary conditions at the inlet were modified to  $a(0, t) = 1$  and  $u(0, t) = \sqrt{We} + u_f$ . We performed the simulations for different forcing amplitudes  $\epsilon = [10^{-2} \ 10^{-5}]$ , each of which resulted in the same optimal forcing frequency  $\omega_{opt} = 0.78$  (refer figure 3.8(a)). The spatial analysis performed for a similar case as shown in figure 3.5(b), gives  $\omega_{opt} = 0.75$ , close to the one obtained from the nonlinear simulations.

#### Free regime

If the external forcing is removed and the jet is allowed to flow naturally, we observe a disordered breakup mechanism especially if the base flows lies in the convective regime. This feature is closely related to the freely flowing amplifier flows which do not have an inherent frequency selection and behave erratically in absence of an external forcing. Contrary to this, for a jet that lies in the absolutely unstable regime, for example at  $Oh = 3.33$  and  $We = 0.01$  (as marked with the magenta cross in figure 3.5), we would expect that the perturbations grow locally without travelling downstream to cause breakups. Performing numerical simulations for the same conditions, as shown as in figure 3.9, we observe that the breakup is not immediate, rather the jet interface shows a resistance to breakup while continuously amplifying close to the nozzle. In fact, the interface continuously bulges to reach radius 8 times the order of the nozzle radius at the end of dimensionless time  $t = 1000$ .

Anticipating that a faster breakup of the jet could be obtained by initiating the jet with a

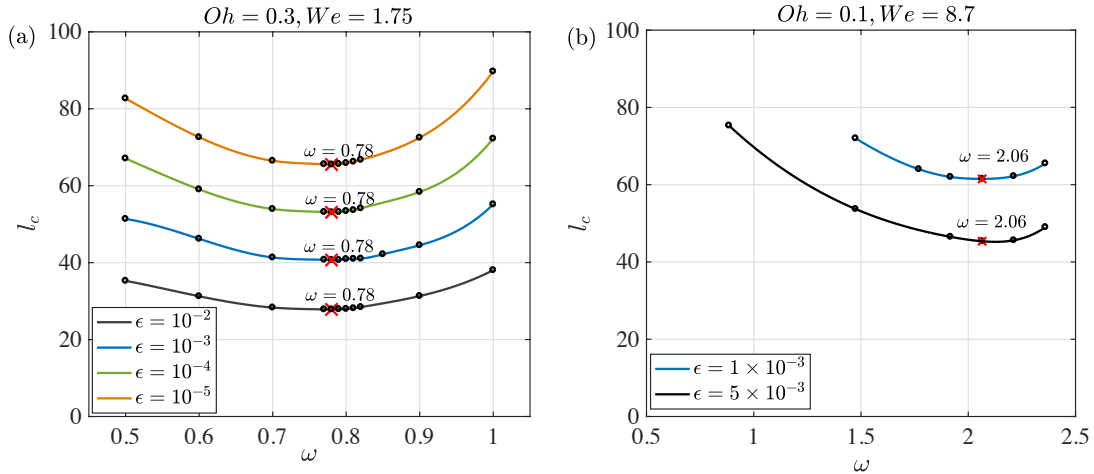


Figure 3.8 – Nonlinear simulations performed for different forcing amplitudes  $\epsilon$  and for base flows characterized by (a)  $Oh = 0.3$  and  $We = 1.75$  and (b)  $Oh = 0.1$  and  $We = 8.7$ , showing the breakup length as a function of the forcing frequency.

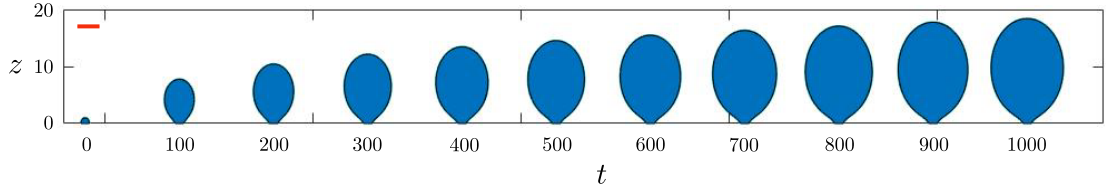


Figure 3.9 – Jet interface evolution as function of time for  $We = 0.01$  and  $Oh = 3.33$ . The red bar corresponds to a radial length scale of 5 dimensionless units.

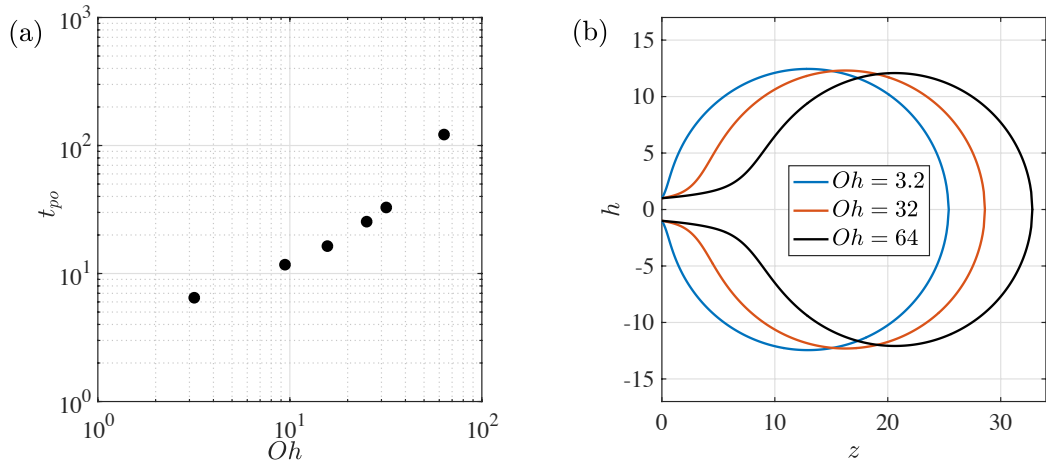


Figure 3.10 – (a) Pinch-off time  $t_{po}$  as a function of  $Oh$  for a fixed  $We = 10^{-3}$ . (b) Interface shape at  $t = 2500$  for three different jet flows characterized by fixed  $We = 10^{-3}$ .

cylinder of constant radius  $h_0$ , instead of a tip of radius  $h_0$  which needs long time to propagate and form a jet, we run simulations with the new initial state defined over a domain size  $L = 50$ , for  $We = 10^{-3}$  and varying  $Oh$  numbers between 3.2 to 64. The high  $Oh$  allows one to cross over into the convective regime. We observed that in all the cases there was a breakup initiated in the cylindrical jet, the time  $t_{po}$  of which is represented in figure 3.10(a) as a function of the  $Oh$  number. Larger the  $Oh$  number, higher the viscosity of the jet and larger was the time needed to cause the first breakup. Post breakup in the cylindrical base state, the tip of the jet continued to bulge till the end of the maximum simulation time ( $t = 2500$ ), similar to the case shown in figure 3.9, without any further breakups. In figure 3.10(b), we show the final shape at  $t = 2500$  for three different  $Oh$  numbers where we see that the neck part of the jet close to the nozzle exit is seen to elongate as the  $Oh$  is increased. Thus, the bulging behaviour seen in the jet cannot be inferred purely on the basis of absolute/convective unstable flows, since it is also evident for very high  $Oh$  numbers. Rather, this peculiar behaviour can be attributed to the small inertia regime ( $We = 10^{-3}$ ) where all the jets between  $Oh = [3.2 \text{ } 64]$  are characterized.

### **3.5 Conclusion**

The main aim of this chapter was to introduce the 1D Eggers & Dupont equations, and the numerical tool employed to analyse the jet using these equations. In the subsequent chapters 4 and 5, we will modify the described governing equations and the numerical scheme slightly to capture the interface dynamics for jets stretched by gravity and for silicone in silica jets.

We also performed the local stability analysis on these reduced one-dimensional equations. The absolute-convective stability analysis categorized the stability of the jet based on the  $We_{crit}$  number whereas the temporal and spatial stability analysis predicted the maximum wavenumber and the optimal frequency ( $\omega_{opt}$ ), respectively, that produces the maximum amplification for a given jet. To analyse the nonlinear governing equations, we then introduced the numerical scheme and the validation of the same using the results of van Hoeve *et al.* (2010), where the validation was found to be satisfactory. The validated numerical code was further used to obtain numerically the  $\omega_{opt}$  resulting in the shortest breakup length. The  $\omega_{opt}$  was found to be independent of the forcing amplitude.

Finally we performed simulations in a very low  $We$  regime, where the jet interface was seen to continuously bulge to have diameters much larger compared to the nozzle radius. Indeed such a behaviour cannot be speculated from the linear stability analysis, which is only valid when the perturbation wavelength is of the order of the radial length scale. The simulation time was kept sufficiently long to observe the evolution of low inertia jets. Running these simulations for exorbitantly long times or introducing a large amplitude nozzle forcing, could possibly result in capturing the jet breakup. We believe that for the selected simulation time, the low inertia jet is not capable of pinching because the inlet flux is continuously distributed in the radial direction without rapidly elongating the jet in the axial direction.

## 4 Amplitude dependent preferred mode of an axisymmetric single phase gravity-driven falling viscous jet

**Remark** This chapter is largely inspired by the publication *Frequency selection in a gravitationally stretched capillary jet in the jetting regime*

Isha Shukla<sup>1</sup> and François Gallaire<sup>1</sup>

<sup>1</sup>Laboratory of Fluid Mechanics and Instabilities, École Polytechnique Fédérale de Lausanne, Lausanne, CH-1015, Switzerland

Submitted in *Journal of Fluid Mechanics*

A capillary jet falling under the effect of gravity continuously stretches while thinning downstream. We report here the effect of external periodic forcing on such a spatially varying jet in the jetting regime. Surprisingly, the optimal forcing frequency producing the most unstable jet is found to be highly dependent on the forcing amplitude. Taking benefit of the one-dimensional Eggers & Dupont (J. Fluid Mech., vol. 262, 1994, 205-221) equations, we investigate the case through nonlinear simulations and linear stability analysis. In the local framework the WKBJ formalism, established for weakly non-parallel flows, fails to capture the nonlinear simulation results quantitatively. However in the global framework, the resolvent analysis supplemented by a simple approximation of the required response norm inducing breakup, is shown to correctly predict the optimal forcing frequency at a given forcing amplitude and the resulting jet breakup length. The results of the resolvent analysis are found to be in good agreement with those of the nonlinear simulations.

## **4.1 Introduction**

Pele's hair, which are thin strands of volcanic glass formed in the air during the fountaining of the molten lava, is an impressive example of the stretching ability of highly viscous fluids. Named after Pele, the Hawaiian goddess of volcanoes, a single strand with a diameter of less than 0.5 mm, can extend up to a length of 2 m (Shimozuru 1994; Eggers & Villermaux 2008). If such viscous strands are pinned at one end, as in the case of honey dripping from a spoon under its own weight, gravity acts as the stretching tool for the viscous fluid producing very thin and stable liquid threads (Senchenko & Bohr, 2005; Javadi *et al.*, 2013). The cross-section of such threads varies continually, as the jet accelerates downstream in the direction of gravity, before breaking into drops.

Physically, the breakup of the jet into drops begins with the excitation of a temporally or spatially amplifying suitable mode due to weak external disturbances. In practice, this weak agitation is usually imposed by controlled harmonic perturbation, either from within or at the outlet of the nozzle, to generate spatially amplifying waves leading to jet breakup. In this direction, the primary objective of this paper is to evaluate the response of an incompressible jet falling in presence of gravity, to externally imposed harmonic perturbations characterized by a fixed frequency and amplitude, and to find the optimal forcing which generates the most amplified response.

The external forcing is vital in the production of controlled micron-sized droplets, a feature essential to several application as in inkjet printers (Basaran 2002; Wijshoff 2010; Basaran *et al.* 2013), pharmaceuticals (Bennett, Brown, Zeman, Hu, Scheuch & Sommerer, 2002) and powder technology (van Deventer, Houben & Koldeweij, 2013), to name a few. In view of the limitations linked to the fabrication of such small droplets, most of the devices used for the drops production depend on the generation of highly thin liquid threads whose diameters are several orders smaller than the nozzle diameter. Some common methods for producing such threads use tangential electrical stresses (in electrospinning devices, Doshi & Reneker 1995; Loscertales, Barrero, Guerrero, Cortijo, Marquez & Ganan-Calvo 2002), using outer co-flows (Marín, Campo-Cortés & Gordillo, 2009) or a rotating spinneret (in fibre spinning applications (Pearson & Matovich, 1969)). Rubio-Rubio *et al.* (2013) showed an alternative method for producing highly elongated jets through the use of gravity, in which the mass conservation of the liquid jet forces its thinning as the liquid accelerates downstream.

The breakup of a liquid thread into drops, governed by the relative strength of the surface tension effect over the viscous and the inertial effects, was first explained by Plateau (1873) and Rayleigh (1879) for a uniform column of fluid. What adds complexity to the well understood viscous jet breakup mechanism is the presence of gravity which significantly stretches the base flow shape. The stability of the such spatially varying gravity jets should ideally be examined using the global stability analysis and by including the non-parallel effects of the base flow. A similar difficulty linked to the non-parallel nature of the flow results from the adaptation of the flow from a wall bounded flow within the nozzle to a free jet (Sevilla, 2011). Turning

back to falling jets stretched by gravity, Sauter & Buggisch (2005) were the first to approach the problem theoretically by defining a linear global mode that correlated with the self sustained oscillations of the falling jet, observed during the jetting (globally stable) to dripping (globally unstable) transition. The work of Sauter & Buggisch (2005) was extended by Rubio-Rubio *et al.* (2013) experimentally and theoretically by increasing the range of liquid viscosities and nozzle diameters. Additionally they retained the entire expression of the curvature term for the formulation of their stability analysis, a feature that helped them to accurately predict the critical flow rate for the stability transition and the oscillating mode compared to the previous author. However, none of these studies predicted the jet stable length as a function of the flow rate and fluid properties, a question which was pursued by Javadi *et al.* (2013) experimentally and theoretically.

More recently, Le Dizès & Villermaux (2017) determined theoretically the stable jet length, wavelength at breakup and resulting drop size due to the most dangerous perturbation applied either at nozzle exit or affecting the jet all along its length for different jet viscosities. Their analysis accounted for both the base state deformation and modification of local instability dispersion relation as the jet thins in the direction of gravity. Notably, extending the work of previous authors (Tomotika, 1936; Frankel & Weihs, 1985; Leib & Goldstein, 1986; Frankel & Weihs, 1987; Senchenko & Bohr, 2005; Sauter & Buggisch, 2005; Javadi *et al.*, 2013) they used the local plane wave decomposition (WKBJ approximation) for their analysis. However, the gain resulting from a perturbation was computed by considering only the exponential ( $e$ ) terms of the WKBJ approximation. Additionally, an *ad hoc* spatial gain of  $e^7$ , of the linear perturbations was assumed to be sufficient for breakup. Thus the level of noise was considered fixed for all the theoretical analysis.

In this paper, we go beyond the global stability analysis of the gravity jets, and always operate in the stable regime where the jet behaves inherently as an amplifier. Precisely, we look at the receptivity of the jet to external perturbations in this regime, through nonlinear simulations and resolvent analysis with the aim of finding the optimal forcing which results in the most amplified disturbance. Unlike Le Dizès & Villermaux (2017), we consider an external forcing characterized by different amplitudes. Our analysis exemplifies the effect of forcing amplitude on the breakup length and the optimal forcing frequency. We also investigate the jet response using the WKBJ approximation and assess its validity for the spatially varying gravity jet. Our entire study is based on the slender-jet approximation (Eggers & Dupont, 1994) of the Navier-Stokes equation for an axisymmetric jet. The reduced one dimensional (1D) model has turned out to be extremely valuable for realistic representation of jets (Ambravaneswaran *et al.* 2002; van Hoeve *et al.* 2010) by accurately capturing the jet interface close to the breakup as well as the formation of ‘satellite’ drops. During the final stage of this work, we became aware of the work of (Lizzi, 2016) who has compared a resolvent analysis to experimental results and also revealed the dependance of the optimal frequency and breakup length as a function of time-harmonic forcing or noise amplitude.

The paper is structured as follows. Section 4.2 describes the governing equations. Section

## Chapter 4. Amplitude dependent preferred mode of an axisymmetric single phase gravity-driven falling viscous jet

---

4.3 discusses the nonlinear simulations where the results are detailed in Section 4.3.2. The local stability analysis of the gravity jet is performed in Section 4.4 where we compare the jet response using stability analysis in Section 4.4.2 and the WKBJ formulation in Section 4.4.3. We then operate in the global framework in Section 4.5 where the significance of the resolvent analysis is elucidated in Section 4.5.2. We show that the reformulated resolvent analysis is self sufficient in predicting the optimal forcing frequency and the breakup length as obtained through the nonlinear simulations. Finally, we apply a white noise disturbance on the jet inlet to explore its behaviour in comparison to the expected response to the optimal forcing in Section 4.6. The conclusion and some perspectives related to the present work are summarized in Section 4.7.

### 4.2 Mathematical formulation

We consider an axisymmetric viscous jet falling vertically from a nozzle under the effect of gravity  $g$ . At the nozzle outlet, the jet has a fixed radius  $\bar{h}_0$  and velocity  $\bar{u}_0$ . The surrounding medium is considered evanescent and is neglected. The density, dynamic viscosity and surface tension of the jet are denoted by  $\rho$ ,  $\mu$  and  $\gamma$ , respectively.

The behaviour of the jet is analysed using the leading-order one-dimensional mass and momentum equations, derived by Eggers & Dupont (1994). The dimensionless form of the equations, obtained by choosing  $\bar{h}_0$  as the characteristic length scale, the inertial time  $\tau_i = \sqrt{\rho \bar{h}_0^3 / \gamma}$  as the characteristic time scale and  $\gamma / \bar{h}_0^2$  as the pressure scale, are written as,

$$\frac{\partial h}{\partial t} = -\frac{1}{2h} \frac{\partial}{\partial z} (h^2 u), \quad (4.1a)$$

$$\frac{\partial u}{\partial t} = -u \frac{\partial u}{\partial z} - \frac{\partial p}{\partial z} + 3Oh_{in} \left( 2 \frac{\partial h}{\partial z} \frac{\partial u}{\partial z} \frac{1}{h} + \frac{\partial^2 u}{\partial z^2} \right) + Bo_{in}, \quad (4.1b)$$

where, the dimensionless pressure  $p(z, t)$  is expressed as,

$$p = \left( \frac{1}{h \left[ 1 + \left( \frac{\partial h}{\partial z} \right)^2 \right]^{\frac{1}{2}}} - \frac{\frac{\partial^2 h}{\partial z^2}}{\left[ 1 + \left( \frac{\partial h}{\partial z} \right)^2 \right]^{\frac{3}{2}}} \right). \quad (4.2)$$

In equation (4.1),  $h(z, t)$  and  $u(z, t)$  represent the height of the jet interface and the velocity at the axial distance  $z$ . The system of equations (4.1) are governed by the dimensionless numbers Ohnesorge ( $Oh_{in}$ ) and Bond ( $Bo_{in}$ ) defined at the inlet. Ohnesorge, expressed as  $Oh_{in} = \mu / \sqrt{\rho \gamma \bar{h}_0}$ , relates the viscous forces to inertial and surface tension forces. The Bond (Eötvös) number denoted by  $Bo_{in} = \rho g \bar{h}_0^2 / \gamma$ , measures the strength of the surface tension forces to body forces. A high  $Oh_{in}$  or  $Bo_{in}$  leads to a stabilised jet interface.

Using the associated characteristic velocity  $\bar{h}_0 / \tau_i$ , the non-dimensional boundary conditions



for the jet at nozzle inlet are reduced to:

$$h(0, t) = 1, \quad (4.3a)$$

$$u(0, t) = \sqrt{We_{in}}. \quad (4.3b)$$

Here,  $We_{in}$  represents the Weber number defined at the nozzle inlet,  $We_{in} = \rho \bar{h}_0 \bar{u}_0^2 / \gamma$ , and it measures the ratio between the kinetic energy and the surface energy.

The steady state form of the continuity equation (4.1a) gives the relation between the steady state shape  $h_b$  and velocity  $u_b$  as,

$$h_b^2 u_b = Q = \sqrt{We_{in}}. \quad (4.4)$$

Here  $Q$  is the dimensionless flow rate, obtained from the nozzle conditions. This gives  $u_b = \sqrt{We_{in}} / h_b^2$ . Using the relation (4.4), the steady state momentum equation (4.1b) reduces to,

$$2Q^2 h_b' - h_b^5 C' + 6Q Oh_{in} (h_b h_b'^2 - h_b^2 h_b'') + h_b^5 Bo_{in} = 0, \quad (4.5)$$

where derivatives are with respect to  $z$  and  $C$  is the jet interfacial curvature, expressed as,

$$-h_b^2 C' = \frac{h_b'}{[1 + (h_b')^2]^{1/2}} + \frac{h_b h_b' h_b'' + h_b^2 h_b'''}{[1 + (h_b')^2]^{3/2}} - \frac{3h_b^2 h_b' (h_b'')^2}{[1 + (h_b')^2]^{5/2}}. \quad (4.6)$$

For the fixed nozzle inlet, equation (4.5) is subject to boundary condition  $h_b = 1$  at  $z = 0$ . Two more boundary conditions are needed to well define this differential problem of order three. However, exempting the jet tip from the base flow calculation gives us the liberty to impose a constant slope ( $h_b' = 0$ ) and curvature ( $h_b'' = 0$ ) at the exit of the jet. It should be noted that the boundary conditions applied at the jet exit should be treated as a way to close the differential problem rather than depicting physical boundary conditions. We made sure that these boundary conditions did not impact the overall base state solution by computing the solution over a large enough domain where the base state solution naturally converges to a solution with  $h_b' = 0$  and  $h_b'' = 0$ .

### 4.3 Nonlinear simulations

The strength of a nonlinear simulation lies in its ability of capturing the exact response of the jet interface, including the shape close to the breakup point where the interface height  $h$  approaches to a zero value. Often, the external forcing does not result in the breakup of fixed sized drops, rather the regular sized drops are followed by much smaller ‘satellite drops’.

Keeping this in view, we analyze the response of the jet in presence of an external forcing. We aim at finding the optimal forcing which results in the most unstable jet. The breakup length, which is the length of the stable jet between the nozzle and the breakup point, is chosen as the quantifier to compare the effect of different forcing, with the optimal forcing resulting in the

## Chapter 4. Amplitude dependent preferred mode of an axisymmetric single phase gravity-driven falling viscous jet

---

shortest possible breakup length.

We begin with the description of the modified nonlinear governing equations used for the simulations followed by the numerical results based on the scheme presented in Section 3.4.2 of Chapter 3. Finally we present the comparison of breakup characteristics of the jet for different inlet forcing.

### 4.3.1 Governing equations

In order to remove the singularity in expression (4.2) for the pressure, when  $h(z, t) \rightarrow 0$ , we define the interface height  $h(z, t)$  in terms of function  $a(z, t)$  where  $a = h^2$ . The governing equations (4.1) thus transform into,

$$\frac{\partial a}{\partial t} = -\frac{\partial}{\partial z}(au), \quad (4.7a)$$

$$\frac{\partial u}{\partial t} = -u\frac{\partial u}{\partial z} - \frac{\partial p}{\partial z} + 3Oh_{in}\left(\frac{\partial}{\partial z}\left(a\frac{\partial u}{\partial z}\right)\frac{1}{a}\right) + Bo_{in}, \quad (4.7b)$$

$$p = \left( \frac{\left(2 - \frac{\partial^2 a}{\partial z^2}\right)a + \left(\frac{\partial a}{\partial z}\right)^2}{2\left(\frac{1}{4}\left(\frac{\partial a}{\partial z}\right)^2 + a\right)^{\frac{3}{2}}} \right). \quad (4.7c)$$

The base state solution for the jet interface ( $a_b = h_b^2$ ) is obtained by solving equation (4.5). We model the external forcing on the jet by perturbing only the inlet velocity using a forcing of the form,

$$u_f(0, t) = \text{IR}(\epsilon e^{i\omega t}), \quad (4.8)$$

where  $\epsilon$  represents the amplitude of the forcing and  $\omega$  represents the angular forcing frequency. In presence of the forcing, the boundary conditions at the inlet are modified to  $a(0, t) = 1$  and  $u(0, t) = \sqrt{We_{in}} + u_f$ . No boundary conditions are defined at the other extremity of the domain close to the tip. Nonetheless, a special treatment is applied for the tip (refer Section 3.4.2 of Chapter 3 for details).

### 4.3.2 Nonlinear simulations results

Using the numerical scheme presented in Section 3.4.2 of Chapter 3, nonlinear simulations were performed for a jet governed by equation (4.7) for fixed inlet characteristics:  $Oh_{in} = 0.3$ ,  $We_{in} = 1.75$  and  $Bo_{in} = 0.1$ . The numerical domain  $L$  is taken sufficiently large to capture the breakup of the jet. The jet interface is initialized by the solution of (4.5) obtained numerically with the MATLAB bvp4c solver. The validation of the numerically obtained base state solution is presented in Appendix 4.8.1. It should be noted that the steady state is implemented only for a part of the numerical domain and the interface is initialized to 0 for the remaining part. The axial span of the base state solution does not affect the quasi-steady jet characteristics,

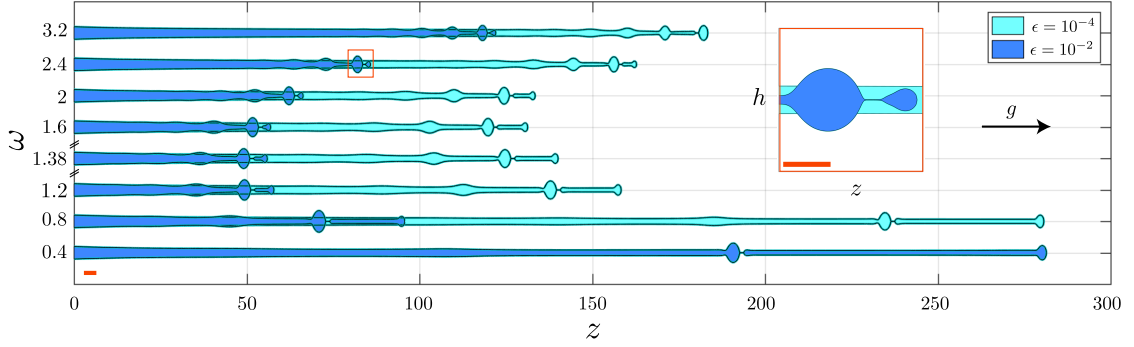


Figure 4.1 – The plot shows the jet intact shape along the axial direction  $z$  for a gravity jet defined by  $Oh_{in} = 0.3$ ,  $Bo_{in} = 0.1$  and  $We_{in} = 1.75$  and perturbed by different inlet forcing frequencies  $\omega$  and forcing amplitudes  $\epsilon = 10^{-2}$  and  $\epsilon = 10^{-4}$ . For clarity, only the shape corresponding to the shortest breakup length for every frequency is plotted. The jets of two different colors represent the shape at *approximately* the same forcing frequency but different forcing amplitudes  $\epsilon$ . We see that for  $\epsilon = 10^{-2}$ , the the breakup length is the minimum for  $\omega = 1.38$  and for  $\epsilon = 10^{-4}$  for  $\omega = 1.68$ . The box in red shows the zoomed image of the jet close to a breakup highlighting the existence of a satellite and a main drop. The zoomed image has radial  $h$  and axial  $z$  dimensions drawn to the same scale each representing a dimensionless size of 6. The red bar in both the plots represents a dimensionless radial length scale of 2, which is also the size of the dimensionless nozzle diameter.

which are the focal point of our numerical analysis. A validation for the same is presented in Appendix 4.8.2.

The jet inlet velocity is subjected to time harmonic forcing of the form given by equation (4.8) with a fixed amplitude  $\epsilon$  and for forcing frequency  $\omega = [0.4 - 3.2]$

The simulations were run for a sufficiently long time to enter a permanent regime wherein the jet breaks up at regular intervals of time and at fixed axial location. In the quasi-steady regime, the breakup period  $\Delta T_{po}$  is defined as the time difference between two consecutive breakups or pinch-offs and the breakup length  $l_c$  as the stable length of the jet between the nozzle and the pinch-off location. We use  $l_c$  as the quantifier to determine the stability of the jet to external forcing such that the most amplified disturbance caused by the optimal frequency  $\omega_{opt}$  will compel the jet to have the shortest possible breakup length.

We begin our analysis for fixed amplitudes  $\epsilon = 10^{-2}$  and  $\epsilon = 10^{-4}$ . The response of the jet due to different forcing frequency  $\omega$  in the permanent regime for the two above mentioned amplitudes can be seen in figure 4.1. Jets enforced by the same disturbance amplitude at the inlet are represented by the same colour. For visual clarity we plot the response only for certain frequencies and for the jet shape pertaining to the shortest breakup length. First, figure 4.1 clearly shows the existence of a main drop and a satellite drop for all the frequencies. Second, for  $\epsilon = 10^{-2}$  we conclude that the optimal forcing frequency is  $\omega_{opt} = 1.38$  because it manifests the jet to have the shortest  $l_c$ . Third, and most strikingly, we notice that for a

#### Chapter 4. Amplitude dependent preferred mode of an axisymmetric single phase gravity-driven falling viscous jet

lower forcing amplitude of  $\epsilon = 10^{-4}$ , the optimal forcing increases to  $\omega_{opt} = 1.68$ . Finally, at all forcing frequencies, the breakup length for jet with  $\epsilon = 10^{-4}$  is always larger than for  $\epsilon = 10^{-2}$ .

To investigate further the breakup characteristics for the amplitudes  $\epsilon = 10^{-2}$  and  $\epsilon = 10^{-4}$  due to  $\omega_{opt}$ , we plot the interface evolution in the permanent regime as shown in figure 4.2(a) and figure 4.2(c), where regular sized main drop formation is followed by the release of a satellite drop. For both the amplitudes, we see a distinct difference between the main and satellite drop radius.

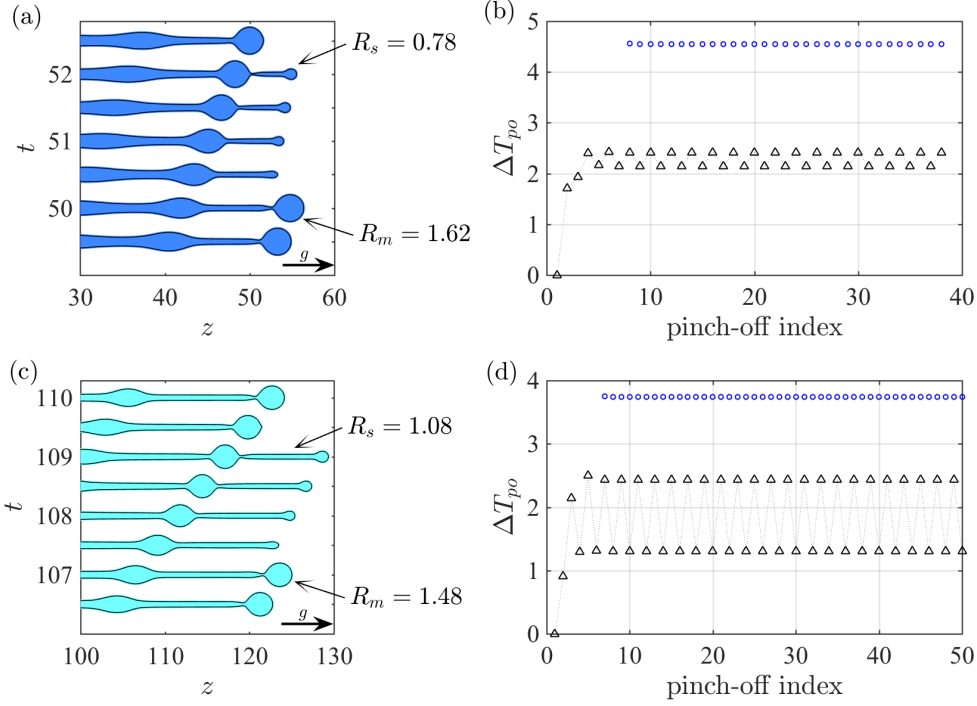


Figure 4.2 – Breakup characteristics for a gravity jet defined by  $Oh_{in} = 0.3$ ,  $Bo_{in} = 0.1$  and  $We_{in} = 1.75$  and perturbed with  $\omega_{opt}$ . Subplots (a) and (b) correspond to a forcing with  $\epsilon = 10^{-2}$  and  $\omega_{opt} = 1.38$ . Subplots (c) and (d) refer to a forcing with  $\epsilon = 10^{-4}$  and  $\omega_{opt} = 1.68$ . Subplots (a) and (c) elaborate the interface profile at the time of breakup with the existence of a satellite drop after the main drop is released. The main and satellite drop radius for both the cases have been highlighted. The axial and radial dimensions of (a) and (c) represent the same length scale. The breakup period  $\Delta T_{po}$  is represented in (b) and (d). The black triangle refers to the  $\Delta T_{po}$  between the consecutive drops and the blue circle represents the one between two consecutive main (or satellite) drops. The breakup frequency  $\omega_{po}$  is equal to 1.38 and 1.68 in (b) and (d) respectively.

The breakup period  $\Delta T_{po}$  resulting from the forcing imposed in figure 4.2a and 4.2c are plotted in figure 4.2b and 4.2d, respectively, where the black triangle represent the  $\Delta T_{po}$  obtained for two consecutive pinch-offs whereas the blue circles denote  $\Delta T_{po}$  obtained for two consecutive pinch-offs of the *same group*, that is to say between two consecutive main (or satellite) drops. From the figure we conclude that even though the breakup period is the same for the group of

main and satellite drops (as shown by blue circles) the time of formation of a satellite drop does not lie exactly midway between the time of formation of the main drops and vice versa. This results in obtaining two oscillating breakup periods (as shown by the black triangles). We further observe that the frequency of breakup ( $\omega_{po} = 2\pi/\Delta T_{po}$ ) obtained using the breakup period for consecutive main (or satellite) drops responds to the externally applied forcing at the jet inlet with  $\omega_{po} = 1.38$  and  $1.68$  for  $\epsilon = 10^{-2}$  and  $10^{-4}$ , respectively.

Finally, for the constant flow rate of the jet, the breakup period related to the consecutive pinchoff's is used for obtaining the drop radius for the satellite and main drops. We notice that at the optimal forcing frequency, the main drop radius  $R_m$  decreases from  $1.62$  to  $1.48$  dimensionless units as  $\epsilon$  reduces from  $10^{-2}$  to  $10^{-4}$ . On the contrary, the satellite drop radius  $R_s$  increases from  $0.78$  to  $1.08$  dimensionless units for  $\epsilon = 10^{-2}$  and  $\epsilon = 10^{-4}$  respectively. The longer intact jet length obtained for lower forcing amplitude  $\epsilon = 10^{-4}$  results in a larger downstream velocity close to the tip due to the presence of gravity. Eventually, it results in the formations of highly stretched satellite drops in comparison to the ones obtained for lower amplitude of  $\epsilon = 10^{-2}$  as seen in figure 4.2a and 4.2c.

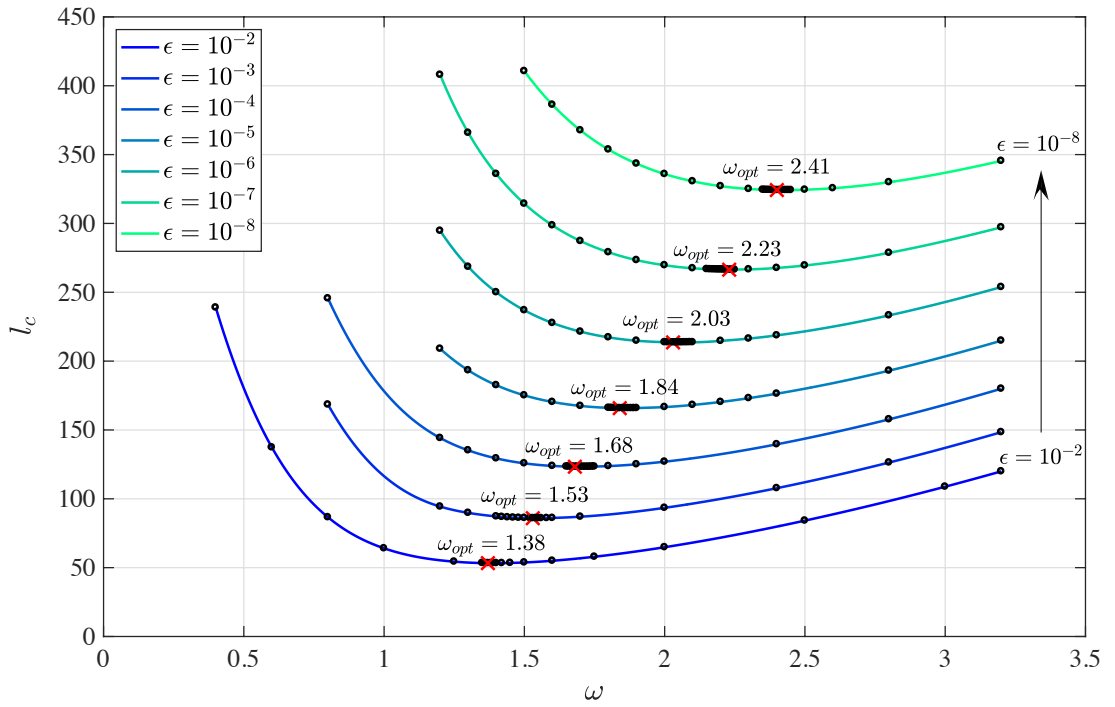


Figure 4.3 – The plot shows the breakup length  $l_c$  as a function of forcing frequency  $\omega$  for a gravity jet defined by  $Oh_{in} = 0.3$ ,  $Bo_{in} = 0.1$  and  $We_{in} = 1.75$ . Each curve is indicative of a fixed forcing amplitude  $\epsilon$ . For a fixed  $\epsilon$ , the optimal forcing frequency related to the shortest  $l_c$  is represented by a red cross. We observe that the optimal frequency increases as  $\epsilon$  decreases and does not appear to saturate even for lower amplitudes of  $10^{-8}$ . The black circles represent the data from numerical simulations.

## Chapter 4. Amplitude dependent preferred mode of an axisymmetric single phase gravity-driven falling viscous jet

---

We now return to the most salient feature observed in figure 4.1, where the optimal forcing frequency  $\omega_{opt}$  increased with a decrease in forcing amplitude. To explore if this effect existed for smaller amplitudes, we simulated the same system for different forcing amplitudes  $\epsilon = [10^{-2} - 10^{-8}]$ , and plotted the breakup length  $l_c$  as a function of the forcing frequency  $\omega$  as shown in figure 4.3, where the optimal forcing frequency for a fixed  $\epsilon$ , is marked with a red cross. The results show an increase in  $l_c$  and  $\omega_{opt}$  as  $\epsilon$  decreases. The increase in breakup length is obvious due to the decreasing destabilizing strength of the forcing amplitude. The increase in optimal forcing frequency, however, is the most interesting observation drawn from the numerical results, since it is expected to saturate for small enough forcing amplitudes. We believe that the increase in  $\omega_{opt}$  as  $\epsilon$  decreases from  $10^{-2}$  to  $10^{-8}$  is a consequence of the stretched base state due to gravity, which results in the downstream stretching of the perturbation wavelength initiated at the nozzle. As the forcing amplitude decreases, the stable jet length  $l_c$  increases and so does the stretching close to the jet tip. Thus to compensate for the larger stretching, the breakup potential of the forcing is sustained by increasing the forcing frequency.

To conclude, the numerical simulations confirm the dependence of the  $\omega_{opt}$  on the forcing amplitude, a factor generally neglected for linear stability analysis as long as  $\epsilon \ll 1$ . The trend also constitutes a major difference from a jet with no gravity effect ( $Bo_{in} = 0$ ), where  $\omega_{opt}$  is independent of  $\epsilon$  (refer Section 3.4.4 of Chapter 3, figure 3.8(a)). Finally, we confirm that the preferred-mode analysis carried out for the jet is solely due to the effect of external forcing. The tip of the jet does not induce any self-sustained breakups (for details refer Appendix 4.8.3).

### 4.4 Local stability analysis

The linear stability theory is applicable for small forcing amplitudes ( $\epsilon \ll 1$ ) and does not take into account its absolute value, a parameter that has already been shown in Section 4.3.2 to influence the optimal forcing frequency. Nevertheless, we proceed to analyse the stability of a gravity jet using the local stability tool where the dispersion relation for purely viscous jets ( $Bo_{in} = 0$ ) is used as a basis for obtaining the absolute/convective instability transition criteria in Section 4.4.1. The dispersion relation for parallel jets is suitably modified to include the spatial variation of the gravitationally stretched base flow and the spatial stability of the jet is performed in Section 4.4.2. Since the base state is spatially evolving, we extend our stability analysis using the WKBJ formulation in Section 4.4.3. The optimal forcing frequency deduced from the WKBJ analysis is in close proximity of the  $\omega_{opt}$  obtained from the global resolvent analysis which will be discussed in Section 4.5.2.

#### 4.4.1 Local stability analysis for spatially varying jets

The saddle point analysis applied on the local dispersion relation (3.14) for parallel jets, described in Section 3.3.2 of Chapter 3, results in obtaining the  $We_{crit}$ , the criteria that marks the transition from absolutely unstable flows to convectively unstable flows, as shown in figure

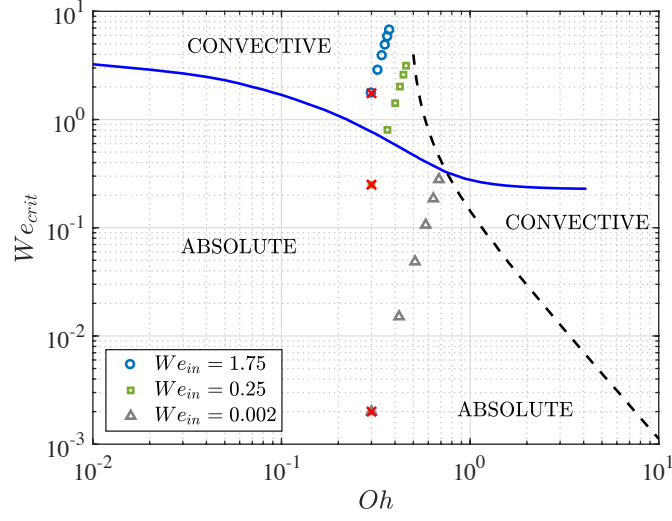


Figure 4.4 – The plot shows the absolute-convective transition (represented by full and dashed lines) for viscous jets ( $Bo_{in} = 0$ ). The local variation in  $Oh_z$  and  $We_z$  for three jets with different  $We_{in}$  (constant  $Oh_{in} = 0.3$ ,  $Bo_{in} = 0.1$ ,  $L = 50$ ) are plotted with markers where the red cross for each represents the inlet condition at  $z = 0$ . The distance between consecutive markers for the same jet represents an axial gap of 10 units.

4.4 with the full and dashed lines. Extending the formalism for parallel jets to spatially varying jets, we derive the dispersion relation for the coupled equations (4.1), governing the growth of small perturbations about the base state. Considering the normal mode expansion, the flow variables  $h(z, t)$  and  $u(z, t)$  are decomposed as:

$$h(z, t) = h_b(z) + \epsilon \hat{h}(z) e^{i(kz - \omega t)}, \quad (4.9a)$$

$$u(z, t) = u_b(z) + \epsilon \hat{u}(z) e^{i(kz - \omega t)}, \quad (4.9b)$$

where  $\epsilon \ll 1$ , with  $\hat{h}$  and  $\hat{u}$  as functions of  $z$ .  $k$  and  $\omega$  are respectively the dimensionless spatial wavenumber and the temporal frequency, which may both be complex. Similarly, for the variable representing the square of interface,  $a(z, t)$  is decomposed as,

$$a(z, t) = a_b + \epsilon \hat{a} e^{i(kz - \omega t)}, \quad (4.10)$$

where  $a_b = h_b^2$  and  $\hat{a} = 2h_b \hat{h}$ . Inserting the above expansion into equation (4.1), linearizing about  $(h_b, u_b)$ , and replacing  $h^2 \rightarrow a$ , will lead to a linearized system of equations which can be formulated as an eigenvalue problem with the eigenmodes represented by  $\hat{\mathbf{q}}(z) = [\hat{a}(z), \hat{u}(z)]$ .

In presence of gravity, the steady state solution is not homogeneous. To express the local stability of a gravity jet, we introduce the terms  $Oh_z$  and  $We_z$ , which are the local dimensionless

## Chapter 4. Amplitude dependent preferred mode of an axisymmetric single phase gravity-driven falling viscous jet

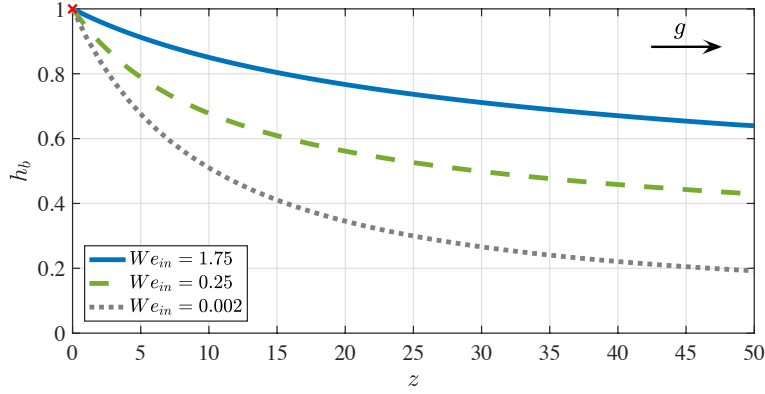


Figure 4.5 – The plot shows the stretching (or necking) close to the nozzle, of the base flow due to the presence of gravity for a jet with  $Oh_{in} = 0.3$ ,  $Bo_{in} = 0.1$  and three different  $We_{in}$ . Clearly, the effect of gravity is prominent for the jet with the smallest  $We_{in}$ .

numbers at an axial distance of  $z$  from the nozzle, expressed as,

$$Oh_z = Oh_{in} \sqrt{\frac{h_{b(0)}}{h_{b(z)}}}, \quad (4.11a)$$

$$We_z = h_{b(z)} u_{b(z)}^2. \quad (4.11b)$$

We then plot their values along the entire axial domain  $L$  above the absolute-convective transition curve in figure 4.4. The variation in local  $Oh_z$  and  $We_z$  along the jet defined within a domain size  $L = 50$ , for  $Oh_{in} = 0.3$  and  $Bo_{in} = 0.1$  and for three different inlet Weber numbers,  $We_{in} = [1.75, 0.25, 0.002]$  are represented by the markers in figure 4.4. The gap between consecutive markers is representative of an axial interval of 10 units. In each case, the red cross represents the inlet of the jet whose base state is shown in figure 4.5. We remind the reader that the case with  $We_{in} = 1.75$  corresponds to the jet whose numerical analysis has been presented in Section 4.3.2.

For  $We_{in} = 1.75$  and  $0.002$ , the entire jet exists in the convective and absolute region, respectively. For intermediate  $We_{in} = 0.25$ , there exists a small pocket of absolute instability close to the nozzle, after which the local parameters modify along the downstream direction resulting in the transfer of the jet into a convectively unstable regime.

The parameter  $Bo_{in}$  indirectly decides the instability of the jet by affecting the base state solution. Since the  $Bo_{in}$  is constant, its relative strength for the stretching of the jet interface depends on the corresponding value of  $We_{in}$ , with the effect being more pronounced for lower values of  $We_{in}$  as shown in figure 4.5.

Next, for the spatially varying base flow, we perform the stability analysis in a local framework wherein the system is considered uniform at each axial location. The modified dispersion relation, which now includes the spatially varying base flow solution and eigenmode  $\hat{\mathbf{q}}(z)$  is



given by,

$$\omega^2 - 2u_b(z)\omega k + \left( \frac{1}{2\sqrt{a_b(z)}} + u_b(z)^2 + 3iOh_z\omega \right) k^2 - 3iOh_z u_b(z) k^3 - \frac{\sqrt{a_b(z)}}{2} k^4 = 0. \quad (4.12)$$

For the convectively unstable jet ( $We_{in} = 1.75$ ), the solution of the dispersion relation (4.12) for a given range of complex  $\omega$  (with  $\omega_i > 0$ ) results in obtaining four spatial branches which are expressed as the roots of the fourth-order polynomial (4.12). The solution consists of upstream (referred as  $k^-$ ) and downstream (denoted by  $k^+$ ) propagating branches. To identify these branches, we successively add an artificial  $\omega_i$  so as to separate the branches into the upper  $k_i > 0$  and lower  $k_i < 0$  planes. For a downstream propagating  $k^+$  branch damped in space, the associated  $k_i > 0$ . Based on this analysis, we obtain two downstream and two upstream propagating waves for the dispersion relation (4.12). The  $k$  branches for the localized dimensionless numbers at the nozzle inlet ( $z = 0$ ) and domain end ( $z = 50$ ) are shown in figure 4.6(a) and 4.6(b) respectively with the two  $k^+$  branches denoted by the black and green colour and the two  $k^-$  waves by the red and blue colour. The presence of two  $k^+$  and  $k^-$  waves is not specific to the present jet characteristics but rather exists for all the tested cases in the range of  $Oh_{in} = [0.1 \ 10]$ ,  $We_{in} = [0.8 \ 10]$ ,  $Bo_{in} = [0 \ 1]$  for  $L = 50$ .

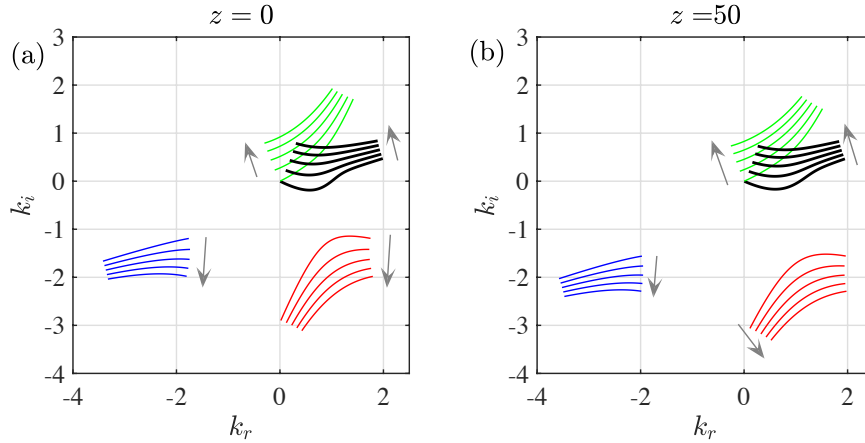


Figure 4.6 – The four  $k$  branches shown in four different colours, obtained as a solution of the dispersion relation for complex  $\omega$  and for increasing values of  $\omega_i$  for a jet defined by  $Oh_{in} = 0.3$ ,  $Bo_{in} = 0.1$  and  $We_{in} = 1.75$ , at (a) the nozzle outlet  $z = 0$  and (b) the jet exit  $z = L = 50$ . The arrows represent the direction of movement of the waves for increasing values of  $\omega_i$ .

#### 4.4.2 Spatial stability analysis

Since the base flow with  $We_{in} = 1.75$  exists in the convectively unstable regime (see figure 4.4), we then proceed to analyse the base flow using the spatial stability framework, wherein the spatial growth rate for the imposed real frequency determines the flow stability.

Given the polynomial nature of the dispersion relation, there are four spatial waves. We have

## Chapter 4. Amplitude dependent preferred mode of an axisymmetric single phase gravity-driven falling viscous jet

---

verified that two of them are  $k^+$ , downstream propagating, waves while the remaining two are  $k^-$ , upstream propagating, waves (see figure 4.6). For a more detailed account on the nature of spatial waves in capillary jets, depending on the flow model, the reader is referred to Guerrero *et al.* (2016).

Among the four  $k$  waves, only one of the  $k^+$  waves is seen to be amplified. To obtain this dominant  $k$  wave we plot the spatial growth rate  $-k_i$  as a function of the real forcing frequency  $\omega$  at nozzle inlet. As shown in figure 4.7(a), among the four  $k$  branches, only the branch denoted in black has a growth rate which is positive in its propagation direction. We chose the  $k$  wave corresponding to this amplified  $k^+$  branch as the dominant wavenumber for all frequencies. The relevant  $k(z)$  branches are then obtained for different  $z$  along the jet as shown in figure 4.7(b) and 4.7(d) by imposing the spatially dependent base flow and  $Oh_z$  in equation (4.12). figure 4.7(b) shows that the most amplified frequency shifts to higher values as one travels away from the nozzle. The associated eigenmode  $\hat{\mathbf{q}}(z)$  also changes as one progresses downstream. Imposing  $\|\hat{\mathbf{q}}\| = 1$  at every axial location as the normalisation condition, together with  $\hat{a}_i = 0$  to set the phase, we see in figure 4.7(c) the evolution of the locus of the real and imaginary parts of the remaining degrees of freedom  $\hat{u}_r$  and  $\hat{u}_i$  as  $z$  increases (remember that  $\hat{u}_r^2 + \hat{u}_i^2 + \hat{a}_r^2 = 1$ ). While this locus is difficult to interpret from a physical point of view, it highlights the change of the eigenmode along the jet axis in such nonparallel gravity driven jets.

The knowledge of the dominant  $k$  wave obtained for a given  $\omega$  allows us to evaluate the response due to different forcing frequencies imposed on the base flow, conveniently expressed as

$$\mathbf{q}'(z, t) = \hat{\mathbf{q}}(\omega, z) \exp \left[ i \left( \int_0^z k(\omega, z') dz' - \omega t \right) \right]. \quad (4.13)$$

The overall response norm defined in a domain size  $L$  is then given as,

$$G_s(\omega, L) = \left\| \int_0^L \hat{\mathbf{q}}(\omega, z) \exp \left[ i \left( \int_0^z k(\omega, z') dz' - \omega t \right) \right] \right\|. \quad (4.14)$$

This allows us to determine the optimal forcing frequency  $\omega_{opt}$  which results in the maximal gain,

$$G_{s,max}(L) = \max_{\omega} [G_s(\omega, L)], \quad (4.15)$$

attained at a frequency  $\omega_{opt}$ . Figure 4.8 (in dotted lines) shows the spatial gain as a function of forcing frequency for two arbitrary domain sizes  $L = 50$  and  $60$ . We notice that  $\omega_{opt}$  shifts from 1.16 to 1.21 as we increase the domain size.

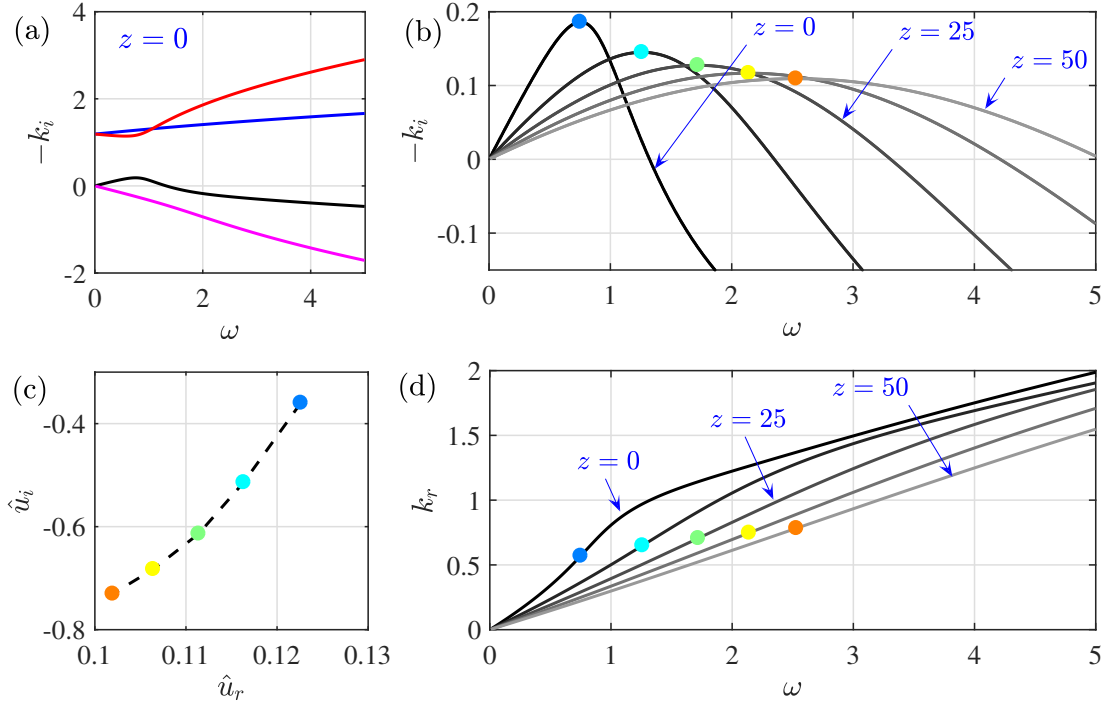


Figure 4.7 – (a) Growth rate ( $-k_i$ ) for a jet defined by  $Oh_{in} = 0.3$ ,  $Bo_{in} = 0.1$  and  $We_{in} = 1.75$ , plotted as a function of the frequency for the four  $k$  branches at the nozzle exit with the dominant  $k$  branch represented in black. (b) Represents the growth rate corresponding to the dominant  $k$  branch at different axial locations; (inset) shows the variation in dominant eigenmode  $\hat{u}$  moving downstream away from the nozzle.

#### 4.4.3 Weakly nonparallel stability analysis (WKBJ)

In order to further incorporate the non-parallelism of the base flow, we extend our spatial analysis by including the WKBJ formalism introduced by Gaster *et al.* (1985) and Huerre & Rossi (1998) for a spatial mixing layer and applied by Viola *et al.* (2016) for swirling flows.

In this framework, we introduce a slow streamwise scale  $Z$ , which relates to the fast scale  $z$  as  $Z = \eta z$ , where  $\eta \ll 1$  is a measure of the weak non-parallelism. The new base flow depends only on  $Z$  and the global response to inlet forcing takes the modulated wave form:

$$\mathbf{q}'(Z, t) \sim A(Z) \hat{\mathbf{q}}(Z) \exp \left[ i \left( \frac{1}{\eta} \int_0^Z k(\omega, Z') dZ' - \omega t \right) \right], \quad (4.16)$$

where  $\hat{\mathbf{q}}(\omega, Z)$  is the local eigenmode and  $k(\omega, Z)$  the local wavenumber at section  $Z$  and a fixed forcing frequency  $\omega$ . The amplitude function  $A(Z)$  acts as an envelope, smoothly connecting the progressive slices of the parallel spatial analysis. At each axial location, we impose  $\hat{\mathbf{q}}^H \cdot \hat{\mathbf{q}} = 1$ , where  $(\cdot)^H$  is the transconjugate. As described in Appendix 4.8.7, imposing an asymptotic expansion and a compatibility condition, the local stability analysis is retrieved

## Chapter 4. Amplitude dependent preferred mode of an axisymmetric single phase gravity-driven falling viscous jet

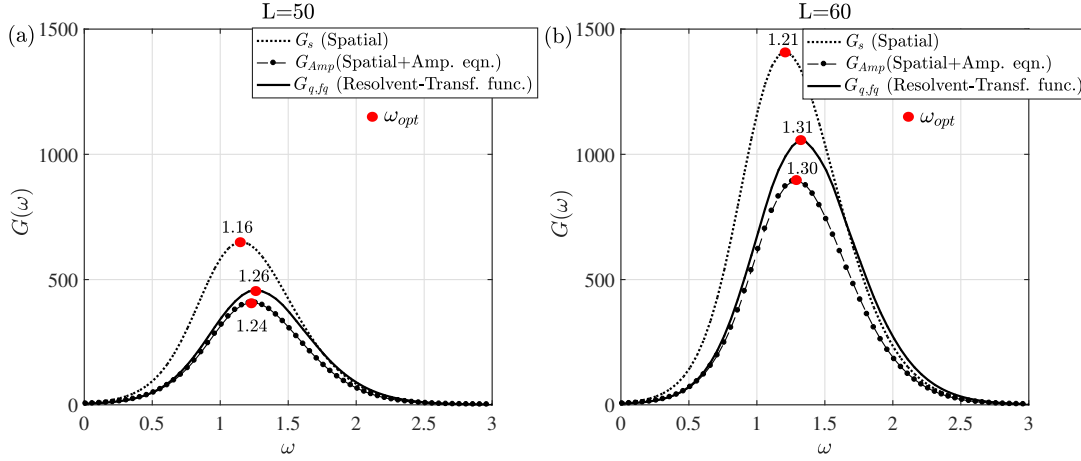


Figure 4.8 – Comparison of the total gain  $G$  at different frequencies  $\omega$  from the resolvent analysis and the spatial analysis for domain sizes (a)  $L = 50$  and (b)  $L = 60$  and for the jet defined by  $Oh_{in} = 0.3$ ,  $Bo_{in} = 0.1$  and  $We_{in} = 1.75$ . The resolvent gain is computed by using the transfer function and the direct mode obtained from the spatial analysis. All the theories predict a shift in  $\omega_{opt}$  as  $L$  is increased.

at zeroth-order in  $\eta$ , while at first order in  $\eta$  the following amplitude equation is obtained:

$$M(Z) \frac{dA(Z)}{dZ} + N(Z) A(Z) = 0, \quad (4.17)$$

whose solution is given as

$$A(Z) = A_0 \exp \left( - \int_0^Z \frac{N(Z')}{M(Z')} dZ' \right). \quad (4.18)$$

The functions  $M(Z)$  and  $N(Z)$  are defined in Appendix 4.8.7. The amplitude at the inlet is set as,  $A(0) = 1$  which simplifies the forcing expression at the inlet to  $\mathbf{q}'(0) = \hat{\mathbf{q}}(0)$ . Finally we express the total spatial gain at first order as:

$$G_{Amp}^2(\omega, L) = \frac{\int_0^Z A^H(z') A(z') \left( \hat{\mathbf{q}}^H(z') \cdot \hat{\mathbf{q}}(z') \right) \left( e^{\int_0^{z'} -2k_i(z'') dz''} \right) dz'}{\hat{\mathbf{q}}^H(0) \cdot \hat{\mathbf{q}}(0)}. \quad (4.19)$$

The global gain of the response due to the forcing frequency, for fixed domain sizes, is reported in figure 4.8, where  $\omega_{opt} = 1.24$  and  $1.30$  for  $L = 50$  and  $60$ , respectively. The WKBJ approximation greatly modifies the gain and shifts the optimal forcing frequency predicted from the spatial analysis which excludes the amplitude equation. However, to truly assess the validity of the amplitude equation one needs to analyse the base flow in the global framework using the resolvent analysis, which will be the focus of our discussion in the next section.

## 4.5 Global stability analysis

Unlike the local stability analysis, the global stability framework allows taking into consideration the axially varying base state due to the stretching effect of gravity. In this framework, we first evaluate the inherent global stability of the base flow in Section 4.5.1. We next perform a resolvent analysis in Section 4.5.2 on the globally stable base flow to evaluate its response in presence of a given perturbation.

### 4.5.1 Global stability

Since the base flow is spatially varying, the perturbations imposed on it are no longer sought in the form of Fourier modes but are expanded in the form:

$$h(z, t) = h_b(z) + \epsilon \tilde{h}(z) e^{\lambda t}, \quad (4.20a)$$

$$u(z, t) = u_b(z) + \epsilon \tilde{u}(z) e^{\lambda t}, \quad (4.20b)$$

where  $\epsilon \ll 1$  and  $\tilde{h}(z), \tilde{u}(z)$  are the global stability modes related to the complex growth-rate  $\lambda$ . Substituting expressions (4.20) in equations (4.1) and linearising around the base state  $(h_b, u_b)$  results in the general eigenvalue problem of the form

$$\lambda \Pi \begin{bmatrix} \tilde{h} \\ \tilde{u} \end{bmatrix} = M \begin{bmatrix} \tilde{h} \\ \tilde{u} \end{bmatrix}, \quad (4.21)$$

with boundary conditions  $\tilde{h}(0, t) = 0$  and  $\tilde{u}(0, t) = 0$ . We do not impose any boundary conditions at the end of domain  $z = L$  since it is not possible *a priori* to distinguish between amplifying perturbations and transient disturbances. This will occur in any problem that involves an ‘active system’ and can support amplifying waves (Briggs (1964) and Leib & Goldstein (1986)). The global stability analysis presented in Rubio-Rubio *et al.* (2013) does not impose any boundary conditions for  $z = L$  since the numerical method naturally converges to the most regular asymptotic solution of the base flow equation (4.5) and eigenvalue problem (4.21), as  $z \rightarrow \infty$ . Nonetheless, we checked that the dominant eigenvalue and eigenmode were unaffected by the presence of Neumann boundary condition at  $z = L$ , namely  $\frac{d\tilde{u}}{dz}(L) = 0$ .

The complete expressions for the linear operator  $M$  can be found in Appendix 4.8.5. The solution of equation (4.21) results into a set of eigenmodes  $(\tilde{h}, \tilde{u})$ , whose growth rate and frequency are given by the real ( $\lambda_r$ ) and imaginary ( $\lambda_i$ ) parts of the related eigenvalue. A base state is stable to self induced oscillations provided  $\lambda_r < 0$ .

To solve the eigenvalue problem, the Chebyshev collocation method is used for obtaining the differential operators. Derivatives with respect to  $z$  are calculated using the standard Chebyshev differentiation matrices. Denoting the non dimensional physical domain as  $L$ , the domain is mapped into the interval  $-1 \leq y \leq 1$  by using the transformation  $z = [(L/2) \times (y + 1)]$ . A validation of the global scheme with the results of Rubio-Rubio *et al.* (2013) is presented in

## Chapter 4. Amplitude dependent preferred mode of an axisymmetric single phase gravity-driven falling viscous jet

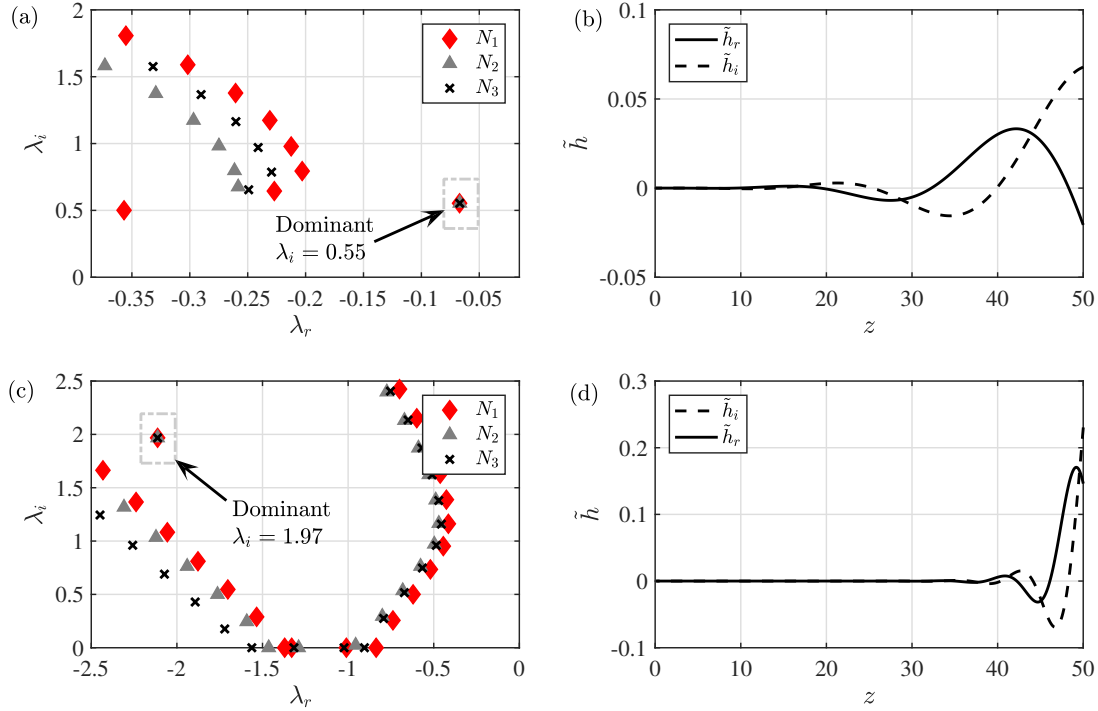


Figure 4.9 – (a),(c) Eigenvalue spectrum  $\lambda$  obtained for three different nodes  $N_1 = 100$ ,  $N_2 = 125$  and  $N_3 = 150$  and (b),(d) the real and imaginary parts of the leading eigenfunction  $\tilde{h}$ , for  $Oh_{in} = 0.3$ ,  $Bo_{in} = 0.1$ ,  $L = 50$  and evaluated for two different values of inlet Weber. (a),(b) Corresponds to  $We_{in} = 0.25$  where the leading eigenvalue has an eigenfrequency  $\lambda_i = 0.55$  (c),(d) Corresponds to  $We_{in} = 1.75$  with  $\lambda_i = 1.97$ . For both the Weber numbers, the entire spectrum has a  $\lambda_r < 0$  rendering the system to be globally stable.

### Appendix 4.8.6.

For the three cases of jets described in figure 4.5, with  $L = 50$ ,  $Oh_{in} = 0.3$ ,  $Bo_{in} = 0.1$  and three different values of  $We_{in}$  a global stability analysis is carried out using different resolutions ( $N_1 = 100$ ,  $N_2 = 125$ ,  $N_3 = 150$ ) to exclude spurious eigenvalues. The eigenvalue spectrum for  $We_{in} = 0.25$ ,  $1.75$  and  $0.002$ , are represented in figure 4.9(a), 4.9(c) and 4.10 respectively. The dominant eigenvalues have  $\lambda_r < 0$  (for  $We_{in} = 0.25$  and  $1.75$ ) and  $\lambda_r > 0$  (for  $We_{in} = 0.0025$ ) thus representing globally stable and unstable jets, respectively. Note however, that the local stability analysis of the globally stable flow with  $We_{in} = 0.25$  predicts the jet to have a small ‘pocket’ of absolute instability close to the nozzle.

Eigenmodes corresponding to the dominant eigenvalues are presented in the accompanying figure. We note that the dominant eigenmode, as represented in 4.9(b), 4.9(d) and 4.10, has an amplitude that grows downstream. Figure 4.10(b) also shows that the wavelength grows downstream. This is a consequence of the fluid acceleration caused by gravity (Tomotika, 1936 and Rubio-Rubio *et al.*, 2013) and can be interpreted from figure 4.7(d) where  $k_r$  is seen to decrease with increasing  $z$  for a fixed forcing frequency  $\omega$ . Further we see that close to

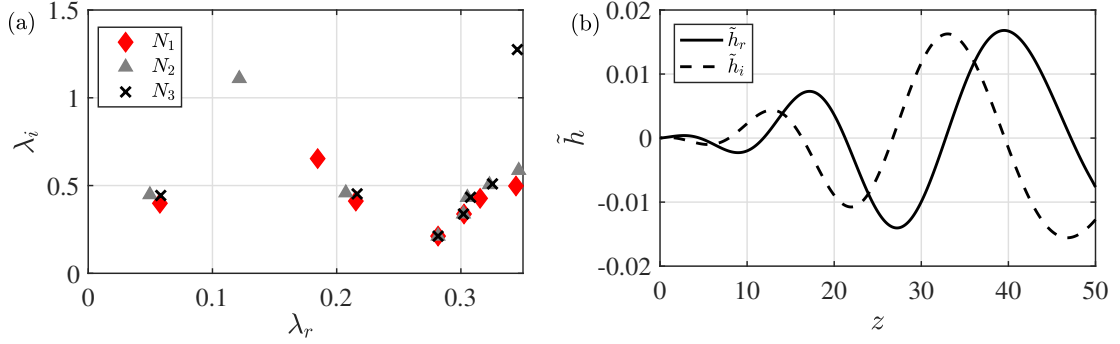


Figure 4.10 – (a) Eigenvalue spectrum  $\lambda$  obtained for three different nodes  $N_1 = 100$ ,  $N_2 = 125$  and  $N_3 = 150$  and (b) the real and imaginary parts of the leading eigenfunction  $\tilde{h}$ , for  $Oh_{in} = 0.3$ ,  $Bo_{in} = 0.1$ ,  $We_{in} = 0.002$  and  $L = 50$ . We note that the leading eigenvalue has a positive growth rate  $\lambda_r > 0$  thus rendering the system to be globally unstable.

the outlet, the eigenmodes evolve at a much larger length scale compared to that related to the variations in steady state jet, thus strengthening the argument that weakly non parallel stability analysis should be used with care for predicting the global stability of the gravity jet.

#### 4.5.2 Global resolvent

Analysing the linear response of the base state for an external harmonic forcing at frequency  $\omega$  is only well defined if the linear operator is stable or in other words the base state is stable, where the imposed perturbations are allowed to travel downstream before spreading in the entire domain under consideration. Else the algebraically amplified solution is superimposed by the unforced naturally growing exponential mode. Keeping this in mind, in this section we present the resolvent analysis for the stable gravity jet ( $We_{in} = 1.75$ ). To compare our results with the nonlinear simulations of Section 4.3, we impose similar inlet forcing conditions and approximate the gain predicted by the resolvent analysis in terms of the forcing amplitude.

##### Problem formulation

The external force  $f$  is modelled as an incoming perturbation in the form of an unsteady upstream boundary condition of the 1D Eggers & Dupont equation (4.1). The resulting linearised equation is represented as,

$$\mathbb{I}\partial_t[\mathbf{s}] = M[\mathbf{s}] + B_f f, \quad (4.22)$$

where as in the eigenvalue problem (4.21)  $\mathbf{s} = [h, u]$ ,  $\mathbb{I}$  represents the identity matrix,  $M$  the linear operator (detailed in Appendix 4.8.5) and  $B_f$  the operator which expresses the effect of the inlet forcing onto the bulk equation. Considering a time-harmonic forcing,  $f = \tilde{f} \exp(-i\omega t)$ , results in an asymptotic flow response  $\mathbf{s} = \tilde{\mathbf{s}} \exp(-i\omega t)$  at the same frequency. Here  $\tilde{\mathbf{s}} = [\tilde{h}, \tilde{u}]$ .

## Chapter 4. Amplitude dependent preferred mode of an axisymmetric single phase gravity-driven falling viscous jet

---

Imposing these transformations in (4.22) we obtain,

$$-(M + i\omega\mathbb{I})\tilde{\mathbf{s}} = B_f\tilde{\mathbf{f}}. \quad (4.23)$$

Equation (4.23) is subjected to two inlet and two outlet boundary conditions. The solution forced only in  $u$  at the nozzle satisfies  $\tilde{h} = 0$  and  $\tilde{u} = 1$ , while for the one that is forced in both  $h$  and  $u$ ,  $\tilde{h}$  and  $\tilde{u}$  can be chosen arbitrarily. We use the former when comparing the results with the nonlinear simulations (where the forcing was applied using the form (4.8)) whereas the latter when comparing to the spatial and WKB analysis of Section 4.4.2 and 4.4.3.

Based on the results of the local and global analysis at  $We_{in} = 1.75$ , the convective instability of the flow ensures that at the outlet any existing  $k^+$  branch, obtained from the spatial analysis, will be transmitted downstream. Since the relevant  $k^+(\omega, L)$  branch for a given  $\omega$  and at  $z = L$  can be obtained from the local analysis of Section 4.4.2, we impose for the solution of the equation (4.23) at  $z = L$  the spatial response, specifically,  $\tilde{h}(L) = \hat{h}\exp(ikL)$  and  $\tilde{u}(L) = \hat{u}\exp(ikL)$ ,  $k$  being the unique root of the dispersion relation corresponding to a downstream amplified wavenumber. It should be noted that for active systems, such as the jet falling under the influence of gravity, it is not possible *a priori* to impose unique boundary conditions at the outlet. Thus, substitution of the resolvent response by the spatial response at the outlet should be treated as an approach to close the differential problem of equation (4.23) rather than depicting the physical boundary conditions. To ensure that these boundary conditions do not affect the final response over a given domain size  $L$ , we impose them for a domain size  $L' > L$ , such that the response for all the frequencies over  $L$  is independent of the imposed boundary condition.

Finally we express the magnitude of the response  $\tilde{\mathbf{s}}$  due to the externally applied forcing in terms of the gain  $G$ , with the maximum gain expressed as,

$$G_{max}^2(L) = \max_{\omega} \frac{\|\tilde{\mathbf{s}}\|^2}{\|\tilde{\mathbf{f}}\|^2} = \max_{\omega} \frac{\|(M + i\omega\mathbb{I})^{-1}B_f\tilde{\mathbf{f}}\|^2}{\|\tilde{\mathbf{f}}\|^2}, \quad (4.24)$$

attained at  $\omega_{opt}$ . To measure the amplitude of the response and the forcing, we define  $Q$  and  $Q_f$  as the weight matrices of the discretised energy norm ( $\|\tilde{\mathbf{s}}\|^2 = \mathbf{s}^\dagger Q\mathbf{s}$ ) and the forcing norm ( $\|\tilde{\mathbf{f}}\|^2 = \mathbf{f}^\dagger Q_f\mathbf{f}$ ), respectively, obtained for the Chebyshev space on the physical domain  $L$  which is mapped into the interval  $-1 \leq y \leq 1$  by using the transformation  $z = [(L/2) \times (y + 1)]$ .  $Q_f$  is a  $2N \times 2N$  matrix enabling us to distinguish forcing on  $u$  only or on both components  $u$  and  $h$ . Following the optimization method using singular value decomposition (SVD) described in Marquet & Sipp (2010) and Garnaud *et al.* (2013), we then express the optimal gain using the following eigenvalue problem,

$$Q_f^{-1}B_f^\dagger(M + i\omega\mathbb{I})^{-1\dagger}Q^\dagger(M + i\omega\mathbb{I})^{-1}B_f\tilde{\mathbf{f}} = \lambda\tilde{\mathbf{f}}, \quad (4.25)$$

whose leading eigenvalue solution  $\lambda$  gives  $G_{max}^2$  and the associated eigenmode solution  $\tilde{\mathbf{f}}$  yields the optimal normalised forcing amplitude in  $(h, u)$  to be applied at the inlet.



Since the linear analysis is based on small perturbations, the exact amplitude of the perturbation is unaccounted for in the expression (4.24). For the resolvent analysis we then define  $G_{h,fu}$  as the gain in  $h$  from a solution forced only in  $u$  and  $G_{q,fq}$  as the gain in  $q$  for a solution forced in  $q$ , where  $q = [a, u]$ . The two expressions for the gain:  $G_{h,fu}$  and  $G_{q,fq}$  are formulated to replicate the forcing and gain definitions in the nonlinear simulations (Section 4.3) and the spatial analysis (Section 4.4.2 and 4.4.3), respectively.

Looking for the gain in  $G_{q,fq}$  requires the inclusion of additional operators  $P$  and  $H$  which express  $q$  in terms of  $s$ , and are given by,

$$\tilde{q} = P\tilde{s}, \quad (4.26a)$$

$$\tilde{f}_q = H\tilde{f}. \quad (4.26b)$$

The operator  $H$  modifies the imposed boundary conditions in terms of  $\tilde{a}$ , whereas the operator  $P$  adequately expresses the response in  $\tilde{a}$  in terms of  $\tilde{h}$  such that  $\tilde{a} = 2h_b\tilde{h}$ . Additionally, to have an explicit comparison with the spatial analysis, we apply a forcing at inlet which is obtained as the eigenmode solution of the spatial problem in Section 4.4.2. Thus,

$$\tilde{f}_q = \hat{\mathbf{q}}(z = 0). \quad (4.27)$$

The gain for the imposed forcing is then obtained as,

$$G_{q,fq}^2(\omega) = \frac{\|\tilde{q}\|^2}{\|\tilde{f}_q\|^2} = \frac{\|P(M + i\omega\mathbb{I})^{-1}B_f H^{-1}\tilde{f}_q\|^2}{\|\tilde{f}_q\|^2}. \quad (4.28)$$

Note however that even though this formalism allows a direct comparison with the spatial analysis, the gain  $G_{q,fq}(\omega)$  does not represent the maximum optimal gain since we do not impose the optimisation of the inlet forcing vector using an SVD formalism as was done in (4.25). Figure 4.11 demonstrates the difference between the gain and  $\omega_{opt}$  computed using the direct mode from spatial analysis (in black) and through an optimisation problem which solves for the optimal mode (in blue). Indeed the resolvent gain based on the optimised mode is much larger in magnitude.

### Results: Comparison with spatial stability analysis

To replicate the type of forcing and the expression of gain used in the spatial analysis in Section 4.4.2 and 4.4.3, we impose the eigenmode solution at the nozzle exit obtained from the spatial analysis as the forcing vector in the resolvent analysis. The resulting gain  $G_{q,fq}$  for two different fixed domain sizes  $L = 50$  and  $L = 60$  are shown in Fig. 4.8. We observe from the figure that the inclusion of the amplitude equation in evaluating the spatial response by far improves the estimation of the true gain obtained from the resolvent analysis. Moreover the predicted  $\omega_{opt}$  producing the largest  $G_{q,fq}$  from the WKBJ analysis is in close agreement with that of the resolvent analysis. The response norm obtained using the different approaches agrees

## Chapter 4. Amplitude dependent preferred mode of an axisymmetric single phase gravity-driven falling viscous jet

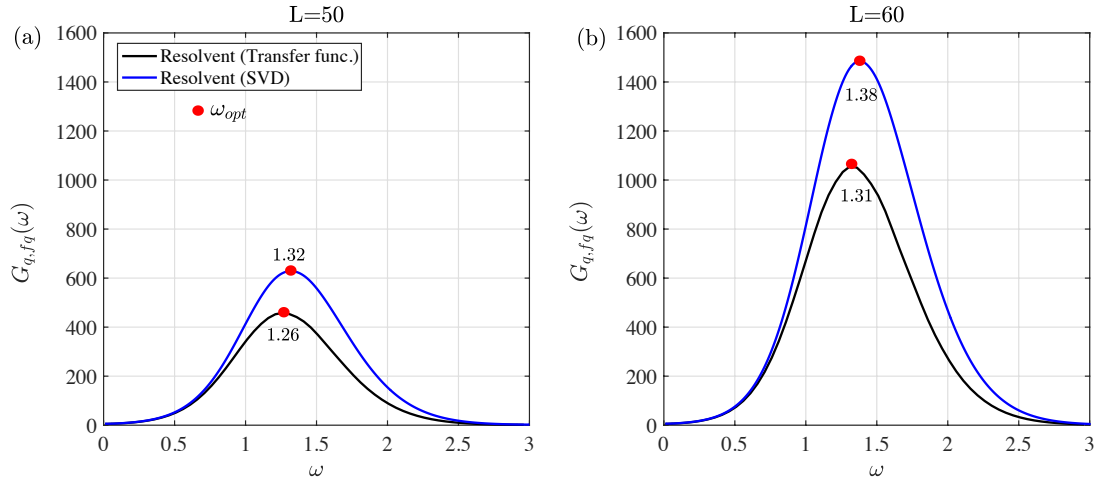


Figure 4.11 – Comparison of the total gain at different frequencies from the resolvent analysis for domain sizes (a)  $L = 50$  and (b)  $L = 60$  and for the jet defined by  $Oh_{in} = 0.3$ ,  $Bo_{in} = 0.1$  and  $We_{in} = 1.75$ . The gain computed by applying the transfer function on the direct eigenmode from the spatial analysis is shown in black and the maximal optimal gain computed through the singular value decomposition analysis is shown in blue.

qualitatively (see Fig. 4.21). Its non-monotonic behaviour at  $\omega = 1.5$  (see Fig. 4.21(c-d)) is well captured and is in accordance with the work presented in Lizzi (2016). However, the difference in gain between the three methods originates as a result of the quantitative disparity in the response obtained at different frequencies. The divergence between the spatial and resolvent analysis is due to the stretching effect of gravity on the base flow. For a parallel base flow, the results obtained from both the methods are found to be identical (as shown in Appendix 4.8.4, Fig. 4.20).

### Results: Comparison with nonlinear simulations

We compare the resolvent analysis with the nonlinear simulations of Section 4.3.2. Classically, the optimal forcing frequency  $\omega_{opt}$  resulting in the maximum gain, can be deduced by plotting the gain  $G_{h,fu}$  as a function of  $\omega$  for a fixed domain size  $L$ . For capillary jets however, the domain size over which the perturbation grows cannot be fixed *a priori*. It is merely an outcome of the analysis which should compare well with the value of  $l_c$  measured in the nonlinear simulations.

In order to circumvent this lack of consistency and in absence of the knowledge of  $l_c$ , we first plot  $G_{h,fu}$  as a function of increasing domain sizes  $L$  and for fixed  $\omega$  as shown in figure 4.12(a) where the gain  $G_{h,fu}(\omega, L)$  is computed for  $\omega = [1 - 2.5]$  with  $\Delta\omega = 0.01$  and for  $L = [10 - 240]$  with  $\Delta L = 10$ . This results in a bundle of constant frequency curves, intersecting each other at different locations in  $L$ . In figure 4.12(a) we now define the dominant frequency at a given  $L$  as the frequency with the maximum gain at  $L$ . A close examination reveals that there is

a continuous transition in the dominant frequency as one moves along increasing domain sizes. This is shown in figure 4.12(b) where for clarity we plot only the envelope  $G_{opt}(L)$  of the dominant frequency for all values of  $L$ .  $G_{opt}(L)$  is attained for  $\omega_{opt}(L)$ .

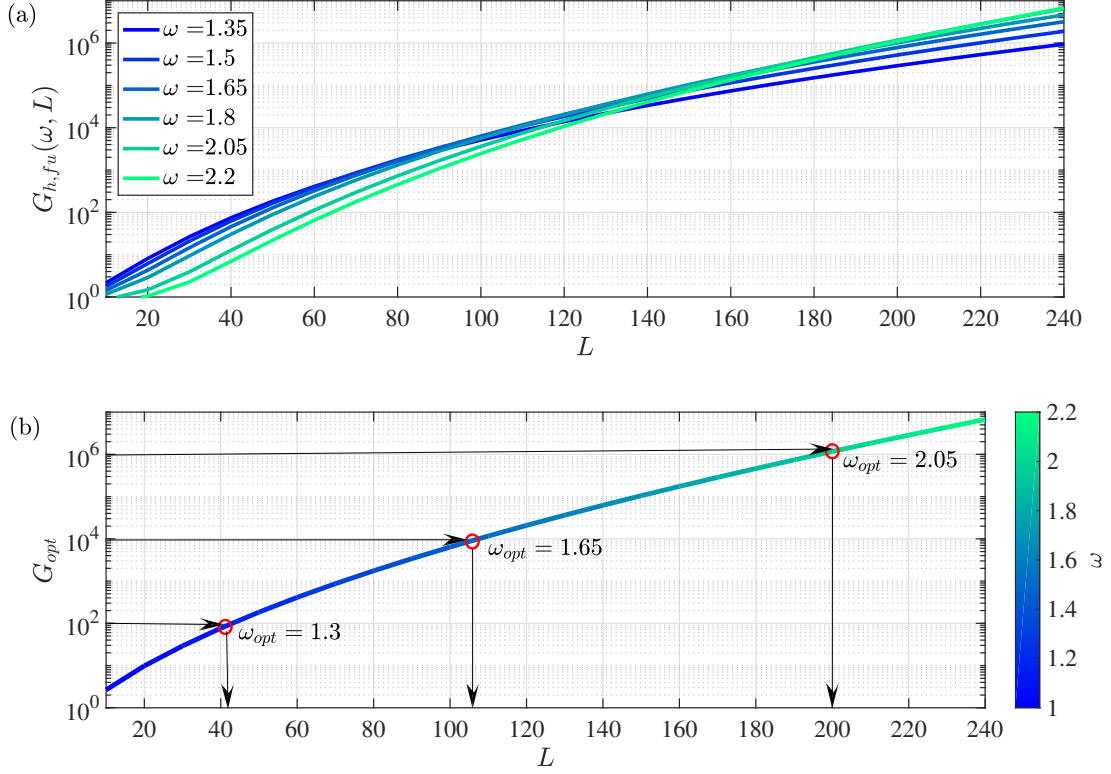


Figure 4.12 – (a) Resolvent gain computed for  $\tilde{h}$  with a forcing applied only in  $u$  for different values of domain sizes for a jet defined by  $Oh_{in} = 0.3$ ,  $Bo_{in} = 0.1$  and  $We_{in} = 1.75$ . Each curve is representative of a constant frequency. (b) The dominant frequency envelope as a function of the domain size  $L$ . The gain represented by  $10^2$ ,  $10^4$  and  $10^6$  is related to forcing amplitudes  $\epsilon = 10^{-2}$ ,  $10^{-4}$  and  $10^{-6}$  respectively. A horizontal projection from the respective gain on the frequency envelope yields the  $\omega_{opt}$  and a vertical projection from the  $\omega_{opt}$  on  $L$  determines the breakup length  $l_c$ .

As discussed previously,  $L$  represents the breakup location along the jet where the nonlinear effects appear. Broadly speaking, nonlinearity enters the system when a small perturbation  $\epsilon$  gives rise to a response of the order of 1, which suggests to approximate  $l_c$  by the value of  $L$  at which

$$G_{opt}(l_c) \approx \frac{1}{\epsilon}. \quad (4.29)$$

In other words, the gain at the breakup location  $L = l_c$  should be equal to  $1/\epsilon$ . Using equation (4.29), we locate the gain in figure 4.12(b) for different forcing amplitudes  $\epsilon = [10^{-2} - 10^{-6}]$ . At the given value of  $G_{h,f_u}$ , a horizontal projection on the dominant frequency envelope will then decide the optimal forcing frequency for the given  $\epsilon$ . Finally, a vertical projection on  $L$  from

## Chapter 4. Amplitude dependent preferred mode of an axisymmetric single phase gravity-driven falling viscous jet

the intersection point on the dominant frequency envelope will provide the relevant breakup length  $l_c$  for the forcing amplitude  $\epsilon$ . Extracting the results from figure 4.12(b), we compare the optimal forcing frequency and the breakup length for different  $\epsilon$  with the nonlinear solutions of Section 4.3.2 in figure 4.13. The close agreement between the two approaches shows the strength of the resolvent analysis in predicting the  $\omega_{opt}$  and  $l_c$  especially without any prior information from the nonlinear simulations. In figure 4.13 the small difference in values in the two methods can likely be attributed to *ad-hoc* definition of the required threshold for nonlinear effects to kick in and breakup to occur.

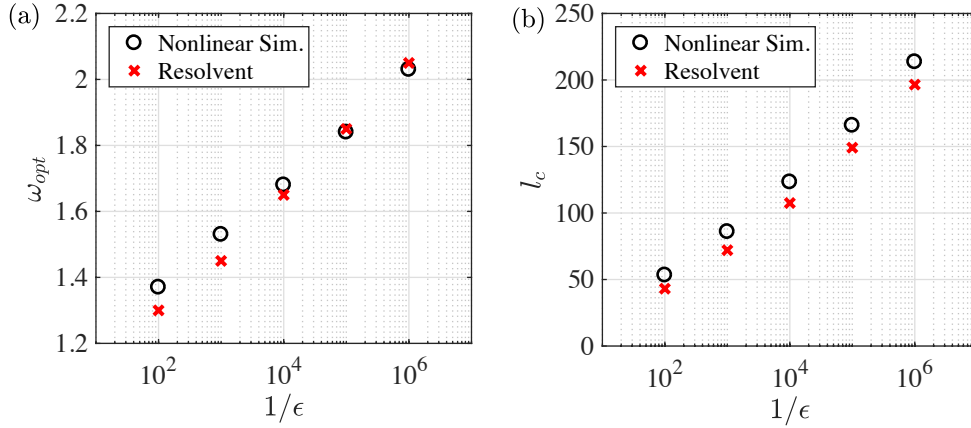


Figure 4.13 – Comparison of breakup characteristics obtained from the nonlinear simulations (figure 4.3) and the resolvent analysis (figure 4.12) for a jet defined by  $Oh_{in} = 0.3$ ,  $Bo_{in} = 0.1$  and  $We_{in} = 1.75$  for (a) the optimal forcing frequency  $\omega_{opt}$  and (b) the breakup length  $l_c$  at different inverse forcing amplitudes  $1/\epsilon$ .

### 4.6 Response to white noise

Up to now, we were only interested in the response of the jet to an external disturbance characterised by a constant forcing frequency. However, in reality the external disturbance is more likely to be composed of a broadband frequency rather than being harmonic. Thus, to model this physical perturbation we carry out nonlinear simulations consistent with the scheme presented in Section 4.3 by exciting the jet at the nozzle by a white noise  $\xi(t)$  defined in the time interval  $[0, T]$  and formulated in a similar way as in Mantić-Lugo & Gallaire (2016). The white noise signal  $\xi(t)$  is characterised by a constant power spectral density (PSD)  $S_{\xi\xi}(\omega) = |\hat{\xi}(\omega)|^2$  where  $\hat{\xi}(\omega)$  is the Fourier transform of  $\xi(t)$  and has an infinite power  $P$  defined as,

$$P = \frac{1}{T} \int_0^T |\xi_T(t)|^2 dt = \frac{1}{\pi} \int_0^\infty |\hat{\xi}|^2 d\omega = \sigma^2, \quad (4.30)$$

where  $\sigma$  is the variance. Even though a pure white noise has infinite power (as  $S_{\xi\xi}(\omega) > 0$ ), physical systems are usually characterized by a band-limited white noise. We thus filter the digital random signal  $\xi_d(t)$  with a band limiting frequency  $\omega_b/2\pi = 1$  to obtain the band

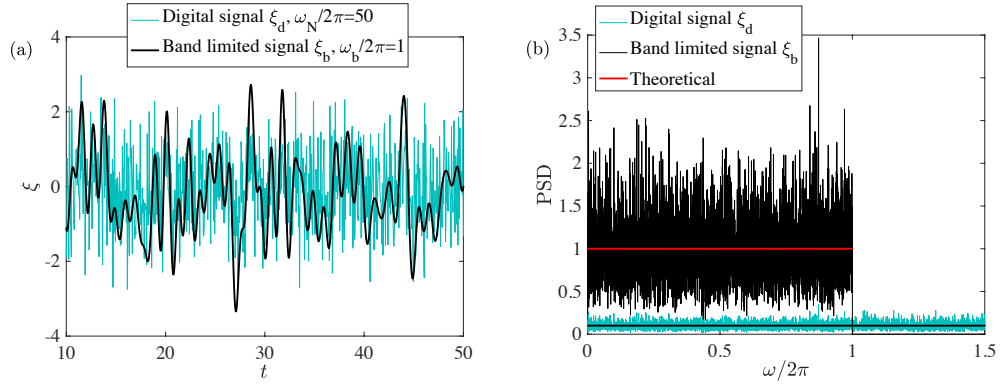


Figure 4.14 – (a) White noise signal with unit power, comparing a signal without filter and filtered using a band limiting frequency  $\omega_b/2\pi$ . (b) Power spectral density comparison of these two signals with their theoretical value. The PSD is estimated using a Welch method in Matlab.

limited white noise  $\xi_b(t)$  as shown in figure 4.14. For  $\xi_d(t)$  the Nyquist frequency is set by  $\omega_N/2\pi$  which depends on the time step ( $\delta t$ ) of the signal, such that  $\omega_N/2\pi = 1/2\delta t$ . Here we chose  $\delta t = 0.01$ . The noise  $\xi_b(t)$  is normalised to have zero mean, unit variance and unit power, with a constant value for PSD, where  $2|\hat{\xi}_b|^2 = 2\pi/\omega_b$  which completely depends on the band limiting frequency. Finally we impose this filtered white noise as an inlet velocity condition for the jet defined by  $Oh_{in} = 0.3$ ,  $Bo_{in} = 0.1$  and  $We_{in} = 1.75$  and governed by the equations (4.7) by replacing the boundary condition (4.8) with,

$$\left. \frac{du}{dt} \right|_{(0,t)} = \epsilon \xi_b(t), \quad (4.31)$$

where  $\epsilon$  is the amplitude of the white noise signal. The forcing is applied at two different amplitudes  $\epsilon = 10^{-2}$  and  $10^{-4}$  and for large times ( $T = 2000$ ) so as to achieve results which are time independent. For the MATLAB solver ode23tb with varying step size, the maximum time step size is set as  $\delta t$  and white noise for intermediate time steps is obtained through interpolation.

At every pinch off on the jet, we note the breakup length  $l_c$ , the pinch off period  $\Delta T_{po}$  and the drop radius  $R_{drop}$  at the time of breakup. The distribution of the breakup characteristics is shown as a histogram in figure 4.15 and 4.16 and compared with the expected response of the jet in presence of the pure  $\omega_{opt}(\epsilon)$ , which corresponds to  $\omega_{opt} = 1.38$  and  $1.65$  for  $\epsilon = 10^{-2}$  and  $10^{-4}$ , respectively. The breakup characteristics for  $\omega_{opt}$  have been discussed in figure 4.2 and are depicted by red bars in figure 4.15 and 4.16.

The drop size distribution shown in figure 4.15(a) highlights the two distribution peaks concentrated around  $\approx 0.9$  and  $\approx 1.65$ , representing the group of satellite and main drops respectively. This behaviour also exists for smaller  $\epsilon = 10^{-4}$  where the radius is aggregated at  $\approx 1.05$  and  $\approx 1.45$ . The results for the main drop size are coherent to the ones obtained in the presence of pure optimal forcing where  $R_{drop} = 1.62$  and  $1.45$  for  $\epsilon = 10^{-2}$  and  $10^{-4}$ , respectively. Thus

## Chapter 4. Amplitude dependent preferred mode of an axisymmetric single phase gravity-driven falling viscous jet

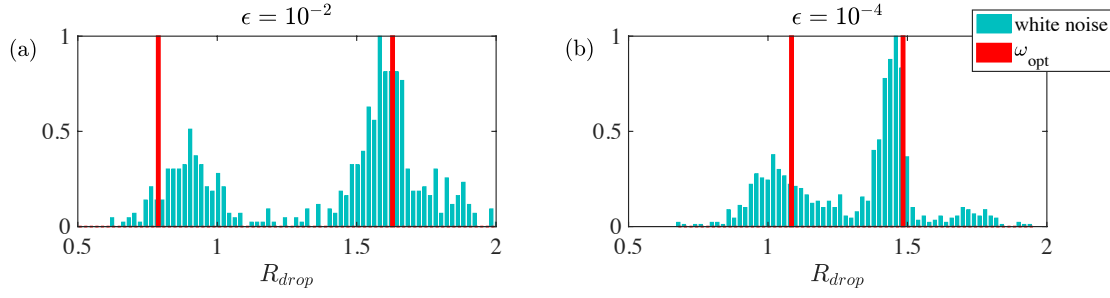


Figure 4.15 – Comparison of the normalised frequency of the drop radius  $R_{drop}$  for jet defined by  $Oh_{in} = 0.3$ ,  $Bo_{in} = 0.1$  and  $We_{in} = 1.75$  and being forced at amplitude (a)  $\epsilon = 10^{-2}$  and (b)  $\epsilon = 10^{-4}$  by their respective optimal forcing frequency  $\omega_{opt}$  (in red bars) and white noise (in cyan bars). For both the amplitudes, the white noise data is concentrated around two main drop sizes, representatives of the main and satellite drops. The most frequent drops sizes are  $R_{drop} = 1.65$  and  $1.45$  for  $\epsilon = 10^{-2}$  and  $10^{-4}$  respectively. These values are close to the ones predicted by the nonlinear simulations of figure 4.2 where the main drop size was predicted to be  $1.62$  and  $1.48$  for  $\epsilon = 10^{-2}$  and  $10^{-4}$  respectively.

even in the presence of the white noise, the response of the jet is dominated by its expected behaviour at  $\omega_{opt}$ .

Unlike the drop radius, the peak of the distribution of breakup length obtained by imposing the white noise is not in close agreement with that of the optimal forcing. Yet, in figure 4.16(a) and (b), we clearly see that the distribution spectrum shifts to large values of breakup length as  $\epsilon$  is decreased, a behaviour similar to the one predicted by  $\omega_{opt}$  where  $l_c$  increases from  $\approx 50$  to  $\approx 125$  as  $\epsilon$  is decreased. Similar conclusions can be drawn for the comparison of  $\Delta T_{po}$  between white noise forcing and forcing with  $\omega_{opt}$  from 4.16(c) and (d) where we plot the breakup period between two consecutive drops.

### 4.7 Conclusion and perspectives

In this work, we inspect the response of a spatially varying gravitationally stretched jet subjected to an inlet velocity perturbation. The forcing is characterised through the frequency and the amplitude, the latter playing a major role in the determination of the optimal forcing frequency. The results of the numerical simulations performed on the nonlinear 1D Eggers & Dupont equations shows an increase in optimal forcing frequency and the breakup length as the forcing amplitude is decreased. We found that the amplitude dependent preferred mode is a characteristic of gravity driven jets only. A pure capillary jet, base state of which is independent of gravity-induced stretching, does not sustain such a behaviour. In such cases, decreasing the forcing amplitude only resulted in an increase of the breakup length with the optimal frequency remaining fixed at all amplitudes.

The linear stability theory characterised the jet flow used for nonlinear simulations as locally unstable and globally stable. Based on the absolute-convective transition criteria, we analysed

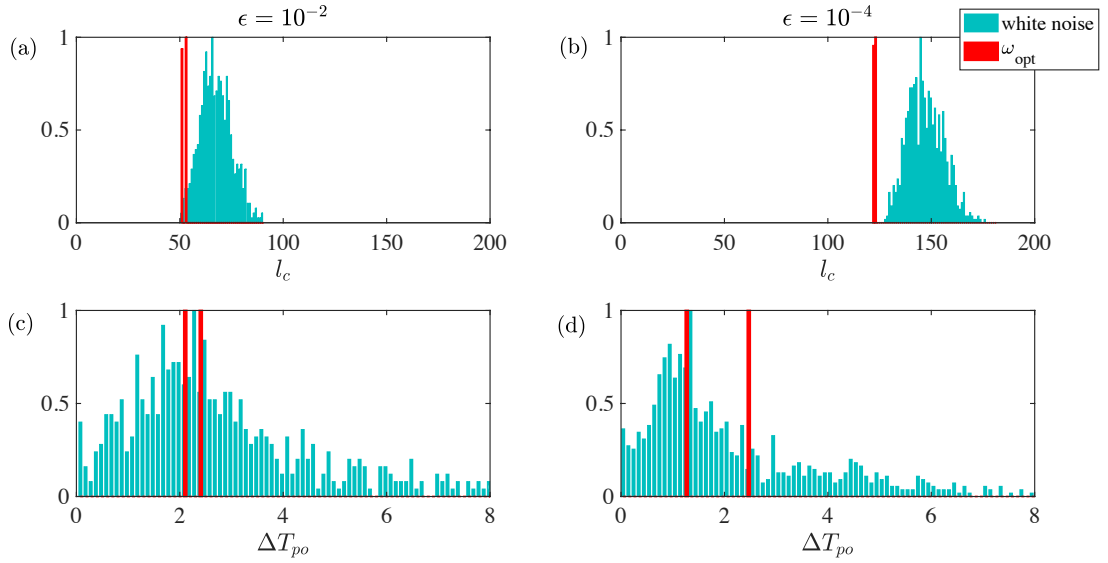


Figure 4.16 – (a)-(b) refer to the comparison of the normalised frequency of the breakup length  $l_c$  and (c)-(d) refer to the comparison of the normalised frequency of the breakup period  $\Delta T_{po}$ , each for a jet defined by  $Oh_{in} = 0.3$ ,  $Bo_{in} = 0.1$  and  $We_{in} = 1.75$ . (a), (c) are subjected to a forcing amplitude  $\epsilon = 10^{-2}$  and (b), (d) to  $\epsilon = 10^{-4}$ . The data in red corresponds to the optimal forcing frequency  $\omega_{opt}$  and in cyan to the white noise. The most frequent white noise breakup length is close to the  $l_c$  prediction in presence of the  $\omega_{opt}$ . For  $\epsilon = 10^{-2}$  and  $10^{-4}$ , the peak breakup period  $\Delta T_{po} = 2.45$  and  $1.35$ , respectively and is in close proximity to the results obtained from the nonlinear simulations of figure 4.2.

the local stability at each section along the axial direction. The solution of the dispersion relation and the subsequent analysis for the downstream propagating spatial waves helped in confirming the predominant wave to be used for the zeroth order spatial gain expression. The strong non-parallelism of the base flow close to the nozzle motivated the incorporation of the WKBJ framework which markedly improved the prediction of the optimal forcing frequency in comparison to the resolvent analysis. However the spatial gain was still observed to be lower than the resolvent. As suggested by Le Dizès & Villermaux (2017), using advanced stability tools (Schmid, 2007) which accounts for non-parallel effects and non-modal growth leads to an estimation of a more realistic spatial response.

This task was tackled using a resolvent analysis which accurately captured the linear response of stable jets in presence of an external forcing. Assuming a simple global amplitude breakup threshold criterion, the linear resolvent analysis becomes capable in predicting both the breakup length and the optimal forcing frequency given the amplitude of the forcing. The results of the nonlinear simulations and the resolvent for different forcing amplitudes are quantitatively comparable, thus underlining the importance of the resolvent analysis. Besides forcing the jet inlet with a fixed frequency, we also studied the response to a white noise, to analyse its natural response to a distributed forcing frequency range. Surprisingly, even in the presence of the white noise, the dominant response of the jet is close to the one seen from the

#### **Chapter 4. Amplitude dependent preferred mode of an axisymmetric single phase gravity-driven falling viscous jet**

---

optimal frequency at that amplitude.

In presence of the external forcing, a dominant feature seen from the nonlinear simulations is the formation of a main and a satellite drop at the time of breakup. Nevertheless, to properly examine the consequence of the forcing amplitude on the final drop size, there is a need to enhance the nonlinear model by including the physics of drop coalescence and disintegration as done by Driessen & Jeurissen (2011). Post breakup, the state of the jet after the pinch-off should be inferred from the system before the breakup. Additionally, the choice for drop curvature is of paramount importance since a given breakup can possess variety of drops shapes-each on different length scales (Kowalewski, 1996).

On a different note, if the final aim is to eliminate the presence of satellite drops, the forcing should be modified such that it leads to the selective production of equisized drops. In this direction the work of Chaudhary & Redekopp (1980), who controlled satellite drops by forcing the jet with a suitable harmonic added to the fundamental; and Driessen *et al.* (2014), who controlled the size of the droplet breaking off from a parallel jet by imposing a superposition of two Rayleigh-Plateau-unstable modes on the jet, could serve as the basis for formulating a theory for the spatially varying gravity jets.

I.S. thanks the Swiss National Science Foundation (grant no. 200021-159957). The authors would like to thank Eunok Yim for extremely valuable discussions on the modelling of white noise disturbance and in the interpretation of the local/global response. The authors would also like to thank Tobias Ansal di and Giorgio Rocca who worked on the foundation of the numerical code for parallel jets as well as Adrien Jean Pierre Bressy for efficiently performing several simulations on the enhanced version of the numerical code provided to him.



## 4.8 Appendix

### 4.8.1 Numerical base state solution validation

In this appendix, we show the validation of our numerically obtained base state solution of the governing equations (4.5) with the experimental results of Rubio-Rubio *et al.* (2013) for three different jet flows. The MATLAB bvp4c solver along with the boundary conditions stated in Section 4.2 accurately captures the stretching (necking) close to the nozzle due to the effect of  $Bo_{in}$ .

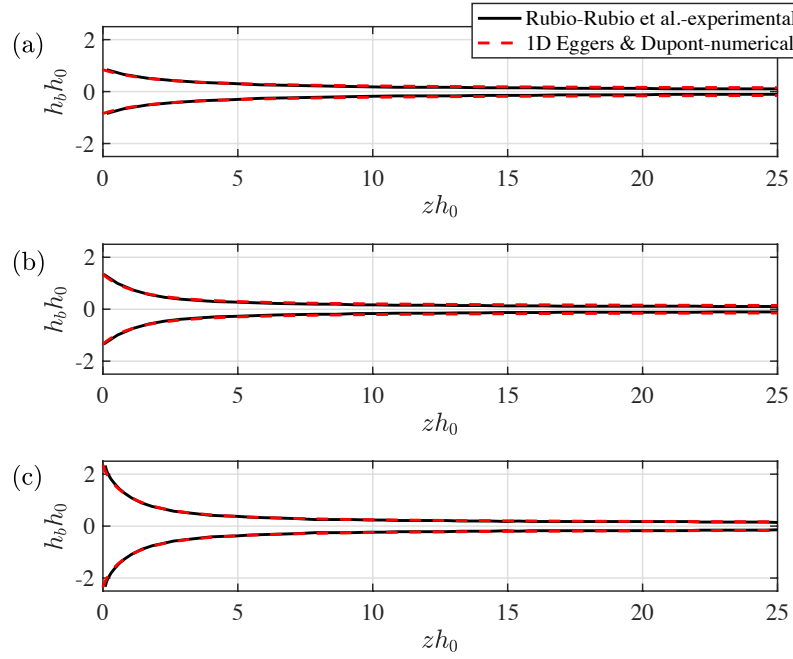


Figure 4.17 – Comparison of the steady state solution with results from Rubio-Rubio *et al.* (2013) for (a)  $Oh_{in} = 2.117$ ,  $We_{in} = 2.62 \times 10^{-2}$ ,  $Bo_{in} = 0.71$  (b)  $Oh_{in} = 0.4799$ ,  $We_{in} = 6.06 \times 10^{-3}$ ,  $Bo_{in} = 1.81$  and (c)  $Oh_{in} = 0.7238$ ,  $We_{in} = 1.85 \times 10^{-3}$ ,  $Bo_{in} = 5.53$ .

### 4.8.2 Effect of initial condition on breakup characteristics

This section demonstrates the effect on breakup characteristics due to different initial conditions of the jet. Using the scheme described in Section 3.4.2 we perform numerical solutions for a jet with  $Oh_{in} = 0.3$ ,  $We_{in} = 1.75$ , and  $Bo_{in} = 0.1$  excited with a forcing of amplitude  $\epsilon = 10^{-2}$  and frequency  $\omega = 0.8$ . In the first case, the jet is initialized as a circular tip of radius 1 (figure 4.18(a)) and in the second case with the base state solution obtained by solving equation (4.5) defined for an axial length of 100 (figure 4.18(b)). In both the cases the numerical domain is considered large enough to capture all the breakups. As shown in figure 4.18, both the jets with different initial conditions have different transient dynamics upto  $t = 55$  (tip) and  $t = 40$  (base state) after which they enter the permanent regime. In this regime, the breakup length  $l_c$

## Chapter 4. Amplitude dependent preferred mode of an axisymmetric single phase gravity-driven falling viscous jet

and period  $\Delta T_{po}$  are identical as shown in subplots (c) and (d), respectively. It is thus safe to conclude that in the permanent regime the jet breakup is independent of the initial base state solution.

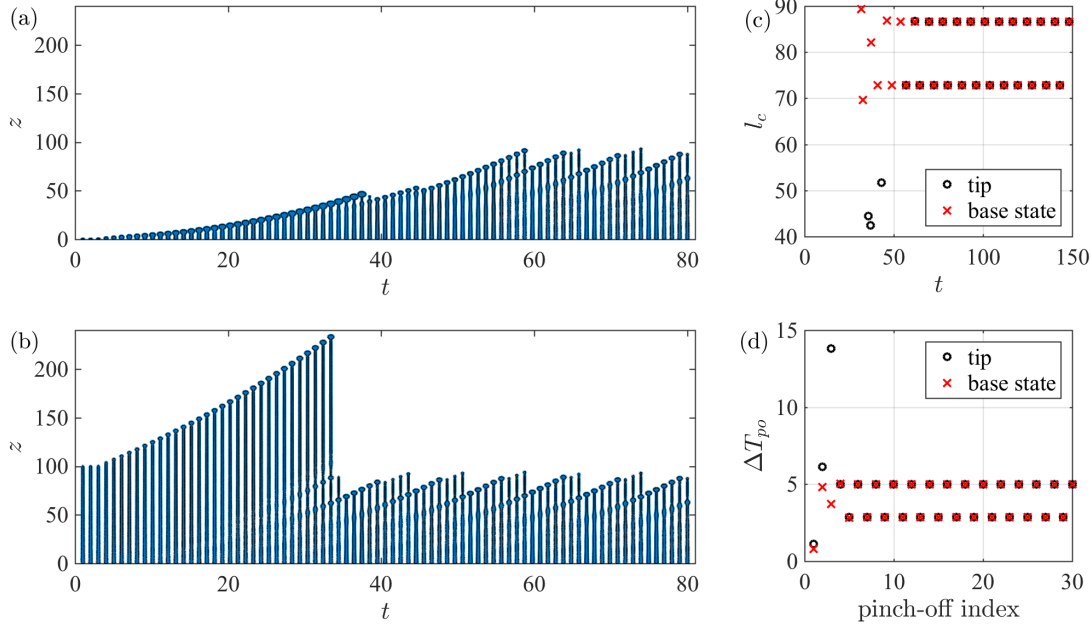


Figure 4.18 – Time-sequence plot of a simulation with  $Oh_{in} = 0.3$ ,  $We_{in} = 1.75$ ,  $Bo_{in} = 0.1$  excited with a forcing of amplitude  $\epsilon = 10^{-2}$  and frequency  $\omega = 0.8$  and initialized (a) as a tip (b) using the base state solution. Comparison of the breakup length and period for both the cases is presented in (c) and (d), respectively.

### 4.8.3 Effect of jet tip on breakup mechanism

In this section we show that the jet tip at the time of breakup does not influence the pinchoff dynamics and that the breakup is not self sustaining. For comparison we use a jet with  $Oh_{in} = 0.3$ ,  $We_{in} = 1.75$ ,  $Bo_{in} = 0.1$  (refer figure 4.19). In the first case (black circles), we do not impose any forcing on the jet inlet to analyse its natural breakup characteristics. In the second case (blue diamonds), we apply a forcing of amplitude  $\epsilon = 10^{-3}$  and frequency  $\omega = 2$  at the inlet velocity. In the third case, we initialize the jet with the same forcing frequency and amplitude, but stop the forcing and let the jet evolve freely when the permanent regime is reached.

In figure 4.19, the forcing is stopped at  $t = 90$ , which corresponds to the 36th breakup. Comparing the breakup dynamics of the interrupted forced jet to a jet with constant or no forcing at all, we conclude that the breakup length is no longer constant but keeps on increasing and finally evolves similarly to a no forced jet.

This suggests that the pinch-off mechanism is not self sufficient to maintain the breakup of

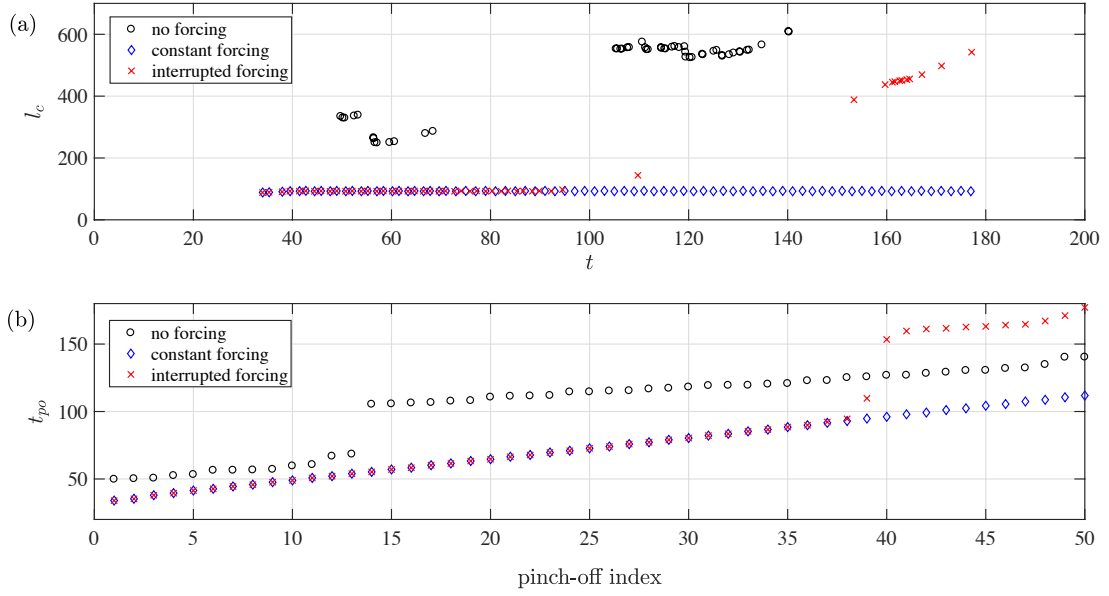


Figure 4.19 – (a) Breakup length  $l_c$  and (b) time of pinch-off  $t_{po}$ , plotted for a jet with  $Oh_{in} = 0.3$ ,  $We_{in} = 1.75$ ,  $Bo_{in} = 0.1$ . The blue diamonds represent constant excitation of the inlet velocity with a forcing of amplitude  $\epsilon = 10^{-3}$  and frequency  $\omega = 2$ . The black circles indicate a jet without any forcing and hence we observe an irregular breakup pattern. The red cross indicates a jet with constant forcing ( $\epsilon = 10^{-3}$ ,  $\omega = 2$ ), where the excitation is stopped around  $t = 90$ .

the jet in the permanent regime and that continuous breakup can be sustained only in the presence of an external forcing, supporting our argument that the pinch-off has no influence on the jet's dynamics afterward.

#### 4.8.4 Comparison between resolvent and spatial analyses

Figure 4.20 shows the comparison of gain, in absence of gravity, as function of forcing frequency using spatial and resolvent analysis for two different domain sizes. For convenience we also plot the resolvent gain  $G_{n, fu}$  expressed in terms of the forcing applied for the nonlinear simulations. We note that all the curves, irrespective of the domain size, predict the same optimal forcing frequency  $\omega_{opt} = 0.74 - 0.76$ , a value close to the nonlinear prediction of figure 3.8(a) seen in Section 3.4.4 of Chapter 3. Moreover, unlike the situation with  $Bo = 0.1$ , we notice that in the absence of gravity the magnitude of the gain at all frequencies is well captured by the spatial analysis.

## Chapter 4. Amplitude dependent preferred mode of an axisymmetric single phase gravity-driven falling viscous jet

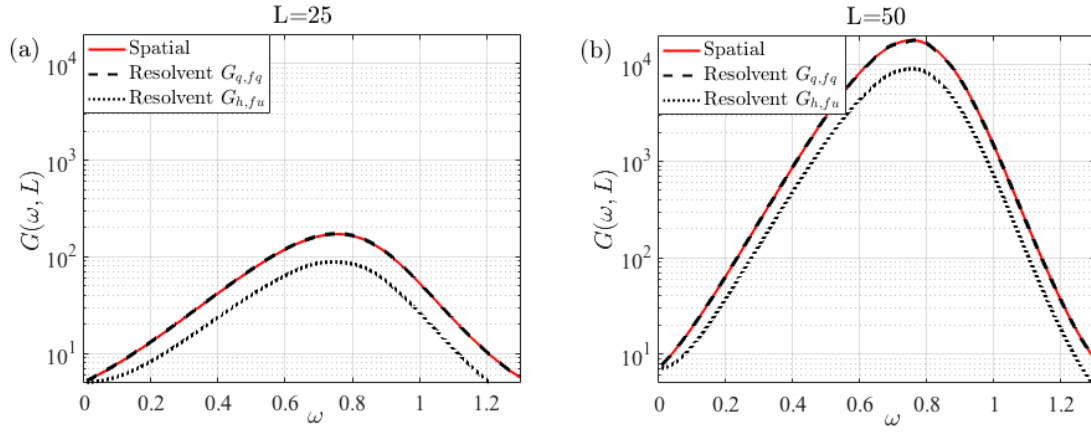


Figure 4.20 – Comparison of gain and  $\omega_{opt}$  obtained from the resolvent analysis and spatial analysis for two different domain sizes (a)  $L = 25$  and (b)  $L = 50$  for a jet in absence of gravity and characterized by  $Oh = 0.3$  and  $We = 1.75$ . Irrespective of the domain size and the method employed, the  $\omega_{opt}$  lies between  $[0.74 \ 0.75]$ .

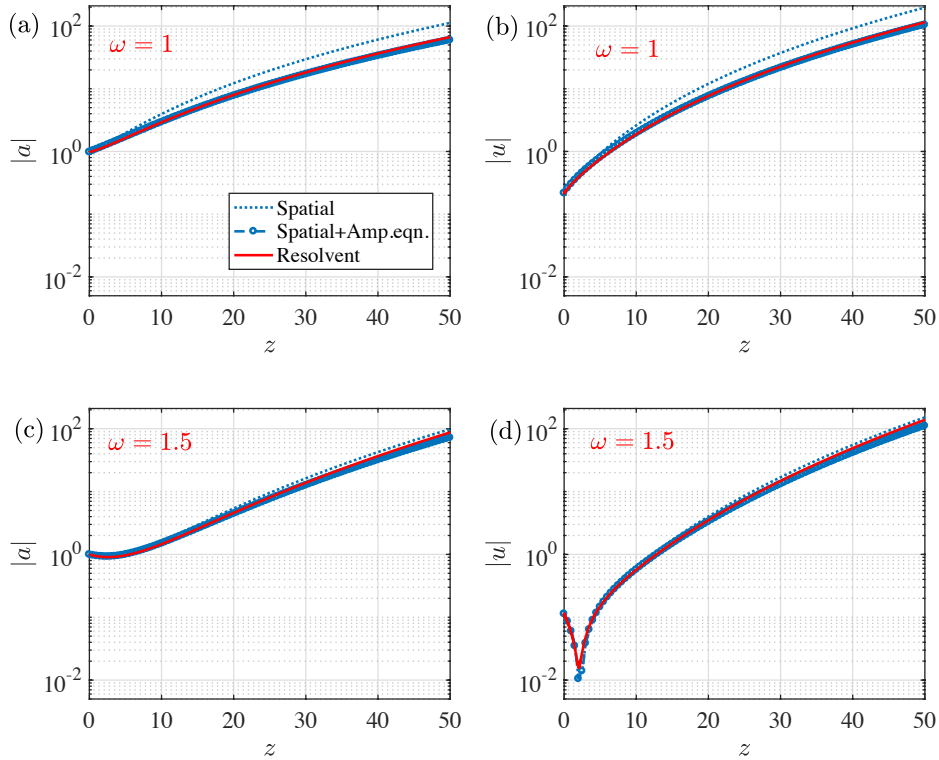


Figure 4.21 – Resolvent and spatial response ( $|a|$  and  $|u|$ ) of the jet characterized by  $Oh_{in} = 0.3$ ,  $We_{in} = 1.75$  and  $Bo_{in} = 0.1$  at (a)-(b)  $\omega = 1$  and (c)-(d)  $\omega = 1.5$  with a domain size  $L = 50$ .

#### 4.8.5 Linear operator for eigenvalue problem

For the eigenvalue problem related to the global stability in Section 4.5.1, the matrix  $M$  is expressed as

$$M = \begin{bmatrix} M_{11} & M_{12} \\ M_{21} & M_{22} \end{bmatrix}, \quad (4.32)$$

where the expressions  $M_{11}$ ,  $M_{12}$ ,  $M_{21}$  and  $M_{22}$  denote the following differential equations:

$$M_{11} = -\frac{Q}{h_b^2}D + \frac{Qh'_b}{h_b^3}\mathbb{I}, \quad (4.33a)$$

$$M_{12} = -\frac{h_b}{2}D - h'_b\mathbb{I}, \quad (4.33b)$$

$$M_{21} = \sum_{k=1}^4 s^{2k-1}T_k - 12Oh_{in}Q\left(\frac{h_b'^2}{h_b^2} + \frac{h_b''}{h_b}\right)D, \quad (4.33c)$$

$$M_{22} = 3Oh_{in}\left(D^2 + \frac{2h'_b}{h_bD}\right) - \frac{Q}{h_b^2}D + \frac{2Qh'_b}{h_b^3}\mathbb{I}. \quad (4.33d)$$

In the group of equations (4.33),  $\mathbb{I}$  is the identity operator,  $D^n \equiv d^n/dz^n$ ,  $s(z) = [1 + (h'_b)^2]^{-1/2}$  and

$$T_1 = \frac{1}{r_b^2}D - \frac{2r'_b}{r_b^3}\mathbb{I}, \quad (4.34a)$$

$$T_2 = D^3 + \frac{h'_b}{h_b}D^2 - \left[\frac{(h'_b)^2}{h_b^2} + \frac{h_b''}{h_b}\right]D - \frac{r h'_b h_b''}{h_b^2}\mathbb{I}, \quad (4.34b)$$

$$T_3 = -6h'_b h_b'' D^2 - 3\left[\frac{(h'_b)^2 h_b''}{h_b} + (h_b'')^2 - h'_b h_b'''\right]D, \quad (4.34c)$$

$$T_4 = 15(h_b'')^2 (h'_b)^2 D. \quad (4.34d)$$

#### 4.8.6 Global stability validation

In this section, we present the validation of the numerical scheme used for the global stability analysis presented in Section 4.5.1. The validation is done against the results of Rubio-Rubio *et al.* (2013) where the stability analysis is based on the same 1D Eggers & Dupont (1994) equations but made dimensionless using different characteristic length and time scales. The results of Rubio-Rubio *et al.* (2013) are based on dimensionless numbers  $We_{in}$ ,  $Bo_{in}$  and  $Kapitza(\Gamma)$ . For the purpose of comparison we obtain the equivalent  $Oh_{in}$  expressed as

$$Oh_{in} = \frac{\Gamma}{3Bo_{in}^{0.25}}. \quad (4.35)$$

For the eigenvalue problem, a non dimensional domain length  $L = 120$  is considered. For obtaining the dominant eigenvalue, the solution was computed for different values of  $N$  lying

## Chapter 4. Amplitude dependent preferred mode of an axisymmetric single phase gravity-driven falling viscous jet

between [150 250]. Figure 4.22 shows the validation of the eigenvalue spectrum with  $N = 200$ , steady state and dominant eigenfunction for  $\Gamma = 5.83$  and  $Bo_{in} = 1.8$  and two different values of  $We_{in}$ . The results obtained from the present model are in good coherence with that obtained from Rubio-Rubio *et al.* (2013). Comparing figure 4.22(a) and (b), we can observe there is critical Weber number  $We_{inc}$  for which the jet becomes marginally unstable as the real part of the leading eigenvalue is slightly positive. For the given values of  $Bo_{in}$  and  $Oh_{in}$ , the  $We_{inc}$  is therefore equal to  $3 \times 10^{-3}$ . If the Ohnesorge number is fixed and the bond number is varied, we can get the corresponding  $We_{inc}$  for each value of  $Bo_{in}$ . Figure 4.23 represents the curve for the  $We_{inc}$ , below which the jet becomes linearly unstable. The results are compared to those obtained from Rubio-Rubio *et al.* (2013).

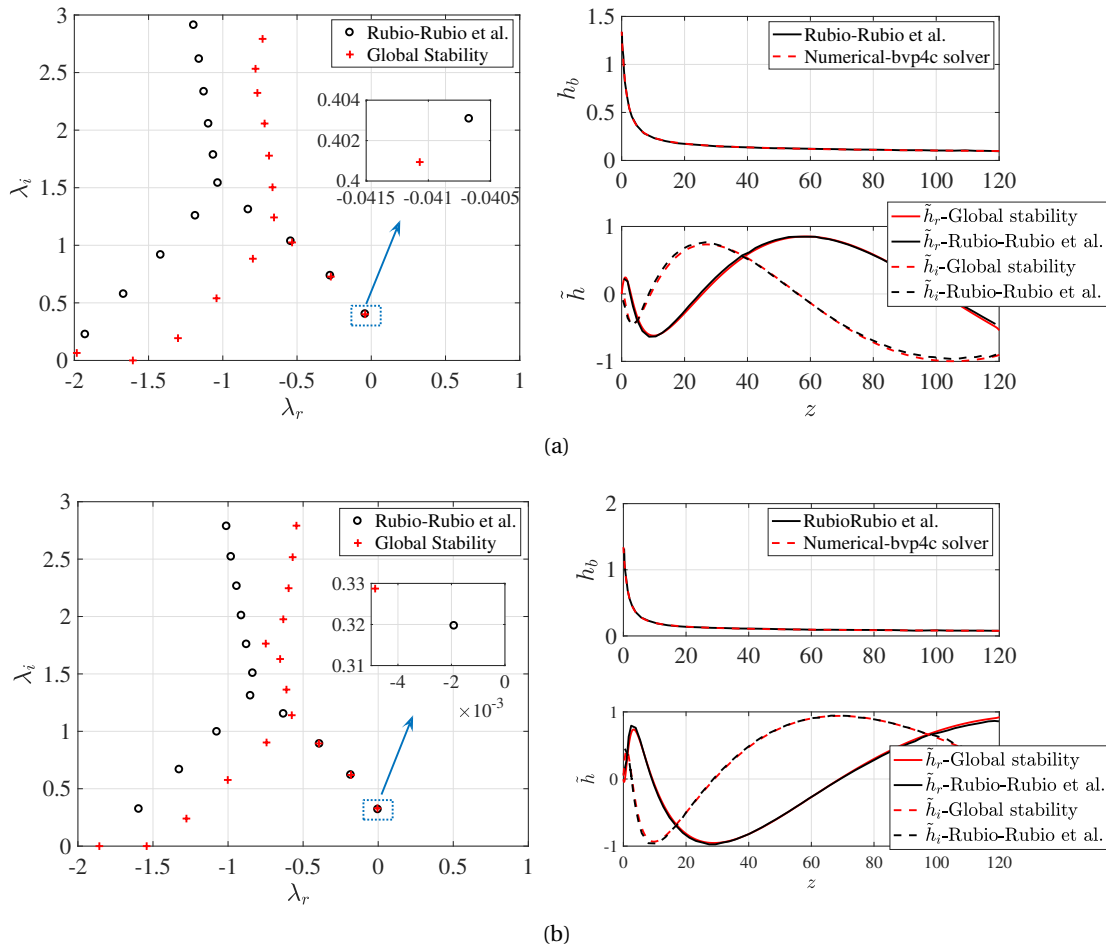
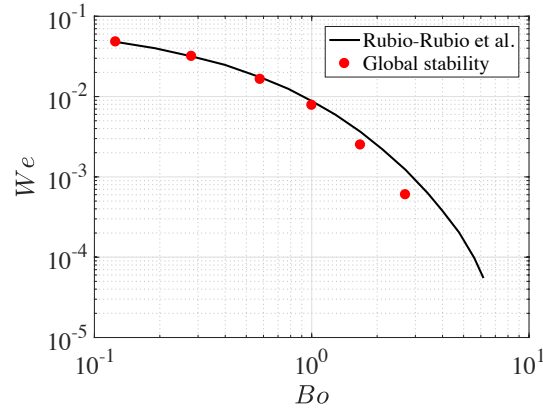


Figure 4.22 – Eigenvalue spectrum  $\lambda$ , steady state shape of the jet  $h_b$ , and the real and imaginary parts of leading eigenfunction,  $\tilde{h}$  for  $Oh_{in} = 1.68$ ,  $Bo_{in} = 1.81$  and (a)  $We_{in} = 8 \times 10^{-3}$  (b)  $We_{in} = 3 \times 10^{-3}$ . Results in *black* are from Rubio-Rubio *et al.* (2013) and in *red* are from the present stability model.

Figure 4.23 – Comparison of critical Weber number,  $We_c$ .

#### 4.8.7 WKBJ formulation for axisymmetric 1D Eggers & Dupont equations

##### Linearized equations

Considering linear perturbations  $(a', u')$  in jet interface and velocity around the base flow  $(a_b, u_b)$ , the linearized system of equations is written as:

$$\frac{\partial a'}{\partial t} = (-A_1 - A_2 D_1) a' + (-A_3 - A_4 D_1) u', \quad (4.36a)$$

$$\frac{\partial u'}{\partial t} = (-B_1 - B_2 D_1 - B_3 D_2 - B_4 D_3) a' + (-B_1 - B_2 D_1 - B_3 D_2) u'. \quad (4.36b)$$

where  $D_i$  with  $i = 1..3$  are the differential operators with respect to  $z$ . Equation (4.36) can be reformed as

$$[\dot{\mathbf{q}}'] = K[\mathbf{q}'], \quad (4.37)$$

where

$$[\mathbf{q}'] = \begin{bmatrix} a' \\ u' \end{bmatrix}, \quad K = \begin{bmatrix} -A_1 - A_2 D_1 & -A_3 - A_4 D_1 \\ -B_1 - B_2 D_1 - B_3 D_2 - B_4 D_3 & -B_1 - B_2 D_1 - B_3 D_2 \end{bmatrix}, \quad (4.38)$$

where the coefficients  $A_{1..4}$  are given as,

$$A_1 = u_b'(z), \quad (4.39a)$$

$$A_2 = u_b(z), \quad (4.39b)$$

$$A_3 = a_b'(z), \quad (4.39c)$$

$$A_4 = a_b(z), \quad (4.39d)$$

## Chapter 4. Amplitude dependent preferred mode of an axisymmetric single phase gravity-driven falling viscous jet

---

and  $B_{1..7}$  are expressed as,

$$B_1 = \frac{15(-2a_b'(z)^3 - 4a_b(z)a_b'(z) + a_b'(z)^3(-a_b''(z)) + a_b(z)a_b'(z)a_b''(z)^2)}{16S^{7/2}} - \frac{3(2a_b(z)a_b^{(3)}(z) - 8a_b'(z) + a_b'(z)a_b''(z)^2 - 2a_b'(z)a_b''(z))}{8S^{5/2}} + \frac{a_b^{(3)}(z)}{2S^{3/2}} - \frac{3(Oh_{in}a_b'(z)u_b'(z))}{a_b(z)^2}, \quad (4.40a)$$

$$B_2 = \frac{15(-2a_b'(z)^4 - 4a_b(z)a_b'(z)^2 + a_b'(z)^4(-a_b''(z)) + a_b(z)a_b'(z)^2a_b''(z)^2)}{32S^{7/2}} - \frac{3(a_b(z)a_b''(z)^2 - 8a_b'(z)^2 + a_b(z)a_b^{(3)}(z)a_b'(z) - 4a_b'(z)^2a_b''(z) - 4a_b(z))}{8S^{5/2}} - \frac{(a_b''(z) + 2)}{2S^{3/2}} + \frac{3Ohu_b'(z)}{a_b(z)}, \quad (4.40b)$$

$$B_3 = \frac{3(a_b'(z)^3 - 2a_b(z)a_b'(z)a_b''(z))}{8S^{5/2}} - \frac{a_b'(z)}{2S^{3/2}}, \quad (4.40c)$$

$$B_4 = \frac{a_b(z)}{2S^{3/2}}, \quad (4.40d)$$

$$B_5 = -u_b'(z), \quad (4.40e)$$

$$B_6 = \frac{3Oh_{in}a_b'(z)}{a_b(z)} - u_b(z), \quad (4.40f)$$

$$B_7 = 3Oh. \quad (4.40g)$$

In the above equation  $S$  replaces the term  $\frac{1}{4}a_b'(z)^2 + a_b(z)$ .

### Linearized equation expressed in terms of slow variable

For the WKB ananlysis, we then introduce the spatial scales. The fast spatial scale  $z$  is replaced by the slow scale  $Z$ , such that  $Z = \eta z$ . The base flow is now expressed as a function of  $Z$  such that  $a_b(Z)$  and  $u_b(Z)$ . Let us consider the following normal mode expansion for the perturbation:

$$\mathbf{q}'(Z, t) = \hat{\mathbf{q}}(Z) \exp \left[ i \left( \frac{1}{\eta} \int_0^Z k(Z', \omega) dZ' - \omega t \right) \right]. \quad (4.41)$$



Injecting the transformations (4.42a-d) into (4.36), the linearized equations on a weakly non-parallel baseflow equations are expressed through equations (4.43)-(4.44),

$$\begin{aligned}\frac{\partial}{\partial t} &\rightarrow -i\omega, \\ \frac{\partial}{\partial z} &\rightarrow ik + \eta \frac{\partial}{\partial Z}, \\ \frac{\partial^2}{\partial z^2} &\rightarrow -k^2 + i\eta \left( \frac{\partial k}{\partial Z} + 2k \frac{\partial}{\partial Z} \right) + \eta^2 \frac{\partial^2}{\partial Z^2}, \\ \frac{\partial^3}{\partial z^3} &\rightarrow -ik^3 - 3\eta k \left( \frac{\partial k}{\partial Z} + k \frac{\partial}{\partial Z} \right) + \eta^2 \left( 3i \frac{\partial k}{\partial Z} \frac{\partial}{\partial Z} + 3ik \frac{\partial^2}{\partial Z^2} + i \frac{\partial^2 k}{\partial Z^2} \right) + \eta^3 \frac{\partial^3}{\partial Z^3}.\end{aligned}\quad (4.42a-d)$$

where the continuity equation converts to:

$$(-i\omega + ik u_b) \hat{a} + (ik a_b) \hat{u} = -\eta \left[ \frac{\partial}{\partial Z} (a_b \hat{u} + u_b \hat{a}) \right], \quad (4.43)$$

and the momentum equation transforms as,

$$\begin{aligned}i\omega \hat{u} &= -\eta \frac{\partial u_b}{\partial Z} \hat{u} - \left( u_b - \eta \frac{3Oh}{a_b} \frac{\partial a_b}{\partial Z} \right) \left( \eta \frac{\partial}{\partial Z} + ik \right) \hat{u} \\ &\quad + 3Oh \left( -k^2 + \eta i \left( \frac{\partial k}{\partial Z} + 2k \frac{\partial}{\partial Z} \right) + \eta^2 \frac{\partial^2}{\partial Z^2} \right) \hat{u} - \left( \eta \frac{3}{4a_b^{5/2}} \frac{\partial a_b}{\partial Z} \right) \hat{a} \\ &\quad + \left( \frac{1}{2a_b^{3/2}} + \frac{3\eta Oh}{a_b} \frac{\partial u_b}{\partial Z} \right) \left( \eta \frac{\partial}{\partial Z} + ik \right) \hat{a} \\ &\quad - \frac{\eta}{2a_b^{3/2}} \frac{\partial a_b}{\partial Z} \left( -k^2 + \eta i \left( \frac{\partial k}{\partial Z} + 2k \frac{\partial}{\partial Z} \right) + \eta^2 \frac{\partial^2}{\partial Z^2} \right) \hat{a} \\ &\quad + \frac{1}{2a_b^{1/2}} \left( -ik^3 - 3\eta k \left( \frac{\partial k}{\partial Z} + k \frac{\partial}{\partial Z} \right) + \mathcal{O}(\eta^2) \right) \hat{a}\end{aligned}\quad (4.44)$$

Defining  $\hat{\mathbf{q}}^{(1)} = [\hat{a}^{(1)} \ \hat{u}^{(1)}]$  and  $\hat{\mathbf{q}}^{(2)} = [\hat{a}^{(2)} \ \hat{u}^{(2)}]$ , we now consider the asymptotic expansion:

$$\hat{\mathbf{q}} \sim A(Z) \hat{\mathbf{q}}^{(1)}(Z) + \eta \hat{\mathbf{q}}^{(2)}(Z) + \dots, \quad (4.45)$$

and inject it into the governing equations (4.43)-(4.44) to obtain the local stability problem at  $\eta^0$  and  $\eta^1$ .

## Chapter 4. Amplitude dependent preferred mode of an axisymmetric single phase gravity-driven falling viscous jet

---

**Order  $\eta^0$**  : At zeroth-order in  $\eta$ , the local stability problem is retrieved:

$$\underbrace{(-i\omega + ik u_b)}_{L_{11}} \hat{a}^{(1)} + \underbrace{(ik a_b)}_{L_{12}} \hat{u}^{(1)} = 0, \quad (4.46a)$$

$$\underbrace{-\frac{ik}{2a_b^{3/2}}(1 - k^2 a_b)}_{L_{21}} \hat{a}^{(1)} + \underbrace{(-i\omega + ik u_b + 3Ohk^2)}_{L_{22}} \hat{u}^{(1)} = 0. \quad (4.46b)$$

The system of equations represented by (4.46) can be reframed using the linear operator  $L$ , such that

$$L[\hat{\mathbf{q}}^{(1)}] = 0, \quad \text{where the linear operator } L = \begin{bmatrix} L_{11} & L_{12} \\ L_{21} & L_{22} \end{bmatrix}. \quad (4.47)$$

Substituting expression for  $\hat{u}^{(1)}$  from (4.46)a into (4.46)b, we finally obtain:

$$\left( -\omega^2 + 2u_b \omega k + \left( -\frac{1}{2\sqrt{a_b}} - u_b^2 - 3iOh\omega \right) k^2 + 3iOhu_b k^3 + \frac{\sqrt{a_b}}{2} k^4 \right) \hat{a}^{(1)} = 0, \quad (4.48)$$

the solution of which gives the four roots of  $k$  for a given  $\omega$ . The relevant  $k$  branch is tracked as discussed in Section 4.4. For a given  $\omega$  and a predetermined  $k$ , the solution of the linear problem (4.47) gives the response  $\hat{\mathbf{q}}^{(1)}$ , a parameter needed to solve the local stability problem at  $\eta^1$ .

**Order  $\eta^1$**  : At first order we obtain,

$$L[\hat{\mathbf{q}}^{(2)}] = Q[A\hat{\mathbf{q}}^{(1)}], \quad (4.49)$$

where operator  $Q$  can be split into two parts:

$$Q[A\hat{\mathbf{q}}^{(1)}] = R[\hat{\mathbf{q}}^{(1)}] \frac{dA}{dZ} + S[\hat{\mathbf{q}}^{(1)}] A. \quad (4.50)$$

Operator  $R$  is expressed as:

$$R = \begin{bmatrix} -u_b & -a_b \\ \left( \frac{1-3k^2 a_b}{2a_b^{3/2}} \right) & (6iOhk - u_b) \end{bmatrix}, \quad (4.51)$$

and  $S$  is defined as,

$$S = \begin{pmatrix} s_{11} & s_{12} \\ s_{21} & s_{22} \end{pmatrix},$$

where the individual parameters are expressed as:

$$\begin{aligned}
 s_{11} &= -\frac{\partial u_b}{\partial Z} - u_b \frac{\partial}{\partial Z}, \\
 s_{12} &= -\frac{\partial a_b}{\partial Z} - a_b \frac{\partial}{\partial Z}, \\
 s_{21} &= \frac{3iOhk}{a_b} \frac{\partial u_b}{\partial Z} - \frac{1}{4a_b^{5/2}} \left( (3 - 2k^2 a_b) \frac{\partial a_b}{\partial Z} + 6ka_b^2 \frac{\partial k}{\partial Z} + 2a_b(-1 + 3k^2 a_b) \frac{\partial}{\partial Z} \right), \\
 s_{22} &= 3iOh \left( \frac{k}{a_b} \frac{\partial a_b}{\partial Z} + \frac{\partial k}{\partial Z} + 2k \frac{\partial}{\partial Z} \right) - u_b \frac{\partial}{\partial Z} - \frac{\partial u_b}{\partial Z}.
 \end{aligned}$$

As explained in Huerre & Rossi, 1998; Viola *et al.*, 2016, in order to have solutions of the inhomogeneous equation  $L[\hat{\mathbf{q}}^{(2)}] = Q[A\hat{\mathbf{q}}^{(1)}]$ , the forcing term  $Q$  should be in the image of the operator  $L$ . This implies that  $Q$  should be orthogonal to the corresponding adjoint eigenfunction  $\tilde{\mathbf{q}}^{(1)}$  of the adjoint operator  $\tilde{L}$ , with respect to the defined inner product,

$$\underbrace{R[\hat{\mathbf{q}}^{(1)}] \tilde{\mathbf{q}}^{(1)} \frac{dA}{dZ}}_{M(Z)} + \underbrace{S[\hat{\mathbf{q}}^{(1)}] \tilde{\mathbf{q}}^{(1)} A}_{N(Z)} = L[\hat{\mathbf{q}}^{(2)}] \tilde{\mathbf{q}}^{(1)} = \hat{\mathbf{q}}^{(2)} \tilde{L}[\tilde{\mathbf{q}}^{(1)}] = 0. \quad (4.53)$$

This leads to the amplitude equation,

$$M(Z) \frac{dA}{dZ} + N(Z) A = 0, \quad (4.54)$$

solving which we obtain the amplitude solution  $A(Z)$  which should then be expressed in terms of the fast length scale  $z$ . Finally, at first order, the response is given by,

$$\mathbf{q}'(z) \sim A(\eta z) \hat{\mathbf{q}}^{(1)}(z) \exp \left( \int_0^z -k_i(z') dz' \right) \exp \left[ i \left( \int_0^z k_r(z') dz' - \omega t \right) \right]. \quad (4.55)$$



## 5 Particle size selection in capillary instability of locally heated co-axial fiber

**Remark** This chapter is largely inspired by the publication of the same name

Saviz Mowlavi<sup>1,2,\*</sup>, Isha Shukla<sup>2,\*</sup>, Pierre-Thomas Brun<sup>3</sup> and François Gallaire<sup>2</sup>

<sup>1</sup>Department of Mechanical Engineering, Massachusetts Institute of Technology, Cambridge, MA 02139, USA

<sup>2</sup>Laboratory of Fluid Mechanics and Instabilities, Ecole Polytechnique Fédérale de Lausanne, 1015 Lausanne, Switzerland

<sup>3</sup>Department of Chemical and Biological Engineering, Princeton University, Princeton, NJ 08540, USA

*Physical Review Fluids* **4**, 064003 (2019)

**Author contributions** P-T.B. and E.G. conceived the project. S.M. and E.G. developed theoretical model. I.S. performed simulations and analyzed data with E.G. E.G. supervised the research. S.M. and I.S. wrote paper.

\*These authors contributed equally to this work.

Harnessing fluidic instabilities to produce structures with robust and regular properties has recently emerged as a new fabrication paradigm. This is exemplified in the work of Gumennik et al. [Nat. Comm. 4:2216, DOI: 10.1038/ncomms3216, (2013)], in which the authors fabricate silicon spheres by feeding a silicon-in-silica co-axial fiber into a flame. Following the localized melting of the silicon, a capillary instability of the silicon-silica interface induces the formation of uniform silicon spheres. Here, we try to unravel the physical mechanisms at play in

selecting the size of these particles, which was notably observed by Gumennik et al. to vary monotonically with the speed at which the fiber is fed into the flame. Using a simplified model derived from standard long-wavelength approximations, we show that linear stability analysis strikingly fails at predicting the selected particle size. Nonetheless, nonlinear simulations of the simplified model do recover the particle size observed in experiments, without any adjustable parameters. This shows that the formation of the silicon spheres in this system is an intrinsically nonlinear process that has little in common with the loss of stability of the underlying base flow solution.

### 5.1 Introduction

Mechanical instabilities in engineered structures have historically been perceived as failure mechanisms. As such, an enduring motivation for their study has been the desire to avoid them. Recently, however, we have started to witness a paradigm shift wherein structural instabilities are instead sought after due to their natural ability to produce regular patterns that would be difficult or costly to achieve otherwise (Reis, 2015). Interestingly, this philosophy has been applied for a long time in fluid mechanics, in particular in the field of inkjet printing. First introduced commercially by Siemens in 1951, continuous inkjet printers have long relied on the Rayleigh-Plateau instability (Plateau, 1873; Rayleigh, 1878) to break a liquid jet emerging from a high-pressure reservoir into a multitude of uniformly-sized droplets, some of which are subsequently deflected towards the substrate by means of an electrostatic field (Martin, Hoath & Hutchings, 2008).

Returning to solid structures, recent utilization of the solid-liquid phase transition inherent to a wide range of materials has opened new doors by enabling the harnessing of fluidic instabilities, such as the aforementioned Rayleigh-Plateau instability, in order to produce solid structures with robust and regular properties (Gallaire & Brun, 2017). In a seminal contribution, Kaufman *et al.* (2012) first adopted this idea and devised a scalable and efficient instability-mediated fabrication process for millimeter to nanometer-sized spherical particles (Rotello, 2004). The procedure begins with thermal drawing of a co-axial rod into a long and thin fiber consisting of a solid core encased in a cladding of a different material. The fiber is then exposed to a uniform heat source, inducing melting of the core and softening of the outer cladding. This, in turn, triggers a Rayleigh-Plateau instability of the core-cladding interface, which results in global break-up of the continuous core into a regular string of spherical particles. These particles are finally solidified upon cooling of the fiber and released by dissolving the cladding.

For certain materials with very high viscosity contrast ratios, such as silicon-in-silica, the above method would produce large particles relatively to the size of the inner core, restricting the smallest attainable sphere diameter. In order to overcome this limitation, Gumennik *et al.* (2013) developed a variant of the method, where instead of being uniformly heated, the fiber is fed at a given velocity into a spatially localized flame. In this way, melting of the inner silicon

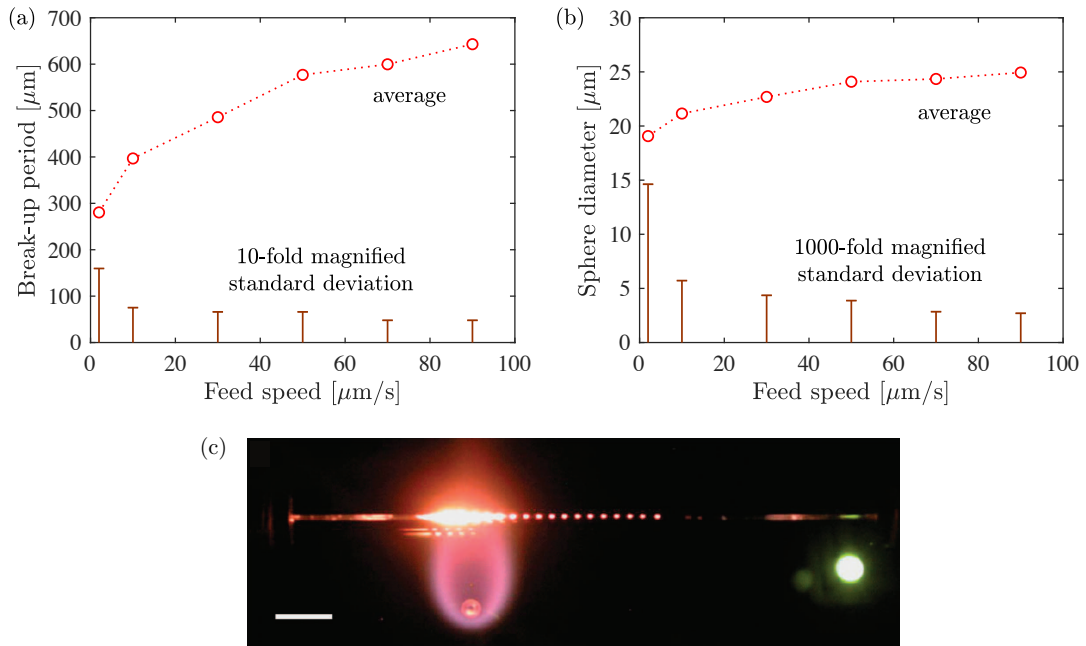


Figure 5.1 – Experimental results from Gumennik *et al.* (2013) on the production of silicon particles by feeding a silicon-in-silica co-axial fiber with a  $2\mu\text{m}$  core radius into a localized flame, triggering melting of the core and Rayleigh-Plateau instability of the silicon-silica interface. (a,b) The circles display the mean break-up period (a) and resulting sphere diameter (b) as a function of the feed speed. The bars show the standard deviation of the data, 10-fold magnified for the break-up period and 1000-fold magnified for the sphere diameter. (c) Photograph of a typical experiment, reproduced from Gumennik *et al.* (2013). The scale bar corresponds to 5 mm.

occurs locally and the formation of the spheres is dynamically coupled with the feed speed. Figure 5.1(a,b) reports the break-up period (a) and corresponding sphere diameter (b) that they obtained using silicon-in-silica fibers with a  $2\mu\text{m}$  core radius and different feed speed values. The circles show the average of the data while the bars show the 10-fold and 1000-fold magnified standard deviation of the break-up period and sphere diameter, respectively. Not only are the particle sizes reportedly smaller than achievable under an isothermal process, but there is also a clear and robust relationship between particle size and feed speed. The latter can therefore serve as a very convenient process parameter for adjusting the desired particle size, as opposed to tuning the temperature and/or material properties. Figure 5.1(c) shows a photograph of a typical experiment from Gumennik *et al.* (2013).

In this article, we try to rationalize the particle size observed in the experiments of Gumennik *et al.* (2013) as well as its dependency on the feed speed. Such understanding of the dominant physical mechanisms at play in selecting the break-up wavelength would constitute a first step towards solving the inverse problem of determining the physical parameters and conditions required to obtain a desired particle size, which is essential to enable practical use of this fabri-

cation technique. We will start by formulating a simple one-dimensional nonlinear governing equation for the motion of the silicon-silica interface, using long-wavelength approximations that have proven very accurate in the study of liquid jets (Eggers & Villermaux, 2008). We will then employ linear stability analysis to try to elucidate the characteristic size of patterns that arise in this reduced governing equation. This approach is motivated by the similitude between the system under study, where spheres are formed at the tip of the molten silicon core, and the production of droplets at the tip of a microfluidic nozzle in a co-flowing ambient liquid (Cramer, Fischer & Windhab, 2004). In the latter case, stability analysis tools have proven relevant at predicting the size of the droplets (Cordero, Gallaire & Baroud, 2011), although the effects of shear at the nozzle (Umbanhowar, Prasad & Weitz, 2000), non-uniformity of the base flow (Augello *et al.*, 2018), and nonlinearity (Pier, Huerre & Chomaz, 2001) are not entirely clear yet. As we will see later, however, linear stability analysis ultimately fails in our case. We therefore resort to a nonlinear stability analysis through numerical simulations of the reduced nonlinear governing equations, which recover, without any adjustable parameters, the relationship between sphere size and feed speed observed in figure 5.1. This eventually shows that the formation of the silicon spheres is an intrinsically nonlinear process, in a way reminiscent of the dynamics of a slowly dripping faucet which has little to do with the instability of a hypothetical continuous jet solution.

The paper proceeds as follows. In Section 5.2, we describe the setup of the problem and derive a reduced one-dimensional model consisting of two coupled nonlinear differential equations governing the dynamics of the silicon-silica interface. Section 5.3 then relates our unsuccessful attempts at predicting the particle size using linear stability analysis. Following this, we turn to numerical simulations of the nonlinear reduced model in Section 5.4, yielding good agreement with experimental results. Conclusions close the paper in Section 5.5.

## 5.2 Problem formulation

Let us consider the situation depicted in figure 5.2, which reproduces the experimental setup of Gumennik *et al.* (2013). A co-axial fiber made of a silicon core encased in a silica cladding is fed into a localized flame at a uniform velocity  $U_0$ . The local increase in temperature due to the flame causes the silicon core to melt while the silica cladding softens, at which point a capillary instability of the silicon-silica interface induces break-up of the core into regular silicon spheres. After the co-axial fiber leaves the flame, the silicon spheres re-solidify while cooling down and remain trapped within the silica matrix.

In this study, we focus on the instability mechanism leading to the formation of the spherical particles. We thus restrict our attention to the region where the silicon core is liquefied, which witnesses temperatures ranging from  $T = 1414^\circ\text{C}$ , the melting point of silicon, to  $T \approx 1760^\circ\text{C}$  in the heart of the flame. Over this temperature range, the molten silicon core has relatively constant density  $\rho_1 \approx 2500 \text{ kg/m}^3$  and viscosity  $\mu_1 \approx 7 \cdot 10^{-4} \text{ Pa.s}$ . By contrast, the silica cladding has similar density  $\rho_2 \approx \rho_1$  but much larger viscosity  $\mu_2 \approx 10^6 - 10^8 \text{ Pa.s}$ , which varies by more



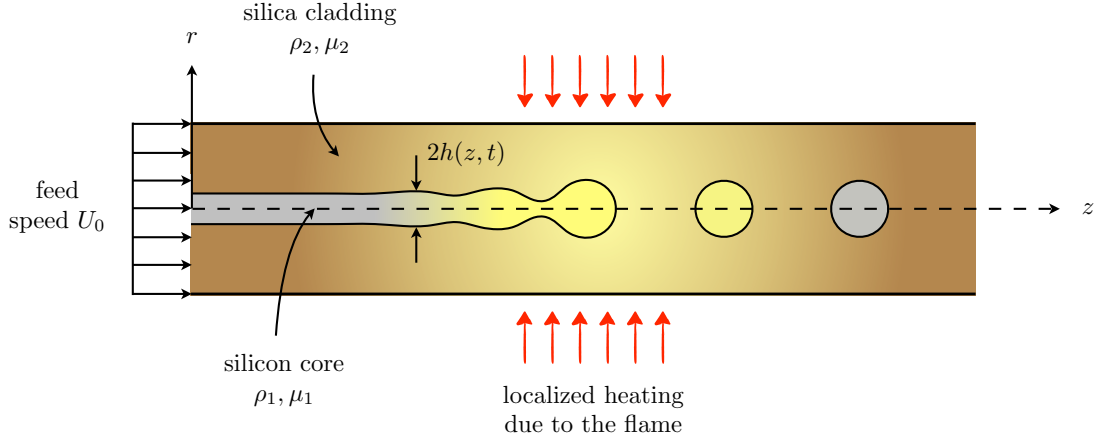


Figure 5.2 – Problem setup. A co-axial fiber consisting of a silicon core encased in a silica cladding is fed through a flame at a constant speed, causing the core to melt (pictured by the transition from gray to yellow color) while the cladding merely softens (pictured by the shift from darker to lighter brown color). Then, a capillary instability at the silicon-silica interface induces break-up of the silicon core into regular spheres, which re-solidify and remain trapped in the silica matrix upon exiting the flame. Note that the colors do not reflect the actual values of the viscosity.

than two orders of magnitude in this same temperature range. Therefore, the axial thermal gradient imposed by the flame gives rise to very strong spatial inhomogeneity in the system. Finally, the interfacial tension between silicon and silica is considered constant at  $\gamma = 1.5 \text{ N/m}$  Gumennik *et al.* (2013).

We assume the flow to be axisymmetric and denote with  $h(z, t)$  the position of the silicon/silica interface. Let  $\mathbf{u}_i = u_i(r, z, t)\mathbf{e}_z + v_i(r, z, t)\mathbf{e}_r$  and  $p_i(r, z, t)$  refer to the velocity and pressure fields in the molten silicon core ( $i = 1$ ) and outer silica ( $i = 2$ ). Before entering the flame, the system is uniformly advected at velocity  $\mathbf{u}_0 = U_0\mathbf{e}_z$  and the silicon core has constant radius  $h_0 = 2 \mu\text{m}$ , defining the base state about which perturbations will grow after melting of the inner silicon. The outer radius of the co-axial fiber is  $R = 140 \mu\text{m}$  and is assumed to remain constant throughout the development of the instability.

### 5.2.1 Equations of motion and boundary conditions

The instability of the silicon-silica interface is driven by capillary forces and counteracted by inertial and viscous effects from both the silicon core and the silica fiber. Assuming for a moment that the silicon core is not affected by the outer silica, the time scale over which the instability is slowed down by inertia and viscosity would respectively be given by  $\tau_{i,1} = (\rho_1 h_0^3 / \gamma)^{1/2} \approx 10^{-7} \text{ s}$  and  $\tau_{v,1} = \mu_1 h_0 / \gamma \approx 10^{-9} \text{ s}$ . The ratio of these time scales, called the Ohnesorge number  $Oh = \tau_{v,1} / \tau_{i,1} \approx 10^{-2}$ , shows that viscous effects in the silicon are negligible compared with inertial effects. We therefore neglect the viscosity of the silicon and

model the dynamics of the inner jet with the axisymmetric Euler equations,

$$\frac{\partial v_1}{\partial t} + v_1 \frac{\partial v_1}{\partial r} + u_1 \frac{\partial v_1}{\partial z} = -\frac{1}{\rho_1} \frac{\partial p_1}{\partial r}, \quad (5.1a)$$

$$\frac{\partial u_1}{\partial t} + v_1 \frac{\partial u_1}{\partial r} + u_1 \frac{\partial u_1}{\partial z} = -\frac{1}{\rho_1} \frac{\partial p_1}{\partial z}. \quad (5.1b)$$

On the other hand, we describe the dynamics of the outer silica with the full axisymmetric Navier-Stokes equations,

$$\frac{\partial v_2}{\partial t} + v_2 \frac{\partial v_2}{\partial r} + u_2 \frac{\partial v_2}{\partial z} = -\frac{1}{\rho_2} \frac{\partial p_2}{\partial r} + \nu_2 \left( \frac{\partial^2 v_2}{\partial r^2} + \frac{\partial^2 v_2}{\partial z^2} + \frac{1}{r} \frac{\partial v_2}{\partial r} - \frac{v_2}{r^2} \right), \quad (5.2a)$$

$$\frac{\partial u_2}{\partial t} + v_2 \frac{\partial u_2}{\partial r} + u_2 \frac{\partial u_2}{\partial z} = -\frac{1}{\rho_2} \frac{\partial p_2}{\partial z} + \nu_2 \left( \frac{\partial^2 u_2}{\partial r^2} + \frac{\partial^2 u_2}{\partial z^2} + \frac{1}{r} \frac{\partial u_2}{\partial r} \right), \quad (5.2b)$$

where  $\nu_2 = \mu_2/\rho_2$ . Since the outer radius of the fiber is two orders of magnitude larger than that of the silicon/silica interface, we consider the outer silica to be unbounded hence (5.2) holds for  $r > h(z, t)$  while (5.1) holds for  $0 \leq r < h(z, t)$ . The continuity equation for both media reads

$$\frac{\partial v_i}{\partial r} + \frac{\partial u_i}{\partial z} + \frac{v_i}{r} = 0, \quad i = 1, 2. \quad (5.3)$$

We are then left with the boundary conditions at the interface  $r = h(z, t)$ . The Laplace pressure due to surface tension imposes a discontinuity of the traction vector

$$(\boldsymbol{\sigma}_1 - \boldsymbol{\sigma}_2) \mathbf{n}|_{r=h} = -\gamma \kappa \mathbf{n}. \quad (5.4)$$

Here,  $\kappa$  is the curvature of the interface,

$$\kappa = \frac{1}{h(1+h'^2)^{1/2}} - \frac{h''}{(1+h'^2)^{3/2}}, \quad (5.5)$$

with  $h'$  and  $h''$  denoting respectively the first and second derivatives of  $h$  with respect to  $z$ ,  $\mathbf{n}$  is the outward normal to the interface,

$$\mathbf{n} = \frac{-h' \mathbf{e}_z + \mathbf{e}_r}{(1+h'^2)^{1/2}}, \quad (5.6)$$

and  $\boldsymbol{\sigma}_1, \boldsymbol{\sigma}_2$  are respectively the stress tensors in the inner and outer fluids,

$$\boldsymbol{\sigma}_1 = -p_1 \mathbf{I}, \quad (5.7)$$

$$\boldsymbol{\sigma}_2 = -p_2 \mathbf{I} + \mu_2 (\nabla \mathbf{u}_2 + \nabla \mathbf{u}_2^T). \quad (5.8)$$

The projection of the stress condition (5.4) along the normal direction gives

$$p_1 - p_2 + \frac{2\mu_2}{1+h'^2} \left[ \frac{\partial v_2}{\partial r} + \frac{\partial u_2}{\partial z} h'^2 - \left( \frac{\partial u_2}{\partial r} + \frac{\partial v_2}{\partial z} \right) h' \right] \Big|_{r=h} = \gamma \kappa. \quad (5.9)$$

The second boundary condition comes from continuity of the normal velocity of the interface with that of the two fluids

$$\frac{\partial h}{\partial t} + u_i \frac{\partial h}{\partial z} = v_i \Big|_{r=h}, \quad i = 1, 2, \quad (5.10)$$

which also ensures continuity of the normal velocity in the fluid across the interface.

### 5.2.2 Inner silicon core

The dynamics of the inner silicon jet can be simplified using a long-wavelength approximation that reduces the axisymmetric system to a one-dimensional equation (Eggers & Dupont, 1994; Eggers & Villerraux, 2008). Exploiting the fact that the radial length scale  $h_0$  of the jet is much smaller than its axial length scale  $\lambda \sim 1/k$ , where  $k$  is a typical interface deformation wavenumber, the velocity and pressure fields can be expanded in Taylor series with respect to  $r$

$$u_1(r, z, t) = \bar{u}_{10}(z, t) + \bar{u}_{12}(z, t)r^2 + \dots, \quad (5.11a)$$

$$v_1(r, z, t) = -\frac{1}{2}\bar{u}'_{10}(z, t)r - \frac{1}{4}\bar{u}'_{12}(z, t)r^3 + \dots, \quad (5.11b)$$

$$p_1(r, z, t) = \bar{p}_{10}(z, t) + \bar{p}_{12}(z, t)r^2 + \dots, \quad (5.11c)$$

where  $v_1$  is chosen to enforce incompressibility of the velocity field. Inserting these expansions into the axisymmetric Euler equations (5.1a) or (5.1b) and solving at leading order gives

$$\frac{\partial \bar{u}_{10}}{\partial t} + \bar{u}_{10} \frac{\partial \bar{u}_{10}}{\partial z} = -\frac{1}{\rho_1} \frac{\partial \bar{p}_{10}}{\partial z}, \quad (5.12)$$

while the kinematic condition (5.10) gives at lowest order

$$\frac{\partial h}{\partial t} + \bar{u}_{10} \frac{\partial h}{\partial z} = -\frac{1}{2} \frac{\partial \bar{u}_{10}}{\partial z} h. \quad (5.13)$$

These are a set of coupled one-dimensional equations for the leading-order inner fluid velocity  $\bar{u}_{10}$  and the interface position  $h$ . The pressure  $\bar{p}_{10}$ , which couples the dynamics of the inner silicon core with the outer silica through the normal stress boundary condition (5.9), remains unknown at this point.

### 5.2.3 Outer silica cladding

For the outer silica, separation of scales again enables us to simplify the governing equations. Since the outer radius  $R$  of the fiber is much larger than its axial length scale  $\lambda \sim 1/k$ , where  $k$  is a typical interface deformation wavenumber, we neglect variations of the axial velocity and suppose that it remains equal to its base flow value  $u_2 = U_0$ . In this way, we assume that perturbations to the interface position only generate a purely radial, expanding or contracting

perturbed velocity field  $v_2(r, z, t)$ . Furthermore, we will only retain terms with a linear contribution in the perturbation, with the exception of the interface curvature  $\kappa$ . Under these assumptions, the continuity equation (5.3) becomes

$$\frac{1}{r} \frac{\partial(r v_2)}{\partial r} = 0, \quad (5.14)$$

and the normal stress boundary condition (5.9) reduces to

$$\bar{p}_{10} - p_2 + 2\mu_2 \left. \frac{\partial v_2}{\partial r} \right|_{r=h} = \gamma \kappa. \quad (5.15)$$

The kinematic boundary condition (5.10) at the interface,

$$\frac{\partial h}{\partial t} + U_0 \frac{\partial h}{\partial z} = v_2 \Big|_{r=h}, \quad (5.16)$$

can be combined with the continuity equation (5.14), integrated in the radial direction, to give an explicit expression for  $v_2$  in terms of the interface deformation,

$$v_2 = \frac{h}{r} \left( \frac{\partial h}{\partial t} + U_0 \frac{\partial h}{\partial z} \right). \quad (5.17)$$

We now make the assumption that the pressure  $p_2$  in the outer silica is approximately constant. This assumption is justified in Appendix 5.6.1, where we show that solving for  $p_2$  using the momentum equation (5.2a) ultimately leads to a dispersion relation that is virtually indistinguishable from that obtained by neglecting  $p_2$ . Inserting the above expression for  $v_2$  into the normal stress condition (5.15) and setting  $p_2 = \text{cst}$  yields an expression for the leading-order inner pressure,

$$\bar{p}_{10} = \gamma \kappa + \frac{2\mu_2}{h} \left( \frac{\partial h}{\partial t} + U_0 \frac{\partial h}{\partial z} \right) + \text{cst}, \quad (5.18)$$

where the first term is the Laplace pressure jump at the interface, and the second term is the normal component of the viscous stress in the outer silica at the interface.

#### 5.2.4 Reduced nonlinear governing equations

As a final step, we insert expression (5.18) for  $\bar{p}_{10}$  into the one-dimensional equation (5.12) describing the dynamics of the inner jet. Combined with (5.13), we arrive at a coupled system of two nonlinear governing equations for the leading-order inner velocity  $\bar{u}_{10}$  and interface radius  $h$ ,

$$\frac{\partial \bar{u}_{10}}{\partial t} + \bar{u}_{10} \frac{\partial \bar{u}_{10}}{\partial z} = -\frac{\gamma}{\rho_1} \frac{\partial \kappa}{\partial z} - \frac{2}{\rho_1} \frac{\partial}{\partial z} \left[ \frac{\mu_2}{h} \left( \frac{\partial h}{\partial t} + U_0 \frac{\partial h}{\partial z} \right) \right], \quad (5.19a)$$

$$\frac{\partial h}{\partial t} + \bar{u}_{10} \frac{\partial h}{\partial z} = -\frac{1}{2} \frac{\partial \bar{u}_{10}}{\partial z} h, \quad (5.19b)$$

with the interface curvature expressed as

$$\kappa = \frac{1}{h(1+h'^2)^{1/2}} - \frac{h''}{(1+h'^2)^{3/2}}. \quad (5.20)$$

We remind the reader that  $\mu_2(z)$  is a strongly varying function of  $z$ . These two governing equations constitute a reduced nonlinear model for the motion of the interface in the silicon-in-silica fiber, and form the starting point of the subsequent analysis.

### 5.3 Linear stability analysis

In this section, we try to rationalize the droplet size experimentally observed by Gumennik *et al.* (2013) using linear stability analysis, which has been successful at elucidating the characteristic size of patterns arising from a wide range of interfacial instabilities (for a review, see Gallaire & Brun (2017)). Although the system under study is non-homogeneous due to the strong axial dependency of the silica viscosity, we perform the stability analysis in a local framework wherein the system is considered uniform at each axial location.

#### 5.3.1 Dispersion relation

We begin by deriving the dispersion relation describing the local instability characteristics of the system defined by the coupled set of equations (5.19). This is done by setting the viscosity of the outer silica to be constant and equal to  $\mu_2(z^*)$ , where  $z^*$  is the axial location of interest. The system (5.19) is then axially uniform and one can find the dispersion relation governing the growth of small perturbations to  $(h, \bar{u}_{10})$  about the base state  $(h_0, U_0)$  by considering the normal mode expansion

$$h(z, t) = h_0 + \epsilon a e^{i(kz - \omega t)}, \quad (5.21a)$$

$$\bar{u}_{10}(z, t) = U_0 + \epsilon b e^{i(kz - \omega t)}, \quad (5.21b)$$

where  $\epsilon \ll 1$ ,  $k$  and  $\omega$  are respectively the perturbation wavenumber and frequency, which may both be complex, and  $a$  and  $b$  are complex constants. Inserting the above expansion into equations (5.19) and linearizing about  $(h_0, U_0)$  leads to the dispersion relation

$$\frac{\rho_1 h_0^3}{\gamma} (\omega - U_0 k)^2 + i \frac{\mu_2 h_0}{\gamma} (k h_0)^2 (\omega - U_0 k) + \frac{1}{2} [(k h_0)^2 - (k h_0)^4] = 0. \quad (5.22)$$

Interestingly, the above dispersion relation is identical to that obtained by Eggers & Dupont (1994) for a jet with density  $\rho = \rho_1$  and viscosity  $\mu = \mu_2/3$  in an inert medium. Although both dispersion relations are obtained using the same long-wavelength approximation, the similarity is nonetheless surprising given the different forms and origins of the viscous term appearing in the reduced governing equations.

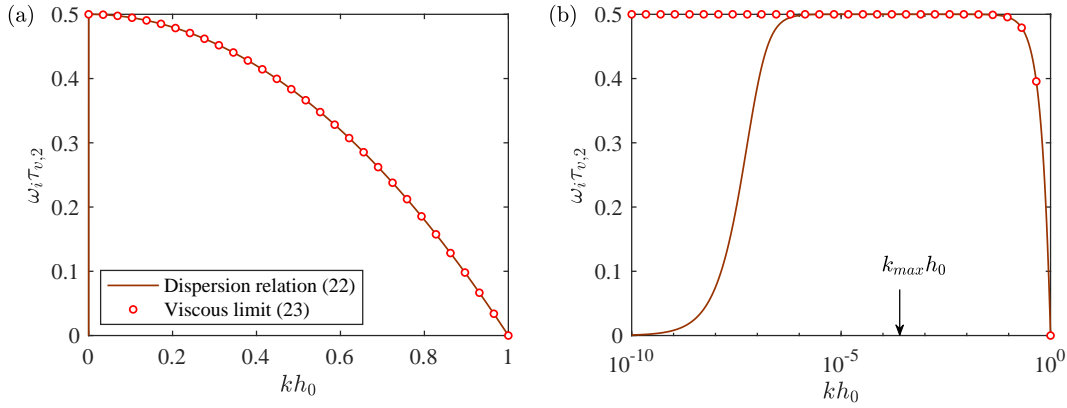


Figure 5.3 – Temporal growth rate  $\omega_i$  as a function of the real wavenumber  $k$  from the dispersion relation (5.22) and its viscous limit (5.23), in (a) linear and (b) logarithmic wavenumber scales. The most unstable wavenumber predicted by (5.22) is  $k_{max}h_0 \approx 2.40 \cdot 10^{-4}$ , while for (5.23) it is  $k_{max} = 0$ .

Before discussing wavelength selection, let us first investigate a possible simplification of the dispersion relation. Equation (5.22) shows that disturbances are driven by surface tension (third term) and simultaneously slowed down by inertia from the inner silicon (first term) and by viscous forces from the outer silica (second term). The time scale associated with the inertial term is on the order of  $\tau_{i,1} = (\rho_1 h_0^3 / \gamma)^{1/2} \approx 10^{-7}$  s while its viscous counterpart is in the range  $\tau_{v,2} = \mu_2 h_0 / \gamma \approx 1\text{--}10^2$  s depending on the local temperature of the system. The ratio of these two time scales defines a mixed Ohnesorge number  $Oh' = \tau_{v,2} / \tau_{i,1} \approx 10^7\text{--}10^9 \gg 1$ , which suggests that inertial effects are negligible. We are therefore tempted to set  $\rho_1 = 0$ , leading to the dispersion relation

$$\omega = U_0 k + i \frac{\gamma}{2\mu_2 h_0} [1 - (kh_0)^2], \quad (5.23)$$

which represents the purely viscous limit of (5.22).

### 5.3.2 Temporal stability

First, we compare the dispersion relations (5.22) and (5.23) on the basis of their temporal stability predictions. The temporal growth rate of perturbations is given by  $\omega_i$ , the imaginary part of  $\omega$ , for real values of  $k$ . Figure 5.3 presents  $\omega_i$  – nondimensionalized with the viscous time scale  $\tau_{v,2} = \mu_2 h_0 / \gamma$  – as a function of the dimensionless wavenumber  $kh_0$ , for  $\mu_2 = 10^6$  Pa.s and all other parameters as given in Section 5.2. This value of  $\mu_2$  is representative of the heart of the flame, where the silica viscosity is lowest hence the interface most unstable. It is therefore not unreasonable to assume that this region will play the largest role in setting the length scale of the resulting spheres. Results are shown for the dispersion relation (5.22) together with its viscous limit (5.23), in linear (a) and logarithmic (b) wavenumber scale. Even

though the agreement between the two dispersion relations is excellent for  $kh_0 > 10^{-5}$ , the viscous limit (5.23) predicts that the most amplified wavenumber is  $k_{max} = 0$ . This makes it ill-posed, since such a wavenumber would correspond to an infinite disturbance wavelength. On the other hand, (5.22) predicts a maximum growth rate at  $k_{max}h_0 \approx 2.40 \cdot 10^{-4}$ .

We now investigate the implications of these results for wavelength selection, which in the temporal framework is dictated by the temporally most unstable wavenumber  $k_{max}$ . Using  $h_0 = 2 \mu\text{m}$ , the value of  $k_{max}$  predicted by (5.22) corresponds to a wavelength  $\lambda_m = 2\pi/k_{max} \approx 52.4 \text{ mm}$  – two orders of magnitude larger than the break-up period reported by Gumennik *et al.* (2013) over a range of advection velocities  $U_0$ , see figure 5.1. Furthermore, the temporal stability predictions for the instability wavelength selected by the system are also insensitive to the advection velocity  $U_0$ , contrary to the observations reported in figure 5.1.

### 5.3.3 Spatio-temporal stability

We now turn to a spatio-temporal stability analysis, which generalizes the previous temporal analysis by taking into account the effect of the advection velocity  $U_0$  of the system on its stability properties and selected perturbation wavelength. In this framework, one characterizes the impulse response of the system to a localized perturbation, which generates a coherent wave packet that will grow in time and space as long as the system is temporally unstable. The asymptotic spatio-temporal behavior of this wave packet in the laboratory frame will naturally depend on the advection velocity of the system, and can be described in terms of an absolute wavenumber  $k_0$  and absolute frequency  $\omega_0$ . These are defined by the following saddle point condition together with the dispersion relation (Huerre & Monkewitz, 1990)

$$\frac{d\omega}{dk}(k_0) = 0, \quad \omega_0 = \omega(k_0), \quad (5.24)$$

where both  $k_0$  and  $\omega_0$  are allowed to be complex. The imaginary part  $\omega_{0i}$  of the absolute frequency  $\omega_0$  characterizes the temporal evolution of the impulse response wave packet observed at a fixed spatial location. Its sign therefore determines the spatio-temporal instability behavior of the system in the laboratory frame. If  $\omega_{0i} > 0$ , then the system is absolutely unstable – localized perturbations grow fast enough to overcome system advection and eventually invade the entire domain. If  $\omega_{0i} < 0$ , then the system is convectively unstable – localized perturbations are convected away before they are able to grow in the laboratory frame.

Here, we calculate the absolute wavenumber  $k_0$  and frequency  $\omega_0$  of the silicon-in-silica fiber using Bers' pinch point condition Bers (1983), an equivalent set of equations to (5.24) that avoids the need to express  $\omega$  as a function of  $k$ , and takes the form

$$\frac{\partial \Delta}{\partial k}(k_0, \omega_0) = 0, \quad \Delta(k_0, \omega_0) = 0, \quad (5.25)$$

where  $\Delta(k, \omega) = 0$  is the local dispersion relation of the system. We apply the above pinch point condition to the dispersion relation (5.22). First, we define the dimensionless frequency

$\tilde{\omega} = \omega \tau_{v,2}$  and wavenumber  $\tilde{k} = kh_0$ , so that (5.22) becomes, in nondimensional form,

$$\Delta(\tilde{k}, \tilde{\omega}) = \frac{1}{Oh'^2} (\tilde{\omega} - Ca\tilde{k})^2 + i\tilde{k}^2 (\tilde{\omega} - Ca\tilde{k}) + \frac{1}{2} (\tilde{k}^2 - \tilde{k}^4) = 0, \quad (5.26)$$

with  $Oh' = \mu_2 / \sqrt{\rho_1 \gamma h_0}$  the mixed Ohnesorge number defined in Section 5.3.1, and  $Ca = \mu_2 U_0 / \gamma$  the capillary number. Then, the first equation in condition (5.25) directly follows as

$$\frac{\partial \Delta}{\partial \tilde{k}}(\tilde{k}, \tilde{\omega}) = -2 \frac{Ca}{Oh'^2} (\tilde{\omega} - Ca\tilde{k}) + 2i\tilde{k}(\tilde{\omega} - Ca\tilde{k}) - iCa\tilde{k}^2 + (\tilde{k} - 2\tilde{k}^3) = 0. \quad (5.27)$$

As before, the results that we will obtain for given values of  $Oh'$  and  $Ca$  must be interpreted locally, in the sense that they relate to specific axial stations in the system. The axial dependency of the silica viscosity  $\mu_2$  imparts an axial variation to both  $Oh'$  and  $Ca$ .  $Oh'$  decreases from  $10^9$  to about  $10^7$  as the fiber enters the flame, independently of the feed speed  $U_0$ . The latter, however, affects the range of values of  $Ca$ . For feed velocity  $U_0 = 1 \mu\text{m/s}$ ,  $Ca$  decreases from  $10^2$  to about 1, while for high feed velocity  $U_0 = 100 \mu\text{m/s}$ ,  $Ca$  correspondingly decreases from  $10^4$  to about  $10^2$ .

We solve the coupled system of equations (5.26) and (5.27) for  $Oh' = 10^7$  and various values of  $Ca$  using a Newton-Raphson iterative scheme with tolerance  $10^{-15}$  on the  $L_2$  norm of the residual. For each value of  $Ca$ , we find that there are two absolute wavenumber and absolute frequency pairs  $(\tilde{k}_0, \tilde{\omega}_0)$  that solve the pinch point condition. These two solution branches are shown in figure 5.4(a) by the red lines labelled branch 1 and branch 2, which trace out (in the direction of the arrow) the locus of absolute wavenumbers  $\tilde{k}_0$  in the complex  $\tilde{k}$ -plane as  $Ca$  is increased from 0 to 2. In the same figure, we display for  $Ca = 0$  the contour levels of  $\tilde{\omega}_i(\tilde{k})$ , the imaginary part of  $\tilde{\omega}$  obtained by solving the dispersion relation (5.26) for complex values of  $\tilde{k}$ . In accordance with the saddle point condition (5.24), which states that  $\tilde{k}_0$  is a saddle point of  $\tilde{\omega}_i(\tilde{k})$ , we observe that the start points of both red curves coincide with a saddle point of the dispersion relation. In the case of branch 1, this saddle point actually corresponds to the temporally most unstable wavenumber  $k_{max}$  identified in the previous section.

Figures 5.4(b)–(e) display the absolute wavenumber  $\tilde{k}_0$  and absolute frequency  $\tilde{\omega}_0$  pertaining to branches 1 and 2 as a function of  $Ca$ , for  $Oh' = 10^7$  and  $10^9$ . The convective or absolute instability behavior of the system for specific values of  $Oh'$  and  $Ca$  is given by the sign of  $\tilde{\omega}_{0i}$ , the imaginary part of the absolute frequency  $\tilde{\omega}_0$ . In our case, however, there are two solution branches that lead to different characterizations. According to branch 1, the system remains absolutely unstable for  $Ca$  between 0 and 2 since  $\tilde{\omega}_{0i}$  is always positive. By contrast, branch 2 indicates a transition from absolute to convective instability with  $\tilde{\omega}_{0i}$  turning negative at  $Ca = 1$ . Since the local spatio-temporal instability behavior of the system is generally dictated by the saddle point with highest  $\tilde{\omega}_{0i}$ , figure 5.4 suggests that branch 1 is the most relevant one for all finite values of  $Ca$ .

In the context of pattern formation, the distinction between absolute and convective instability is crucial for wavelength selection (Duprat, Ruyer-Quil, Kalliadasis & Giorgiutti-Dauphiné,



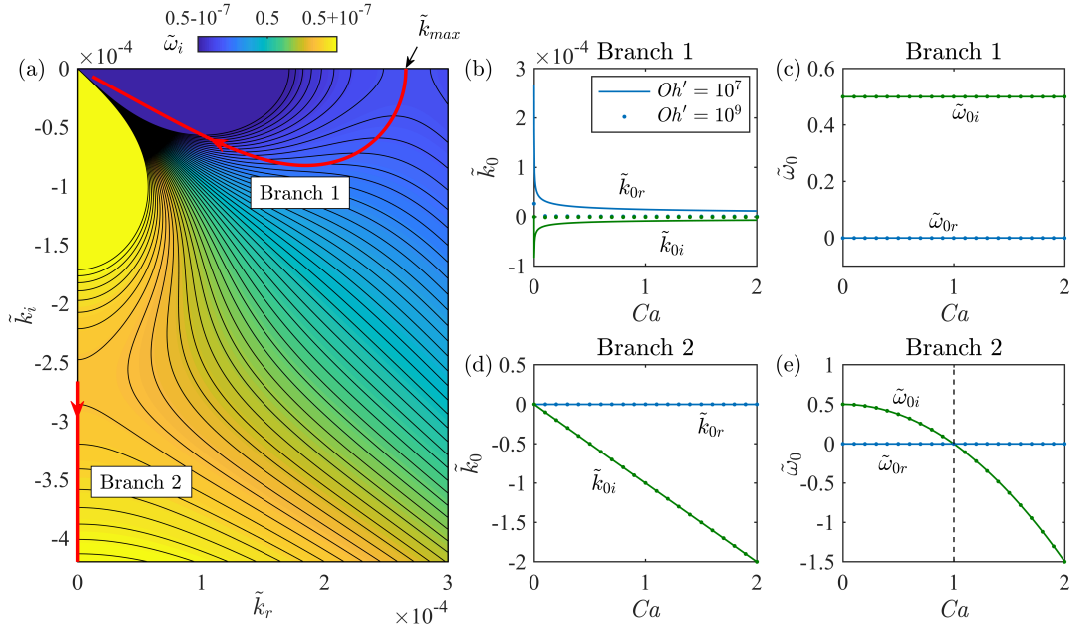


Figure 5.4 – Spatio-temporal stability properties of the dispersion relation (5.22). (a) Level curves of  $\tilde{\omega}_i$  as a function of complex  $\tilde{k}$  for  $Ca = 0$  and  $Oh' = 10^7$ , given by (5.26). The red lines trace out the locus of absolute wavenumbers  $\tilde{k}_0$  as  $Ca$  is increased from 0 to 2, which is obtained from the coupled system of equations (5.26) and (5.27). There are two solution branches, denoted here branch 1 and branch 2. (b)–(e) Absolute wavenumber  $\tilde{k}_0$  and absolute frequency  $\tilde{\omega}_0$  pertaining to these two solution branches as a function of  $Ca$ , for  $Oh' = 10^7$  (solid line) and  $Oh' = 10^9$  (dots).

2007; Gallaire & Brun, 2017), even in systems with streamwise-varying properties. Flows which locally undergo a transition from convective to absolute instability at some downstream station exhibit a saturated pattern with a well-defined wavelength given by  $2\pi U_0/\omega_{0r}$ , where  $\omega_{0r}$  is the real part of the local absolute frequency  $\omega_0$  at the upstream boundary of the absolute instability region (Pier, Huerre, Chomaz & Couairon, 1998; Pier & Huerre, 2001). Conversely, flows which are convectively unstable everywhere amplify incoming disturbances as the latter travel downstream, resulting in a broader distribution of pattern wavelengths. Returning to our system, we observe that the absolute frequency  $\tilde{\omega}_0$  corresponding to branch 1 is virtually unchanged as  $Oh'$  and  $Ca$  vary, with its real and imaginary parts  $\tilde{\omega}_{0r}$  and  $\tilde{\omega}_{0i}$  being equal to 0 and 0.5, respectively. We have verified that this remains true for values of  $Ca$  as large as  $10^4$ . This implies that within the operating conditions of the experiments of Gumennik *et al.* (2013), the instability is everywhere locally absolute in the region where the inner silicon is liquefied. As such, the dominant wavelength selected by the system, which is in principle determined by  $2\pi U_0/\omega_{0r}$ , is predicted to be infinite for all values of the feed speed  $U_0$ . In conclusion, it becomes clear that the behavior of small interface perturbations – governed by linear stability analysis – is irrelevant to the length scale of the resulting silicon spheres.

## 5.4 Nonlinear stability analysis

In view of the failure of linear stability analysis at predicting the break-up wavelength selected by the system, we hypothesize that nonlinear effects play a predominant role and we turn in this section to numerical simulations of the nonlinear governing equations (5.19). From here on, the inlet will refer to the melting location of the silicon core, which happens when its temperature increases above  $T = 1414^\circ\text{C}$ , the melting point of silicon.

### 5.4.1 Dimensionless governing equations

In order to nondimensionalize the governing equations (5.19), we select the silicon core inlet radius  $h_0$  as the characteristic length scale and the feed speed  $U_0$  as the characteristic velocity scale. We denote  $v = \bar{u}_{10}/U_0$  the dimensionless velocity,  $\bar{z} = z/h_0$  the dimensionless axial coordinate, and  $\bar{t} = t/(h_0/U_0)$  the dimensionless time. Additionally, in order to remove the singularity in expression (5.20) for the curvature, we describe the interface radius in terms of the dimensionless function  $f = (h/h_0)^2$ . Then, the inlet conditions translate as  $f(\bar{z} = 0, \bar{t}) = 1$  and  $v(\bar{z} = 0, \bar{t}) = 1$ . The governing equations (5.19) become

$$We \left( \frac{\partial v}{\partial \bar{t}} + v \frac{\partial v}{\partial \bar{z}} \right) = - \frac{\partial \bar{\kappa}}{\partial \bar{z}} - \frac{\partial}{\partial \bar{z}} \left[ \frac{Ca_{\bar{z}}}{f} \left( - \frac{\partial(fv)}{\partial \bar{z}} + \frac{\partial f}{\partial \bar{z}} \right) \right], \quad (5.28a)$$

$$\frac{\partial f}{\partial \bar{t}} = - \frac{\partial(fv)}{\partial \bar{z}}, \quad (5.28b)$$

$$\bar{\kappa} = \frac{(2 - f'')f + f'^2}{2(f'^2/4 + f)^{3/2}}, \quad (5.28c)$$

where  $We$  and  $Ca_{\bar{z}}$  are respectively the Weber and axially-dependent capillary numbers. Here, the Weber number, expressed as  $We = \rho_1 h_0 U_0^2 / \gamma$ , measures the relative importance of the kinetic energy of the silicon core with respect to the silicon-silica interfacial energy. The axially-dependent capillary number, expressed as  $Ca_{\bar{z}} = \mu_2(\bar{z}) U_0 / \gamma$ , compares the viscous force due to the spatially-varying outer silica viscosity with the silicon-silica surface tension force. We now proceed, in the next section, to the description of the numerical scheme used for solving (5.28).

### 5.4.2 Numerical scheme

The governing equations (5.28) are first discretized in space, after which the resulting ODEs are integrated in time. Diffusion terms are evaluated using second-order finite differences, with a central scheme for intermediate nodes and a forward or backward scheme for boundary nodes. Advection terms are obtained using a weighted upwind scheme inspired by Spalding's hybrid difference scheme Spalding (1972). Unlike the latter, which approximates the convective derivative using a combination of central and upwind schemes, we evaluate the derivative based on a combination of forward and backward finite differences. An advection term  $da/dz$

is evaluated at node  $i$  as

$$\left(\frac{da}{dz}\right)_i = \beta \left(\frac{da}{dz}\right)_{i,b} + (1 - \beta) \left(\frac{da}{dz}\right)_{i,f}, \quad (5.29)$$

where indices  $b$  and  $f$  refer to the backward and forward finite difference schemes, and  $\beta$  is a weight coefficient that depends on the local value of velocity  $v$  at node  $i$  together with a parameter  $\alpha$ ,

$$\beta = \frac{\tanh(\alpha v_i) + 1}{2}. \quad (5.30)$$

For the range of feed velocities considered in this study, numerical stability was always ensured by using a 10-point stencil. Thus, the backward difference term relies on a stencil that spans nodes  $i-5$  to  $i+4$ , and the forward difference term employs nodes  $i-4$  to  $i+5$ . For large enough downstream or upstream velocities,  $\beta$  will tend to 1 or 0 respectively; hence (5.29) reduces to a regular upwind difference scheme. For smaller velocity magnitudes in between, (5.29) produces a weighted combination of backward and forward differences. In our simulations, we choose  $\alpha = 50$  so that the transition between the backward and forward difference schemes mostly occurs when  $|v| < 0.05$ . Finally, advection terms at nodes close to the boundary are evaluated based on the values of the closest 9 adjoining nodes.

After obtaining all spatial derivatives, the resulting ODEs are integrated using the MATLAB solver `ode23tb`, which implements a trapezoidal rule and backward differentiation formula known as TR-BDF2 (Bank *et al.*, 1985), and uses a variable time step to reduce the overall simulation time. The jet interface is initialized as a cylinder of constant radius (equal to the inner core inlet radius  $h_0$ ) and constant velocity (equal to feed speed  $U_0$ ), that is  $f(z, 0) = 1$  and  $v(z, 0) = 1$ . The boundary conditions at the inlet are defined as  $f(0, t) = 1$  and  $v(0, t) = 1$ . No boundary conditions are defined at  $z = L$ , where  $L$  is the size of the spatial domain.

At every time step, the solution is evaluated for three conditions: (i) *Pinch-off (break-up)*: It is defined as when the value of  $f$  passes below a threshold value of  $10^{-5}$ . The corresponding time  $T_{po}$  is saved and the position of the jet tip is updated as  $N_{tip} = N_{po}$ , where  $N_{po}$  is the pinch-off location. The solution for  $f$  and  $v$  beyond  $N_{tip}$  is set to zero. For subsequent time steps,  $N_{tip}$  has two possibilities – it can either advance or recede, which requires the following two conditions. (ii) *Advancing jet*: The values of  $f$  at nodes  $N_{tip} - 1$  and  $N_{tip}$  are extrapolated to find  $f$  at  $N_{tip} + 1$ . If the extrapolated value is larger than a predefined value of  $5 \cdot 10^{-3}$ , the parameter  $N_{tip}$  is incremented by 1, and  $f$  and  $v$  at the new  $N_{tip}$  are assigned values extrapolated from its previous two neighbours. (iii) *Receding jet*: If the value of  $f$  at  $N_{tip}$  falls below a predefined value of  $10^{-3}$ ,  $f$  and  $v$  at  $N_{tip}$  are set to zero and the parameter  $N_{tip}$  is reduced by 1. These three conditions enable the numerical integration of the governing equations in a way that captures accurately the break-up of the jet and the motion of the tip.

A validation of the code is presented in Appendix 5.6.2. In the next section, we discuss the parameter values and domain size that we selected for our numerical simulations, in order to

resemble the experimental conditions of Gumennik *et al.* (2013).

### 5.4.3 Numerical domain and parameter values

We first deduce the values of  $We$  and  $Ca_{\bar{z}}$  corresponding to the operating conditions of Gumennik *et al.* (2013). In their experiments, a silicon-in-silica co-axial fiber is fed into a flame at a constant speed  $U_0$ , which varies between 1 and 100  $\mu\text{m/s}$ . Since the flame is located slightly downstream of the inlet, the temperature of the co-axial fiber changes along its axial direction. Gumennik *et al.* (2013) state that the temperature increases over a length of 5 mm, from  $T = 1414^\circ\text{C}$  at the inlet, corresponding to the liquefaction point of silicon, to  $T \approx 1760^\circ\text{C}$  in the heart of the flame. This affects the temperature-dependent silica viscosity  $\mu_2$ , which becomes a function of the axial coordinate. Correlating the temperature profile along the axial direction, shown in figure 5.5(a), with the relationship between silica viscosity and temperature, shown in figure 5.5(b), the profile of silica viscosity along the axial direction can be obtained in figure

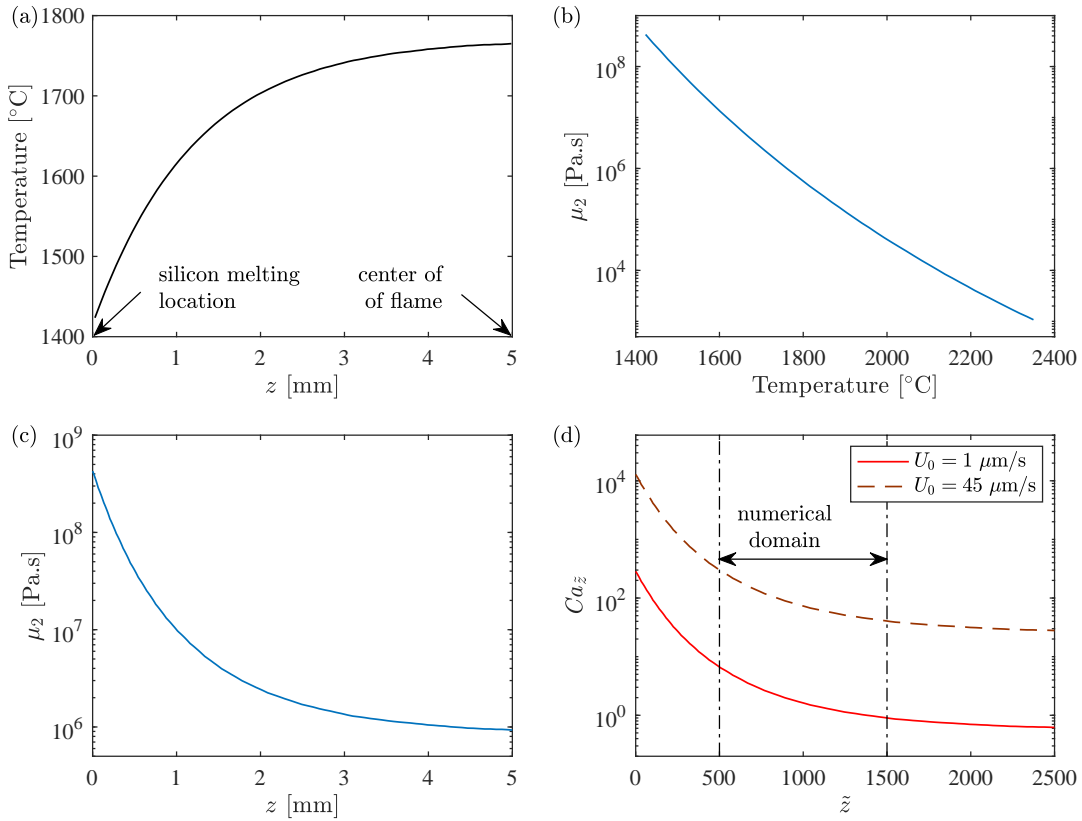


Figure 5.5 – (a) Axial temperature profile between the liquefaction point of silicon and the center of the flame. (b) Silica viscosity  $\mu_2$  as a function of temperature. Both plots are taken from Gumennik *et al.* (2013). (c) Silica viscosity profile along the axial direction. (d) Capillary number  $Ca_{\bar{z}}$  as a function of dimensionless axial coordinate, for  $U_0 = 1 \mu\text{m/s}$  and  $45 \mu\text{m/s}$ . The dash-dotted lines indicate the extent of the numerical domain.

5.5(c). Note that the data in figures 5.5(a)–(b) is from Gumennik *et al.* (2013). Observe that  $\mu_2$  decreases by more than two orders of magnitude, from  $10^8$  to  $10^6$  Pa.s, over a few millimeters.

Based on the physical parameters, the Weber number  $We$  lies between  $10^{-11}$  and  $10^{-13}$  depending on the feed speed  $U_0$ , which is computationally out of reach. Nevertheless, we show in Appendix 5.6.3 that the break-up location and period are  $We$ -independent in the numerically-tractable range  $0.005 < We < 0.1$ . Thus, below a certain limit, the Weber number can be seen as a numerical artefact which has a negligible influence on the droplet size in comparison to the capillary number. We henceforth pick  $We = 0.05$  in our simulations, regardless of the feed speed  $U_0$ . The capillary number  $Ca_{\tilde{z}}$  inherits the axial dependency of the silica viscosity  $\mu_2(z)$ , and therefore decreases by more than two orders of magnitude along the fiber. Furthermore,  $Ca_{\tilde{z}}$  scales linearly with the feed speed  $U_0$ . For instance, as shown in figure 5.5(d),  $Ca_{\tilde{z}}$  decreases from 284 to 0.62 for  $U_0 = 1 \mu\text{m/s}$ , while it decreases from 12800 to 27.9 for  $U_0 = 45 \mu\text{m/s}$ .

Finally, we restrict the size of the numerical domain considered in the simulations in order to render the computational time tractable, as explained in Appendix 5.6.4. Starting from the domain  $\tilde{z} \in [0, 2500]$  between the melting location of the silicon and the heart of the flame, we eliminate the region  $\tilde{z} < 500$  in order to avoid high capillary numbers  $Ca_{\tilde{z}}$  that would require prohibitively expensive computations. We also ignore the region  $\tilde{z} > 1500$  since the jet breaks up before then. This leads us to the truncated domain  $\tilde{z} \in [500, 1500]$  pictured in figure 5.5(d), in which we perform all the simulations shown in the next section using  $We = 0.05$  and  $U_0$ -dependent  $Ca_{\tilde{z}}$  profiles, such as those overlaid in the same figure.

### 5.4.4 Numerical results

Using the numerical scheme described in Section 5.4.2, together with the numerical domain and parameter values presented in Section 5.4.3, we compute solutions to the nonlinear governing equations (5.28) for different feed speeds  $U_0$ . The simulations are run for a sufficiently long time to enter a quasi-steady regime wherein the jet breaks up at regular intervals of time and at the same axial location. In this regime, figure 5.6 shows cascade plots of the evolution of the silicon-silica interface at fixed time intervals and over two consecutive break-up periods, for two different feed speeds of (a)  $10 \mu\text{m/s}$  and (b)  $40 \mu\text{m/s}$ . The interface is plotted in terms of the dimensionless silicon core radius  $\tilde{h} = h/h_0$ , and the red bar corresponds to a horizontal length scale of 5 dimensionless units. Note that the jets have very slender profiles – their dimensionless inlet diameter is equal to 2, whereas they travel over an axial distance of approximately one thousand. Indeed, for  $U_0 = 10 \mu\text{m/s}$ , the tip reaches a maximum dimensionless axial distance of 880 and the break-up occurs at around 750. With a higher feed speed of  $40 \mu\text{m/s}$ , the tip is capable of reaching a distance of 1400 with break-up taking place at around 1100. The magnified plots to the right show the shape of the jet tip right after break-up, with equal length scale employed for the horizontal and vertical axes.

In the quasi-steady regime, a minimum of eight consecutive break-up (or pinch-off) times  $T_{po}$

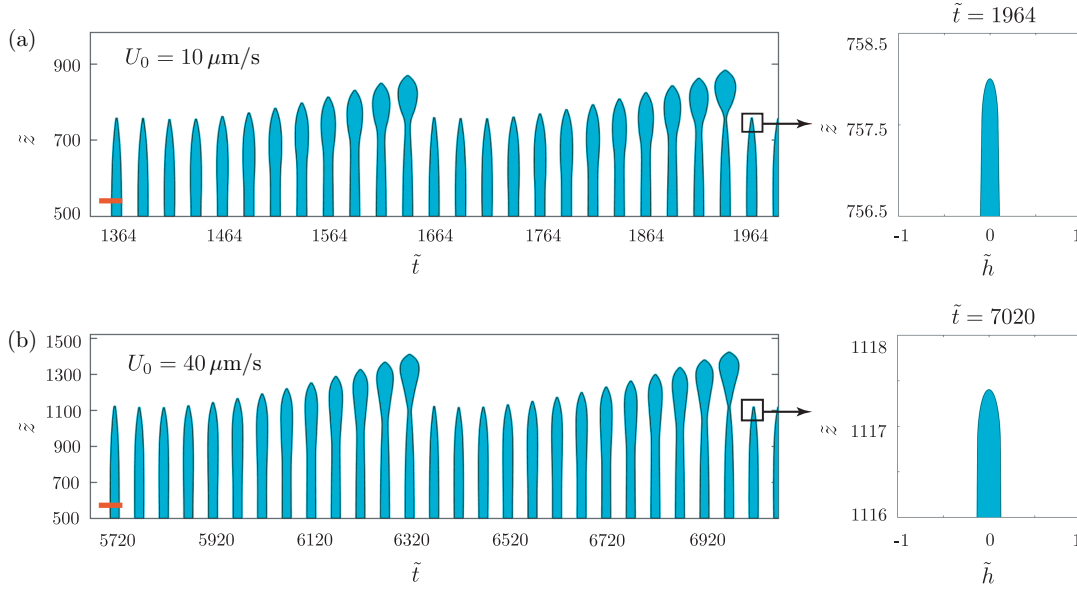


Figure 5.6 – Cascade plots of the evolution of the silicon-silica interface for feed speeds (a)  $U_0 = 10 \mu\text{m/s}$  and (b)  $U_0 = 40 \mu\text{m/s}$ . The dimensionless silicon core radius  $\tilde{h} = h/h_0$  is plotted at fixed time intervals, and the red bar corresponds to a horizontal length scale of 5 dimensionless units. The magnified plots to the right show the shape of the jet tip right after break-up, with equal length scale for the horizontal and vertical axes.

are saved. These values are then used to calculate the break-up period  $\Delta T_{po}$ , which is defined as the average time between two consecutive pinch-offs. Figure 5.7 shows the dimensional break-up period  $\Delta T_{po}$  as a function of the feed speed  $U_0$ , as well as the dimensional distance  $\lambda_{po} = U_0 \Delta T_{po}$  traveled by the fiber over one break-up period. In order to explain the decrease of  $\Delta T_{po}$  with  $U_0$ , we recall from figure 5.6 that as  $U_0$  increases, the co-axial fiber travels farther into the domain and closer to the center of the flame. There, the lower silica viscosity results in enhanced capillary instability of the interface, causing faster jet break-up and hence smaller break-up periods as reported in figure 5.7(a). The sublinear trend displayed by the distance traveled  $\lambda_{po}$  in figure 5.7(b) is also explained by the decrease of  $\Delta T_{po}$  with  $U_0$ . Note that even though  $\lambda_{po}$  reaches dimensions comparable to the size of the numerical domain, the break-up always occurs within the latter. This is because part of the mass influx between two consecutive break-ups contributes to a radial expansion of the silicon core, as seen in figure 5.6.

In order to compare our numerical observations with the experimental results of Gumennik *et al.* (2013), we calculate the diameter  $D$  of the silicon spheres resulting from the break-up process using the mass conservation equation

$$\pi h_0^2 \lambda_{po} = \frac{\pi}{6} D^3. \quad (5.31)$$

Figure 5.8 displays the sphere diameter  $D$  as a function of the feed speed  $U_0$  for our simu-

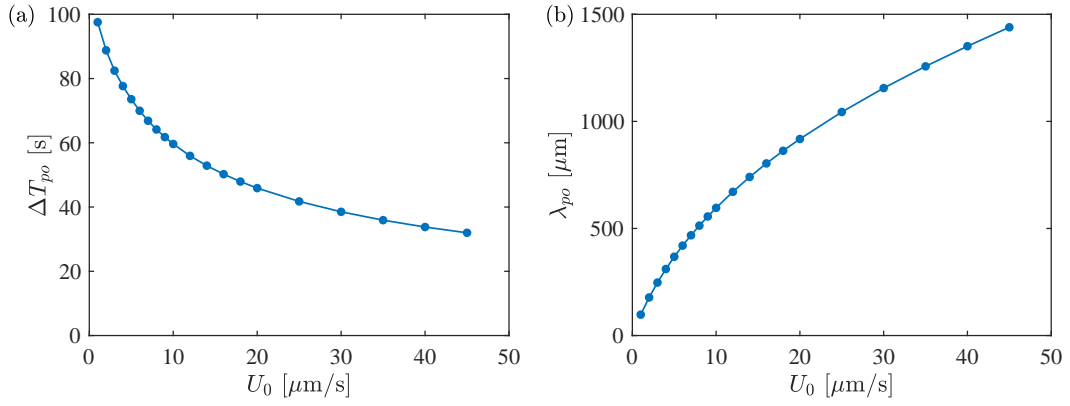


Figure 5.7 – (a) Break-up period  $\Delta T_{po}$  and (b) distance travelled by the co-axial fiber over one break-up period,  $\lambda_{po} = U_0 \Delta T_{po}$ , as a function of the feed velocity  $U_0$ .

lations and for the experiments of Gumennik *et al.* (2013). We observe a good qualitative agreement between the two sets of data, with the governing equations (5.28) being able to capture the increase in sphere diameter with feed speed, as well as its saturation at high feed speeds. Furthermore, the drop diameter predicted by the numerics is roughly comparable in magnitude to that observed in experiments, which is remarkable given that not a single fitting parameter has been used in our calculations.

There are different reasons that could explain the discrepancy between our numerical results and the experiments. First, although the temperature profile that we considered in figure 5.5(a) comes from Gumennik *et al.* (2013), it was not directly measured from their experiments. Second, we noted in Appendix 5.6.4 that truncating part of the entrance region out of the numerical domain results in a significant – albeit unavoidable – error at low feed speeds. Yet, this error becomes negligible for larger feed speeds, and hence we mostly attribute the

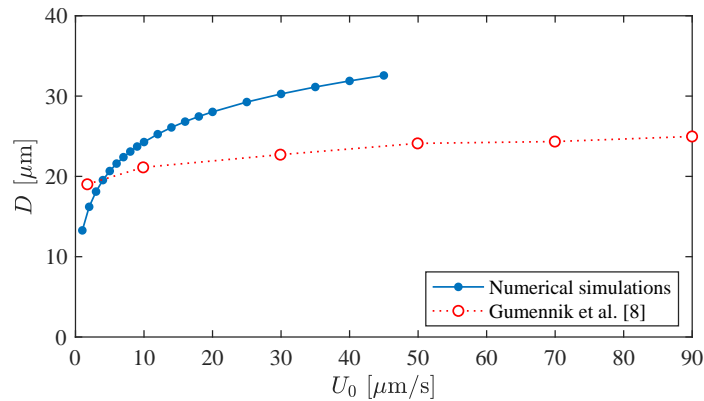


Figure 5.8 – Mean silicon sphere diameter  $D$  as a function of the feed speed  $U_0$ . Comparison between our numerical simulations of (5.28) and experimental data by Gumennik *et al.* (2013).

discrepancy between the results to the effects of surface tension. The latter is assumed to be equal to  $1.5 \text{ N/m}$ ; however, Gumennik *et al.* (2013) evaluated this value based on Kroll & Schulte (2006), in which a range  $\gamma = 1.5 \pm 0.3 \text{ N/m}$  is actually given. In fact, we show in Appendix 5.6.5 that surface tension has a non-negligible effect on the sphere size, with the two being inversely proportional to each other. Additionally, we assumed that the surface tension at the silicon-silica interface remains constant over the entire temperature range of  $1414 - 1760^\circ\text{C}$ , unlike the viscosity of silica. In reality, studies show that the surface tension of silica in air (Kingery, 1959) and silicon in air (Shishkin & Basin, 2004; Yuan, Mukai, Takagi, Ohtaka, Huang & Liu, 2002; Hibiya, Nakamura, Mukai, Niu, Imaishi, Nishizawa, Yoda & Koyama, 1998) can vary between  $0.28 - 0.3 \text{ N/m}$  and  $0.7 - 0.9 \text{ N/m}$ , respectively, over a temperature range of  $1400 - 1800^\circ\text{C}$ . Thus, a precise estimation of the surface tension at the silica-silicon interface could possibly lead to more accurate sphere size predictions.

## 5.5 Conclusions and perspectives

In this article, we have tried to elucidate the physical mechanisms responsible for selecting the size of spherical silicon particles in the experimental setup of Gumennik *et al.* (2013). Such particles are obtained by feeding a silicon-in-silica co-axial fiber into a flame at a certain speed, triggering local melting of the silicon and Rayleigh-Plateau instability of the silicon-silica interface. We first derived a reduced model for the motion of the interface, consisting of two coupled one-dimensional nonlinear equations (5.19). Then, we analyzed the dynamics and dominant length scale of the instability that arises in this model using local linear stability analysis in its temporal and spatio-temporal flavors. Ultimately, however, we reached the conclusion that such linearized tools fail at predicting the particle size observed experimentally. Finally, we performed numerical simulations of the reduced nonlinear model. Without any adjustable parameters, we were able to recover in these simulations the particle size observed experimentally by Gumennik *et al.* (2013), as well as its qualitative behavior as the feed speed of the fiber is changed.

Recalling the failure of the linear stability predictions, the success of the nonlinear analysis suggests that nonlinear effects play a predominant role in selecting the size of the silicon spheres. In other words, the break-up wavelength is largely independent of the initial growth of infinitesimal perturbations to the silicon-silica interface, which is contrary to the behavior of most pattern-forming systems (Cross & Hohenberg, 1993; Gallaire & Brun, 2017). One might argue that the strong non-uniformity of the system – imparted by the axial variation of silica viscosity over more than two orders of magnitude – may explain the failure of local linear stability analysis. A global stability analysis would take such non-uniformity into account; however, numerical convergence of the resulting eigenvalue problem will be problematic due to the extreme variation in silica viscosity. Nonetheless, we are confident that the good agreement observed between the numerical simulations and the experiments in figure 5.8 is by and large attributable to the nonlinearity of the viscous term originating from the outer silica, as opposed to the axial variation of the silica viscosity itself.



To prove this point, we compared in Appendix 5.6.6 numerical simulations of equations (5.28) for a silicon-in-silica fiber at constant capillary number with numerical simulations of equations (5.40) for a jet in an inert medium. Both simulations were performed in the low Weber number limit  $We = 0.01$ , and using  $Ca = 1$  and  $1/3$  for (5.28) and (5.40), respectively. In this way, the dispersion relations of both equations are identical – that is, their linear stability properties are indistinguishable. Even so, we were surprised to observe that their nonlinear behaviors are markedly different: as shown in figure 5.14, equations (5.28) for the silicon-in-silica fiber produce regularly-spaced droplets, while equations (5.40) for the jet in an inert medium lead to the formation of one ever-growing pendant drop. Given that the only difference between these two sets of equations is the nonlinear form of the viscous term, we conclude that the length scale of the droplets produced in the silicon-in-silica fiber is really set by the nonlinearity of the viscous contribution from the outer silica<sup>1</sup>. Thus, we hypothesize that the latter might amount to some kind of body force that pinches off droplets once they grow big enough, in the same spirit as the dynamics of a dripping faucet (Michael & Williams, 1976; Peregrine, Shoker & Symon, 1990).

## 5.6 Appendix

### 5.6.1 Validity of constant outer pressure assumption

In this appendix, we show that solving explicitly for the outer silica pressure – instead of assuming that it is constant, as in Section 5.2.3 – leads to governing equations with a dispersion relation that is numerically identical with (5.22). First, we note that under the assumption that  $u_2 = U_0$  and keeping only the terms with a linear contribution in the perturbation, the Navier-Stokes momentum equation (5.2a) reduces to

$$\frac{\partial v_2}{\partial t} + U_0 \frac{\partial v_2}{\partial z} = -\frac{1}{\rho_2} \frac{\partial p_2}{\partial r} + \nu_2 \left( \frac{\partial^2 v_2}{\partial r^2} + \frac{\partial^2 v_2}{\partial z^2} + \frac{1}{r} \frac{\partial v_2}{\partial r} - \frac{v_2}{r^2} \right). \quad (5.32)$$

Next, we insert expression (5.17) for  $v_2$  inside (5.32) and, like before, we only retain the terms with a linear contribution in the perturbation to get

$$\frac{h}{r} \left( \frac{\partial^2 h}{\partial t^2} + 2U_0 \frac{\partial^2 h}{\partial t \partial z} + U_0^2 \frac{\partial^2 h}{\partial z^2} \right) = -\frac{1}{\rho_2} \frac{\partial p_2}{\partial r} + \nu_2 \frac{h}{r} \frac{\partial^2}{\partial z^2} \left( \frac{\partial h}{\partial t} + U_0 \frac{\partial h}{\partial z} \right). \quad (5.33)$$

(Here, we would like to point out that the viscous term does not cancel entirely, despite what is stated in section 3.5.1 of the review by Eggers & Villermaux (2008). This is due to the axial dependency of the radial velocity field  $v_2(r, z, t)$ , inherited from the interface height  $h(z, t)$  and overlooked by the aforementioned authors.) Equation (5.33) can now be integrated along  $r$  to find an expression for the pressure  $p_2$ , provided one has a suitable boundary condition. The harmonicity of the pressure field ensures that radial and axial length scales are comparable,

<sup>1</sup>Although a nonlinear viscous term might sound paradoxical due to the linearity of viscous diffusion, it is worth remembering that here, it is the geometric nonlinearity of the silicon-silica interface that makes the outer velocity field – hence the viscous diffusion – a nonlinear function of the interface position.

which implies that  $p_2$  decays exponentially in the radial direction over a length scale  $\lambda \sim 1/k$  when the interface is deformed by a wavenumber  $k$ . Since we are ultimately looking for the dispersion relation of the system, we thus consider that the pressure vanishes at  $r = h + 1/k$  and integrate (5.33) to obtain

$$p_2 = \rho_2 h \left( \frac{\partial^2 h}{\partial t^2} + 2U_0 \frac{\partial^2 h}{\partial t \partial z} + U_0^2 \frac{\partial^2 h}{\partial z^2} \right) \ln \left( \frac{h}{r} + \frac{1}{kr} \right) - \mu_2 h \frac{\partial^2}{\partial z^2} \left( \frac{\partial h}{\partial t} + U_0 \frac{\partial h}{\partial z} \right) \ln \left( \frac{h}{r} + \frac{1}{kr} \right). \quad (5.34)$$

Finally, we plug the above expression for  $p_2$  into the normal stress condition (5.15), which yields an expression for the leading-order inner pressure,

$$\begin{aligned} \bar{p}_{10} = & \underbrace{\rho_2 h \left( \frac{\partial^2 h}{\partial t^2} + 2U_0 \frac{\partial^2 h}{\partial t \partial z} + U_0^2 \frac{\partial^2 h}{\partial z^2} \right) \ln \left( 1 + \frac{1}{kh} \right)}_{\text{inertial term from pressure in outer silica}} - \underbrace{\mu_2 h \frac{\partial^2}{\partial z^2} \left( \frac{\partial h}{\partial t} + U_0 \frac{\partial h}{\partial z} \right) \ln \left( 1 + \frac{1}{kh} \right)}_{\text{viscous term from pressure in outer silica}} \\ & + \underbrace{\gamma \kappa}_{\text{Laplace pressure jump}} + \underbrace{\frac{2\mu_2}{h} \left( \frac{\partial h}{\partial t} + U_0 \frac{\partial h}{\partial z} \right)}_{\text{normal component of viscous stress in silica}}. \end{aligned} \quad (5.35)$$

Compared with the expression (5.18) we obtained earlier, there are here two additional contributions to the inner pressure  $\bar{p}_{10}$ . Recalling that the radial length scale  $h_0$  of the jet is much smaller than its axial length scale  $\lambda \sim 1/k$ , we have  $kh_0 \ll 1$  and a dominant balance comparison between the two viscous contributions gives

$$\frac{\text{viscous term from pressure in silica}}{\text{normal component of viscous stress in silica}} \sim \frac{1}{2} \ln \left( 1 + \frac{1}{kh_0} \right) (kh_0)^2 \ll 1. \quad (5.36)$$

The viscous term inherited from the silica pressure  $p_2$  can therefore be neglected in (5.35), leading to the simplified expression

$$\bar{p}_{10} = \rho_2 h \left( \frac{\partial^2 h}{\partial t^2} + 2U_0 \frac{\partial^2 h}{\partial t \partial z} + U_0^2 \frac{\partial^2 h}{\partial z^2} \right) \ln \left( 1 + \frac{1}{kh} \right) + \gamma \kappa + \frac{2\mu_2}{h} \left( \frac{\partial h}{\partial t} + U_0 \frac{\partial h}{\partial z} \right). \quad (5.37)$$

Combining the above expression with (5.12) and (5.13) yields

$$\begin{aligned} \frac{\partial \bar{u}_{10}}{\partial t} + \bar{u}_{10} \frac{\partial \bar{u}_{10}}{\partial z} = & \rho_2 h \left( \frac{\partial^2 h}{\partial t^2} + 2U_0 \frac{\partial^2 h}{\partial t \partial z} + U_0^2 \frac{\partial^2 h}{\partial z^2} \right) \ln \left( 1 + \frac{1}{kh} \right) \\ & - \frac{\gamma}{\rho_1} \frac{\partial \kappa}{\partial z} - \frac{2}{\rho_1} \frac{\partial}{\partial z} \left[ \frac{\mu_2}{h} \left( \frac{\partial h}{\partial t} + U_0 \frac{\partial h}{\partial z} \right) \right], \end{aligned} \quad (5.38a)$$

$$\frac{\partial h}{\partial t} + \bar{u}_{10} \frac{\partial h}{\partial z} = -\frac{1}{2} \frac{\partial \bar{u}_{10}}{\partial z} h, \quad (5.38b)$$

where  $\kappa$  is given by (5.20), and the log term is new compared with the governing equations (5.19) obtained earlier by neglecting  $p_2$ . Note that due to the presence of the wavenumber  $k$  in the log term, equations (5.38) are not governing equations in the true sense. Nonetheless,

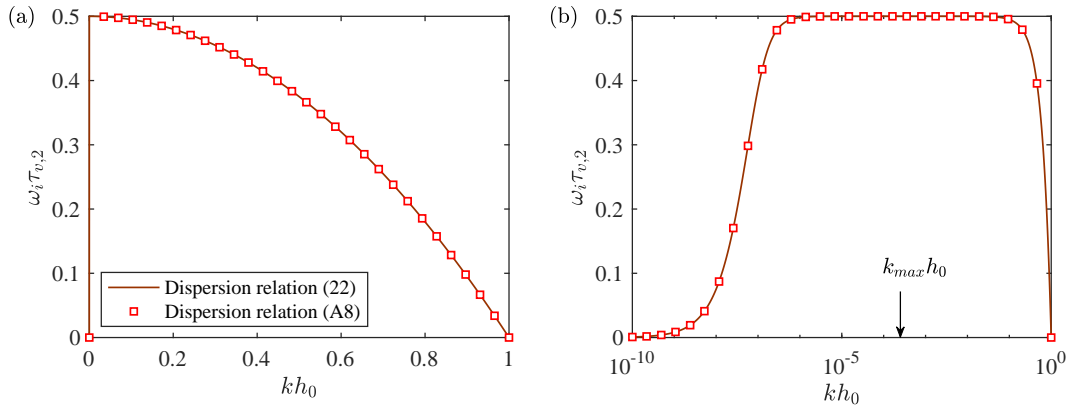


Figure 5.9 – Temporal growth rate  $\omega_i$  as a function of the real wavenumber  $k$  from the dispersion relations (5.22) and (5.39), in (a) linear and (b) logarithmic wavenumber scale. The growth rates of both (5.22) and (5.39) are maximum at  $k_{max}h_0 \simeq 2.40 \cdot 10^{-4}$ .

the corresponding dispersion relation is

$$\begin{aligned} \frac{\rho_1 h_0^3}{\gamma} \left[ 1 + \frac{1}{2} \frac{\rho_2}{\rho_1} \ln \left( 1 + \frac{1}{kh_0} \right) (kh_0)^2 \right] (\omega - U_0 k)^2 \\ + i \frac{\mu_2 h_0}{\gamma} (kh_0)^2 (\omega - U_0 k) + \frac{1}{2} [(kh_0)^2 - (kh_0)^4] = 0. \end{aligned} \quad (5.39)$$

In figure 5.9, we plot the dispersion relations (5.22) and (5.39) under the same conditions as in Section 5.3.2. The two dispersion relations are virtually indistinguishable from each other, and the maximum growth rate happens at  $k_{max}h_0 \simeq 2.40 \cdot 10^{-4}$  in both cases. This validates our assumption that  $p_2$  is approximately constant – as far as linearized dynamics are concerned, at least. Indeed, the additional log term appearing in (5.38) is nonlinear and could possibly affect the nonlinear behavior of the system. Ultimately, though, the good agreement we have obtained with the results of Gumennik *et al.* (2013) in figure 5.8 lends confidence to the constant outer pressure assumption.

### 5.6.2 Numerical code validation for a jet in an inert medium

We validate our numerical code with simulations of the reduced governing equations obtained by Eggers & Dupont (1994) for a jet with density  $\rho$  and viscosity  $\mu$  in an inert medium. These one-dimensional equations are obtained from the same long-wavelength approximation that we have used to derive the governing equations (5.28) of the silicon-in-silica jet. Written in the same nondimensional variables  $f = (h/h_0)^2$  and  $v = \bar{u}_{10}/U_0$  as in Section 5.4, they take the

form

$$We \left( \frac{\partial v}{\partial \tilde{t}} + v \frac{\partial v}{\partial \tilde{z}} \right) = - \frac{\partial \tilde{\kappa}}{\partial \tilde{z}} + \frac{3Ca}{f} \frac{\partial}{\partial \tilde{z}} \left( f \frac{\partial v}{\partial \tilde{z}} \right), \quad (5.40a)$$

$$\frac{\partial f}{\partial \tilde{t}} = - \frac{\partial(fv)}{\partial \tilde{z}}, \quad (5.40b)$$

$$\tilde{\kappa} = \frac{(2 - f'')f + f'^2}{2(f'^2/4 + f)^{3/2}}. \quad (5.40c)$$

Here,  $We = \rho h_0 U_0^2 / \gamma$  and  $Ca = \mu U_0 / \gamma$ , and  $z$  and  $t$  refer to the dimensionless axial coordinate and time, respectively. Observe that the only difference between these equations and equations (5.28) for the silicon-in-silica jet consists in the exact expression of the nonlinear viscous term (that which contains the capillary number). In (5.40), the viscous term originates from the axial velocity of the jet, while in (5.28) it is due to the radial velocity of the outer silica. Nevertheless, as pointed out in Section 5.3.1, the linear dispersion relations associated with (5.40) and (5.28) are identical, save for a factor 3 multiplying  $Ca$ .

As explained in Section 3.4.2 of Chapter 3, we validate our numerical scheme for the governing equations (5.40) using the results of van Hoeve *et al.* (2010). The validation is based on the experimental parameters, which translates to the dimensionless numbers  $Ca = 0.295$  and  $We = 8.7$ . The validated scheme is then applied for the silicone-in-silica jet by replacing the viscous term only.

### 5.6.3 Silicon-in-silica fiber with constant capillary number

In this appendix, we perform numerical simulations of the governing equations (5.28) for the silicon-in-silica co-axial fiber, but using a *constant* capillary number  $Ca$ . Such an assumption serves as a basis for understanding the behavior of the real system with spatially-varying capillary number  $Ca_{\tilde{z}}$ . Specifically, our goal here is two-fold: we show that the Weber number is a numerical artefact provided  $We$  is small enough, and we study the numerical convergence of our scheme.

We compute the jet break-up characteristics for different values of  $Ca \in [0.1, 2]$  and  $We \in [0.005, 0.1]$ . The simulation time is kept sufficiently large (about 1000 dimensionless time units) to obtain a quasi-steady regime where drops are formed at regular intervals of time and at the same distance from the nozzle exit. The domain size is fixed at  $50h_0$  for low capillary numbers but is progressively increased for higher capillary numbers. Indeed, higher capillary numbers correspond to increased viscous effects, slowing down the growth of interface perturbations and resulting in droplets forming further away from the nozzle.

Figure 5.10(a) reports the break-up radius as a function of  $Ca$ , for different values of  $We$ . Clearly, the break-up characteristics are  $We$ -independent for  $We \leq 0.05$ . Thus, approximating the break-up characteristics for any  $We$  smaller than 0.05 with the corresponding values at  $We = 0.05$  is a valid assumption, which we extend in Section 5.4 to the case of spatially-varying

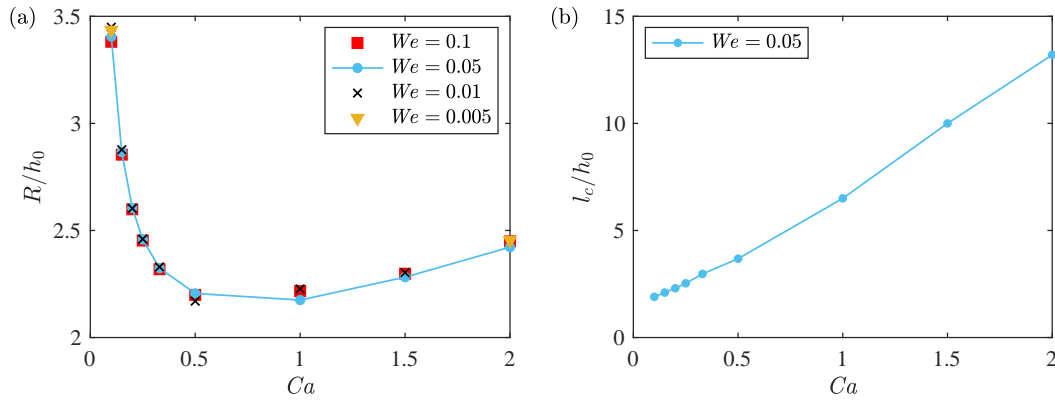


Figure 5.10 – (a) Dimensionless drop radius  $R/h_0$  as a function of constant capillary number  $Ca$ , for different values of Weber number  $We \in [0.005, 0.1]$ . (b) Dimensionless break-up length  $l_c/h_0$  as a function of constant capillary number for  $We = 0.05$ . The break-up dynamics resembles dripping at low  $Ca$  and jetting at higher  $Ca$ .

capillary number.

Note, interestingly, that the break-up period follows a non-monotonous trend as  $Ca$  is increased from 0.1 to 2. As shown in figure 5.10(b), the break-up occurs further away from the nozzle as  $Ca$  is increased, in a way that is reminiscent of a transition from dripping to jetting (Utada *et al.*, 2007). It could therefore be possible that the non-monotonicity of the curve in figure 5.10(a) is related to an absolute to convective instability transition (Guillot *et al.*, 2007). More research is needed to confirm this assertion, however, and this goes beyond the scope of this paper.

Finally, a grid size-dependency test was performed for various values of  $Ca$  and  $We = 0.05$ . It was observed that the break-up period and hence the drop radius have a weak dependence on

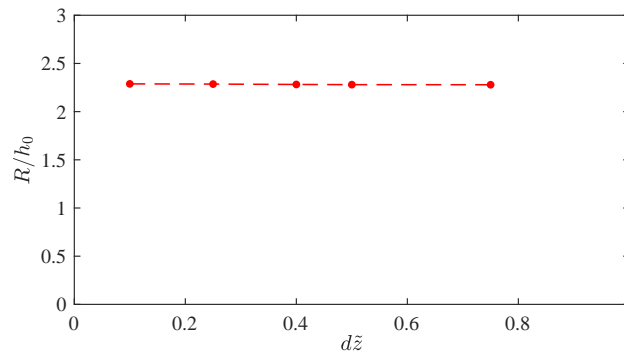


Figure 5.11 – Drop radius as a function of grid size for  $Ca = 1.5$  and  $We = 0.05$ . The results show a weak dependence of the break-up characteristics on the grid size.

the grid size, as shown in figure 5.11 for the case  $Ca = 1.5$ . As the nondimensional grid size  $d\tilde{z}$  is increased from 0.1 to 0.75, the drop radius  $R$  decreases by merely 0.39%. Thus, we selected grid sizes  $d\tilde{z}$  comprised between 0.1 and 0.56 for the simulations presented in this appendix, and between 0.45 and 0.65 for the simulations in Section 5.4.

#### 5.6.4 Selection of a truncated numerical domain

In this appendix, we describe how we select a restricted region of the total physical domain for the numerical simulations in Section 5.4, in order to balance computational cost and accuracy. Experimental observations from Gumennik *et al.* (2013) show that the jet always breaks up before reaching the heart of the flame. As a starting point, we thus restrict our attention to the 5-mm-long region between the inlet and the heart of the flame, which we denote  $\tilde{z} \in [0, 2500]$ .

In addition, we have to alter the entrance location of the numerical domain, due to the fact that our numerical scheme can only work robustly with capillary numbers  $Ca_{\tilde{z}}$  below 400. As seen in figure 5.5(d), for higher values of  $U_0$  this limit is clearly exceeded at  $\tilde{z} = 0$ . Thus, with the aim of computing drop characteristics for feed speeds up to  $U_0 = 50 \mu\text{m/s}$ , we decide to reduce the domain size to  $\tilde{z} \in [500, 2500]$ . In this way, the capillary number at  $\tilde{z} = 500$  for  $U_0 = 50 \mu\text{m/s}$  is 332, well within the computational limit. Eliminating the region  $\tilde{z} \in [0, 500]$  is a reasonable approximation since the silica viscosity in this region is large enough that the jet instability will not grow appreciably. Indeed, for feed speed  $U_0 = 25 \mu\text{m/s}$ , moving the entrance location from  $\tilde{z} = 500$  to 400 and 200 produces a relative difference in sphere size of 4.4% and 10% while the corresponding computational cost increases 2-fold and 9-fold, respectively.

Finally, we reduce the numerical domain size to  $\tilde{z} \in [500, 1500]$  on the assumption that the silica viscosity in the region  $\tilde{z} < 1500$  is sufficiently low to capture jet break-up. This assumption

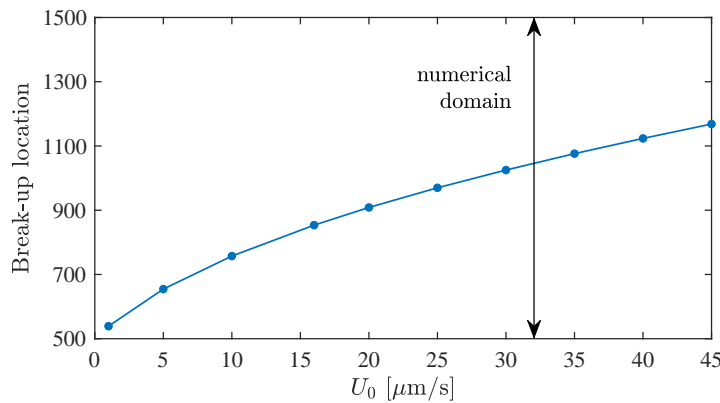


Figure 5.12 – Break-up location as a function of feed speed  $U_0$  for the truncated numerical domain  $\tilde{z} \in [500, 1500]$ . While the break-up always takes place within the truncated domain, its location progressively moves downstream and shifts towards the end of the domain as  $U_0$  is increased.

is verified by analyzing the break-up location as a function of the feed speed. Figure 5.12 shows that for feed speeds in the range of  $1 - 45 \mu\text{m/s}$ , the jet breaks up within the truncated numerical domain  $\tilde{z} \in [500, 1500]$ . Furthermore, we verified that the sphere radius obtained with feed speeds 1, 10, and  $40 \mu\text{m/s}$  did not change between domains  $\tilde{z} \in [500, 1500]$  and  $\tilde{z} \in [500, 1700]$ .

### 5.6.5 Effect of surface tension on sphere size

Here, we evaluate the effect of surface tension between silicon and silica on particle size, as predicted by our model. Figure 5.13 shows the predicted sphere diameter for three different values of the surface tension, all comprised within the error range provided by Kroll & Schulte (2006). It is observed that the sphere size is inversely proportional to the surface tension. For example, for a feed speed of  $10 \mu\text{m/s}$ , decreasing the surface tension by 20% from  $\gamma = 1.5 \text{ N/m}$  to  $1.2 \text{ N/m}$  increases the predicted sphere diameter by 4.9%, from  $D = 24.3 \mu\text{m}$  to  $25.5 \mu\text{m}$ . Conversely increasing the surface tension by 20% from  $\gamma = 1.5 \text{ N/m}$  to  $1.8 \text{ N/m}$  decreases the predicted sphere diameter by 4.1%, from  $D = 24.3 \mu\text{m}$  to  $23.3 \mu\text{m}$ . This is not surprising since a higher value of surface tension implies more driving force for the pinching, hence faster break-ups that result into smaller drop sizes.

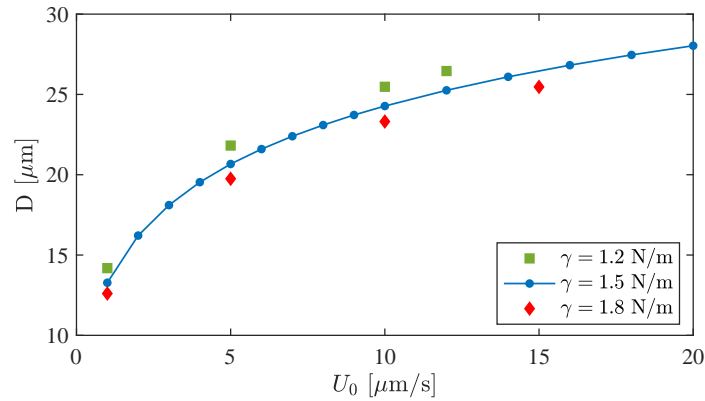


Figure 5.13 – Effect of surface tension on drop size. Relative errors of 20% in the magnitude of the surface tension can cause corresponding errors of 4–5% in the drop diameter.

### 5.6.6 Comparison of nonlinear behaviors of silicon-in-silica fiber at constant capillary number and viscous jet

The purpose of this appendix is to compare the nonlinear behavior of equations (5.28) for a silicon-in-silica fiber at constant capillary number with that of equations (5.40) for a jet in an inert medium. We consider the low Weber number limit  $We = 0.01$ , and use  $Ca = 1$  and  $1/3$  for (5.28) and (5.40), respectively, in such a way that the linear dispersion relations of the two systems are identical; the only difference between them resides in the nonlinear

form of the viscous term. In (5.28), the viscous term originates from the radial velocity of the outer silica, while in (5.40) it is due to the axial velocity of the jet. In both cases, we start from a hemispherical shape  $h/h_0 = (1 - \tilde{z}^2)^{1/2}$  and we numerically compute the evolution of the system over a thousand nondimensional time units, using a spatial grid size  $d\tilde{z} = 0.04$ . Figure 5.14 shows the resulting cascade plots of the dimensionless interface radius  $\tilde{h} = h/h_0$  at fixed time intervals for (a) equations (5.28) describing the silicon-in-silica fiber and (b) equations (5.40) describing the viscous jet.

Surprisingly, equations (5.28) for the silicon-in-silica fiber produce regularly-spaced droplets, while equations (5.40) for the viscous jet lead to the formation of one ever-growing pendant drop.

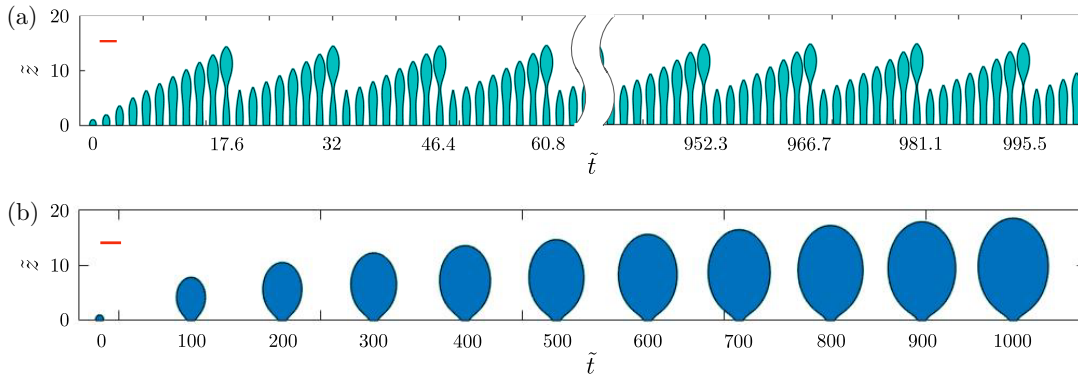


Figure 5.14 – Comparison of the nonlinear behaviors of (a) equations (5.28) for a silicon-in-silica fiber at  $We = 0.01$  and constant  $Ca = 1$ , and (b) equations (5.40) for a jet in an inert medium at  $We = 0.01$  and  $Ca = 1/3$ . The parameter values are chosen such that the two systems share the same dispersion relation, with their only difference being the nonlinear form of the viscous term. In both cases, the dimensionless interface radius  $\tilde{h} = h/h_0$  is plotted at fixed time intervals, and the red bar corresponds to a horizontal length scale of 5 dimensionless units.



## 6 Film thickness distribution in gravity-driven pancake-shaped droplets rising in a Hele-Shaw cell

**Remark** This chapter is largely inspired by the publication of the same name

Isha Shukla<sup>1</sup>, Nicolas Kofman<sup>1</sup>, Gioele Balestra<sup>1</sup>, Lailai Zhu<sup>1,2,3</sup> and François Gallaire<sup>1</sup>

<sup>1</sup>Laboratory of Fluid Mechanics and Instabilities, École Polytechnique Fédérale de Lausanne, Lausanne, CH-1015, Switzerland

<sup>2</sup>Department of Mechanical and Aerospace Engineering, Princeton University, Princeton, New Jersey 08544, USA

<sup>3</sup>Linné Flow Centre and Swedish e-Science Research Centre (SeRC), KTH Mechanics, Stockholm SE-10044, Sweden

*Journal of Fluid Mechanics* **874**(2019): 1021 – 1040

**Author contributions** N.K. and E.G. conceived project. I.S. and E.G. performed experiments and analyzed data. L.Z. and E.G. performed simulations and analyzed data. G.B. and E.G. developed theoretical model. E.G. supervised the research. I.S. and G.B., wrote paper.

We study here experimentally, numerically and using a lubrication approach; the shape, velocity and lubrication film thickness distribution of a droplet rising in a vertical Hele-Shaw cell. The droplet is surrounded by a stationary immiscible fluid and moves purely due to buoyancy. A low density difference between the two mediums helps to operate in a regime with capillary number  $Ca$  lying between 0.03 – 0.35, where  $Ca = \mu_o U_d / \gamma$  is built with the surrounding oil viscosity  $\mu_o$ , the droplet velocity  $U_d$  and surface tension  $\gamma$ . The experimental data shows that in this regime the droplet velocity is not influenced by the thickness of the

## Chapter 6. Film thickness distribution in gravity-driven pancake-shaped droplets rising in a Hele-Shaw cell

---

thin lubricating film and the dynamic meniscus. For iso-viscous cases, experimental and three-dimensional numerical results of the film thickness distribution agree well with each other. The mean film thickness is well captured by the Aussillous & Quéré (2000) model with fitting parameters. The droplet also exhibits the “catamaran” shape that has been identified experimentally for a pressure-driven counterpart (Huerre *et al.*, 2015). This pattern has been rationalized using a two-dimensional lubrication equation. In particular, we show that this peculiar film thickness distribution is intrinsically related to the anisotropy of the fluxes induced by the droplet’s motion.

### 6.1 Introduction

Transport of droplets and bubbles in confined environments is a common process in engineering applications, such as microscale heat transfer and cooling using a slug flow (Kandlikar, 2012; Magnini, Pulvirenti & Thome, 2013), enhanced oil recovery based on foam injections where bubbles move in porous media (Farajzadeh, Andrianov & Zitha, 2009) and microfluidic engineering using droplets as micro-reactors (Song, Chen & Ismagilov, 2006) and cell-encapsulating micro-compartments (He, Edgar, Jeffries, Lorenz, Shelby & Chiu, 2005), to name a few. The study of transported droplets in confined dimensions also extends to biological science where red blood cells traversing passages with non-axisymmetric geometries were analysed (Halpern & Secomb, 1992).

Pioneering work has been initiated for a long bubble translating inside a straight cylindrical tube by Taylor (1961) conducting experiments and Bretherton (1961) combining experiments and asymptotic analysis. The analysis of Bretherton showed that the lubrication equations, at a very small capillary number  $Ca$ , were similar to their one-dimensional version assuming spanwise invariance. He established the famous asymptotic relation between the uniform film thickness  $H_\infty$  and the capillary number in the  $Ca < 10^{-3}$  regime, namely,  $H_\infty/W = P(3Ca)^{2/3}/2$ , where  $W$  is the tube diameter and  $P$  a coefficient. The capillary number  $Ca = \mu_o U_d / \gamma$  is built with the carrier phase dynamic viscosity  $\mu_o$ , the droplet velocity  $U_d$  and the surface tension  $\gamma$  between the two fluids. Aussillous & Quéré (2000) proposed

$$\frac{H_\infty}{W} = \frac{1}{2} \frac{P(3Ca)^{2/3}}{1 + PQ(3Ca)^{2/3}}, \quad (6.1)$$

as the *Taylor’s law* including an empirical coefficient  $Q = 2.5$ , with the coefficient  $P$  inherited from Bretherton (1961); this law was validated against the experimental data of Taylor (1961) for  $Ca < 2$ . The empirical relation was rationalised by incorporating into the analysis of Bretherton the so-called “tube-fitting” condition, namely, that the bubble-film combination should fit inside the tube (Klaseboer, Gupta & Manica, 2014). Besides those work considering the steady translation, Yu, Zhu, Shim, Eggers & Stone (2018) has recently investigated how the lubrication film evolves between two steady states of a Bretherton bubble by combining theory, experiments and simulations.

Contrary to the translating bubble in a capillary tube, a bubble moving in a Hele-Shaw cell (two closely gapped parallel plates) resembles a flattened pancake. This configuration is relevant to microfluidic applications (Baroud *et al.*, 2010) where the thickness of the microfluidic chips is much smaller than their horizontal dimension. Owing to the mathematical similarity between the governing equations of the depth-averaged Hele-Shaw flow and those of the two-dimensional (2D) irrotational flow as proved by Stokes (1898) and commented by Lamb (1993), potential flow theory was adopted to study the motion of a Hele-Shaw bubble theoretically (Taylor & Saffman, 1959) and numerically (Tanveer, 1986). Based on the stress jump derived by Bretherton (1961) and Park & Homsy (1984), 2D depth-averaged simulations including the leading-order effects of the dynamic meniscus were also carried out (Meiburg, 1989).

Motivated by the applications of droplet-based microfluidics, several works have been recently conducted to investigate the dynamics of a pressure-driven Hele-Shaw droplet. Huerre *et al.* (2015) and Reichert *et al.* (2018) performed high-precision experiments using reflection interference contrast microscopy technique to study the pressure-driven droplets, observing the so-called “catamaran” droplet shape. Simulations based on a finite volume method (Ling *et al.*, 2016) and a boundary integral method (BIM) (Zhu & Gallaire, 2016) were carried out, confirming such a peculiar interfacial feature. It has to be mentioned that the much earlier work of Burgess & Foster (1990) performing a multi-region asymptotic analysis subtly revealed this feature for a Hele-Shaw bubble, which was rather unnoticed.

Limited work has been conducted for the gravity-driven droplets in a Hele-Shaw cell. Eri & Okumura (2011) and Yahashi, Kimoto, & Okumura (2016) studied experimentally such configurations, trying to build up the scaling laws for the viscous drag friction of the Hele-Shaw droplets. Recently, Keiser *et al.* (2018) conducted experiments to study a sedimenting Hele-Shaw droplet, focusing on its velocity as a function of confinement, viscosity contrast and the lubrication capacity of the carrier phase.

In this work, we combine experiments, simulations and a lubrication model solved numerically to study the buoyancy-driven translation of a droplet inside a vertical Hele-Shaw cell. We examine the droplet velocity, film thickness and how they vary with the density and viscosity difference between the droplet and carrier phase. We introduce the experimental setup in Section 6.2, followed by the experimental results of the droplet mean velocity and film thickness in Section 6.3.1 and Section 6.3.2 respectively. The comparison between the three-dimensional (3D) BIM simulations and the experiments is shown in Section 6.3.3. The lubrication equation employed to model the problem is presented in Section 6.4 where the numerical solution of the lubrication equation is compared to the 3D simulation results in Section 6.4.1. The film thickness pattern is rationalised by solving the linearised 2D lubrication equation, which is presented in Section 6.4.2. We finally summarise our results in Section 6.5 with some discussions.

## 6.2 Experimental setup

A vertical Hele-Shaw cell made of two parallel glass plates, separated by a gap  $W$ , is filled with silicone oil of dynamic viscosity 560 mPa s and density  $972 \text{ kg m}^{-3}$ , measured at  $20^\circ\text{C}$ . An oil drop is injected into the silicone oil medium from the bottom using a syringe as shown in figure 6.1(a). The drop moves as a result of buoyancy. The higher the density difference between the inner and outer medium, the higher the drop velocity  $U_d$ . The spanwise and streamwise cell dimensions are sufficiently large compared to the drop size to avoid any finite size effects from the lateral walls. On the other hand, the droplet is highly confined in the wall normal direction. The droplet radius  $a$  is always larger than the cell gap  $W$ . Given the compliance of the glass walls, the thickness of which is bounded by our optical measurement tools, the cell gap  $W$  lies in the range of  $[4.59 - 4.8] \text{ mm}$  and is recorded every time before the drop injection (see table 6.2).

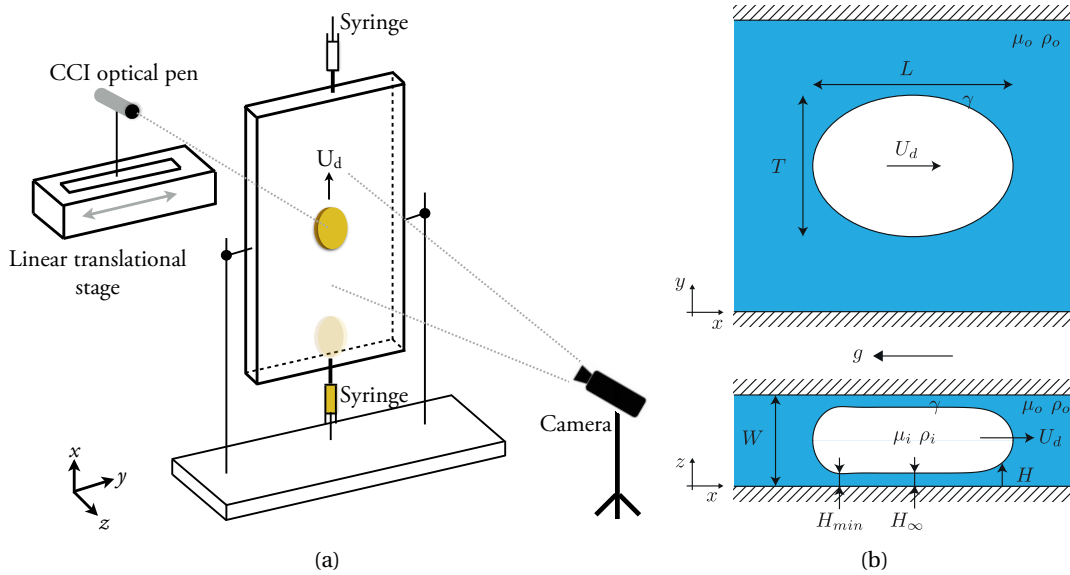


Figure 6.1 – (a) Schematic of the experimental set-up. (b) Sketch of the problem: a droplet with density  $\rho_i$  and dynamic viscosity  $\mu_i$  moving at velocity  $U_d$  in a Hele-Shaw cell of height  $W$ , where the carrier phase has a dynamic viscosity  $\mu_o$  and its density  $\rho_o > \rho_i$ . The in-plane ( $x, y$ ) projection shows the drop's longitudinal and transversal lengths,  $L$  and  $T$ , respectively. The out-of-plane ( $x, z$ ) drop shape shows the thickness  $H_\infty$  of the uniform thin film and the minimum thickness  $H_{min}$  of the film along the centreline.

The injected oils are tested beforehand to ensure non-wetting conditions for the oil droplet on the cell plates. The outer silicone oil totally wets the glass plate and forms a thin film of thickness  $H$ , between the drop and the glass's interface (see figure 6.1(b)), which is measured using a CCI optical pen (see details in Appendix 6.6.1). The pen is either placed fixed such that it measures the film thickness only along the centreline  $L$  (*centreline film thickness*) or is mounted on a linear translational stage to perform lateral scans while the drop moves longitudinally. With an acquisition frequency of 200-500 Hz, scanning amplitude of 20-30 mm

and frequency of 2-3 Hz, the obtained experimental data are interpolated in Matlab to obtain the film thickness maps for the entire drop. Droplet size and velocity determine the optimal acquisition frequency for the thickness sensor, and the scanning amplitude and frequency for the linear translational stage.

We observe that for the chosen inner oil volumetric range, the droplet in-plane shape is no longer a circle but closer to an oval, hence we refer to the drop longitudinal length (along the direction of gravity) as  $L$  and to the transverse length as  $T$ , as shown in figure 6.1(b). The drop motion is captured using a Phantom Miro M310 camera with a Nikon 105 mm macro lens. The spatio-temporal analysis of the movie ensures uniform drop velocity as the drop moves along a longitudinal distance of  $5L$  or more.

The drop volume  $Q$  is expressed as a pancake of radius  $a$  and height  $W-2H_\infty$ , where  $H_\infty$  is the mean film thickness. We can simplify  $Q$  as  $\pi a^2 W$  when  $H_\infty \ll W$ . For the volumetric range used for the inner oils, we found that the longitudinal and transverse lengths,  $L$  and  $T$ , scale as the pancake radius  $a$ . The aspect ratio  $\alpha$  is expressed as the ratio  $a/W$ . Keeping the cell gap  $W$  fixed, data for different aspect ratios are obtained using three different volumes (0.5ml, 1ml, 1.5ml) for each oil.

Six oils with physical properties as mentioned in table 6.1 are used. The surface tension  $\gamma$  between the inner and outer medium is measured using Teclis tensiometer and the oil viscosity and density are measured using Anton Paar SVM<sup>TM</sup> 3000 viscometer. The experiment is performed at 20°C-22°C.

The ratio  $\lambda$  between the dynamic viscosity of the inner and outer phase lies between [0.09 – 0.54]. In addition to this range, another set of experiments is performed with  $\lambda = 1.01$ , where the outer medium is silicone oil ( $\mu_o = 319$  mPa s,  $\rho_o = 970.5$  kg m<sup>-3</sup>) and the inner medium is a mixture of ricin oil and 10% ethanol ( $\mu_i = 322$  mPa s,  $\rho_i = 943.3$  kg m<sup>-3</sup>) for three different drop volumes. The interfacial surface tension between these oils is 4.46 mN m<sup>-1</sup>. Notations for physical parameters and their definitions are detailed in table 6.2.

Inner oil	$\mu_i$ (mPa s)	$\rho_i$ (kg m <sup>-3</sup> )	$\gamma$ (mN m <sup>-1</sup> )
Linseed oil	49	929	2.88
Sunflower oil	69.5	921.5	2.73
Sesame oil	71	919.1	2.64
Olive oil	79.3	913.3	2.55
Peanut oil	83.8	913.3	3.11
Ricin oil (type 1) + 10% ethanol	302	943.1	4.97
Ricin oil (type 2) + 10% ethanol	322	943.3	4.46

Table 6.1 – Dynamic viscosity  $\mu_i$  and density  $\rho_i$  of the inner oils. Those of the outer oil are  $\mu_o = 560$  mPa s and  $\rho_o = 972$  kg m<sup>-3</sup> except for the case of Ricin (type 2) + 10% ethanol for which the outer oil has  $\mu_o = 319$  mPa s,  $\rho_o = 970.5$  kg m<sup>-3</sup>. The interfacial surface tension between the inner-outer oils is  $\gamma$ . These properties were obtained at a room temperature 20°C.

## Chapter 6. Film thickness distribution in gravity-driven pancake-shaped droplets rising in a Hele-Shaw cell

Symbol	Definition	Expression	Working range
$W$	cell gap	-	4.59-4.8 mm
$U_d$	drop velocity	-	0.4-1.6 mm s <sup>-1</sup>
$Q$	injected drop volume	-	0.44-1.5 ml
$a$	pancake equivalent radius	$\sqrt{Q/\pi W}$	5.8-10.3 mm
$\alpha$	aspect ratio	$a/W$	1.25-2.27
$\Delta\rho$	density difference	$ \rho_i - \rho_o $	27.3-58.8 kg m <sup>-3</sup>
$\mu_i$	dynamic viscosity - droplet	-	49-322 mPa s
$\mu_o$	dynamic viscosity - outer medium	-	319-560 mPa s
$\gamma$	interfacial surface tension	-	2.5-5.0 mN m <sup>-1</sup>
$\lambda$	dynamic viscosity ratio	$\mu_i/\mu_o$	0.09-1.01
$Ca$	capillary number	$\mu_o U_d/\gamma$	0.03-0.35
$Bo$	Bond number	$\Delta\rho g a^2/\gamma$	1.8-23.3

Table 6.2 – List of notation, definition and working range.

### 6.3 Experimental acquisition of the drop characteristics and their comparison with 3D BIM simulations

#### 6.3.1 Experimental results for drop velocity

Considering the bulk dissipation only, the resulting viscous drag force acting on the drop scales as  $F_d \sim (\mu_i + \mu_o) U_d \pi a^2 W^{-1}$ . Unlike Okumura (2018), we consider both the inner and outer viscosities since they are of the same order. Balancing the total drag force with the buoyancy force,  $F_g \sim \Delta\rho g \pi a^2 W$ , we obtain a scaling for the droplet mean velocity as

$$U_d \sim \frac{\Delta\rho g W^2}{(\mu_i + \mu_o)}, \quad (6.2)$$

where  $\Delta\rho$  is the density difference and  $g = 9.81 \text{ m s}^{-2}$ .

Under the assumption of cylindrical penny-shaped wetting drops, a theoretical expression for the drop velocity can be obtained from Maxworthy (1986), Bush (1997) and Gallaire, Meliga, Laure & Baroud (2014). Gallaire *et al.* (2014) deduced the drop velocity in a Hele-Shaw cell, subjected to both buoyancy and Marangoni flow, using depth-averaged Stokes equations, called the Brinkman equations. In the absence of Marangoni effect and at leading order, Bush (1997) and Gallaire *et al.* (2014) predicted the mean drop velocity as

$$U_d = \frac{\Delta\rho g W^2}{12\mu_o(\lambda + 1)}. \quad (6.3)$$

Introducing the Bond number  $Bo$  (refer table 6.2) we can rewrite equation (6.3) using the

### 6.3. Experimental acquisition of the drop characteristics and their comparison with 3D BIM simulations

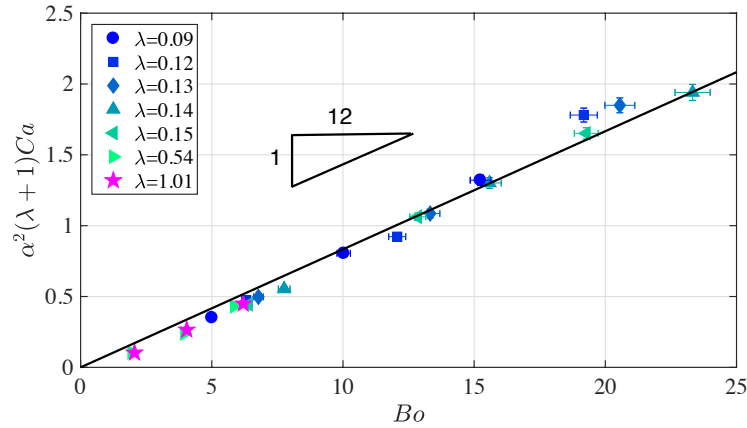


Figure 6.2 – Experimental data  $\alpha^2(\lambda+1)Ca$  versus the Bond number  $Bo$ , where  $Ca \in [0.03, 0.35]$ . The markers correspond to different viscosity ratios  $\lambda$  of the inner-outer medium. The data closely fits equation (6.4) represented by the straight line.

aspect ratio  $\alpha$  as,

$$12\alpha^2(\lambda+1)Ca = Bo. \quad (6.4)$$

The experimental data are plotted against the theoretical equation (6.4) in figure 6.2. Following the trend predicted by equation (6.4), figure 6.2 signifies the dominant forces in play are buoyancy and viscous drag due to the volume of fluid displaced by the drop. The dissipation induced in the thin film as well as the one in the dynamic meniscus region are found not to play a role in the selected parameter range. However it has been observed that for low  $Ca$  ranges, the dissipation in the thin film (Keiser *et al.*, 2018) and in the dynamic meniscus (Reyssat, 2014) have to be taken into account.

#### 6.3.2 Experimental results for film thickness

Film thickness maps were measured for different droplet velocities. Since the thickness sensor fails to capture the data in presence of high thickness gradient, no data is acquired along the drop edges, as shown in figure 6.3(d), where the black curve represents the drop in-plane boundary. For different aspect ratios, qualitatively similar thickness maps were obtained, with a high film thickness on the front edge, a constant film thickness in the centre and very low film thickness along the lateral edges of the drop, overall resembling a catamaran-like shape. The spanwise and streamwise cut made along the film thickness are shown in figure 6.3(b-c). The centreline film thickness indicated by the streamwise cut at  $y = 0$  (figure 6.3(b)) clearly shows a monotonically decreasing film thickness pattern, followed by a region of constant film thickness  $H_\infty$  which then reaches a minimum value of  $H_{min}$ . At the rear of the droplet, the strong thickness gradient reverses the direction to have an increasing thickness profile close to the drop receding edge, thus posing technical issues to capture the film thickness.

## Chapter 6. Film thickness distribution in gravity-driven pancake-shaped droplets rising in a Hele-Shaw cell

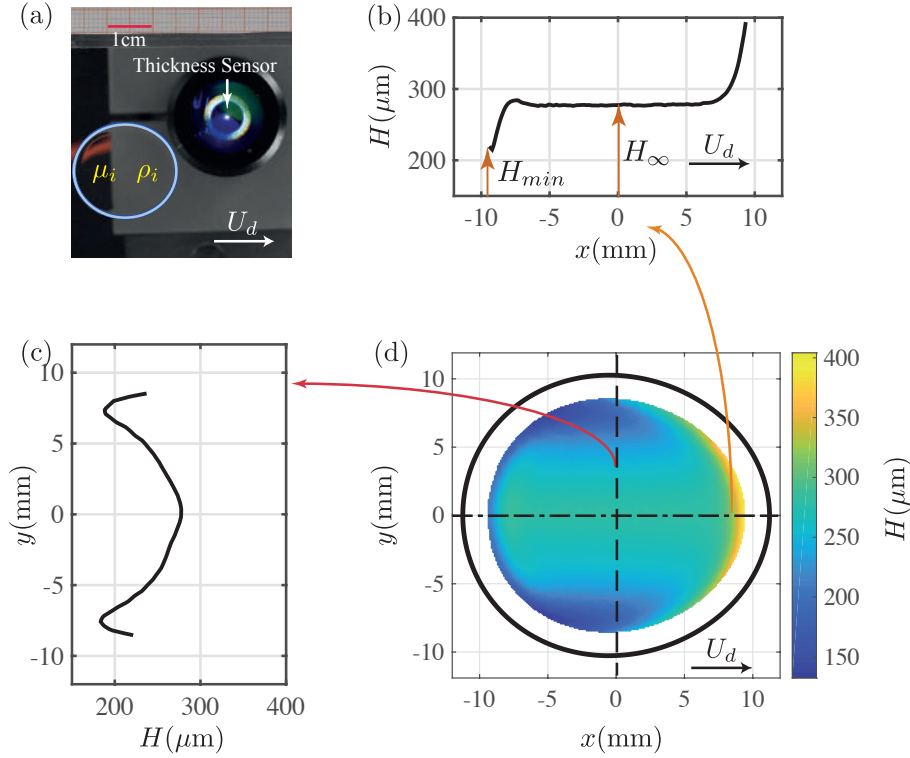


Figure 6.3 – Drop characteristics for droplet with  $\lambda \sim 1$  moving with mean velocity  $U_d = 0.64\text{mm/s}$ ,  $Ca = 4 \times 10^{-2}$  and  $Bo = 6.2$ . (a) The blue curve shows the in-plane drop shape fitting based on equation (6.6) with  $L/2 = 11.22\text{ mm}$ ,  $T/2 = 10.21\text{ mm}$  and fitting coefficient  $c = -7.485 \times 10^{-6}\text{ mm}^{-1}$ . The film thickness in the streamwise and spanwise directions  $y = 0$  and  $x = 0$  of the drop are shown in (b) and (c) respectively. Figure (b) shows the typical centreline thickness profile with monotonic decreasing thickness, followed by constant thickness  $H_\infty$  and ending with the minimum film thickness  $H_{min}$ . (c) The film thickness profile along the spanwise direction highlights the two minima along the lateral edge of the drop at  $y \sim \pm 7.5\text{ mm}$  which are clearly noticed in (d) where we see the in-plane shape in black and the obtained film thickness map. The data is missing along the drop boundaries due to the presence of high thickness gradient that cannot be captured by the thickness sensor.

A similar centreline film thickness profile was obtained for all the droplets with a distinct value of  $H_\infty$  and  $H_{min}$ . These profiles are very similar to the ones of Bretherton (1961) for pressure-driven droplets, and as already noted in other works of pancakes (Huerre *et al.*, 2015, Zhu & Gallaire, 2016 and Reichert *et al.*, 2018). Nondimensionalising the mean and minimum values along the centreline using the cell gap  $W$  and plotting them as a function of  $Ca$  shows a saturating trend for higher  $Ca$  (figure 6.4). The experimental data are fitted based on the *Taylor's law* model (Taylor, 1961; Aussillous & Qu  r  , 2000), according to which apart from the static and dynamic meniscus regions, the lubrication film has a constant thickness of  $H_\infty$



### 6.3. Experimental acquisition of the drop characteristics and their comparison with 3D BIM simulations

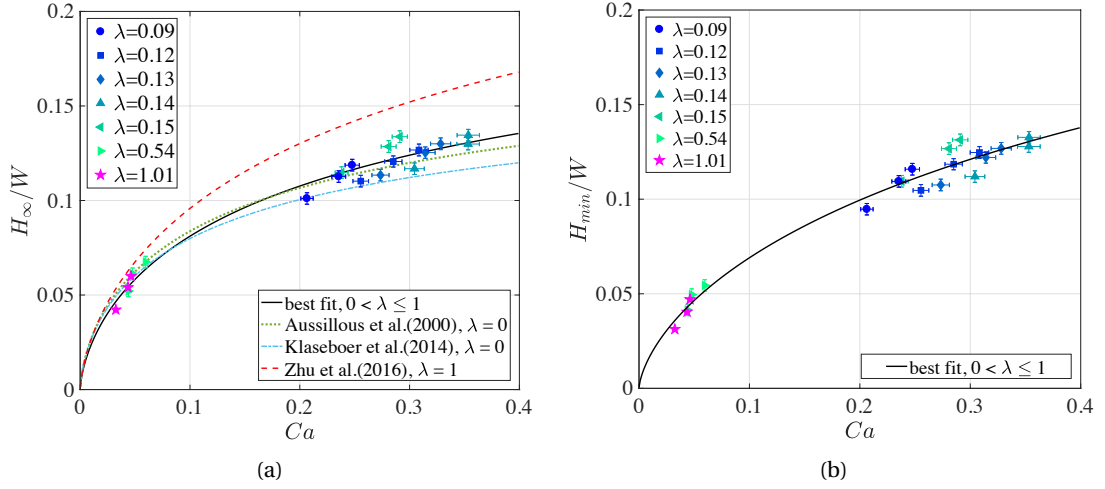


Figure 6.4 – (a) Dimensionless mean ( $H_{\infty}/W$ ) and (b) minimum ( $H_{min}/W$ ) film thickness, as a function of  $Ca$ . The black curve represents the best fit curve obtained using the *Taylor's law* model with  $P = 0.544$ ,  $Q = 2.061$  for  $H_{\infty}/W$  and with  $P = 0.372$ ,  $Q = 1.247$  for  $H_{min}/W$ . For the mean film thickness, predictions based on the coefficients  $P, Q$  from the *Taylor's law* ((Aussillous & Qu  r  , 2000), (Klaseboer *et al.*, 2014) and Zhu & Gallaire (2016)) are also shown.

given as:

$$\frac{H_{\infty}}{W} = \frac{1}{2} \frac{P(3Ca)^{2/3}}{1 + PQ(3Ca)^{2/3}}, \quad (6.5)$$

where the coefficients  $P = 0.544$  and  $Q = 2.061$  are obtained from the best fit curve for the experimental data. The nonlinear equation (6.5) is fitted using the Matlab function *sseval* such that the objective function, defined as the sum of squared errors between the real data of  $H_{\infty}/W$  and the one predicted by equation (6.5), using any pair of parameters  $P$  and  $Q$ , is the minimum. The L2 error norm for  $H_{\infty}/W$  between the fitted and actual data is 0.02.

The fitting coefficients compare well with Aussillous & Qu  r   (2000) and Klaseboer *et al.* (2014), where the mean film thickness model for bubbles ( $\lambda = 0$ ) is based on the *Taylor's law* with coefficient  $P = 0.643$ , and  $Q = 2.5$  and  $2.79$  respectively. Fitting coefficients obtained from a 3D BIM simulation of Zhu & Gallaire (2016) for pressure-driven flows and  $\lambda = 1$  show the same order of magnitude as the experimental ones, with  $P = 0.6$  and  $Q = 1.5$ .

In figure 6.4(a), we see that our experimental data for mean film thickness are bounded by the predicted values for the two extreme viscosity ratios of  $\lambda = 0$  and  $\lambda = 1$ . Comparing the thickness predictions by Klaseboer *et al.* (2014) and Zhu & Gallaire (2016) for  $Ca = 0.1$  we see that the thickness variation is 20% as  $\lambda$  increases from 0 to 1. This is consistent with the 18% (approximately) increase as reported in Martinez & Udell (1990) for pressure-driven drops in an axisymmetric tube. Further, this variation in thickness reduces to a merely 11% for  $Ca = 0.05$ , as  $\lambda$  changes from 0 to 1.

## Chapter 6. Film thickness distribution in gravity-driven pancake-shaped droplets rising in a Hele-Shaw cell

---

The same model when used for fitting the minimum film thickness profile  $H_{min}/W$  gives fitting coefficients  $P = 0.372$ ,  $Q = 1.247$  with an L2 error norm between the fitted and actual data as 0.025.

Motivated by the qualitative agreement for the mean film thickness value between the experimental data and the 3D BIM simulations for pressure-driven droplets (figure 6.4(a)), we perform a 3D BIM simulation using the solver developed in Zhu & Gallaire (2016), suitably adapted for gravity-driven droplets. Details of the numerical scheme are referred to that paper.

### 6.3.3 Comparison with 3D simulations

The current numerical simulations only address the cases where the inner and outer viscosities are the same, namely  $\lambda = 1$ . To realize it experimentally, three different drop volumes, 0.44ml, 1ml and 1.5ml, were injected in the Hele-Shaw cell resulting in  $Ca=0.032$ , 0.043 and 0.046 with the corresponding  $Bo=1.81$ , 4.04 and 6.2. The error in volume injected decreased from 10% to 3% as we moved from the smallest to the largest drop volume.

The experimental film thickness maps for the chosen  $Ca$  range show that the precise shape of the pancake in-plane shape is close to an oval. Hence, the experimental in-plane drop shape is obtained by fitting the following equation

$$\frac{x^2}{(L/2)^2} + \frac{y^2}{(T/2)^2} e^{cx} = 0, \quad (6.6)$$

on an instantaneous image of the drop where  $c$  is a fitting parameter (figure 6.3(a)).

Experimentally, due to large thickness gradient along the drop edges, the CCI sensor fails to capture the thickness in these regions. Thus the map is obtained for an area smaller than the in-plane shape of the drop (black curve in figure 6.5). On the contrary, the numerical simulations are capable of retrieving the complete film thickness map, but for making a visually effective comparison between the experiments and numerics, only the part of the numerical result, with the same area as the experimental data, is shown in figure 6.5. Its top/bottom half corresponds to the numerical/experimental data. The red dashed curve refers to the numerical in-plane shape of the drop.

Both the experiments and simulations capture the formation of catamarans at the lateral transition regions, a uniform film thickness in the centre and a very high film thickness at the front edge of the drop. The agreement is almost quantitative. The relative error in the uniform film thickness  $H_\infty$  for drop volumes 0.44 ml, 1 ml and 1.5 ml, is 5%, 3% and 2% with absolute values as  $12 \mu\text{m}$ ,  $7 \mu\text{m}$  and  $6 \mu\text{m}$ , respectively.

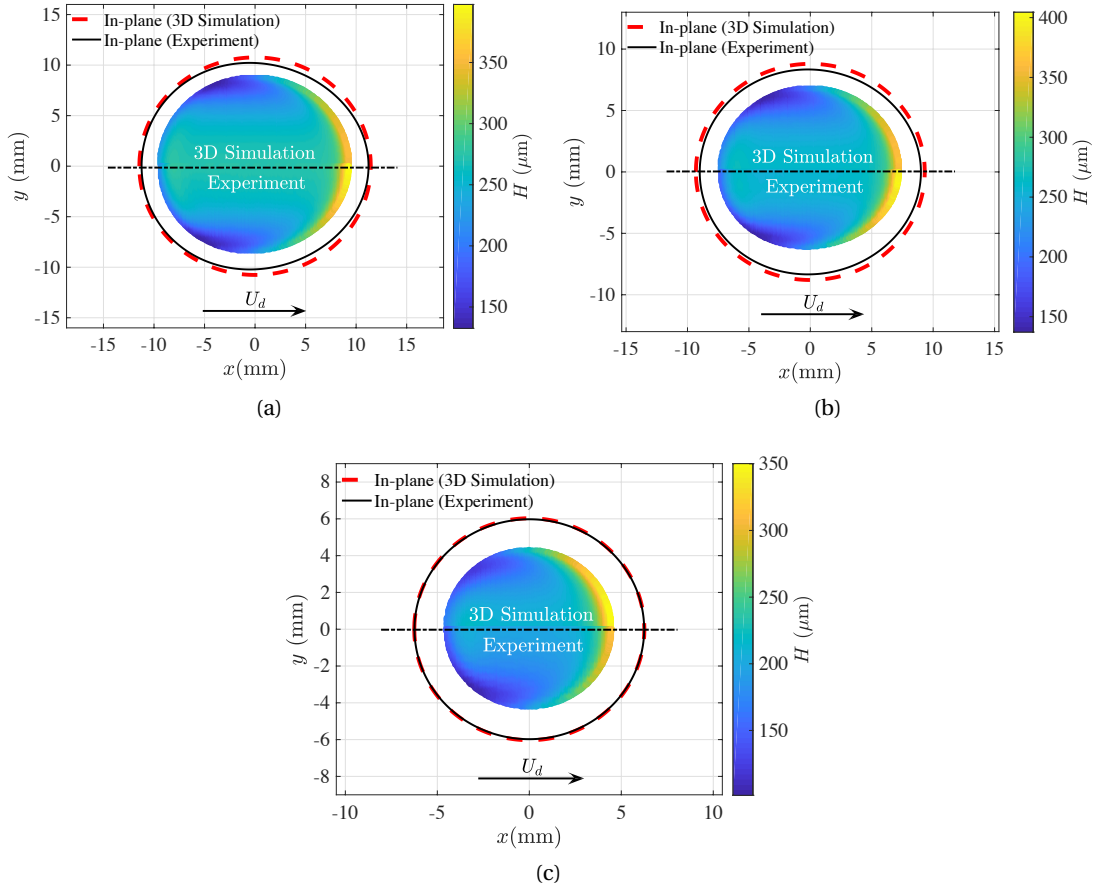


Figure 6.5 – Film thickness map whose top (resp. bottom) half corresponds to the 3D BIM (resp. experimental) data for three drop volumes (a) 1.5 ml ( $Ca = 0.046$ ,  $Bo = 6.2$ ), (b) 1 ml ( $Ca = 0.043$ ,  $Bo = 4.04$ ) and (c) 0.44 ml ( $Ca = 0.032$ ,  $Bo = 1.81$ ). The viscosity ratio  $\lambda \approx 1$ . The experimental and numerical in-plane shapes are represented by black and red dashed curves, respectively. The numerical results for  $H_\infty$  along the centreline deviate with the experimental data by a factor of 2%, 3% and 5% for the three cases, respectively.

The numerical solution is further validated by making several streamwise (figure 6.6) and spanwise (figure 6.7) cuts along the largest drop of volume 1.5 ml. Along the centreline, the 3D BIM simulation captures precisely the lubrication film variation: large film thickness at front edge, followed by a constant thickness profile, ending in a small oscillation before posing an increasing trend at the rear edge. There is a good quantitative comparison between the experiments and numerics, with a slight variation in the film thickness along the advancing meniscus.

## 6.4 Analysis of the film thickness pattern

In order to rationalise the film thickness pattern observed in Section 6.3.3, we model hereafter the problem using a lubrication approach. For simplicity, we formulate the 2D lubrication

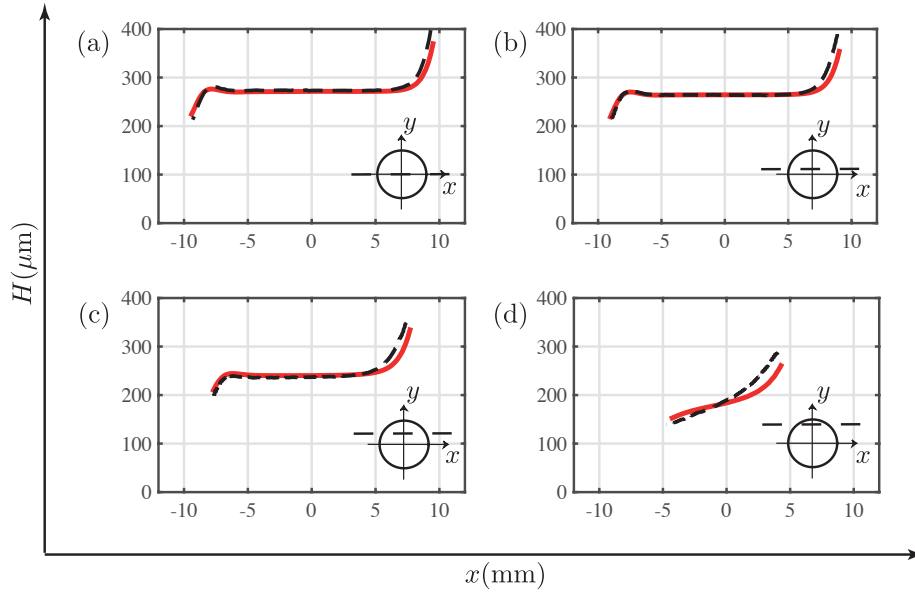


Figure 6.6 – Film thickness cuts made along the streamwise directions at (a)  $y = 0$ , (b)  $y = 2.5$  mm, (c)  $y = 5$  mm and (d)  $y = 7.5$  mm, where  $Ca = 0.046$ ,  $Bo = 6.2$ . Black dashed lines represent the experimental results and red lines the numerical predictions. The decrease in the film thickness towards the lateral edges can be observed by comparing (a) and (d) where the mean film thickness decreases by around 30% signifying the appearance of catamarans close to  $(x, y) \approx (-4, 7.5)$  mm.

equation assuming the drop dynamic viscosity  $\mu_i = 0$ .

#### 6.4.1 Formulating the nonlinear 2D lubrication equation

Applying the long-wavelength assumption (Oron, Davis & Bankoff, 1997) and by neglecting inertia, the 2D nonlinear lubrication equation (see details in Appendix 6.6.2) for the film thickness  $H$  separating the interface from the wall, in the reference frame moving at the drop velocity  $U_d$ , can be derived. Using the pancake radius  $a$  as the characteristic length and  $a/U_d$  as the characteristic time, the dimensionless lubrication equation for the steady profile in the dimensionless coordinate system  $\bar{x}, \bar{y}$  is written as

$$\frac{\partial}{\partial \bar{x}} \left[ \bar{H}^3 \left( \frac{1}{3Ca} \bar{\kappa}_x - \frac{Bo}{3Ca} \right) - \bar{H} \right] + \frac{\partial}{\partial \bar{y}} \left( \bar{H}^3 \frac{1}{3Ca} \bar{\kappa}_y \right) = 0, \quad (6.7)$$

where  $\bar{\kappa}$  is the mean curvature of the interface, given by  $\bar{\kappa} = \nabla \cdot \mathbf{n}$ , where the unit normal vector  $\mathbf{n}$  on the interface is given by

$$\mathbf{n} = \frac{(-\bar{H}_x, -\bar{H}_y, 1)^T}{\sqrt{1 + \bar{H}_x^2 + \bar{H}_y^2}}. \quad (6.8)$$

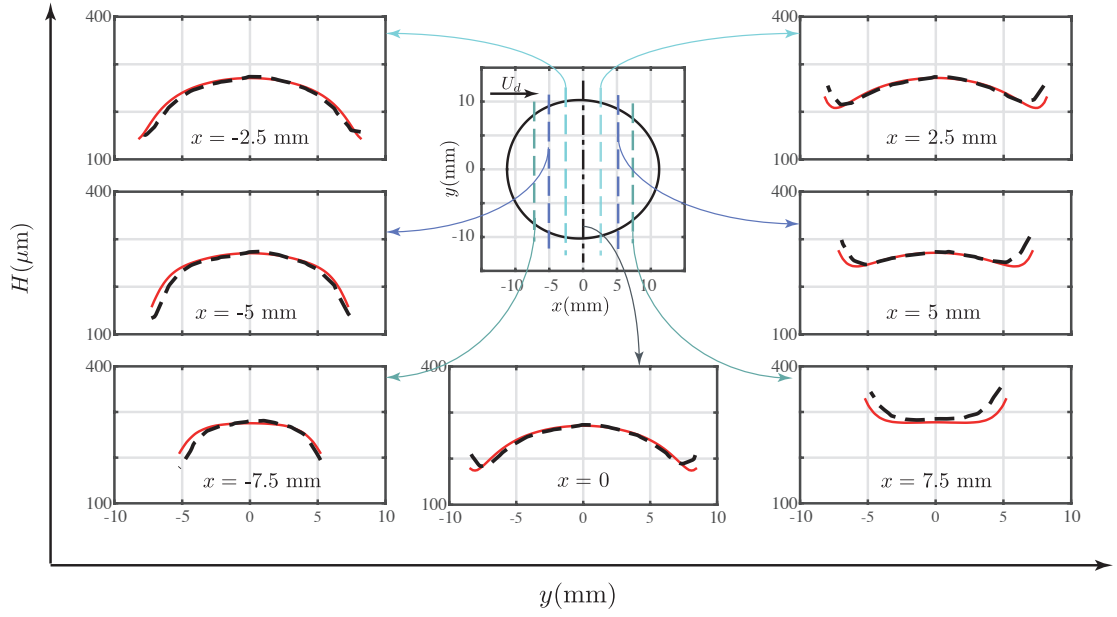


Figure 6.7 – Film thickness variation along the spanwise directions at  $x = 0$ ,  $x = \pm 2.5$  mm,  $x = \pm 5$  mm and  $x = \pm 7.5$  mm, where  $Ca = 0.046$ ,  $Bo = 6.2$ . Black dashed lines represent the experimental results and red lines the numerical results. Transverse cuts enclosed by the region  $x = -2.5$  mm to  $x = -5$  mm highlight the minima in the lubrication film along the lateral edges.

Note the anisotropy of the fluxes in equation (6.7): both the buoyancy and the motion in the  $\bar{x}$  direction do not affect the flux in the  $\bar{y}$  direction, breaking the isotropy induced by the capillary pressure gradient.

The nonlinear equation (6.7) together with the equation for the interface curvature  $\bar{\kappa}$  are solved numerically by the commercial finite element solver COMSOL Multiphysics. The two variables for this coupled system of partial differential equations are  $\bar{H}$  and  $\bar{\kappa}$ . As boundary conditions we impose the film thickness  $\bar{H} = W/2a$  and the mean curvature  $\bar{\kappa} = \bar{\kappa}_{f,r}$  at the droplet mid height. The mean curvature boundary condition in the static meniscus is composed by a component in the  $(\bar{r}, \theta)$ -plane and a component in the  $(\bar{r}, \bar{z})$ -plane. In the spirit of Meiburg (1989) and Nagel (2014), we consider the local capillary number defined with the normal velocity to the static cap for the mean curvature boundary condition model:

$$\bar{\kappa}_{f,r}(\bar{r}, \theta) = \underbrace{\frac{2a}{W} \left( \frac{1 + T_{f,r}(3Ca|\cos\theta|)^{2/3}}{1 + Z_{f,r}(3Ca|\cos\theta|)^{2/3}} \right)}_{(\bar{r}, \bar{z})\text{-plane}} + \underbrace{\frac{\pi}{4} \frac{1}{\bar{r}}}_{(\bar{r}, \theta)\text{-plane}}, \quad (6.9)$$

where the coefficients with subscript  $f$  have to be used for  $\theta \in [-\pi/2, \pi/2]$  and the ones with subscript  $r$  for  $\theta \in [\pi/2, 3\pi/2]$ , where  $\theta$  and  $\bar{r}$  are defined as  $\theta = \arctan(\bar{y}/\bar{x})$  and  $\bar{r} = (\bar{x}^2 + \bar{y}^2)^{1/2}$ , respectively. The values of the coefficients are  $T_f = 2.285$ ,  $T_r = -0.5067$ ,  $Z_f = 0.4075$  and  $Z_r = -0.1062$ . The curvature boundary condition model in the  $(\bar{r}, \bar{z})$ -plane is inspired by

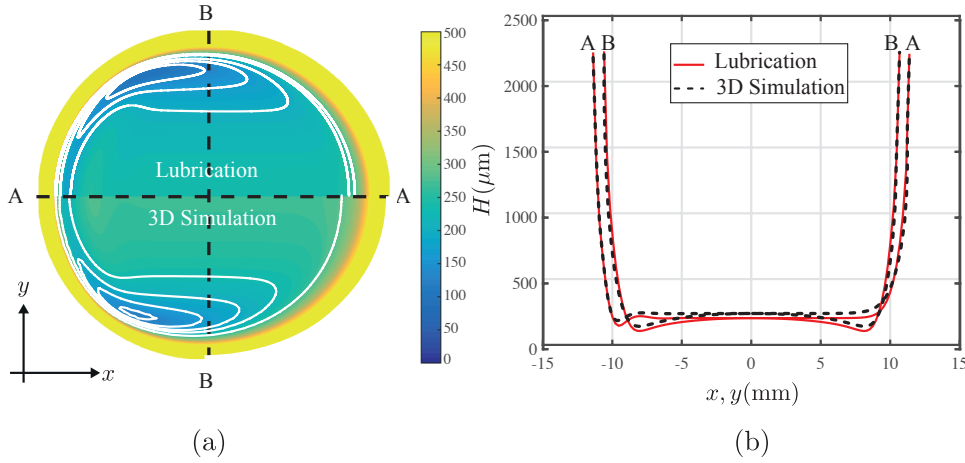


Figure 6.8 – (a) Comparison between the solution of the nonlinear lubrication equation assuming  $\lambda = 0$  (top half) and that of the 3D BIM simulations assuming  $\lambda = 1$  (bottom half), where  $Ca = 4.6 \times 10^{-2}$  and  $Bo = 6.2$ . (b) Comparison for cuts made along the streamwise direction A-A and spanwise direction B-B.

the equivalent model of Balestra, Zhu & Gallaire (2018), which has been developed by an extensive study for the 2D planar Stokes problem. The validity of this model has recently been corroborated by Atasi, Haut, Dehaeck, Dewandre, Legendre & Scheid (2018) for pancake bubbles. The correction  $\pi/4$  for the in-plane curvature  $1/\bar{r}$  in the  $(\bar{r}, \theta)$ -plane, where  $\bar{r} = 1$  for a circular geometry, has been derived asymptotically by Park & Homsy (1984). Note that a more involved model could be used to describe the out-of-plane curvature  $((\bar{r}, \bar{z})$ -plane) in the lateral transition regions (Burgess & Foster, 1990).

In the present work we extract the pancake shape from the results of the 3D BIM simulations for  $\lambda = 1$ . As explained in Section 6.3.3, the in-plane boundaries of the deformed pancake in the  $(\bar{r}, \theta)$ -plane can be well described by equation (6.6).

It has to be stressed that the used lubrication equation should not, a priori, be used in the static meniscus region close to the boundary, where the interface slope is large. However, we have found that such an approach gives surprisingly good results if one uses the model for the static rim curvature (6.9) for the curvature boundary condition (see Balestra (2018) for a discussion of the axisymmetric case), which directly sets the film thickness profile in that region. Hence, such an approach can be used to numerically obtain the film thickness profile over the entire domain, also behind its validity range.

The comparison between the film thickness profile obtained by the solution of the nonlinear lubrication equation using the model equation (6.9) for the static cap mean curvature  $\bar{\kappa}_{f,r}(r, \theta)$ , with the one obtained by the 3D BIM simulations, is shown in figure 6.8. One can observe that both methods predict the formation of catamarans at the lateral transition regions, a uniform film thickness in the centre and oscillations at the back. In spite of the strong

assumptions made for this model, the agreement is surprisingly good, even with an iso-viscous drop ( $\mu_i = \mu_o$ ). The relative error in the uniform film thickness is of 10% and its absolute value is  $30 \mu\text{m}$ . The thin-film pattern shown by both approaches, as well as by the experiments, is therefore indeed a robust feature. Supported by this agreement, we investigate the thin-film pattern using the linearized version of this simple 2D lubrication model, which is computationally much cheaper than the 3D Stokes simulations.

#### 6.4.2 Qualitative analysis of thickness pattern using the linearized 2D lubrication equation

The qualitative nature of the film thickness pattern can be inferred by performing a linear analysis of the 2D lubrication equation (6.7). With the use of the film thickness decomposition  $\tilde{H} = \bar{H}_\infty + \varepsilon h$ , where  $\bar{H}_\infty = H_\infty / a$ , the linear equation for the first-order film thickness correction reads:

$$\frac{\bar{H}_\infty^3}{3Ca} \underbrace{(h_{\tilde{x}\tilde{x}\tilde{x}\tilde{x}} + 2h_{\tilde{x}\tilde{x}\tilde{y}\tilde{y}} + h_{\tilde{y}\tilde{y}\tilde{y}\tilde{y}})}_{\Delta^2 h} - \left(1 + \frac{\bar{H}_\infty^2 Bo}{Ca}\right) h_{\tilde{x}} = 0. \quad (6.10)$$

The film thickness  $\bar{H}_\infty$  is expressed using the empirical model (6.5) (Taylor (1961), Aussillous & Quéré (2000) and Balestra *et al.* (2018)), with  $P = 0.643$  and  $Q = 2.2$ .

Equation (6.10) for the film thickness correction around the uniform film thickness  $\bar{H}_\infty$  can be solved as a boundary-value problem, as recently conducted by Atasi *et al.* (2018). In contrast to the nonlinear solution of Sec. 6.4.1, here we only solve the lubrication equation from the thin-film region up to the beginning of the dynamic meniscus region. This is equivalent to looking at the first-order correction of the uniform thin film region due to the matching of the film thickness in the dynamic meniscus region to a larger value. In the present context, we impose a film thickness correction  $h = A$  and a mean curvature of the order  $\Delta h = 1/A + 1/\bar{r}$  on the perimeter, with  $A$  as a constant value of  $10^{-3} \times \bar{H}_\infty$ . This boundary condition does not have to be understood as a rigorous matching approach, but rather as a way to find the structure of the film thickness profile in the region where it is close to be uniform. A rigorous matching for the limit  $Ca \ll 1$ , can be found in Park & Homsy (1984). The maps of the film thickness correction  $h$ , together with some profiles along the streamwise and spanwise directions, are shown in figure 6.9.

First, it can be clearly observed that the linear lubrication equation with a perturbed film thickness and curvature along the domain boundary is able to reproduce the catamaran-like pattern observed in pancake droplets as seen in Section 6.3.3 and Section 6.4.1. The film thickness is the smallest in the lateral part of the pancake (see figure 6.9(a)), so that its 3D shape resembles the hull of a catamaran. Therefore, we can conclude that this pattern is the generalization of the one-dimensional oscillations found by Bretherton (1961) at the rear of an axisymmetric bubble for a 2D concave structure, like a pancake droplet, and is intrinsically related to the anisotropy of the equation.

## Chapter 6. Film thickness distribution in gravity-driven pancake-shaped droplets rising in a Hele-Shaw cell

Second, the film thickness correction along the streamwise direction  $\bar{x}$  (see figure 6.9(c)) deviates from a uniform profile as expected from Bretherton's theory (Bretherton, 1961). The film thickness oscillates at the rear meniscus and increases monotonically at the front meniscus. Note that the film thickness correction in the uniform film region of a pancake is not vanishing as the base film thickness  $\bar{H}_\infty$  is given by equation (6.5), which is an asymptotic estimate for  $Bo = 0$  but not an exact solution of the lubrication equation with  $Bo \neq 0$ . Furthermore, it can be observed that the more one moves away from  $\bar{y} = 0$ , the more the thickness of the film is reduced. Therefore, the thickness of the film left by the front meniscus is not uniform.

To better highlight this crucial point, we show in figure 6.9(d) the normalized difference between the film thickness correction and its value at  $\bar{y} = 0$ . The film thickness decreases as  $|\bar{y}|$  increases, before increasing again close to the edge to match the boundary condition.

These qualitative observations can be rationalised by simplifying the linear lubrication equation (6.10) for the different regions of the domain (see figure 6.9(b)). The lubrication equation

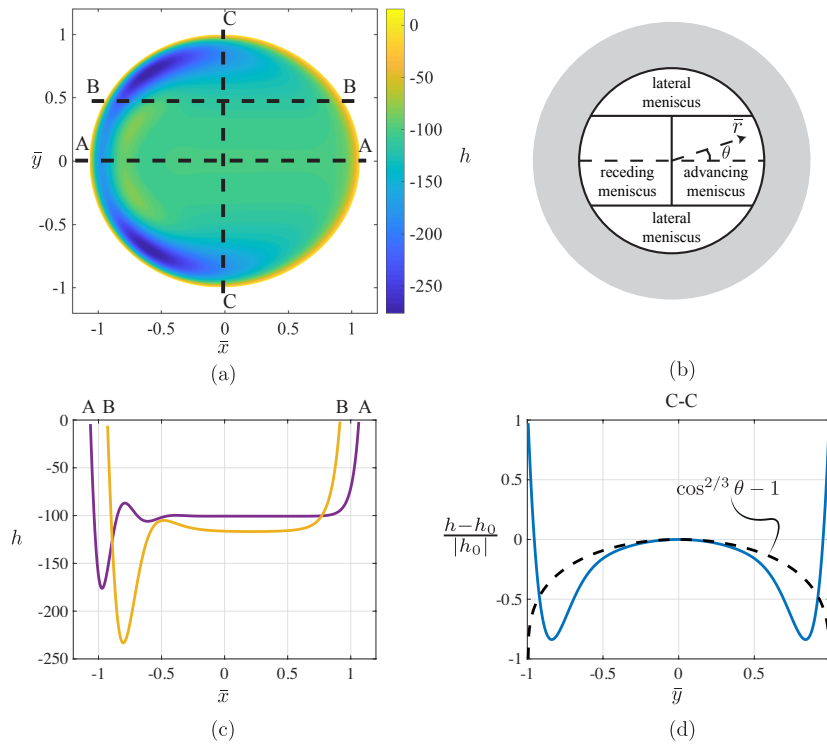


Figure 6.9 – Linear film thickness correction  $h$  around the uniform film thickness  $\bar{H}_\infty$  for a pancake droplet (a,c,d). The film thickness correction map is shown in (a), the cuts along the streamwise direction at two different  $\bar{y}$ -locations are plotted in (c) and the normalized difference of the film thickness correction along the spanwise cut C-C with respect to  $h_0 = h(\bar{y} = 0)$  along this cut is shown in (d), where the law  $(\cos \theta)^{2/3}$  is indicated by the black dashed line.  $A = 10^{-3} \times \bar{H}_\infty$ ,  $Ca = 4.6 \times 10^{-2}$ ,  $Bo = 6.2$  and  $\alpha = 2.2$ . The polar coordinates  $(\bar{r}, \theta)$  are introduced and the boundaries are highlighted by the grey area in (b).



(6.10) in polar coordinates can be simplified to

$$\frac{\bar{H}_\infty^3}{3Ca} h_{\bar{r}\bar{r}\bar{r}\bar{r}} - \left(1 + \frac{\bar{H}_\infty^2 Bo}{Ca}\right) \left(\cos\theta h_{\bar{r}} - \frac{\sin\theta}{\bar{r}} h_\theta\right) = 0. \quad (6.11)$$

For small polar angles  $\theta$ , the contribution  $(\sin\theta/\bar{r})h_\theta$ , which corresponds to the flux in the tangential direction, can be neglected so that the linear lubrication equation becomes, after integration along  $\bar{r}$ :

$$h_{\bar{r}\bar{r}\bar{r}} = K_p h, \quad (6.12)$$

with

$$K_p = \left(\frac{3Ca}{\bar{H}_\infty^3} + \frac{3Bo}{\bar{H}_\infty}\right) \cos\theta, \quad (6.13)$$

which is the linearised one dimensional equation for the Landau-Levich-Derjaguin-Bretherton problem (Landau & Levich (1942), Derjaguin (1943) and Bretherton (1961)) in the radial direction  $\bar{r}$  projected on the streamwise direction. Therefore, we know from the solution of Bretherton (1961) that the film thickness is oscillating at the rear meniscus and monotonically increasing at the front one. Focusing for now on  $Bo = 0$ , we know that the thickness deposited by a front meniscus depends on the velocity normal to the interface. In this case, one has therefore  $\bar{H}_\infty \sim Ca_p^{2/3}$  with  $Ca_p = Ca \cos\theta$  as the local capillary number at a given polar angle  $\theta$ . Hence, the film thickness in the central region of the pancake varies like  $(Ca \cos\theta)^{2/3}$ . Similar results have been reported for a pressure-driven red blood cell traversing in a non-axisymmetric passage (Halpern & Secomb, 1992) and in pancake droplets by Reichert *et al.* (2018). Once a given film thickness is set by the front meniscus, the same thickness will be present over the entire thin film region at the corresponding spanwise location  $\bar{y}$ . The good agreement between the dependence in  $(\cos\theta)^{2/3}$  of the film thickness and the profile along the spanwise direction obtained by resolving the 2D lubrication equation is shown in figure 6.9(d).

Similarly, the oscillations at the rear meniscus depend on the polar angle. For a pancake droplet, due to the film thickness nonuniformity resulting from the nonuniform deposition at the front, the wavelength of the oscillations at the back scales as  $\lambda_{osc} \sim (Ca \cos\theta)^{1/3}$ . Given the 1/3 power-law dependence, the wavelength is almost unchanged, before rapidly reducing to 0 when  $\theta \rightarrow \pm\pi/2$  (see figure 6.9(a)).

It is important to note that a plane cut of the film thickness at a given angle  $\theta$  does not present a region of constant film thickness. A pancake droplet cannot be seen just as the collection of different one-dimensional profiles obtained by the solution to equation (6.12) for different polar angles  $\theta$ . In fact, the film thickness at any spanwise location  $\bar{y}$  is set by the front meniscus at the corresponding polar angle  $\theta$  and equation (6.12) only indicates the scaling of this film thickness as well as the oscillations at the back.

## Chapter 6. Film thickness distribution in gravity-driven pancake-shaped droplets rising in a Hele-Shaw cell

---

For  $\theta \rightarrow \pm\pi/2$ , which corresponds to the lateral meniscus region (see figure 6.9(b)), the tangential flux term  $(\sin\theta/\bar{r})h_\theta$  in equation (6.11) can no longer be neglected. Burgess & Foster (1990) performed an involved analysis of the lubrication equation in this region for a pancake droplet at low capillary numbers and found that the local film thickness in the so-called lateral transition regions scales as  $Ca^{4/5}$  rather than as  $Ca^{2/3}$ . Therefore, for  $Ca \ll 1$ , the film thickness in these lateral regions is much smaller than the one in the other regions. This explains why one observes catamaran-like structures in the lateral regions of pancake droplets. Note that for the  $Ca$ -range considered in the present study, the film thickness in the lateral transition regions is still sufficiently large so that the viscous dissipation can be neglected also in these regions, as confirmed by the results of Sec. 6.3. Furthermore, Burgess & Foster (1990) have also shown that the polar extent of these lateral regions scales as  $Ca^{1/5}$ , whereas their radial extent scales as  $Ca^{2/5}$  instead of as  $Ca^{1/3}$  that one has for the length of rear and front dynamic menisci of axisymmetric droplets (see also Hodges, Jensen & Rallison (2004)).

### 6.5 Conclusions and perspectives

We report the velocity, mean film thickness and thickness map for a droplet moving due to buoyancy in a vertical Hele-Shaw cell. The mean drop velocity compares well with the leading order velocity expression of Gallaire *et al.* (2014). This signifies that buoyancy and viscous drag force are the dominant forces in our experimental parameter range with the viscous dissipation in the film thickness and in the dynamical meniscus having a negligible effect on the droplet velocity. On the contrary, the dimensionless mean film thickness data was dependent on the dimensionless droplet velocity, expressed as  $Ca$ , and was fitted with the *Taylor's law* model (Aussillous & Quéré, 2000).

We also obtained the complete film thickness maps using a CCI optical pen mounted on a linear translation stage. Based on a boundary integral method, 3D Stokes equations were solved. These numerical results for  $\lambda = 1$  were in very good agreement with our experimental results. The thickness pattern had a distinct catamaran-like shape as experimentally observed for pressure-driven flows in Huerre *et al.* (2015) and Reichert *et al.* (2018).

To understand the nature of the thickness patterns observed experimentally and numerically, the problem was approached using a lubrication equation, which was solved as a boundary value problem, rather than as an initial value problem, as recently conducted by Atasi *et al.* (2018). In spite of all the crude assumptions done for developing the model, its nonlinear solution for the film thickness profile of a pancake bubble compared surprisingly well with the results of 3D BIM simulations, evidencing the robustness of the thin-film pattern.

In order to unravel the structure of the film thickness profile, we linearized the lubrication model and solved for the linear thickness corrections around a uniformly-thick film. We have been able to show that not only the oscillations at the rear meniscus, but also the catamaran-like pattern can be directly retrieved by solving the linear 2D lubrication equation when perturbing the film thickness at the boundaries, which mimics the presence of a meniscus of

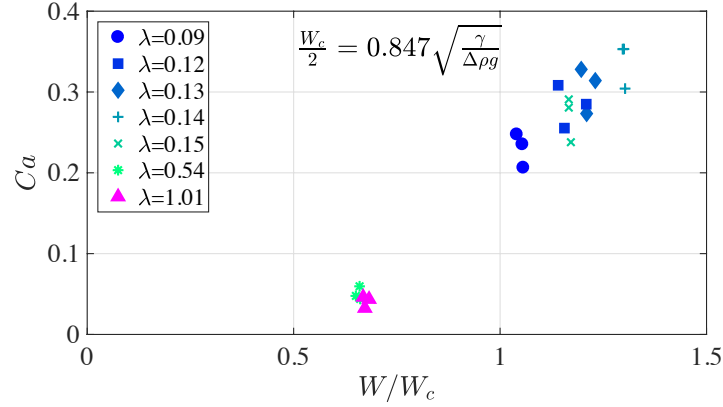


Figure 6.10 – As stated by Lamstaes & Eggers (2017), for a planar geometry the drops should get stuck when  $W < W_c$ . Our experiments show that the pancake-shaped drops continue to move beyond this limitation.

greater film thickness. In particular, the catamaran-like structure results from the anisotropic flux induced by the motion of the walls with respect to the pancake and the need to match the film thickness to larger values in the dynamic meniscus region surrounding the region where the thin film is rather uniform. This pattern is therefore independent of the force driving the motion. In fact, in totally different contexts, the same pattern is also found in drops levitating on a moving substrate (Hodges *et al.*, 2004; Lhuissier, Tagawa, Tran & Sun, 2013) as well as in oleoplaning drops (Daniel, Timonen, Li, Velling & Aizenberg, 2017). In the central part of the pancake droplet, the thickness left by the front meniscus scales as  $(Ca \cos \theta)^{2/3}$ , and depends therefore on the velocity normal to the interface. This scaling no longer holds in the lateral transition region, where the component of the flux tangential to the interface becomes important and the thickness of the film is much smaller, resulting in the formation of the catamaran-like structure.

Finally, we would like to highlight a contrasting feature seen between drops moving in a cylindrical tube and that in a Hele-Shaw cell. In cylindrical tubes the main difference between the pressure-driven and buoyancy-driven bubble motion, as found by Bretherton (1961), is that buoyant bubbles may remain stuck if the capillary radius is less than  $0.918l_c$ , where the capillary length  $l_c = \sqrt{\gamma/\Delta\rho g}$ . This failure results from the impossibility to match the static gravity-corrected meniscus shape with the flat thin film region. A similar result was obtained recently in the planar geometry by Lamstaes & Eggers (2017) with a prefactor of 0.847. Interestingly enough, we suspect that there is no such bubble arrest in Hele-Shaw cells, as a consequence of the additional direction which adds a degree of freedom in the curvature. As shown in figure 6.10, our experimental results show marked drop motion when the half cell gap is below  $0.847l_c$ .

I. S. thanks the Swiss National Science Foundation (grant no. 200021-159957). The computer

## Chapter 6. Film thickness distribution in gravity-driven pancake-shaped droplets rising in a Hele-Shaw cell

---

time is provided by the Swiss National Supercomputing Centre (CSCS) under project ID s603. An ERC starting grant “SimCoMiCs 280117” is gratefully acknowledged. L. Z. thanks a VR International Postdoc Grant “2015- 06334” from the Swedish Research Council.

## 6.6 Appendix

### 6.6.1 CCI working principle

We hereby describe the principle of the Confocal Chromatic Imaging technique. An achromatic lens decomposes the incident white light into a continuum of monochromatic images which constitutes the measurement range. The light reflected by a sample surface put inside this range is collected by a beam splitter. A pinhole allows then to block the defocused light that does not come from the sample surface. Eventually, the spectral repartition of the collected light is analyzed by a spectrometer. The wavelength of maximum intensity is detected and the distance value is deduced from a calibration curve. Several reflecting interfaces can be detected at the same time, allowing thickness measurement of thin transparent layers.

### 6.6.2 Derivation of two-dimensional nonlinear lubrication equation for pancake droplets

The derivation of the model equation presented in Section 6.4.2 is briefly outlined hereafter. Considering the same physical properties for the droplet and the outer medium as outlined in Section 6.1, and under the assumption of negligible inertia (Oron *et al.*, 1997) with  $\rho_i \ll \rho_o$ , and  $\mu_i \ll \mu_o$  the three dimensional momentum equations reads

$$0 = -\frac{\partial p}{\partial x} + \mu_o \left( \frac{\partial^2 u}{\partial x^2} + \frac{\partial^2 u}{\partial y^2} + \frac{\partial^2 u}{\partial z^2} \right) - \rho_o g, \quad (6.14)$$

$$0 = -\frac{\partial p}{\partial y} + \mu_o \left( \frac{\partial^2 v}{\partial x^2} + \frac{\partial^2 v}{\partial y^2} + \frac{\partial^2 v}{\partial z^2} \right), \quad (6.15)$$

$$0 = -\frac{\partial p}{\partial z} + \mu_o \left( \frac{\partial^2 w}{\partial x^2} + \frac{\partial^2 w}{\partial y^2} + \frac{\partial^2 w}{\partial z^2} \right). \quad (6.16)$$

Using  $L$  as the characteristic length scale in  $x$  and  $y$  direction and the film thickness  $H$  as the characteristic length scale in  $z$  direction, the film aspect ratio  $\epsilon$  is defined as  $\epsilon = H/L$ . The long wavelength approximation is employed since  $\epsilon \ll 1$ . Mass conservation indicates that the characteristic velocity in  $z$  direction ( $W$ ) is much smaller than the other two components ( $U$

in  $x$  and  $V$  in  $y$  direction),  $W \sim \epsilon U \ll U$  and  $W \sim \epsilon V \ll V$ . The Stokes equation simplifies as

$$0 = -\frac{\partial p}{\partial x} + \mu_o \frac{\partial^2 u}{\partial z^2} - \rho_o g, \quad (6.17)$$

$$0 = -\frac{\partial p}{\partial y} + \mu_o \frac{\partial^2 v}{\partial z^2}, \quad (6.18)$$

$$0 = -\frac{\partial p}{\partial z}. \quad (6.19)$$

Integrating equation (6.19) in  $z$  and applying dynamic boundary conditions yields  $p = p_0 - \gamma \kappa$  where  $\kappa$  is the mean curvature of the interface. Integrating equation (6.17) and (6.18) twice in  $z$  and considering  $u(z=0) = -U_d$  and the zero-slip boundary condition  $v(z=0) = 0$  as well as the zero-shear-stress interface  $\partial u(z=H)/\partial z = 0$  and  $\partial v(z=H)/\partial z = 0$  yields the velocity components:

$$u = \frac{(\gamma \kappa_x - \Delta \rho g)}{\mu_o} \left( H - \frac{z}{2} \right) z - U_d, \quad (6.20)$$

$$v = \frac{\gamma \kappa_y}{\mu_o} \left( H - \frac{z}{2} \right) z. \quad (6.21)$$

Since the inner medium density  $\rho_i \ll \rho_o$ , we replace  $\rho_o$  by  $\Delta \rho$  in equation (6.20) where  $\Delta \rho = \rho_o - \rho_i$  represents the density difference between the inner and outer fluid. Integrating equation (6.20) and (6.21) in  $z$  from 0 to  $H$  yields the flux in  $x$  and  $y$  direction as

$$Q^u = \frac{H^3}{3\mu_o} (\gamma \kappa_x - \Delta \rho g) - U_d H, \quad (6.22)$$

$$Q^v = \frac{H^3}{3\mu_o} \gamma \kappa_y. \quad (6.23)$$

Finally integrating the continuity equation and applying the Leibniz Integral rule and the kinematic boundary condition at the interface yield the mass conservation equation expressed as

$$\frac{\partial H}{\partial t} + \frac{\partial Q^u}{\partial x} + \frac{\partial Q^v}{\partial y} = 0. \quad (6.24)$$

Introducing equation (6.22) and (6.23) in equation (6.24) finally yields the lubrication equation:

$$\frac{\partial H}{\partial t} + \frac{\partial}{\partial x} \left[ \frac{H^3}{3\mu_o} \underbrace{(\gamma \kappa_x)}_{\text{I}} - \underbrace{\Delta \rho g}_{\text{II}} - \underbrace{U_d H}_{\text{III}} \right] + \frac{\partial}{\partial y} \left[ \frac{H^3}{3\mu_o} \underbrace{\gamma \kappa_y}_{\text{I}} \right] = 0. \quad (6.25)$$

The terms **I** in the spatial variation of the flux corresponds to the surface tension effects, term **II** to the variation due to the buoyancy force and term **III** accounts for the reference frame moving with the drop. Note the anisotropy of the fluxes: both the buoyancy and the motion in the  $x$  direction do not affect the flux in the  $y$  direction, breaking the isotropy induced by the

## Chapter 6. Film thickness distribution in gravity-driven pancake-shaped droplets rising in a Hele-Shaw cell

---

capillary pressure gradient.

Using the pancake radius  $a$  as the characteristic length and  $a/U_d$  as the characteristic time, the dimensionless lubrication equation for the steady profile in the dimensionless coordinate system  $\bar{x}, \bar{y}$  is written as equation (6.7).

## 7 Conclusions and perspectives

Since major conclusions were drawn at the end of each chapter, we present here only brief overview of each chapter with some future perspectives for certain sections.

### 7.1 Summary

The thesis mainly concentrates on amplifier flows which have a large amplification potential in presence of external noise. Defining this as the stepping stone, we started our analysis in **chapter 2** with a canonical example of amplifier flows-the backward facing step (BFS). Based on the theory developed and implemented by Edouard Boujo and Eunok Yim, we carried out the second order sensitivity analysis of a spanwise modulated BFS. The sensitiveness of the flow in presence of active and passive controls was analysed. The sensitivity analysis was aimed at reducing the separation length by anticipating the reattachment point, a feature which has close resemblance to the total gain in a BFS, owing to the fact that the reattachment point defines the size of recirculation bubble which in turn controls the flow separation and hence the flow evolution in the entire domain.

**chapter 2** also briefly introduced the method of *vaccination*, wherein the control in BFS (without any spanwise control) in presence of incoming noise was investigated through nonlinear simulations. The control in such flows was employed by using the optimal forcing which has been already investigated by previous works. By modulating the amplitude of the control forcing, one could see that the response envelope of the flow in presence of the white noise was suitably diminished, especially for a certain frequency band below the optimal forcing frequency.

Drawing the general conclusion from **chapter 2** for amplifier flows, where small amplitude control was seen to cause notable change in flow response, we advanced our study on amplifier flows by taking the example of free interface capillary jets in **chapter 3** and **chapter 4**. Similar to the BFS, where we chose a length scale (separation length) as the measure for the response to external forcing, we chose the breakup length in the case of jets as the basis for comparing

the effect of different controls.

**Chapter 3** laid a foundation for the jet flow analysis using the one-dimensional (1D) Eggers & Dupont equations. We studied the parallel capillary jets through local analysis and investigated the flow through simulations based on the complete nonlinear form of 1D Eggers & Dupont equations. The spatio-temporal analysis performed on the linear equations marked the transition from an absolutely unstable to a convectively unstable jet, the latter providing a regime where the spatial instability analysis is well posed. The spatial analysis performed in this regime resulted in obtaining the most unstable frequency  $\omega_{opt}$  which caused the largest spatial growth rate  $-k_i$ . A comparison was made with the numerical analysis where the strength of a given forcing was determined by the resulting breakup length. The smallest breakup length was related to the optimal forcing. The  $\omega_{opt}$  obtained from the nonlinear simulations was indeed in accordance with the local spatial stability analysis. Moreover,  $\omega_{opt}$  was found to be independent of the forcing amplitude or the domain size.

Using a similar approach, we then proceeded to analyse the effect of external forcing on capillary jets stretched under the effect of gravity in **chapter 4**. Since such an analysis can only be performed for stable jets which are susceptible to external forcing, we began our analysis by performing the linear stability analysis of the gravitationally stretched jet using both the local and global framework. The spatial analysis was further extended using the WKBJ formulation.

The effect of the external forcing on the stable jet was first analysed numerically where we concluded that the  $\omega_{opt}$  producing the shortest breakup length was a function of the forcing amplitude  $\epsilon$ . Smaller the  $\epsilon$ , larger was the  $\omega_{opt}$ , a result which was in contraction to the one obtained for parallel jets. A decrease in the forcing amplitude resulted in a larger breakup length, which would further imply larger downstream stretching of the imposed forcing. Hence for a forcing to be ‘felt’ at a given downstream station, its frequency had to be increased.

We next reformulated a resolvent analysis so as to represent the forcing type used for the numerical simulations and expressed the optimal gain using the singular value decomposition of the resolvent operator. First, by expressing the gain as a function of the domain size in  $z$  at constant forcing frequency and, second by specifying the gain expression in terms of the forcing amplitude, we could predict not only the  $\omega_{opt}$  for a given forcing amplitude  $\epsilon$  but also the resulting breakup length as observed from the nonlinear simulations. Finally we performed simulations in presence of white noise with a fixed noise level. As expected for amplifier flows, the jet had a preferential response for frequencies defined in a certain range. More evidently, the preferred frequency range at the given noise level was found to be close to the one obtained by pure harmonic forcing of the  $\omega_{opt}$  for the same forcing amplitude.

Using the 1D Eggers & Dupont equation as an inspiration, we then attempted to analyse the drop size of silicone spheres obtained when a solid silicone-in-silica co-axial fibre is fed into a flame at a certain speed in **chapter 5**. The work is based on the experimental work of Gumennik *et al.* (2013). The authors found that the size of these particles varied monotonically with the speed at which the fibre is fed into the flame. To analyse the physical mechanism behind the



drop size selection, Saviz Mowlavi performed the linear analysis based on a simplified model derived from standard long-wavelength approximations. Owing to the failure of the linear stability analysis, we resorted to nonlinear simulations of the simplified model to recover the particle size seen in experiments. Without any adjustable parameters, the simulations predicted a drop size at the same order of magnitude as the one observed in the experiments.

Finally, to explore some physical aspects of the drops obtained after the nonlinear breakup of a jet, we performed experiments in a Hele-Shaw cell to estimate the pancake-shaped drop velocity and the lubrication film thickness distribution of a droplet rising in a vertical cell in **chapter 6**. We found that for the chosen experimental range of parameters, the drop velocity was independent of the lubrication film thickness and that of the dynamics meniscus. Additionally the droplet displayed the ‘catamaran’ like film thickness pattern which agreed well with the three-dimensional numerical results of Lailai Zhu. The pattern was then rationalized by Gioele Balestra using a two-dimensional lubrication equation.

## 7.2 Perspectives

In the following sections we present some perspectives for the linear, nonlinear and experimental analysis.

### 7.2.1 Sensitivity analysis of spatially varying jet

For the spatially varying jet presented in **Chapter 4**, we found that the optimal forcing frequency was amplitude dependent. However, the analysis was performed only on a fixed case of stable jet. Even though a similar behaviour is expected for other cases of stable jet, it would be interesting to generate maps of optimal forcing for varying ranges of flow parameters and forcing amplitudes. Instead of resorting to computationally expensive numerical simulations, one can benefit from the resolvent analysis whose validity has already been proven in predicting the  $\omega_{opt}$  and the corresponding breakup length  $l_c$  for a given forcing amplitude  $\epsilon$ . The resolvent framework can be extended to formulate the sensitivity operator which analyses the sensitiveness of a defined function due to a small change in the applied control.

For instance one can evaluate the sensitiveness of the breakup length  $l_c$  for a small variation in forcing amplitude  $\epsilon$  or frequency  $\omega$  close to the optimal forcing. Since we are always interested in the optimal forcing producing the shortest breakup length, we define the objective function as the minimum obtainable  $l_c$ , subject to a given control  $f$ . This can be represented as,

$$\min_f \mathcal{F}(l_c, f) \quad \text{subject to} \quad \partial_t \mathbf{q} = L[\mathbf{q}] + f, \quad (7.1)$$

where  $L$  is the linear operator describing the governing equations and the control  $f = \epsilon \exp(i\omega t)$ . We define the sensitivity operators:  $\nabla l_{c,\epsilon}$  and  $\nabla l_{c,\omega}$ , which represent the variation in  $l_c$  due to a small variation in forcing amplitude  $\delta\epsilon$  and forcing frequency  $\delta\omega$ , respectively. Mathematically

expressed as,

$$\nabla l_{c,\epsilon} = \frac{d\mathcal{F}}{d\epsilon}, \quad (7.2a)$$

$$\nabla l_{c,\omega} = \frac{d\mathcal{F}}{d\omega}, \quad (7.2b)$$

the sensitivity operator aids in evaluating the net sensitivity of  $l_c$  for a small variation in  $\epsilon$  at constant  $\omega$ , expressed as,

$$\delta l_{c,\epsilon} = (\nabla l_{c,\epsilon}, \delta\epsilon). \quad (7.3)$$

Similarly the sensitivity of the breakup length to a small variation on  $\omega$  at constant  $\epsilon$  can be expressed as,

$$\delta l_{c,\omega} = (\nabla l_{c,\omega}, \delta\omega). \quad (7.4)$$

However, similar to the resolvent analysis the sensitivity analysis would also be only partially representative of the breakup in a jet due to the fact that linear analysis fails to predict the bimodal drop distribution often observed during the breakup process. The only plausible way to capture individually the occurrence and the size of the main and satellite drops is through nonlinear simulations. Thus we next propose some improvements that could be applied in our current numerical scheme to capture accurately the main and satellite drop formation.

### 7.2.2 Improvements for numerical scheme for capturing drop dynamics

The numerical scheme implemented in this thesis to analyse the breakup of different types of jets is limited in its functionality since the information of the drop evolution is lost soon after the instant of jet breakup. The absence of a drop capturing scheme raises several questions. For instance one does not know if the main and satellite drops formed at the time of breakup will coalesce into a single drop or disintegrate into several more while moving downstream.

Moreover the methods which could be employed for controlling satellite drop formation cannot be verified in absence of a scheme which does not take into account the drop evolution post breakup. For instance, Hilbing & Heister (1996) studied the main and satellite drop size variation as the amplitude of the forcing was increased progressively at constant forcing frequency (see figure 7.1(c)). At low amplitudes, the satellite drop size was found to be much smaller in comparison to the main drop, a feature which could eventually assist in the merging of the two drops due to the large disparity in velocity. However, there is no information regarding the drop size dependence on the forcing amplitude when a spatially varying jet is forced at its (amplitude dependent) optimal frequency. For example, as shown in figure 7.1(a) and 7.1(b), if the gravitationally stretched jet is forced at  $\omega_{opt}$  for the given forcing amplitude, the difference between the size of satellite and main drop  $\Delta R$  was seen to increase if the amplitude was increased. At  $\epsilon = 10^{-4}$ ,  $\Delta R = 0.4$  which increased to  $\Delta R = 0.84$  at  $\epsilon = 10^{-2}$ . Thus the complex dependence of the individual drop size on the forcing amplitude compels the

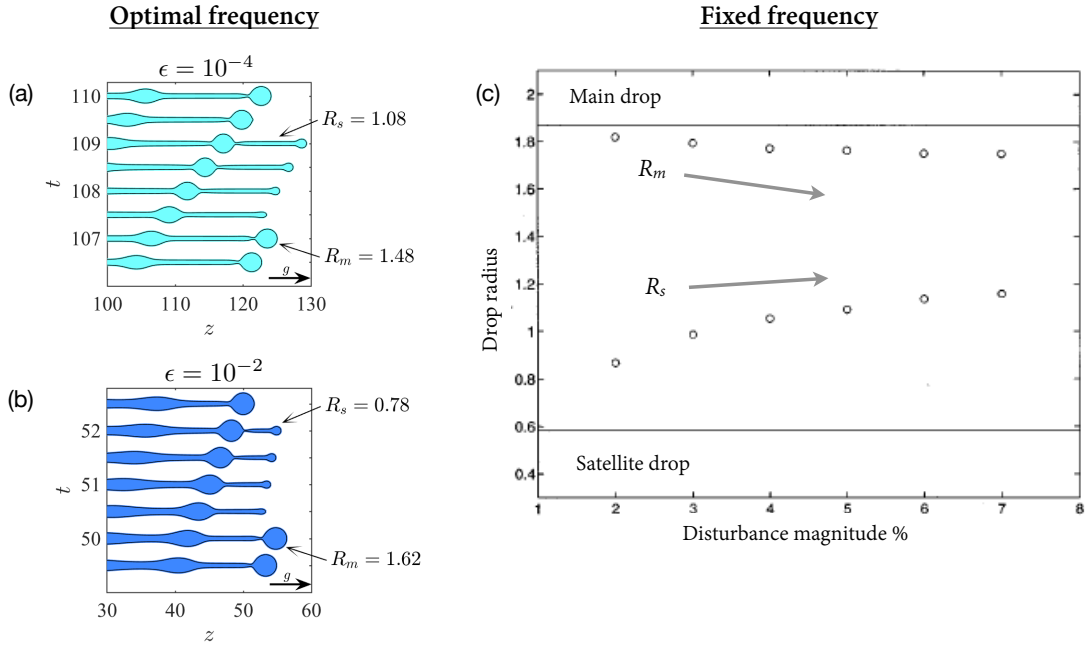


Figure 7.1 – Main and satellite drop size captured through nonlinear simulations for a spatially varying jet flow and excited at the (amplitude dependent) optimal forcing frequency at forcing amplitude (a)  $\epsilon = 10^{-4}$  and (b)  $\epsilon = 10^{-2}$ . (c) Main/satellite drop size variation as a function of forcing amplitude, in a parallel jet being forced at a fixed frequency. Image obtained from (Hilbing & Heister, 1996).

inclusion of drop capture beyond the breakup location.

In this direction, we propose certain steps which will eventually lead to a better control of satellite drop formation:

#### Defining the slope based on drop scale

For spatially varying jets, often the breakup can display a variety of shapes existing on different length scales (refer figure 7.1(a)-7.1(b)). The current numerical scheme, which only accounts for the slope of the tip is not sufficient for capturing drop tips with varying curvature, especially if the pinchoff is similar to figure 7.2(a) or resembling the shape due to Klystron effect when a high speed jet collides with the ejected drop (refer figure 1.12).

One possible way to implement slopes of varying scales could be by applying a nonuniform grid. At the time of breakup, the entire jet will be subdivided into several segments having their own intact length. The grid size should be scaled in accordance with the individual intact lengths, the smaller the span of the liquid segment, smaller would be the discretisation size. Additionally, we believe that the stretching extent of a drop pre or post breakup indirectly depends on the velocity at which it is travelling. Thus this information should be used as a control while deciding the arbitrary value assigned to the adjacent node to the tip.

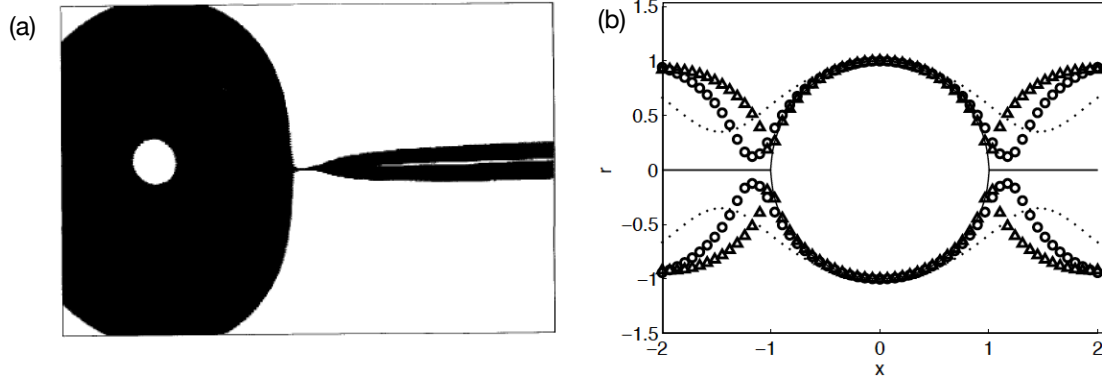


Figure 7.2 – (a) Enlargement of the breakup region highlighting the large drop and the creation of the thin micro-thread, both with highly different slopes. Image obtained from Kowalewski (1996). (b) Interface solution with the exact solution (solid line) and regularised approximations (markers). The values of the regularisation radius  $R_c$  are 0.5 ( $\cdot$ ), 0.2 ( $\circ$ ) and 0.01 ( $\Delta$ ). Image obtained from Driessen & Jeurissen (2011)

### Capturing drop evolution beyond breakup

For simultaneously simulating the intact jet and the drops being ejected from it, inspiration can be taken from the work of Driessen & Jeurissen (2011) who develop a model to calculate the flow evolution between consecutive breakups for parallel jets. Indeed the drop evolution post-breakup requires the information from the system pre-breakup. Since the singularities are treated by defining the breakup at some predefined arbitrary value, they regularize the singularity using a small modification of the momentum flux. This regularization sets a lower limit for the length and time scales. The regularization is performed on the surface tension term by using the cutoff radius  $R_c$  which is the control parameter, chosen to scale with the spatial step. Thus the exact solution of the non regularized system is reached by refining the grid (see figure 7.2(b)). Due to the regularization, even when the jet radius approaches zero, the capillary tension goes to a finite value. This allows the existence of a stable liquid column between the free floating liquid segments.

### Forcing by a combination of frequencies and amplitudes

The successful implementation of the drop capture scheme will finally aid in the analysis of the satellite drop elimination using different methods. Indeed the forcing amplitude can be of importance in eliminating the satellite drops but at the cost of producing a drop size which may be out of bounds for the necessary application. To have simultaneously a precise control over the drop size and the satellite drops, the jet could be forced at inlet with a combination of forcing frequencies which are both close to  $\omega_{opt}$  for that forcing amplitude.

This approach is inspired by the work of Driessen *et al.* (2014), who demonstrated a novel method of producing a stream of widely spaced high-velocity droplets by imposing a superposition of two Rayleigh-Plateau unstable modes on a liquid jet, as shown in figure 7.3. The

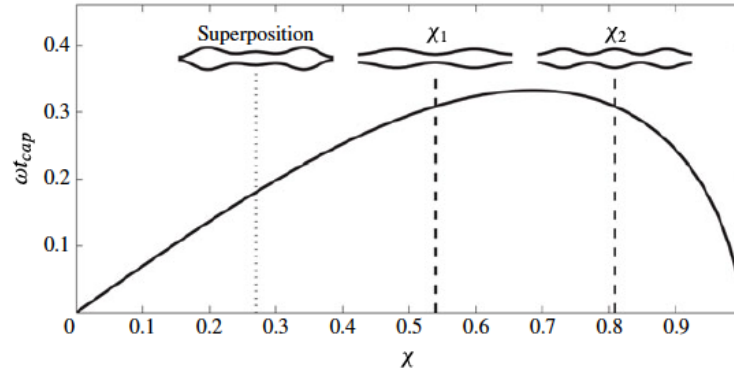


Figure 7.3 – The plots shows the dispersion relation of the Rayleigh-Plateau instability for an infinite inviscid jet ( $We \gg 1$ , and  $Oh \ll 1$ ).  $\chi_1$  and  $\chi_2$  represent the different perturbation wavenumbers induced on the jet where the contours represent their individual radius perturbations. The superposition of the two modes is also shown. Image extracted from Driessen *et al.* (2014).

chosen modes had a wavelength close to the most unstable mode. The interference pattern resulting from the superimposition of the two modes caused local asymmetries in the capillary tension, which eventually altered the velocity of the initial droplets. Drops with very different velocities finally resulted in coalescing together and producing a stream of larger drops.

A similar approach can be applied for the spatially varying gravity jets. Unlike Driessen *et al.* (2014), the two forcing frequency, chosen around  $\omega_{opt}$  should have identical growth rates  $-k_i$ . However, the spatially varying  $\omega_{opt}$  and the resulting variation in  $-k_i$  requires a deeper analysis of the response in presence of combination frequencies. The decay in growth rate in presence of a combination frequency is not as straightforward as the method applied by Driessen *et al.* (2014) for parallel jets.

Indeed the entire analysis is based on choosing two frequencies which have identical growth rate. However, one does not know a priori the effect of the gap (between the  $\omega_{opt}$  and the individual frequencies) on the final breakup length or the drop size. This could be analysed both numerically and analytically by formulating a sensitivity operator which looks at the effect of the frequency gap on the breakup length. Even though the sensitivity analysis cannot predict the drop size, it would be interesting to find ways of relating the results of the linear and nonlinear analysis.

### 7.2.3 Obtaining the limit condition for static drops in Hele-Shaw cell

The conclusion of **chapter 6** discusses the difference between the drop motion in a Hele-Shaw cell in comparison to the one in a cylindrical tube. Unlike the cylindrical tubes where Bretherton (1961) found that buoyant drops may remain stuck if the capillary radius is less than  $0.918l_c$ , where  $l_c$  is the capillary length, the drop motion in the Hele-Shaw cell presents

no such conclusion for our chosen experimental parameters. However, it would be interesting to investigate the critical flow parameters and its relation with the aspect ratio (drop radius to cell gap width), which eventually leads to a buoyant drop getting stuck in the Hele-Shaw. Performing experiments with varying properties could also lead us to see if the limit proposed by Lamstaes & Eggers (2017) for the drops to get stuck in Hele-Shaw cells,  $0.847l_c$ , is valid in certain flow regimes. In addition, the Hele-Shaw cell-inclination can be used as a scale for changing the net magnitude of gravitational pull acting on the drop. Although the asymmetry caused by the inclined cell would set a limit to the maximum drop size, it would allow us to investigate the relation between the magnitude of gravitational force and the appearance of the ‘catamaran’ shape.

# Bibliography

- AHMED, A. & BAYS-MUCHMORE, B. 1992 Transverse flow over a wavy cylinder. *Physics of Fluids A: Fluid Dynamics* **4** (9), 1959–1967.
- AHMED, A., KHAN, M.J. & BAYS-MUCHMORE, B. 1993 Experimental investigation of a three-dimensional bluff-body wake. *AIAA journal* **31** (3), 559–563.
- ÅKERVIK, E., EHRENSTEIN, U., GALLAIRE, F. & HENNINGSON, D. S. 2008 Global two-dimensional stability measures of the flat plate boundary-layer flow. *European Journal of Mechanics-B/Fluids* **27** (5), 501–513.
- ALIZARD, F., CHERUBINI, S. & ROBINET, J.-C. 2009 Sensitivity and optimal forcing response in separated boundary layer flows. *Physics of Fluids* **21** (6), 064108.
- AMBRAVANESWARAN, B., PHILLIPS, S. D. & BASARAN, O. A. 2000 Theoretical analysis of a dripping faucet. *Physical Review Letters* **85** (25), 5332.
- AMBRAVANESWARAN, B., SUBRAMANI, H. J., PHILLIPS, S. D. & BASARAN, O. A. 2004 Dripping-jetting transitions in a dripping faucet. *Physical Review Letters* **93** (3), 034501.
- AMBRAVANESWARAN, B., WILKES, E. D. & BASARAN, O. A. 2002 Drop formation from a capillary tube: Comparison of one-dimensional and two-dimensional analyses and occurrence of satellite drops. *Physics of Fluids* **14** (8), 2606–2621.
- ARMALY, B. F., DURST, F., PEREIRA, J.C.F. & SCHÖNUNG, B. 1983 Experimental and theoretical investigation of backward-facing step flow. *Journal of Fluid Mechanics* **127**, 473–496.
- ATASI, O., HAUT, B., DEHAECK, S., DEWANDRE, A., LEGENDRE, D. & SCHEID, B. 2018 How to measure the thickness of a lubrication film in a pancake bubble with a single snapshot? *Applied Physics Letters* **113** (17), 173701.
- AUGELLO, L. 2015 Instability of two-phase co-axial jets at small reynolds number. PhD thesis, EPFL, Lausanne.
- AUGELLO, L., FANI, A. & GALLAIRE, F. 2018 The influence of the entry region on the instability of a coflowing injector device. *Journal of Physics: Condensed Matter* **30** (28), 284003.

## Bibliography

---

- AUSSILLOUS, P. & QUÉRÉ, D. 2000 Quick deposition of a fluid on the wall of a tube. *Physics of Fluids* **12** (10), 2367–2371.
- BALESTRA, G. 2018 Pattern formation in thin liquid films: from coating-flow instabilities to microfluidic droplets. PhD thesis, EPFL, Lausanne.
- BALESTRA, G., ZHU, L. & GALLAIRE, F. 2018 Viscous Taylor droplets in axisymmetric and planar tubes: from Bretherton's theory to empirical models. *Microfluidics and Nanofluidics* **22** (6), 67.
- BANK, R. E., COUGHRAN, W. M., FICHTNER, W., GROSSE, E. H., ROSE, D. J. & SMITH, R. K. 1985 Transient simulation of silicon devices and circuits. *IEEE Transactions on Electron Devices* **32** (10), 1992–2007.
- BARBET, B., ATTEN, P. & SOUCEMARIANADIN, A. 1997 Two-mode EHD stimulation of a continuous jet: Generation of drops and satellites. *Journal of Imaging Science and Technology* **41** (6), 570–576.
- BARKLEY, D., GOMES, M. G. M. & HENDERSON, R. D. 2002 Three-dimensional instability in flow over a backward-facing step. *Journal of Fluid Mechanics* **473**, 167–190.
- BAROUD, C. N., GALLAIRE, F. & DANGLA, R. 2010 Dynamics of microfluidic droplets. *Lab on a Chip* **10** (16), 2032–2045.
- BARRÉ, S., FLEURY, V., BOGEY, C., BAILLY, C. & JUVÉ, D. 2006 Experimental study of the spectral properties of near-field and far-field jet noise. *12th AIAA/CEAS Aeroacoustics Conference* **6**, 73–92.
- BASARAN, O. A. 2002 Small-scale free surface flows with breakup: Drop formation and emerging applications. *AIChE Journal* **48** (9), 1842–1848.
- BASARAN, O. A., GAO, H. & BHAT, P. P. 2013 Nonstandard inkjets. *Annual Review of Fluid Mechanics* **45**, 85–113.
- BEARMAN, P.W. & OWEN, J.C. 1998 Reduction of bluff-body drag and suppression of vortex shedding by the introduction of wavy separation lines. *Journal of Fluids and Structures* **12** (1), 123–130.
- BENDER, C. M. & ORSZAG, S. 1978 *Advanced mathematical methods for Engineers and Scientists*. McGraw-Hill, New York.
- BENNETT, W. D., BROWN, J. S., ZEMAN, K. L., HU, S.-C., SCHEUCH, G. & SOMMERER, K. 2002 Targeting delivery of aerosols to different lung regions. *Journal of Aerosol Medicine* **15** (2), 179–188.
- BERS, A. 1975 *Linear waves and instabilities*. Physique des Plasmas.



- BERS, A. 1983 *Space-time evolution of plasma instabilities-absolute and convective*. North-Holland, Amsterdam.
- BLACKBURN, H. M., BARKLEY, D. & SHERWIN, S. J. 2008 Convective instability and transient growth in flow over a backward-facing step. *Journal of Fluid Mechanics* **603**, 271–304.
- BOTTARO, A., CORBETT, P. & LUCHINI, P. 2003 The effect of base flow variation on flow stability. *Journal of Fluid Mechanics* **476**, 293–302.
- BOUJO, E., EHRENSTEIN, U. & GALLAIRE, F. 2013 Open-loop control of noise amplification in a separated boundary layer flow. *Physics of Fluids* **25** (12), 124106.
- BOUJO, E., FANI, A. & GALLAIRE, F. 2015 Second-order sensitivity of parallel shear flows and optimal spanwise-periodic flow modifications. *Journal of Fluid Mechanics* **782**, 491–514.
- BOUJO, E., FANI, A. & GALLAIRE, F. 2019 Second-order sensitivity in the cylinder wake: optimal spanwise-periodic wall actuation and wall deformation. *Physical Review Fluids* **4** (5), 053901.
- BOUJO, E. & GALLAIRE, F. 2014*a* Controlled reattachment in separated flows: a variational approach to recirculation length reduction. *Journal of Fluid Mechanics* **742**, 618–635.
- BOUJO, E. & GALLAIRE, F. 2014*b* Manipulating flow separation: sensitivity of stagnation points, separatrix angles and recirculation area to steady actuation. *Proceedings of the Royal Society A: Mathematical, Physical and Engineering Sciences* **470** (2170), 20140365.
- BOUJO, E. & GALLAIRE, F. 2015 Sensitivity and open-loop control of stochastic response in a noise amplifier flow: the backward-facing step. *Journal of Fluid Mechanics* **762**, 361–392.
- BRANDT, L., SIPP, D., PRALITS, J. O. & MARQUET, O. 2011 Effect of base-flow variation in noise amplifiers: the flat-plate boundary layer. *Journal of Fluid Mechanics* **687**, 503–528.
- BRENNER, M. P., SHI, X. D. & NAGEL, S. R. 1994 Iterated instabilities during droplet fission. *Physical Review Letters* **73** (25), 3391.
- BRETHERTON, F. P. 1961 The motion of long bubbles in tubes. *Journal of Fluid Mechanics* **10** (2), 166–188.
- BRIGGS, R. J. 1964 *Electron-stream interaction with plasmas*. MIT Press Cambridge MA.
- BRUN, P.-T., DAMIANO, A., RIEU, P., BALESTRA, G. & GALLAIRE, F. 2015 Rayleigh-Taylor instability under an inclined plane. *Physics of Fluids* **27** (8), 084107.
- BURGESS, D. & FOSTER, M. R. 1990 Analysis of the boundary conditions for a Hele-Shaw bubble. *Physics of Fluids A* **2** (7), 1105–1117.
- BUSH, J. W. M. 1997 The anomalous wake accompanying bubbles rising in a thin gap: a mechanically forced Marangoni flow. *Journal of Fluid Mechanics* **352**, 283–303.
- CHARRU, F. 2011 *Hydrodynamic instabilities*. Cambridge University Press.

## Bibliography

---

- CHAUDHARY, K. C. & MAXWORTHY, T. 1980 The nonlinear capillary instability of a liquid jet. Part 2. Experiments on jet behaviour before droplet formation. *Journal of Fluid Mechanics* **96** (2), 275–286.
- CHAUDHARY, K. C. & REDEKOPP, L. G. 1980 The nonlinear capillary instability of a liquid jet. Part 1. Theory. *Journal of Fluid Mechanics* **96** (2), 257–274.
- CHOI, H., JEON, W.-P. & KIM, J. 2008 Control of flow over a bluff body. *Annual Review of Fluid Mechanics* **40**, 113–139.
- CHOMAZ, J.-M. 2005 Global instabilities in spatially developing flows: non-normality and nonlinearity. *Annual Review of Fluid Mechanics* **37**, 357–392.
- CHOMAZ, J. M., HUERRE, P. & REDEKOPP, L. G. 1988 Bifurcations to local and global modes in spatially developing flows. *Physical Review Letters* **60** (1), 25.
- CHRISTOPHER, G. F. & ANNA, S. L. 2007 Microfluidic methods for generating continuous droplet streams. *Journal of Physics D: Applied Physics* **40** (19), R319.
- CLANET, C. & LASHERAS, J. C. 1999 Transition from dripping to jetting. *Journal of Fluid Mechanics* **383**, 307–326.
- CORDERO, M. L., GALLAIRE, F. & BAROUD, C.N. 2011 Quantitative analysis of the dripping and jetting regimes in co-flowing capillary jets. *Physics of Fluids* **23** (9), 094111.
- COSSU, C. 2014 On the stabilizing mechanism of 2D absolute and global instabilities by 3D streaks. *arXiv preprint arXiv:1404.3191*.
- CRAMER, C., FISCHER, P. & WINDHAB, E.J. 2004 Drop formation in a co-flowing ambient fluid. *Chemical Engineering Science* **59** (15), 3045–3058.
- CROSS, M.C. & HOHENBERG, P.C. 1993 Pattern formation outside of equilibrium. *Reviews of Modern Physics* **65** (3), 851.
- CROW, S. C. & CHAMPAGNE, F. H. 1971 Orderly structure in jet turbulence. *Journal of Fluid Mechanics* **48** (3), 547–591.
- CUBAUD, T. & MASON, T. G. 2008 Capillary threads and viscous droplets in square microchannels. *Physics of Fluids* **20** (5), 053302.
- DANIEL, D., TIMONEN, J. V. I., LI, R., VELLING, S. J. & AIZENBERG, J. 2017 Oleoplaning droplets on lubricated surfaces. *Nature Physics* **13** (10), 1020.
- DEL GUERCIO, G., COSSU, C. & PUJALS, G. 2014a Optimal perturbations of non-parallel wakes and their stabilizing effect on the global instability. *Physics of Fluids* **26** (2), 024110.
- DEL GUERCIO, G., COSSU, C. & PUJALS, G. 2014b Optimal streaks in the circular cylinder wake and suppression of the global instability. *Journal of Fluid Mechanics* **752**, 572–588.

- DEL GUERCIO, G., COSSU, C. & PUJALS, G. 2014c Stabilizing effect of optimally amplified streaks in parallel wakes. *Journal of Fluid Mechanics* **739**, 37–56.
- DERGHAM, G., SIPP, D. & ROBINET, J.-C. 2013 Stochastic dynamics and model reduction of amplifier flows: the backward facing step flow. *Journal of Fluid Mechanics* **719**, 406–430.
- DERJAGUIN, B. V. C. R. 1943 On the thickness of the liquid film adhering to the walls of a vessel after emptying. *Acta Physicochimica URSS* **20**, 349–352.
- VAN DEVENTER, H., HOUBEN, R. & KOLDEWEIJ, R. 2013 New atomization nozzle for spray drying. *Drying Technology* **31** (8), 891–897.
- DOSHI, J. & RENEKER, D. H. 1995 Electrospinning process and applications of electrospun fibers. *Journal of Electrostatics* **35** (2-3), 151–160.
- DRIESSEN, T. & JEURISSEN, R. 2011 A regularised one-dimensional drop formation and coalescence model using a total variation diminishing (TVD) scheme on a single eulerian grid. *International Journal of Computational Fluid Dynamics* **25** (6), 333–343.
- DRIESSEN, T., SLEUTEL, P., DIJKSMAN, F., JEURISSEN, R. & LOHSE, D. 2014 Control of jet breakup by a superposition of two Rayleigh-Plateau-unstable modes. *Journal of Fluid Mechanics* **749**, 275–296.
- DUNNE, B. & CASSEN, B. 1956 Velocity discontinuity instability of a liquid jet. *Journal of Applied Physics* **27** (6), 577–582.
- DUPRAT, C., RUYER-QUIL, C., KALLIADASIS, S. & GIORGIUTTI-DAUPHINÉ, F. 2007 Absolute and convective instabilities of a viscous film flowing down a vertical fiber. *Physical Review Letters* **98** (24), 244502.
- EGGERS, J. 1997 Nonlinear dynamics and breakup of free-surface flows. *Reviews of Modern Physics* **69** (3), 865.
- EGGERS, J. & DUPONT, T. F. 1994 Drop formation in a one-dimensional approximation of the Navier-Stokes equation. *Journal of Fluid Mechanics* **262**, 205–221.
- EGGERS, J. & VILLERMAUX, E. 2008 Physics of liquid jets. *Reports on Progress in Physics* **71** (3), 036601.
- ERI, A. & OKUMURA, K. 2011 Viscous drag friction acting on a fluid drop confined in between two plates. *Soft Matter* **7** (12), 5648–5653.
- FARAJZADEH, R., ANDRIANOV, A. & ZITHA, P. L. J. 2009 Investigation of immiscible and miscible foam for enhancing oil recovery. *Industrial & Engineering chemistry research* **49** (4), 1910–1919.
- FARRELL, B. F. & IOANNOU, P. J. 1996 Generalized stability theory. Part I: Autonomous operators. *Journal of the Atmospheric Sciences* **53** (14), 2025–2040.

## Bibliography

---

- FISCHER, P. F., LOTTES, J. W. & KERKEMEIER, S. G. 2008 Nek5000 Web page. <http://nek5000.mcs.anl.gov>.
- FRANKEL, I. & WEIHS, D. 1985 Stability of a capillary jet with linearly increasing axial velocity (with application to shaped charges). *Journal of Fluid Mechanics* **155**, 289–307.
- FRANKEL, I. & WEIHS, D. 1987 Influence of viscosity on the capillary instability of a stretching jet. *Journal of Fluid Mechanics* **185**, 361–383.
- GALLAIRE, F. & BRUN, P.-T. 2017 Fluid dynamic instabilities: theory and application to pattern forming in complex media. *Philosophical Transactions of the Royal Society A* **375** (2093), 20160155.
- GALLAIRE, F., MELIGA, P., LAURE, P. & BAROUD, C. N. 2014 Marangoni induced force on a drop in a Hele-Shaw cell. *Physics of Fluids* **26** (6), 062105.
- GARCÍA, F. J. & CASTELLANOS, A. 1994 One-dimensional models for slender axisymmetric viscous liquid jets. *Physics of Fluids* **6** (8), 2676–2689.
- GARNAUD, X., LESSHAFFT, L., SCHMID, P. J. & HUERRE, P. 2013 The preferred mode of incompressible jets: linear frequency response analysis. *Journal of Numerical Mathematics* **716**, 189–202.
- GASTER, M., KIT, E. & WYGNANSKI, I. 1985 Large-scale structures in a forced turbulent mixing layer. *Journal of Fluid Mechanics* **150**, 23–39.
- GONZÁLEZ, H. & GARCÍA, F. J. 2009 The measurement of growth rates in capillary jets. *Journal of Fluid Mechanics* **619**, 179–212.
- GUERRERO, J., GONZÁLEZ, H. & GARCÍA, F. J. 2016 Spatial modes in one-dimensional models for capillary jets. *Physical Review E* **93** (3), 033102.
- GUILLOT, P., COLIN, A., UTADA, A.S. & AJDARI, A. 2007 Stability of a jet in confined pressure-driven biphasic flows at low Reynolds numbers. *Physical Review Letters* **99** (10), 104502.
- GUMENNIK, A., WEI, L., LESTOQUOY, G., STOLYAROV, A.M., JIA, X., REKEMEYER, P.H., SMITH, M.J., LIANG, X., GRENA, B.J.-B., JOHNSON, S.G. & OTHERS 2013 Silicon-in-silica spheres via axial thermal gradient in-fibre capillary instabilities. *Nature Communications* **4**, 2216.
- HALPERN, D. & SECOMB, T. W. 1992 The squeezing of red blood cells through parallel-sided channels with near-minimal widths. *Journal of Fluid Mechanics* **244**, 307–322.
- HAMMOND, D. A. & REDEKOPP, L. G. 1997 Global dynamics of symmetric and asymmetric wakes. *Journal of Fluid Mechanics* **331**, 231–260.
- HARRJE, D. T. & REARDON, F. H. 1972 Liquid propellant rocket combustion instability. *NASA Special Publication* **194**.

- HE, M., EDGAR, J. S., JEFFRIES, G. D. M., LORENZ, R. M., SHELBY, J. P. & CHIU, D. T. 2005 Selective encapsulation of single cells and subcellular organelles into picoliter- and femtoliter-volume droplets. *Analytical Chemistry* **77** (6), 1539–1544.
- HEATON, C. J., NICHOLS, J. W. & SCHMID, P. J. 2009 Global linear stability of the non-parallel batchelor vortex. *Journal of Fluid Mechanics* **629**, 139–160.
- HECHT, F. 2012 New development in FreeFem++. *Journal of Numerical Mathematics* **20** (3-4), 251–265.
- HERBERT, T. 1988 Secondary instability of boundary layers. *Annual Review of Fluid Mechanics* **20** (1), 487–526.
- HIBIYA, T., NAKAMURA, S., MUKAI, K., NIU, Z.-G., IMAISHI, N., NISHIZAWA, S. I., YODA, S. I. & KOYAMA, M. 1998 Interfacial phenomena of molten silicon: Marangoni flow and surface tension. *Philosophical Transactions of the Royal Society of London. Series A: Mathematical, Physical and Engineering Sciences* **356** (1739), 899–909.
- HILBING, J. H. & HEISTER, S. D. 1996 Droplet size control in liquid jet breakup. *Physics of Fluids* **8** (6), 1574–1581.
- HILL, D. 1992 A theoretical approach for analyzing the restabilization of wakes. *30th Aerospace Sciences Meeting and Exhibit*.
- HINCH, E.J. 1991 *Perturbation Methods*. Cambridge University Press.
- HODGES, S. R., JENSEN, O. E. & RALLISON, J. M. 2004 Sliding, slipping and rolling: the sedimentation of a viscous drop down a gently inclined plane. *Journal of Fluid Mechanics* **512**, 95–131.
- VAN HOEVE, W., GEKLE, S., SNOEIJER, J. H., VERSLUIS, M., BRENNER, M. P. & LOHSE, D. 2010 Breakup of diminutive Rayleigh jets. *Physics of Fluids* **22** (12), 122003.
- HUERRE, A., THEODOLY, O., LESHANSKY, A. M., VALIGNAT, M.-P., CANTAT, I. & JULLIEN, M.-C. 2015 Droplets in microchannels: dynamical properties of the lubrication film. *Physical Review Letters* **115** (6), 064501.
- HUERRE, P. & MONKEWITZ, P.A. 1990 Local and global instabilities in spatially developing flows. *Annual Review of Fluid Mechanics* **22** (1), 473–537.
- HUERRE, P. & MONKEWITZ, P. A. 1985 Absolute and convective instabilities in free shear layers. *Journal of Fluid Mechanics* **159**, 151–168.
- HUERRE, P. & ROSSI, M. 1998 Hydrodynamic instabilities in open flows. *Collection alea saclay monographs and texts in statistical physics* **1** (3), 81–294.
- HWANG, Y., KIM, J. & CHOI, H. 2013 Stabilization of absolute instability in spanwise wavy two-dimensional wakes. *Journal of Fluid Mechanics* **727**, 346–378.

## Bibliography

---

- JAVADI, A., EGGERS, J., BONN, D., HABIBI, M. & RIBE, N. M. 2013 Delayed capillary breakup of falling viscous jets. *Physical Review Letters* **110**, 144501.
- KANDLIKAR, S. G. 2012 History, advances, and challenges in liquid flow and flow boiling heat transfer in microchannels: a critical review. *Journal of Heat Transfer* **134** (3), 034001.
- KARNIADAKIS, G. E., ISRAELI, M. & ORSZAG, S. A. 1991 High-order splitting methods for the incompressible Navier-Stokes equations. *Journal of Computational Physics* **97** (2), 414–443.
- KAUFMAN, J.J., TAO, G., SHABAHANG, S., BANAIEI, E.-H., DENG, D.S., LIANG, X., JOHNSON, S.G., FINK, Y. & ABOURADDY, A.F. 2012 Structured spheres generated by an in-fibre fluid instability. *Nature* **487** (7408), 463–467.
- KEISER, L., JAAFAR, K., BICO, J. & REYSSAT, É. 2018 Dynamics of non-wetting drops confined in a Hele-Shaw cell. *Journal of Fluid Mechanics* **845**, 245–262.
- KINGERY, W.D. 1959 Surface tension of some liquid oxides and their temperature coefficients. *Journal of the American Ceramic Society* **42** (1), 6–10.
- KLASEBOER, E., GUPTA, R. & MANICA, R. 2014 An extended Bretherton model for long Taylor bubbles at moderate capillary numbers. *Physics of Fluids* **26** (3), 032107.
- KOWALEWSKI, T. A. 1996 On the separation of droplets from a liquid jet. *Fluid Dynamics Research* **17** (3), 121–145.
- KROLL, P. & SCHULTE, H. J. 2006 Nano-sized crystals of silicon embedded in silica glass: large scale models and aspects of the electronic structure. *MRS Online Proceedings Library Archive* **958**.
- LAM, K. & LIN, Y.F. 2008 Large eddy simulation of flow around wavy cylinders at a subcritical Reynolds number. *International Journal of Heat and Fluid Flow* **29** (4), 1071–1088.
- LAM, K., LIN, Y.F., ZOU, L. & LIU, Y. 2012 Numerical study of flow patterns and force characteristics for square and rectangular cylinders with wavy surfaces. *Journal of Fluids and Structures* **28**, 359–377.
- LAMB, H. 1993 *Hydrodynamics*. Cambridge University Press.
- LAMSTAES, C. & EGGERS, J. 2017 Arrested bubble rise in a narrow tube. *Journal of Statistical Physics* **167** (3-4), 656–682.
- LANDAU, L. & LEVICH, B. 1942 Dragging of a liquid by a moving plate. *Acta Physicochimica URSS* **17** (42), 42–54.
- LANZERSTORFER, D. & KUHLMANN, H. C. 2012 Global stability of the two-dimensional flow over a backward-facing step. *Journal of Fluid Mechanics* **693**, 1–27.
- LE DIZÈS, S. & VILLERMAUX, E. 2017 Capillary jet breakup by noise amplification. *Journal of Fluid Mechanics* **810**, 281–306.

- LEE, S.-J. & NGUYEN, A.-T. 2007 Experimental investigation on wake behind a wavy cylinder having sinusoidal cross-sectional area variation. *Fluid Dynamics Research* **39** (4), 292.
- LEIB, S. J. & GOLDSTEIN, M. E. 1986 The generation of capillary instabilities on a liquid jet. *Journal of Fluid mechanics* **168**, 479–500.
- LHUISSIER, H., TAGAWA, Y., TRAN, T. & SUN, C. 2013 Levitation of a drop over a moving surface. *Journal of Fluid Mechanics* **733**, R4.
- LIN, Y.F., LAM, K., ZOU, L. & LIU, Y. 2013 Numerical study of flows past airfoils with wavy surfaces. *Journal of Fluids and Structures* **36**, 136–148.
- LING, Y., FULLANA, J.-M., POPINET, S. & JOSSE RAND, C. 2016 Droplet migration in a Hele-Shaw cell: effect of the lubrication film on the droplet dynamics. *Physics of Fluids* **28** (6), 062001.
- LIZZI, P. A. C. 2016 Capillary breakup of stretched liquid jets. PhD thesis, UC3M, Leganés.
- LOSCERTALES, I. G., BARRERO, A., GUERRERO, I., CORTIJO, R., MARQUEZ, M. & GANAN-CALVO, A. M. 2002 Micro/nano encapsulation via electrified coaxial liquid jets. *Science* **295** (5560), 1695–1698.
- MAGNINI, M., PULVIRENTI, B. & THOME, J. R. 2013 Numerical investigation of hydrodynamics and heat transfer of elongated bubbles during flow boiling in a microchannel. *International Journal of Heat and Mass Transfer* **59**, 451–471.
- MANTIĆ-LUGO, V. & GALLAIRE, F. 2016 Saturation of the response to stochastic forcing in two-dimensional backward-facing step flow: A self-consistent approximation. *Physical Review Fluids* **1** (8), 083602.
- MANTIĆ-LUGO, V., C., ARRATIA, C. & GALLAIRE, F. 2014 Self-consistent mean flow description of the nonlinear saturation of the vortex shedding in the cylinder wake. *Physical Review Letters* **113**, 084501.
- MARÍN, A. G., CAMPO-CORTÉS, F. & GORDILLO, J. M. 2009 Generation of micron-sized drops and bubbles through viscous coflows. *Colloids and Surfaces A: Physicochemical and Engineering Aspects* **344** (1-3), 2–7.
- MARQUET, O. & SIPP, D. 2010 Global sustained perturbations in a backward-facing step flow. *Seventh IUTAM Symposium on Laminar-Turbulent Transition* **18**, 525–528.
- MARQUET, O., SIPP, D. & JACQUIN, L. 2008 Sensitivity analysis and passive control of cylinder flow. *Journal of Fluid Mechanics* **615**, 221–252.
- MARTIN, G.D., HOATH, S.D. & HUTCHINGS, I.M. 2008 Inkjet printing-the physics of manipulating liquid jets and drops. *Journal of Physics: Conference Series* **105**, 012001.

## Bibliography

---

- MARTINEZ, M. J. & UDELL, K. S. 1990 Axisymmetric creeping motion of drops through circular tubes. *Journal of Fluid Mechanics* **210**, 565–591.
- MAXWORTHY, T. 1986 Bubble formation, motion and interaction in a Hele-Shaw cell. *Journal of Fluid Mechanics* **173**, 95–114.
- MEIBURG, E. 1989 Bubbles in a Hele-Shaw cell: Numerical simulation of three-dimensional effects. *Physics of Fluids A* **1** (6), 938–946.
- MEIER, G.E.A., KLÖPPER, A. & GRABITZ, G. 1992 The influence of kinematic waves on jet break down. *Experiments in Fluids* **12** (3), 173–180.
- MELIGA, P., BOUJO, E. & GALLAIRE, F. 2016 A self-consistent formulation for the sensitivity analysis of finite-amplitude vortex shedding in the cylinder wake. *Journal of Fluid Mechanics* **800**, 327–357.
- MELIGA, P., SIPP, D. & CHOMAZ, J.-M. 2010 Open-loop control of compressible afterbody flows using adjoint methods. *Physics of Fluids* **22** (5), 054109.
- MICHAEL, D.H. & WILLIAMS, P.G. 1976 The equilibrium and stability of axisymmetric pendent drops. *Proceedings of the Royal Society of London A* **351** (1664), 117–127.
- NAGEL, M. 2014 Modeling droplets flowing in microchannels. PhD thesis, EPFL, Lausanne.
- NICHOLS, J. & LELE, S. 2010 Global mode analysis of turbulent high-speed jets. *Annual Research Briefs 2010, Center for Turbulence Research*.
- OKUMURA, K. 2018 Viscous dynamics of drops and bubbles in Hele-Shaw cells: Drainage, drag friction, coalescence, and bursting. *Advances in Colloid and Interface Science* **255**, 64–75.
- ORON, A., DAVIS, S. H. & BANKOFF, S. G. 1997 Long-scale evolution of thin liquid films. *Reviews of Modern Physics* **69** (3), 931.
- PARK, C. W. & HOMSY, G. M. 1984 Two-phase displacement in Hele-Shaw cells: theory. *Journal of Fluid Mechanics* **139**, 291–308.
- PEARSON, J. R. A. & MATOVICH, M. A. 1969 Spinning a molten threadline. Stability. *Industrial & Engineering Chemistry Fundamentals* **8** (4), 605–609.
- PEREGRINE, D. H., SHOKER, G. & SYMON, A. 1990 The bifurcation of liquid bridges. *Journal of Fluid Mechanics* **212**, 25–39.
- PIER, B. 2002 On the frequency selection of finite-amplitude vortex shedding in the cylinder wake. *Journal of Fluid Mechanics* **458**, 407–417.
- PIER, B. & HUERRE, P. 2001 Nonlinear self-sustained structures and fronts in spatially developing wake flows. *Journal of Fluid Mechanics* **435**, 145–174.



- PIER, B., HUERRE, P. & CHOMAZ, J.-M. 2001 Bifurcation to fully nonlinear synchronized structures in slowly varying media. *Physica D: Nonlinear Phenomena* **148** (1), 49–96.
- PIER, B., HUERRE, P., CHOMAZ, J.-M. & COUAIRON, A. 1998 Steep nonlinear global modes in spatially developing media. *Physics of Fluids* **10** (10), 2433–2435.
- PIMBLEY, W. T. & LEE, H. C. 1977 Satellite droplet formation in a liquid jet. *IBM Journal of Research and Development* **21** (1), 21–30.
- PLATEAU, J. A. F. 1873 *Statique expérimentale et théorique des liquides soumis aux seules forces moléculaires*. Gauthier-Villars.
- PUJALS, G., DEPARDON, S. & COSSU, C. 2011 Transient growth of coherent streaks for control of turbulent flow separation. *International Journal of Aerodynamics* **1** (3-4), 318–336.
- RAYLEIGH, L. 1878 On the instability of jets. *Proceedings of the London Mathematical Society* **1** (1), 4–13.
- RAYLEIGH, LORD 1879 On the capillary phenomena of jets. *Proceedings of the Royal Society of London* **29** (196-199), 71–97.
- REICHERT, B., HUERRE, A., THEODOLY, O., VALIGNAT, M.-P., CANTAT, I. & JULLIEN, M.-C. 2018 Topography of the lubrication film under a pancake droplet travelling in a Hele-Shaw cell. *Journal of Fluid Mechanics* **850**, 708–732.
- REIS, P.M. 2015 A perspective on the revival of structural (in) stability with novel opportunities for function: From buckliphobia to buckliphilia. *Journal of Applied Mechanics* **82** (11), 111001.
- REYSSAT, E. 2014 Drops and bubbles in wedges. *Journal of Fluid Mechanics* **748**, 641–662.
- ROTELLO, V. M. 2004 *Nanoparticles: building blocks for nanotechnology*. Springer Science & Business Media.
- RUBIO-RUBIO, M., SEVILLA, A. & GORDILLO, J. M. 2013 On the thinnest steady threads obtained by gravitational stretching of capillary jets. *Journal of Fluid Mechanics* **729**, 471–483.
- RUTLAND, D. F. & JAMESON, G. J. 1971 A non-linear effect in the capillary instability of liquid jets. *Journal of Fluid Mechanics* **46** (2), 267–271.
- SAUTER, U. S. & BUGGISCH, H. W. 2005 Stability of initially slow viscous jets driven by gravity. *Journal of Fluid Mechanics* **533**, 237–257.
- SAVART, F. 1833 Wemoire sur la constitution des veines liquids lancees par des orifices circulaires en mince paroi. *Annales de Chimie* **53**, 337–386.
- SCHMID, P. J. 2007 Nonmodal stability theory. *Annual Review of Fluid Mechanics* **39** (1), 129–162.

## Bibliography

---

- SCHMID, P. J. & HENNINGSON, D. S. 2001 Stability and transition in shear flows.
- SEEMANN, R., BRINKMANN, M., PFOHL, T. & HERMINGHAUS, S. 2011 Droplet based microfluidics. *Reports on Progress in Physics* **75** (1), 016601.
- SENCHENKO, S. & BOHR, T. 2005 Shape and stability of a viscous thread. *Physical Review E* **71** (5), 056301.
- SERSON, D., MENEGHINI, J.R. & SHERWIN, S.J. 2017 Direct numerical simulations of the flow around wings with spanwise waviness. *Journal of Fluid Mechanics* **826**, 714–731.
- SEVILLA, A. 2011 The effect of viscous relaxation on the spatiotemporal stability of capillary jets. *Journal of Fluid Mechanics* **684**, 204–226.
- SEVILLA, A. & MARTINEZ-BAZAN, C. 2004 Vortex shedding in high Reynolds number axisymmetric bluff-body wakes: local linear instability and global bleed control. *Physics of Fluids* **16** (9), 3460–3469.
- SHIMOZURU, D. 1994 Physical parameters governing the formation of Pele's hair and tears. *Bulletin of Volcanology* **56** (3), 217–219.
- SHISHKIN, A.V. & BASIN, A.S. 2004 Surface tension of liquid silicon. *Theoretical Foundations of Chemical Engineering* **38** (6), 660–668.
- SINHA, S.N., GUPTA, A.K. & OBERAI, M. 1981 Laminar separating flow over backsteps and cavities. I-Backsteps. *AIAA journal* **19** (12), 1527–1530.
- SIPP, D. & MARQUET, O. 2013 Characterization of noise amplifiers with global singular modes: the case of the leading-edge flat-plate boundary layer. *Theoretical and Computational Fluid Dynamics* **27** (5), 617–635.
- SONG, H., CHEN, D. L. & ISMAGILOV, R. F. 2006 Reactions in droplets in microfluidic channels. *Angewandte Chemie International Edition* **45** (44), 7336–7356.
- SPALDING, D. B. 1972 A novel finite difference formulation for differential expressions involving both first and second derivatives. *International Journal for Numerical Methods in Engineering* **4** (4), 551–559.
- STOKES, G. G. 1898 Mathematical proof of the identity of the stream lines obtained by means of a viscous film with those of a perfect fluid moving in two dimensions. *Report of the Sixty-Eighth Meeting of the British Association for the Advancement of Science* **143**.
- STONE, H. A., STROOCK, A. D. & AJDARI, A. 2004 Engineering flows in small devices: microfluidics toward a lab-on-a-chip. *Annual Review of Fluid Mechanics* **36**, 381–411.
- SUBRAMANI, H. J., YEOH, H. K., SURYO, R., XU, Q., AMBRAVANESWARAN, B. & BASARAN, O. A. 2006 Simplicity and complexity in a dripping faucet. *Physics of Fluids* **18** (3), 032106.

- TAMMISOLA, O., GIANNETTI, F., CITRO, V. & JUNIPER, M.P. 2014 Second-order perturbation of global modes and implications for spanwise wavy actuation. *Journal of Fluid Mechanics* **755**, 314–335.
- TANNER, M. 1972 A method for reducing the base drag of wings with blunt trailing edge. *The Aeronautical Quarterly* **23** (1), 15–23.
- TANVEER, S. 1986 The effect of surface tension on the shape of a Hele-Shaw cell bubble. *Physics of Fluids* **29** (11), 3537–3548.
- TAYLOR, G. I. & SAFFMAN, P. G. 1959 A note on the motion of bubbles in a Hele-Shaw cell and porous medium. *The Quarterly Journal of Mechanics and Applied Mathematics* **12** (3), 265–279.
- TAYLOR, G. I. 1961 Deposition of a viscous fluid on the wall of a tube. *Journal of Fluid Mechanics* **10** (2), 161–165.
- TOMBAZIS, N. & BEARMAN, P.W. 1997 A study of three-dimensional aspects of vortex shedding from a bluff body with a mild geometric disturbance. *Journal of Fluid Mechanics* **330**, 85–112.
- TOMOTIKA, S. 1936 Breaking up of a drop of viscous liquid immersed in another viscous fluid which is extending at a uniform rate. *Proceedings of the Royal Society of London. Series A-Mathematical and Physical Sciences* **153** (879), 302–318.
- TREFETHEN, L. N., TREFETHEN, A. E., REDDY, S. C. & DRISCOLL, T. A. 1993 Hydrodynamic stability without eigenvalues. *Science* **261** (5121), 578–584.
- UMBANHOWAR, P.B., PRASAD, V. & WEITZ, D.A. 2000 Monodisperse emulsion generation via drop break off in a coflowing stream. *Langmuir* **16** (2), 347–351.
- UTADA, A. S., FERNANDEZ-NIEVES, A., STONE, H. A. & WEITZ, D. A. 2007 Dripping to jetting transitions in coflowing liquid streams. *Physical Review Letters* **99** (9), 094502.
- UTADA, A. S., LORENCEAU, E., LINK, D. R., KAPLAN, P. D., STONE, H. A. & WEITZ, D. A. 2005 Monodisperse double emulsions generated from a microcapillary device. *Science* **308** (5721), 537–541.
- VAILATI, A., ZINNATO, L. & CERBINO, R. 2012 How archer fish achieve a powerful impact: hydrodynamic instability of a pulsed jet in *Toxotes jaculatrix*. *Public Library of Science One* **7** (10), e47867.
- VAN DYKE, M. 1982 *An Album of Fluid Motion*. The Parabolic Press, Stanford, California, USA.
- VIOLA, F., ARRATIA, C. & GALLAIRE, F. 2016 Mode selection in trailing vortices: harmonic response of the non-parallel batchelor vortex. *Journal of Fluid Mechanics* **790**, 523–552.

## Bibliography

---

- WEIBEL, D. B., DiLUZIO, W. R. & WHITESIDES, G. M. 2007 Microfabrication meets microbiology. *Nature Reviews Microbiology* **5** (3), 209.
- WIJSHOFF, H. 2010 The dynamics of the piezo inkjet printhead operation. *Physics Reports* **491** (4-5), 77–177.
- WILLIAMS, C. 2006 Ink-jet printers go beyond paper. *Physics World* **19** (1), 24.
- XING, J. H., BOGUSLAWSKI, A., SOUCEMARIANADIN, A., ATTEN, P. & ATTANÉ, P. 1996 Experimental investigation of capillary instability: results on jet stimulated by pressure modulations. *Experiments in Fluids* **20** (4), 302–313.
- YAHASHI, M., KIMOTO, N., & OKUMURA, K. 2016 Scaling crossover in thin-film drag dynamics of fluid drops in the Hele-Shaw cell. *Scientific Reports* p. 31395.
- YILDIRIM, O. E., XU, Q. & BASARAN, O. A. 2005 Analysis of the drop weight method. *Physics of Fluids* **17** (6), 062107.
- YU, Y. E., ZHU, L., SHIM, S., EGGERS, J. & STONE, H. A. 2018 Time-dependent motion of a confined bubble in a tube: transition between two steady states. *Journal of Fluid Mechanics* **857**, R4.
- YUAN, Z. F., MUKAI, K., TAKAGI, K., OHTAKA, M., HUANG, W. L. & LIU, Q. S. 2002 Surface tension and its temperature coefficient of molten tin determined with the sessile drop method at different oxygen partial pressures. *Journal of Colloid and Interface Science* **254** (2), 338–345.
- ZDRAVKOVICH, M.M. 1981 Review and classification of various aerodynamic and hydrodynamic means for suppressing vortex shedding. *Journal of Wind Engineering and Industrial Aerodynamics* **7** (2), 145–189.
- ZHANG, K., KATSUCHI, H., ZHOU, D., YAMADA, H. & HAN, Z. 2016 Numerical study on the effect of shape modification to the flow around circular cylinders. *Journal of Wind Engineering and Industrial Aerodynamics* **152**, 23–40.
- ZHU, L. & GALLAIRE, F. 2016 A pancake droplet translating in a Hele-Shaw cell: lubrication film and flow field. *Journal of Fluid Mechanics* **798**, 955–969.

# Isha SHUKLA

## PERSONAL DATA

---

PLACE AND DATE OF BIRTH: India | 17 November 1987  
CURRENT ADDRESS: Chemin de Fontadel 31, Prilly-1008, Switzerland  
PHONE: +41 786 036 493  
EMAIL: [isha.shukla@epfl.ch](mailto:isha.shukla@epfl.ch) or [isha.shukla@gmail.com](mailto:isha.shukla@gmail.com)

## EDUCATION

---

2019	Ph.D in Mechanical Engineering, École Polytechnique Fédérale de Lausanne, Switzerland.
2014	Master in Mechanical Engineering, École Polytechnique Fédérale de Lausanne, Switzerland. (5.01/6)
2011	Bachelor in Mechanical Engineering, National Institute of Technology Durgapur, India. (9.38/10)

## WORK EXPERIENCE

---

2019	PhD thesis at Laboratory of Fluid Mechanics and Instabilities, École Polytechnique Fédérale de Lausanne, Switzerland. <i>“Response of noise-amplifier flows: From linear control to nonlinear jet breakup”.</i>
2015	Mechanical Engineer, SOLIDpower, Yverdon, Switzerland & GEM (Group of Energy Materials), École Polytechnique Fédérale de Lausanne, Switzerland.
2013	Summer Internship for Masters at European Organization for Nuclear Research(CERN), Switzerland. <i>“Strength and Thermal analysis of the components (Hybrid plate, clamping ring) of the HIE Isolde Project to be integrated in the new Superconducting Linear Accelerator (SC LINAC)”.</i>
2012	Executive Engineer at National Thermal Power Corporation limited (NTPC) Ltd., India. <i>“Training in operation, maintenance, commissioning, erection, protection and interlocks related to thermal power plants”.</i>
2010	Summer Internship for Bachelors at European Organization for Nuclear Research(CERN), Switzerland. <i>“Development and characterization of TGEMs and RETGEMs detectors for ALICE upgrade”.</i>

## PROFESSIONAL SKILLS

---

OS	Mac OS, LINUX, Windows.
Softwares	C/C++, Matlab, NEK5000, ANSYS Fluent, Belsim VALI, GAMBIT (basics) & OpenFOAM (basics).
Others	L <sup>A</sup> T <sub>E</sub> X, MS Office applications.

## ACADEMIC SKILLS

---

TA	<i>Production Management</i> (EPFL Master 2014-2015, by R. Glardon), <i>Numerical Flow Simulation</i> (EPFL Master 2015-2017, by M. Sawley), <i>Hydrodynamics</i> (EPFL Master 2015-2018, by F. Gallaire), <i>Fluid Flow</i> (EPFL Bachelor 2017, by F. Gallaire), <i>Two-phase flows and heat transfer</i> (EPFL Master 2018, by F. Gallaire).
Mentor	<i>Breakup of gravity-driven jets</i> (EPFL Master semester project 2018).

## PUBLICATIONS AS FIRST AUTHOR

---

- |      |   |
|------|---|
| 2019 | “Frequency selection in a gravitationally stretched capillary jet in the jetting regime”, (submitted in <i>Journal of Fluid Mechanics</i> ).            |
| 2019 | “Particle size selection in capillary instability of locally heated co-axial fiber”, <i>Physical Review Fluids</i> , 4, 064003.                         |
| 2019 | “Film thickness distribution in gravity-driven pancake-shaped droplets rising in a Hele-Shaw cell”, <i>Journal of Fluid Mechanics</i> , 874, 1021-1040. |
| 2011 | “Wall $y^+$ approach for dealing with the turbulent flow through a constant area duct”, <i>AIP Conference Proceedings</i> , 1440, 144-153.              |

## PUBLICATIONS AS SECOND AUTHOR

---

- |      |   |
|------|---|
| 2019 | “Optimal spanwise-periodic control for recirculation length in a backward-facing step flow”, (submitted in <i>Physical Review Fluids</i> ). |
|------|---|

## CONFERENCE TALKS

---

- |      |   |
|------|---|
| 2015 | “Optimisation of the design of SOFC systems with anode off-gas recirculation”, 28 <sup>th</sup> <i>International conference on Efficiency, Cost, Optimization, Simulation and Environmental Impact of Energy systems</i> (ECOS), Pau, France. |
| 2018 | “Gravity-driven pancake droplets in a Hele-Shaw cell: Film thickness distribution and effect of velocity on mean film thickness”, 12 <sup>th</sup> <i>European Fluid Mechanics Conference</i> (EFMC), Vienna, Austria.                        |

## AWARDS

---

- |      |  |
|------|--|
| 2011 | Second Position, Bachelors in Mechanical Engineering, National Institute of Technology Durgapur, India.                    |
| 2011 | Third Position, Bachelors (among all specialisations), National Institute of Technology Durgapur, India.                   |
| 2010 | Selected for the Summer Student program at European Organization for Nuclear Research (CERN), Geneva, Switzerland, 2010.   |
| 2010 | O.P Jindal Scholarship for the academic year 2009 for excellence in studies, leadership qualities and personality factors. |

## LANGUAGES

---

- |        |                             |
|--------|-----------------------------|
| FLUENT | English, Hindi and Bengali. |
| BASIC  | French (Level A2)           |



